Semi-classical description of matter wave interferometers and hybrid quantum systems

Semiklassische Beschreibung von Materiewellen-Interferometern und hybriden Quantensystemen
Zur Erlangung des Grades eines Doktors der Naturwissenschaften (Dr. rer. nat.)
genehmigte Dissertation von Dipl. Phys. Mathias Schneider aus Bad Schwalbach
Tag der Einreichung: 16. Dezember 2014, Tag der Prüfung: 16. Februar 2015
Darmstadt 2015 -- D 17

1. Gutachten: Prof. Dr. Reinhold Walser
2. Gutachten: Prof. Dr. Gernot Alber

TECHNISCHE
UNIVERSITÄT
DARMSTADT

Fachbereich Physik
Theoretische Quantendynamik / Institut für Angewandte Physik

Semi-classical description of matter wave interferometers and hybrid quantum systems
Semiklassische Beschreibung von Materiewellen-Interferometern und hybriden Quantensystemen

Genehmigte Dissertation von Dipl. Phys. Mathias Schneider aus Bad Schwalbach

1. Gutachten: Prof. Dr. Reinhold Walser
2. Gutachten: Prof. Dr. Gernot Alber

Tag der Einreichung: 16. Dezember 2014
Tag der Prüfung: 16. Februar 2015

Darmstadt 2015 -- D 17

Contents

1. **Introduction** 5

I. **Theoretical foundations** 7

2. **Classical description of atomic gases** 9
- 2.1. Hamiltonian mechanics . . . 9
  - 2.1.1. Propagators and Lie group formalism . . . 11
  - 2.1.2. Symplectic phase space notation . . . 13
- 2.2. Dynamics of statistical ensembles . . . 14
  - 2.2.1. From microscopic to macroscopic . . . 14
  - 2.2.2. Classical phase space distributions . . . 15
  - 2.2.3. Moments and cumulants . . . 18
  - 2.2.4. Special case: noninteracting particles . . . 20
- 2.3. Quadratic Hamiltonians and examples . . . 22
  - 2.3.1. Free propagation . . . 25
  - 2.3.2. Linear gravity . . . 28
  - 2.3.3. Harmonic oscillator . . . 29
- 2.4. Effective few-particle distributions . . . 30
  - 2.4.1. Reduced distributions . . . 32
  - 2.4.2. Time evolution and the BBGKY-hierarchy . . . 33
  - 2.4.3. Effective single-particle distributions . . . 35

3. **Quantum-mechanical description of atomic gases** 39
- 3.1. Brief reminder of basic single-particle quantum mechanics . . . 39
  - 3.1.1. Example: Release from harmonic trap . . . 42
- 3.2. Quantum mechanical phase space distributions . . . 46
  - 3.2.1. Single-particle Wigner function . . . 46
  - 3.2.2. Time evolution . . . 48
  - 3.2.3. Example: Release from harmonic trap II . . . 49
- 3.3. Interacting boson gases . . . 52
  - 3.3.1. Reduced distributions for binarily interacting gas of bosons . . . 52
  - 3.3.2. Mean field theory at zero temperature . . . 55

3.3.3. Wigner functions with mean field interaction 60

II. Applications 63

4. The Lambert density solution 65
4.1. Seperating anstatz solution to stationary Liouville equation with interaction 65
4.1.1. Energy and particle number of D-dimensional isotropic, harmonic systems 68
4.1.2. Extreme parameter regimes of the Lambert density 70
4.2. Comparison of the Lambert density to the Gross-Pitaevskii solution 76
4.3. The Lambert density of a thermal gas in a chip trap potential 78

5. Condensates in hybrid systems 85
5.1. Model 85
5.1.1. Modified hydrodynamic equations 85
5.1.2. Time and space dependence of immersed object 86
5.2. Perturbation theory 87
5.2.1. Local density approximation 88
5.3. First-order effects on BEC 89
5.3.1. Perturbation functions 89
5.3.2. Sound waves in one dimension 90
5.3.3. Beyond local density approximation 92
5.3.4. Particle loss 94

6. Phase space description of atom interferometers 97
6.1. Optical beam splitters for two-level atoms 98
6.1.1. Kapitza-Dirac diffraction 100
6.1.2. Bragg diffraction 102
6.2. Beam splitter in phase space 106
6.2.1. Beam splitter model 106
6.2.2. Formulation in terms of density matrices and Wigner functions 108
6.2.3. Obtaining the position density 113
6.3. Mach-Zehnder interferometer 118
6.3.1. Model for interferometer elements 119
6.3.2. Wave function formulation 120
6.3.3. Phase space formulation 121
6.3.4. Quadratic Hamiltonians 123
6.3.5. Example 1: Free evolution 128
6.3.6. Example 2: Linear gravity 135

7. Ray tracing with coherent matter waves in three dimensions 143
7.1. Ray tracing concepts . . . 143
7.1.1. Classical transport . . . 144
7.1.2. Non-classical interferometer elements . . . 145
7.1.3. Forward versus backward propagation . . . 149
7.2. Computing observables . . . 152
7.2.1. Pilot distributions . . . 153
7.2.2. Integrating phase space distributions . . . 156
7.2.3. Description of algorithm . . . 159
7.3. Results of simulating a Mach-Zehnder interferometer . . . 159
7.3.1. Interference fringes of an asymmetric interferometer . . . 162
7.3.2. Free expansion of interference fringes . . . 163
7.3.3. Symmetric interferometer with linear gravity . . . 168

Summary 171

III. Appendix 173

A. Gaussian distributions 175
A.1. Basic properties . . . 175
A.2. Integrals over arbitrary axes . . . 176
A.3. Hermite polynomials . . . 178
A.4. Gauss-Hermite quadrature . . . 178
A.5. Oscillating integrands with Gaussian-like envelope . . . 180

B. The Lambert function 183
B.1. Definition and approximations . . . 183
B.2. Useful integrals . . . 184

Bibliography 185

Zusammenfassung 197

Publications, Posters, and Talks 199

Curriculum vitae 201

Erklärung zur Dissertation 203

1 Introduction

Cold and ultra-cold neutral atoms in external traps have become a workhorse in modern atomic physics and quantum optics. A key aspect of these systems is their high controllability, allowing for investigation of fundamental questions as well as practical measurement devices with unprecedented precision.

An important milestone on the way to controlling atoms in a trap was the development of laser cooling. Noteworthy in this context are works of CHU, COHEN-TANNOUDJI, and PHILLIPS [1–3] who were awarded the NOBEL prize in 1997. The major breakthrough in cold-atom physics, however, was the experimental realization of BOSE-EINSTEIN condensation in atomic gases in 1995 [4–6] which was honored with the NOBEL prize in 2001, awarded to CORNELL, KETTERLE, and WIEMAN. The theoretical concept of this exotic state of matter dates back to the early days of quantum mechanics [7–9]. The availability of atomic condensates or ultra-cold atoms gathered a huge amount of interest and the number of related scientific publications exploded. Among these, many theoretical works closely followed experimental observations [10–16]. Basic results and general overviews on the physics of BOSE-EINSTEIN condensates are given in the books of PETHICK and SMITH [17], PITEVSKII and STRINGARI [18], and the review article of DALFOVO [19].

In the first decade of the new millenium, bulk research interest shifted from the condensate itself to sophisticated applications of it. Quite popular are systems of ultra-cold atoms in optical lattices [20, 21] which constitute versatile simulators of various quantum systems. Moreover, condesates are brought in contact with another quantum-mechanical object like microscopic cantilevers [22, 23] or carbon nanotubes [24–28] to name but a few. These are used both ways: to coherently manipulate, as well as to read out microscopic details of the contacted object. Last but not least, in fact being the main focus of this work, cold atoms are utilized for building matter wave interferometers [29, 30]. The availability of these devices, allowing measurements with unmatched precision, opened possibilities for novel experiments on fundamental questions [31, 32]. These include, for instance, measurements of the gravitational acceleration [33] and tests of the equivalence principle [34, 35]. In this spirit, the QUANTUS collaboration[1] (Quantengase unter Schwerelosigkeit) is working on platforms for studying cold atomic gases and matter wave interferometers in micro gravity [36–39]. Therefore, a freely falling capsule in the ZARM drop tower in Bremen (figure 1.1) is utilized as a host for experiments. Based on this, future plans involve cold gas experiments during a parabola flight on a sounding rocket.

A particular advantage of eliminating external influences, like gravitational acceleration, is the possibility of very long expansion times after releasing an atomic cloud from its trap. Numer-

---

[1] `http://www.iqo.uni-hannover.de/quantus.html`

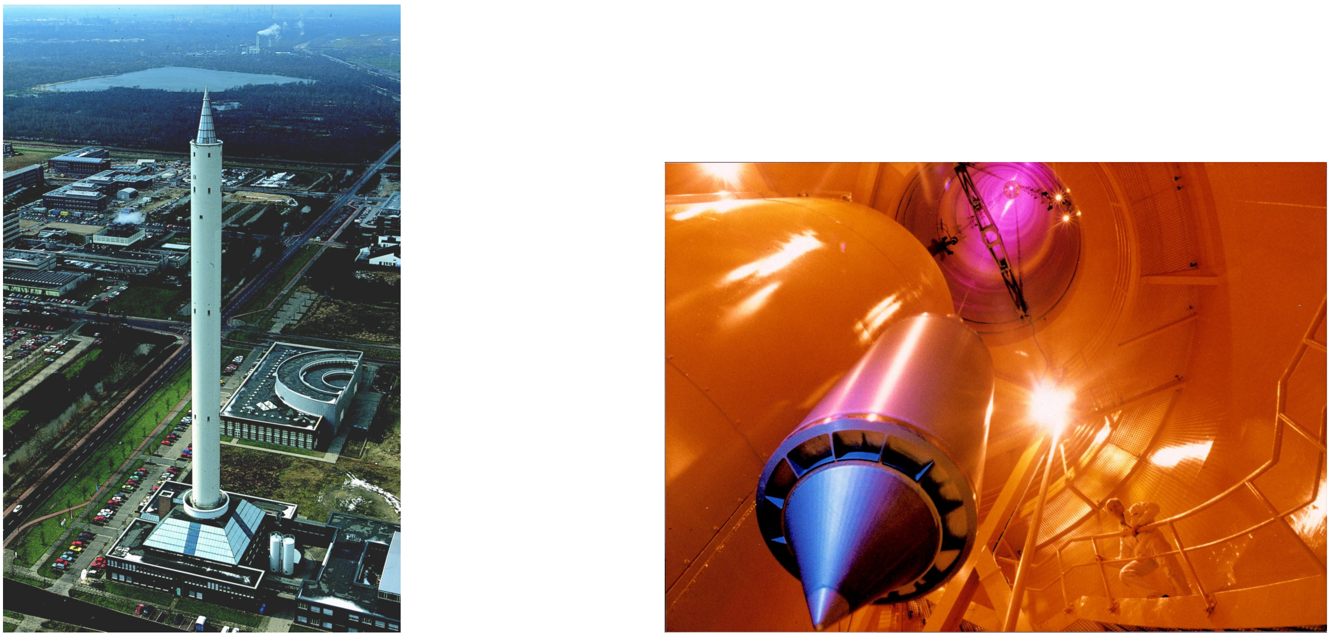

(a) Tower from the outside **(b)** Tower from the inside

Figure 1.1.: ZARM drop tower in Bremen

ically simulating these scenarios, however, brings forth some challenges. A micrometer-scaled initial distribution may expand over millimeters, requiring evaluation on grids that are finely spaced and cover large areas at the same time. One solution of this problem is the scaling approach, describing the time-dependent state in a co-expanding frame [40–43]. The ray tracing approach that is described and used in this work is based on a similar idea. The evolution of distribution function follows trajectories in phase space. These constitute a coordinate transformation that converts the initial state into the evolved one.

In the first part of this work, we present the theoretical background for describing the physics of atomic gases. The classical theory is discussed in chapter 2 while the quantum-mechanical formalism is considered in chapter 3. Next, in the applications-part, we start with studying a stationary solution of the nonlinear Liouville equation in chapter 4. The latter governs the dynamics of phase space distributions. Thereafter, we examine the influence of micro-mechanical objects (carbon nanotubes, fullerenes, etc.) on a condensate of atoms, using semi-classical hydrodynamic equations. Finally, the last two chapters are dedicated to matter wave interferometry. We present a formalism for describing the evolution of phase space distributions through an interferometer setup in chapter 6, before presenting a ray tracing formalism for simulating matter wave interferometers in chapter 7.

Part I.

Theoretical foundations

2 Classical description of atomic gases

Since a great deal of this work is based on the classical or semi-classical description of atomic clouds, we consider classical mechanics in this chapter, and its applications to atomic gases. Classical mechanics, as being taught in undergraduate courses, is covered by many textbooks. Among these, the undisputed standard is ’the GOLDSTEIN’ [44], comprising what could be called common knowledge for physicist. Moreover, the book of SCHECK [45] elaborates on the geometrical aspects of the subject and the contribution of ABRAHAM [46] concentrates on required mathematics. Especially important for this work, however, are the formal similarities between classical and quantum mechanics. These are nicely exposed in the book of BALESCU [47].

Our presentation of classical mechanics is organized as follows. First we recapitulate basic formulations and results of Hamiltonian mechanics in section 2.1. Using LIE-group formalism [48], expressions are already reminiscent to what is familiar from quantum mechanics. The truly striking analogies come about, when introducing distribution functions for classical ensembles in chapter 2.2. Next, in section 2.3, we discuss the important special case of quadratic systems. Nomenclature and results from this chapter will be used over and over again in the rest of this work. Finally, we show how a system of interacting particles can be described by effective few-particle distribution functions in section 2.4.

2.1 Hamiltonian mechanics

Consider a system of N particles moving through D-dimensional position space under the influence of an external potential V. In classical mechanics, the state of such a system is uniquely described by DN generalized coordinates $\underline{q} = (q_1, ..., q_{DN})$ and their time derivatives $\dot{\underline{q}}$. We leave the dimension of the problem D unspecified here because in addition to the realistic case of $D = 3$ it is often instructive to discuss simple one-dimensional models, $D = 1$. Moreover, in many cases, continuous symmetries may be exploited to construct effective models of reduced dimension.

In order to systematically obtain the equations of motion, one starts with writing down the LANGRANGE function of the system,

$$L(\underline{q}, \dot{\underline{q}}) = T(\dot{\underline{q}}) - V(\underline{q}), \tag{2.1}$$

being the difference between kinetic energy T and potential energy V. Of course, this is not the most general form of LANGRANGE functions one might encounter. For example, it does not describe the dynamics of charged particles in a magnetic field which would have required a velocity dependent potential energy, $V(\underline{q},\underline{\dot{q}})$. The form written above is, however, general enough to cover all systems that will be considered in this work.

Once the Lagrangian $L(\underline{q},\underline{\dot{q}})$ is known, one can calculate the generalized momenta as $p_i = \partial L/\partial \dot{q}_i$. Furthermore, the Hamilton function is obtained via a Legendre transform of the Langrange function,

$$H(\underline{q},\underline{p}) = \sum_{i=1}^{DN} \dot{q}_i p_i - L. \tag{2.2}$$

It plays a central role in classical mechanics for generating time evolution. This is expressed by Hamilton's equations

$$\dot{q}_i = \frac{\partial H(\underline{q},\underline{p})}{\partial p_i}, \tag{2.3a}$$

$$\dot{p}_i = -\frac{\partial H(\underline{q},\underline{p})}{\partial q_i}, \tag{2.3b}$$

providing equations of motion. Its solutions are closed trajectories in the $2DN$-dimensional *phase space* which is spanned by generalized positions q_i and associated conjugated momenta p_i. The entirety of all possible trajectories is called *phase space flow*. It may be represented as a function Φ, mapping phase space coordinates at a certain time instance onto time-evolved phase-space points at a later time instance, $(\underline{q},\underline{p},t) \to (\underline{q}',\underline{p}',t') \equiv \Phi(\underline{q},\underline{p};t_1,t_2)$. Alternatively, grouping the $2DN$ coordinates together to form a composite phase space vector $\underline{z} \equiv (\underline{q},\underline{p})$, one can express phase space flow by an operator

$$\underline{z}(t_1) \to \underline{z}(t_2) = \hat{\mathscr{U}}(t_1,t_2)\underline{z}(t_1), \tag{2.4}$$

acting on elements of the $2DN$-dimensional phase space. In general, this mapping is non-linear. Clearly, the only case where phase space flow can be adequately represented graphically, is for single-particle dynamics in one dimension, i.e. $D = 1$, $N = 1$, which implies a two-dimensional phase space.

A very useful characterization of trajectories is the action

$$S = \int_{t_i}^{t_j} \mathrm{d}t\, L\Big(\underline{q}(t),\underline{\dot{q}}(t),t\Big) \tag{2.5}$$

that is accumulated along the solution $(\underline{q}(t),\underline{\dot{q}}(t))$. It provides the notion of a length in phase space.

One central goal of classical mechanics (and any other theory) is to find expressions which describe the behavior of quantities that are – at least in principle – measurable. These quantities generally depend on all phase space coordinates. Obvious examples are the total energy, the total angular momentum of the system or, simply, positions and momenta of individual particles, q_i and p_i. All conceivable properties of a classical system can be described by real functions of $2DN$ phase space coordinates. They are called *dynamical functions* $a(\underline{q},\underline{p})$. It is straightforward, using HAMILTON's equations (2.3), to find the equation of motion for any arbitrary dynamical function to be

$$\dot{a} = -\{H,a\} = -\hat{\mathscr{L}}a. \tag{2.6}$$

We have used the POISSON bracket notation,

$$\{a,b\} = \sum_i \left(\frac{\partial a}{\partial q_i}\frac{\partial b}{\partial p_i} - \frac{\partial a}{\partial p_i}\frac{\partial b}{\partial q_i} \right), \tag{2.7}$$

to write the equation of motion (2.6) in a compact form. The action of the POISSON bracket containing the Hamiltonian on dynamical functions a can be compactly subsumed into the LIOUVILLE operator $\hat{\mathscr{L}} \equiv \{H,\cdot\}$. It is similar to a first-order differential operator, i.e. it is linear and satisfies the product rule.

2.1.1 Propagators and Lie group formalism

The evolution equation for dynamical functions (2.6) can be formally solved, writing

$$a(t) = \hat{\mathscr{U}}(t_0,t)\,a(t_0), \tag{2.8}$$

where we have defined the classical propagator as

$$\hat{\mathscr{U}}(t_0,t) = e^{-(t-t_0)\hat{\mathscr{L}}}. \tag{2.9}$$

Note that we have tacitly implied the Hamiltonian to be independent of time. Abandoning this constraint, the formal solution can be easily generalized, by replacing the product $\Delta t\,\hat{\mathscr{L}}$ with the integral $\int_0^{\Delta t} \mathrm{d}t\,\hat{\mathscr{L}}$. For notational convenience, however, we ignore any explicit time-dependence of the Hamiltonian in the current discussion. The operator $\hat{\mathscr{U}}$ constitutes the phase space mapping or phase space flow discussed above.

It is quite illuminating to consider some general mathematical properties of propagators. For instance, every $\hat{\mathscr{U}}$ that solves HAMILTON's equation must satisfy the relations

$$\hat{\mathscr{U}}(t,t)\,a(t) = a(t), \tag{2.10}$$

$$\hat{\mathscr{U}}(t_1,t_2)\,\hat{\mathscr{U}}(t_0,t_1)\,a(t_0) = \hat{\mathscr{U}}(t_0,t_2)\,a(t_0). \tag{2.11}$$

In prose, the former expression (2.10) states the existence of a neutral element that leaves subjected functions unaltered. It is the mathematical version of the trivial insight that system properties should not change when evolving them for a vanishing time span. The latter relation (2.11) says that subsequent application of propagators result in a composite propagator and, vice versa, every propagator can be subdivided with respect to consecutive time spans. Both features, (2.10) and (2.11), make the set of all $\hat{\mathscr{U}}(t)$ with $t \in \mathbb{R}$ a group or, to be more specific, the LIE group of time translations of dynamical phase space functions. The privileged function H is called the *generator* of the group.

Split operator approximation

If exact solutions are not available for a particular classical problem, one may exploit a specific form of the HAMILTON function to develop useful approximation schemes. Usually, the Hamiltonian is the sum of kinetic and potential energy, $H(\underline{z}) = T(\underline{p}) + V(\underline{q})$, where the former only depends on momenta and the latter only on positions. By virtue of the Liouvillian being linear, it can be split accordingly into two parts, $\hat{\mathscr{L}} = \hat{\mathscr{L}}_T + \hat{\mathscr{L}}_V$, also acting separately on positions and momenta. This decomposition of the LIOUVILLE operator can be utilized to draw conclusions about the form of the propagator, being the operator exponential

$$\hat{\mathscr{U}}(t) = \exp\left(-t(\hat{\mathscr{L}}_T + \hat{\mathscr{L}}_V)\right). \tag{2.12}$$

Indeed, operator exponentials like this have kind of a tradition in quantum mechanics [49]. Most famous in this regard is the BAKER-CAMPBELL-HAUSDORFF formula (BCH) [48, 50, 51] for joining the product of two operator exponentials into a single one. To third order, it reads

$$\exp(\hat{A})\,\exp(\hat{B}) = \exp\left(\hat{A} + \hat{B} + \tfrac{1}{2}[\hat{A},\hat{B}] + \tfrac{1}{12}[\hat{A},[\hat{A},\hat{B}]] + \tfrac{1}{12}[\hat{A},[\hat{B},\hat{B}]] + \ldots\right), \tag{2.13}$$

using the commutator $[\hat{A},\hat{B}] = \hat{A}\hat{B} - \hat{B}\hat{A}$. An expression which is dual to BCH is the ZASSENHAUS formula [50, 51], expanding the exponential of a sum of operators into a product of operator exponentials,

$$\exp(\hat{A}+\hat{B}) = \exp\left(\hat{A}\right)\,\exp\left(\hat{B}\right)\,\exp\left(-\tfrac{1}{2}[\hat{A},\hat{B}]\right)\,\exp\left(\tfrac{1}{3}[\hat{B},[\hat{A},\hat{B}]] + \tfrac{1}{6}[\hat{A},[\hat{A},\hat{B}]]\right)\cdot \ldots \quad . \tag{2.14}$$

With this recipe, one can expand the compact propagator (2.12) into expressions that are potentially more convenient for calculations. One prominent example of great importance is the construction of higher order symplectic integrators for numerical propagation of Hamiltonian systems [52]. To first order, for example, evolution about a small time span is approximately given as

$$\hat{\mathscr{U}}(t) = e^{-\hat{\mathscr{L}}t} \approx e^{-\frac{1}{2}\hat{\mathscr{L}}_V t} e^{-\hat{\mathscr{L}}_T t} e^{-\frac{1}{2}\hat{\mathscr{L}}_V t}. \tag{2.15}$$

Canonical transformations

One particularly useful feature of the introduced group of transformations is the invariance of the general structure of phase space dynamics. That is, if $a(t = t_i)$ satisfies HAMILTON's equations of motion (2.6) then so does $\hat{\mathscr{U}} a(t_j > t_i)$. This structure preserving feature is however not unique to time-evolution generated by H. In fact, every one-parameter group of transformations defined as

$$\left\{ e^{s\hat{\mathscr{L}}_G} \middle| s \in \mathbb{R} \right\}, \qquad\qquad \hat{\mathscr{L}}_G \, a = \{G, a\}, \tag{2.16}$$

i.e. that is generated by an arbitrary dynamical variable G, leaves equation (2.6) invariant. These structure preserving maps are called *canonical transformations*. In practice, they are often used to simplify or facilitate the solution of dynamical equations.

2.1.2 Symplectic phase space notation

The insight that phase space is the appropriate frame for describing classical dynamics suggests a formulation of HAMILTON's equations in terms of a unified phase space vector $\underline{z}$, instead of treating positions and momenta coordinates separately. Defining $\underline{z} = (\underline{q}, \underline{p})^{\mathsf{T}}$, equation (2.6) is expressed as

$$\begin{aligned} \dot{a} &= (\nabla_z a)^{\mathsf{T}} \, \mathsf{J} \, \nabla_z H \\ &= -(\nabla_z H)^{\mathsf{T}} \, \mathsf{J} \, \nabla_z a, \end{aligned} \tag{2.17}$$

containing the matrix representation of the Liouvillian

$$\hat{\mathscr{L}} = (\nabla_z H)^{\mathsf{T}} \, \mathsf{J} \, \nabla_z . \tag{2.18}$$

In these expressions, we have used the matrix representation of the symplectic form [45, 46]

$$\mathsf{J} = \begin{pmatrix} \mathbb{O} & \mathbb{1} \\ -\mathbb{1} & \mathbb{O} \end{pmatrix} \tag{2.19}$$

with identity $\mathbb{1}$ and zero matrix $\mathbb{O}$ of the DN-dimensional space. It can be interpreted as a metric in phase space which is skew-symmetric, $\mathsf{J}^{\mathsf{T}} = -\mathsf{J}$. Furthermore, considering a canonical transformation $z_i \to z_i' \equiv e^{s\hat{\mathscr{L}}_G} z_i$ with transformation matrix elements $\mathsf{U}_{ij} \equiv \partial z_i / \partial z_j'$ it can be shown that the identity

$$\mathsf{U}^{\mathsf{T}} \mathsf{J} \mathsf{U} = \mathsf{J} \tag{2.20}$$

is satisfied. Beyond that, any matrix J is called *symplectic* if it satisfies condition (2.20). Note that in general the transformation matrix U may depend on phase space coordinates. Only in case of a quadratic Hamiltonian, U is associated with a linear map. We elaborate on quadratic Hamiltonians in section 2.3.

2.2 Dynamics of statistical ensembles

The formalism discussed in the previous section is particularly suitable for describing single or few particle physics with negligible inner degrees of freedom, i.e. point-like or rigid bodies. However, considering macroscopic systems like crystal lattices or, in case of this work, atomic gases, one is confronted with several practical and conceptual problems. Subsection 2.2.1 provides a brief qualitative discussion of these problems, motivating the quantitative treatment in subsection 2.2.2. This will eventually lead to the concept of classical phase space distributions. The associated formalism bears some striking resemblances to the quantum mechanical formulation which will be presented in the following chapter.

2.2.1 From microscopic to macroscopic

Macroscopic systems are many-body systems with an astronomically high number of constituents. Even the clouds of cold and ultra-cold atoms that are produced in the laboratories typically consist of $10^3 \ldots 10^5$ atoms. Directly using the formalism of Hamiltonian mechanics as presented in the last section, we would have to solve differential equations with an exorbitant number of degrees of freedom. Neither analytical treatment, nor numerical computations are possible in such a microscopic description, respecting every particle.

In addition to overburdening complexity, there is another reason to seek a more effective description. In any experiment, one starts with preparing an initial state. This means the system of interest has to be controlled such that certain observables attain definite values. In terms of dynamical functions as defined in the last section, this would imply to have precise control on all particles, being able to reproduce a definite phase space configuration each time an experiment is started. In practice of course, initial many-body states are not prepared by microscopic control but rather by setting macroscopic conditions such as temperature, particle number, system boundaries, trapping potentials etc. Clearly, these conditions do not determine a unique microscopic configuration. They rather allow for a multitude of different configurations, each having a certain probability. The entity of all possible realizations with their associated probabilities is called an *statistical ensemble*. This way, we can assign a *macroscopic observable* to each dynamical function by summing over all values of $a(\underline{z})$ weighted with an associated probability factor.

Besides, aiming for realistic descriptions of N-particle systems in three dimensions, we will specify $D = 3$ in the following.

2.2.2 Classical phase space distributions

We want to cast the ideas formulated in the last subsection into a mathematical mapping from the microscopic to the macroscopic world. Based on the dynamical functions $a(\underline{z})$ living in $6N$-dimensional phase space, their macroscopic pendants shall be given by

$$A(\mathbf{x}) = \int \mathrm{d}^{6N}z \, a\left(\mathbf{x}\middle|\underline{z}\right) f^{(N)}(\underline{z}). \tag{2.21}$$

The classical N-particle phase space distribution function $f^{(N)}(\underline{z}) = f^{(N)}(\underline{q},\underline{p})$, which we have introduced here, assigns a probability factor to each configuration. Thus, we require it to be normalized,

$$\int \mathrm{d}^{6N}z \, f^{(N)}(\underline{z}) = 1. \tag{2.22}$$

Furthermore, being a probability distribution, f is positive for all phase space coordinates, $f^{(N)}(\underline{z}) \geq 0$.

An example for mapping (2.21) is the total energy. For the systems we are interested in, the energy in terms of microscopic phase space coordinates is given by the Hamilton function $a(\mathbf{x}|\underline{z}) = H(\underline{z})$. The energy in macroscopic description is just the expectation value of H that corresponds to a certain distribution function. Another example is the microscopic density of point-like particles, represented by a distribution of delta peaks,

$$n^{(\mathrm{mic})}(\mathbf{x}|\underline{z}) = \sum_{i=1}^{N} \delta(\mathbf{x} - \mathbf{x}_i), \tag{2.23}$$

where the vector $\mathbf{x}_i$ that comprises those coefficients of $\underline{z}$ that describe the position coordinates of the i-th particle. Clearly, this microscopic density is a highly irregular function, giving infinite values for $\mathbf{x} = \mathbf{x}_i$ and zero in between. Its macroscopic pendant according to definition (2.21) is the total particle number N, independent of a particular choice of the distribution $f^{(N)}$. Under macroscopic density $n(\mathbf{x})$, however, one usually understands the mean particle density at some point in space. To this end, one can define a coarse grained density, avaraging expression (2.23) over an extended area $\mathscr{A}$ in position space,

$$\tilde{n}^{(\mathrm{mic})}(\mathbf{x}|\underline{z}) = \frac{1}{||\mathscr{A}||} \int_{\mathscr{A}} \mathrm{d}^3x' \, n^{(\mathrm{mic})}(\mathbf{x} + \mathbf{x}'|\underline{z}), \tag{2.24}$$

with $||\mathscr{A}||$ denoting the volume of the area $\mathscr{A}$. Now, if the spatial extent of $\mathscr{A}$ is large enough to cover many particles on average but at the same time far smaller than macroscopic length scales on the order of, say, the system's size, the macroscopic density defined as

$$n(\mathbf{x}) = \int \mathrm{d}^{6N}z \, \tilde{n}^{(\mathrm{mic})}(\mathbf{x}|\underline{z}) f^{(N)}(\underline{z}), \tag{2.25}$$

is indeed a smooth function describing the particle density on macroscopic length scales.

Below, we will derive equations of motion for distribution functions using results from the last section. Note however that the form of the initial distribution f_0 cannot be explained with Hamiltonian mechanics in general. Arguments leading to particular f_0 usually involve irreversible, i.e. non-Hamiltonian processes. A popular example for finding a distribution exclusively with statistical arguments is the *canonical ensemble* [53]

$$f(\underline{z}) = \frac{\exp\left(-\frac{H(\underline{z})}{k_B T}\right)}{\int \mathrm{d}^{6N}z\ \exp\left(-\frac{H(\underline{z})}{k_B T}\right)} \tag{2.26}$$

valid for a systems in equilibrium with a thermal bath at temperature T. The BOLTZMANN constant is denoted k_B.

Time evolution

Suppose we have prepared the system such that the initial dynamical function a can be written as $a(\mathbf{x}|\underline{z}, t_0) \equiv a_0(\mathbf{x}|\underline{z})$. By definition (2.21), the corresponding macroscopic observable value at initial time instance is

$$A_0(\mathbf{x}) = A(\mathbf{x}, t = 0) = \int \mathrm{d}^{6N}z\ a_0(\mathbf{x}|\underline{z}) f_0^{(N)}(\underline{z}). \tag{2.27}$$

There are now two ways to formulate its time evolution.

First, making use of HAMILTON's equations, one may propagate the dynamical function $a(\mathbf{x}|\underline{z}, t) = \hat{\mathcal{U}}(t_0, t)\, a_0(\mathbf{x}|\underline{z})$, writing

$$A(\mathbf{x}, t) = \int \mathrm{d}^{6N}\underline{z}\ a_0\left(\mathbf{x} \,\middle|\, \hat{\mathcal{U}}(t)\underline{z}\right) f_0^{(N)}(\underline{z}). \tag{2.28}$$

This equation can be described as follows. The initial dynamical function a is expressed in terms of a collection of phase space points $\{\underline{z}_{0i}\}$. As the system evolves, these points are displaced according to the equations of motion, yielding a new dynamical function that emanates from the old one by following the trajectories,

$$a_0(\mathbf{x}|\underline{z}) \to a(\mathbf{x}|\underline{z}, t) = a_0\left(\mathbf{x} \,\middle|\, \hat{\mathcal{U}}(t)\underline{z}\right). \tag{2.29}$$

The associated weight factors $f_0^{(N)}(\underline{z})$, however, remain constant in time. Thinking of the distribution function $f^{(N)}$ as the classical analog to the quantum mechanical state, this formulation corresponds to the HEISENBERG picture of quantum mechanics, i.e., the states are constant while the observables evolve in time. Therefore, one can call this approach the Heisenberg picture of classical statistical mechanics.

The second alternative to formulate time evolution implies evolving distribution function and constant dynamical functions. It can be derived by substituting the evolved coordinates,

$$\underline{z} \to \underline{\tilde{z}} = \hat{\mathscr{U}}(t)\,\underline{z}. \tag{2.30}$$

Being a canonical transformation, the Jacobian of the coordinate transformation described by $\hat{\mathscr{U}}(t) = e^{-t\hat{\mathscr{L}}}$ is unity and thus the integral (2.28) can be transformed to

$$A(\mathbf{x}, t) = \int \mathrm{d}^{6N}\tilde{z}\; a_0(\mathbf{x}|\underline{\tilde{z}})\, f_0^{(N)}\left(\hat{\mathscr{U}}^{-1}(t)\,\underline{\tilde{z}}\right). \tag{2.31}$$

Indeed, we have expressed the time-dependent macroscopic observable value A in terms of a constant microscopic observable $a_0(\mathbf{x}\,|\,\underline{\tilde{z}})$ and a time-dependent distribution function

$$f^{(N)}(\underline{z}, t) = f_0^{(N)}\left(\hat{\mathscr{U}}^{-1}(t)\,\underline{z}\right). \tag{2.32}$$

This may be called the Schrödinger picture of classical statistical mechanics. It is of course equivalent to formulation (2.28). Equation (2.32) suggests a palpable notion of phase space dynamics. The values of a propagated distribution at certain phase space coordinates are given by the initial distribution evaluated at the back-propagated coordinates. The latter follow the solutions of Hamilton's equations as indicated by the propagator $\hat{\mathscr{U}}^{-1}$. In analogy to the previous section, where we discussed the evolution of dynamical variables in phase space, the time-dependence of the distribution function can also be cast into an evolution equation

$$\dot{f}^{(N)} = \{H, f^{(N)}\} = \hat{\mathscr{L}}\, f^{(N)}. \tag{2.33}$$

This is the famous Liouville equation of classical statistical mechanics. It is equivalent to Hamilton's equations. Moreover, the evolution of dynamical variables a, subject to Hamilton's equations (2.6), and the evolution of distribution functions $f^{(N)}$, subject to Liouville's equation (2.33), are generated by the same dynamical function, the Hamiltonian H. Mind, however, the opposite sign comparing equations (2.6) and (2.33). This sign change also comes to attention when comparing the equations of motion in the Heisenberg picture (2.28) and the Schrödinger picture (2.31). In prose, assume we know the initial distribution and want to compute its value for a certain phase space configuration at a later time. We can either (i) propagate the whole distribution *forward* in time via Liouville's equation (2.33) and plug in the desired point, or (ii) we take the phase space configuration we are interested in, propagate *backwards* in time utilizing Hamilton's equations (2.3), and look up the value of the initial distribution at the back-propagated phase space point.

The equivalence of Hamiltonian and Liouvillian holds only in case of conservative systems. While the former only exists for conserved total energy, it is possible to introduce generalizations of the Liouvillian, describing dynamics of non-conservative, e.g. dissipative, systems.

2.2.3 Moments and cumulants

Rather than explicitly writing the distribution function, it is often convenient to characterize f by small set of numbers. This may be achieved by calculating the moments of the distribution, given by

$$\left\langle \underline{z}^{\underline{m}} \right\rangle \equiv \int \mathrm{d}^{6N} z \prod_{n=1}^{6N} z_n^{m_n} f(\underline{z}), \tag{2.34}$$

where we have used tuple notation with $\underline{m} \equiv (m_1, ..., m_{6N})$. We may include the special case $\langle \underline{z}^{(0,...,0)} \rangle$ being just the normalization constant of the distribution. Linear moments,

$$\langle z_i \rangle = \int \mathrm{d}^{6N} z \, z_i \, f(\underline{z}), \tag{2.35}$$

simply yield the expectation value of the quantity z_i, for example the mean position or mean momentum of a single particle along a certain axis. In addition to that, second moments,

$$\left\langle z_i z_j \right\rangle = \int \mathrm{d}^{6N} z \, z_i z_j \, f(\underline{z}), \tag{2.36}$$

also contain information about the width of the distribution.

Efficiently describing distribution functions by a minimal set of numbers is best realized by considering the characteristic function and its expansion into cumulants [54]. The *characteristic function* is defined as FOURIER transform of the distribution,

$$\phi(\underline{s}) = \left\langle \exp(i\underline{s}^{\mathsf{T}}\underline{z}) \right\rangle = \int \mathrm{d}^{6N} z \ \exp(-i\underline{s}^{\mathsf{T}}\underline{z}) \, f(\underline{z}). \tag{2.37}$$

Expanding the logarithm of ϕ into increasing powers of $\underline{s}$, the *cumulants* $\langle\!\langle \underline{z}^{\underline{m}} \rangle\!\rangle$ are given as the expansion coefficients,

$$\ln \phi(\underline{s}) \equiv \sum_{M=1}^{\infty} i^{-M} \sum_{|\underline{m}|=M} \frac{1}{\underline{m}!} \underline{s}^{\underline{m}} \left\langle\!\left\langle \underline{z}^{\underline{m}} \right\rangle\!\right\rangle, \tag{2.38}$$

with $|\underline{m}| = m_1 + ... + m_{6N}$ and $\underline{m}! = m_1 \cdot ... \cdot m_{6N}$. This expression cannot be inverted to yield a general formula to calculate all cumulants. However, by simply comparing powers of $\underline{s}$ one can express, for instance, the three lowest cumulants in terms of moments,

$$\langle\!\langle z_i \rangle\!\rangle = \langle z_i \rangle \, , \tag{2.39}$$

$$\langle\!\langle z_i z_j \rangle\!\rangle = \left\langle z_i z_j \right\rangle - \langle z_i \rangle \left\langle z_j \right\rangle , \tag{2.40}$$

$$\langle\!\langle z_i z_j z_k \rangle\!\rangle = \langle z_i z_j z_k \rangle - \langle z_i z_j \rangle \langle z_k \rangle - \langle z_i z_k \rangle \langle z_j \rangle - \langle z_j z_k \rangle \langle z_i \rangle + 2 \langle z_i \rangle \langle z_j \rangle \langle z_k \rangle . \tag{2.41}$$

The great advantage of the cumulant expansion comes from the fact that in many practical cases either a limited number of cumulants contribute (cf. law of large numbers [53, 54]) or higher cumulants cannot be reliably determined due to limited number of measurements. Hence, all essential informations about a distribution are quite often covered by the first two cumulants. Hence, we can approximate the characteristic function as

$$\begin{aligned}\phi(\underline{s}) &\approx \exp\left[i \sum_i \langle\!\langle z_i \rangle\!\rangle s_i - \tfrac{1}{2} \sum_{ij} \langle\!\langle z_i z_j \rangle\!\rangle s_i s_j \right] \\ &\equiv \exp\left[i \bar{\underline{z}}^{\mathsf{T}} \underline{s} - \tfrac{1}{4} \underline{s}^{\mathsf{T}} \mathsf{C} \underline{s} \right] \qquad (2.42)\end{aligned}$$

defining the vector

$$\bar{\underline{z}} \equiv \langle\!\langle \underline{z} \rangle\!\rangle = \left(\langle\!\langle z_1 \rangle\!\rangle, \ldots, \langle\!\langle z_{6N} \rangle\!\rangle \right)^{\mathsf{T}} \qquad (2.43)$$

and the matrix

$$\mathsf{C} \equiv 2 \langle\!\langle \underline{z}\underline{z}^{\mathsf{T}} \rangle\!\rangle = 2 \begin{pmatrix} \langle\!\langle z_1 z_1 \rangle\!\rangle & \cdots & \langle\!\langle z_{6N} z_1 \rangle\!\rangle \\ \vdots & & \vdots \\ \langle\!\langle z_1 z_{6N} \rangle\!\rangle & \cdots & \langle\!\langle z_{6N} z_{6N} \rangle\!\rangle \end{pmatrix}. \qquad (2.44)$$

The distribution function associated with the characteristic function (2.42) is obtained by inverse FOURIER transformation, yielding a Gaussian in $6N$ dimensions

$$f(\underline{z}) \approx \frac{\exp\left[-(\underline{z} - \bar{\underline{z}})^{\mathsf{T}} \mathsf{C}^{-1} (\underline{z} - \bar{\underline{z}}) \right]}{\sqrt{\pi^{6N} \det \mathsf{C}}}. \qquad (2.45)$$

In the remainder of this work, we will write any Gaussian in the form of expression (2.45), explicitly revealing its first two cumulants[1]. We call C the *correlation matrix* and $\bar{\underline{z}}$ the *offset* of the distribution. Expression (2.45) can be easily generalized to the D-dimensional case, replacing the normalization factor $(\pi \det \mathsf{C})^{D/2}$ in the denominator of (2.45).

In many cases, Gaussian functions provide adequate (if not perfect) approximations to distributions that facilitate analytic treatment. They are therefore of great importance in a large number of theoretical models. Some useful properties are presented in appendix A.

---

[1] One might be bothered, by the factor of two in the definition of matrix C in (2.44) and the consequential absence of the factor 1/2 in the exponent of expression (2.45). This complies, however, to most of the literature on quantum mechanical harmonic oscillators (see e.g. [55, 56]) which write the Gaussian ground state wave function in the form $\psi_0(x) \propto \exp(-\frac{1}{2}x^2/a_{\mathrm{ho}}^2)$, with $a_{\mathrm{ho}}^2 = \hbar/(M\omega)$. The factor 1/2 disappears when calculating the absolute square, i.e. the position distribution.

2.2.4 Special case: noninteracting particles

One of the simplest models utilizing classical distribution functions is that of an ideal gas of N identical particles in an external potential. Discussing the distribution functions of a many-particle system, it is convenient to subdivide the phase space coordinates along all degrees of freedom, $\underline{z} = (z_1, ..., z_{6N})$, into groups of coordinates belonging to same particles,

$$\underline{z} = (\mathbf{z}_1, ..., \mathbf{z}_N) \qquad \text{with } \mathbf{z}_i = (\mathbf{x}_i, \mathbf{p}_i)^\mathsf{T}, \tag{2.46}$$

being the six-dimensional phase space coordinate of the i-th particle. This way, any N-particle distribution is a function of N single-particle coordinates,

$$f^{(N)}(\underline{z}) = f^{(N)}(\mathbf{z}_1, ..., \mathbf{z}_N). \tag{2.47}$$

One elementary mathematical requirement for functions describing classical distributions of identical particles is invariance under permutation of particles. It can be formulated simply as

$$f^{(N)}(..., \mathbf{z}_i, ..., \mathbf{z}_j, ...) = f^{(N)}(..., \mathbf{z}_j, ..., \mathbf{z}_i, ...).$$

Furthermore, neglecting interactions between particles, the Hamiltonian is written

$$\begin{aligned} H(\underline{z}) =& H_{\text{kin}}(\underline{z}) + H_{\text{trap}}(\underline{z}) \\ =& \sum_i \left(\frac{\mathbf{p}_i^2}{2M} + V_{\text{ext}}(\mathbf{x}_i) \right) \\ =& \sum_i h(\mathbf{z}_i), \end{aligned} \tag{2.48}$$

where V_{ext} denotes the trap potential or, generally, the trap potential plus all single-particle energies that may be involved in the system, e.g., gravity, superimposed optical lattices, etc. Expression (2.48) is merely a sum of single-particle terms which means that the dynamics of each particle is not influenced by the presence of the other particles. Since we require the Hamiltonian to be also symmetric under particle permutation, all single-particle contributions $h(\mathbf{z}_i)$ are indeed the same function evaluated at different phase space coordinates. In this model, loosely speaking, every particle evolves on his own, and thus one has to solve effectively a single-particle problem. Nevertheless, inter-particle interaction does enter the model when preparing, e.g., thermalized initial states. For the system to relax to thermal equilibrium, energy has to be exchanged between the system's constituents which is accomplished by mutual interactions. In case of an ideal gas, however, these interactions are assumed to be weak enough to not significantly influence the shape of the equilibrated distribution function or its dynamics. It is a powerful approximation for gases in a high temperature thermal state, where inter-particle distances are huge compared to typical interaction lengths.

We now specify the LOUIVILLE equation (2.33) for noninteracting distributions. In order to make the notation in following calculations more compact, we use the symbol ∂_i for differentiation with respect to the momentum coordinates of the i-th particle while ∇_i is exclusively reserved for spatial derivatives,

$$\partial_i \equiv \frac{\partial}{\partial \mathbf{p}_i}, \quad \nabla_i \equiv \frac{\partial}{\partial \mathbf{x}_i}. \tag{2.49}$$

Accordingly, the Hamiltonian (2.48) generates time evolution such that the distribution is subject to

$$\partial_t f^{(N)} = \sum_i \Big(-\frac{\mathbf{p}_i}{M} \nabla_i + (\nabla_i V_{\text{ext}})\, \partial_i \Big) f^{(N)}. \tag{2.50}$$

As mentioned above, we effectively deal with a single-particle problem. Thus, the N-particle distribution function $f^{(N)}$ is merely a product of N identical single-particle distributions,

$$f^{(N)}(\mathbf{z}_1, ..., \mathbf{z}_N) = \prod_{i=1}^{N} f(\mathbf{z}_i). \tag{2.51}$$

Again, by virtue of permutation symmetry, all single-particle contributions can be expressed as the same function evaluated at different coordinates. In this case, it is practical to work with an effective single-particle distribution, defined as

$$f(\mathbf{z}_1) = N \int \mathrm{d}^6 z_2 ... \mathrm{d}^6 z_N \, f^{(N)}(\mathbf{z}_1, ..., \mathbf{z}_N), \tag{2.52}$$

instead of $f^{(N)}$. Obviously, f is normalized to the total particle number N. The corresponding LIOUVILLE equation reads

$$\partial_t f = -\frac{\mathbf{p}}{M} \nabla f + (\nabla V_{\text{ext}}) \partial f. \tag{2.53}$$

The effective single-particle distribution is a function of only two three-dimensional coordinates, $f^{(1)}(\mathbf{x}, \mathbf{p})$. The description of many-particle problems with single-particle distributions will be discussed in detail in section 2.4.

The connection to the HEISENBERG picture can be drawn by considering the total time derivative of the distribution $\mathrm{d}f/\mathrm{d}t$. Plugging in equation (2.53) for the partial time derivative yields

$$\frac{\mathrm{d}f}{\mathrm{d}t} = (\dot{\mathbf{x}} - \partial H) \cdot \nabla f + (\dot{\mathbf{p}} + \nabla H) \cdot \partial f. \tag{2.54}$$

Clearly, the round brackets vanish if HAMILTON's equations (2.3) are satisfied. It implies that the values of the phase space distribution remain constant along the trajectories generated by

Hamiltonian dynamics. This notion can be expressed more manifestly by writing the solution of (2.54) as

$$f(\mathbf{x},\mathbf{p},t) = \int \mathrm{d}^3x' \, \mathrm{d}^3p' \, \delta\Big(\mathbf{X}(\mathbf{x},\mathbf{p},t) - \mathbf{x}'\Big) \, \delta\Big(\mathbf{P}(\mathbf{x},\mathbf{p},t) - \mathbf{p}'\Big) \, f_0(\mathbf{x}',\mathbf{p}'). \tag{2.55}$$

Here, we have utilized the coordinates of the classical trajectories, **X** and **P**, traveling backwards in time, being solutions of HAMILTON's equations

$$-\dot{\mathbf{X}} = \frac{\partial H}{\partial \mathbf{p}}, \qquad -\dot{\mathbf{P}} = -\frac{\partial H}{\partial \mathbf{x}}, \tag{2.56}$$

with initial conditions

$$\mathbf{X}(\mathbf{x},\mathbf{p},0) = \mathbf{x}, \qquad \mathbf{P}(\mathbf{x},\mathbf{p},0) = \mathbf{p}. \tag{2.57}$$

This relationship provides the basis for our ray tracing approach formulated in chapter 7.

2.3 Quadratic Hamiltonians and examples

In this section, we examine systems that are described by quadratic noninteracting Hamiltonians. These are well suited for analytical treatment and will hence be used again and again in the rest of this work to provide illustrative examples as well as benchmarks for numerical algorithms. Moreover, classical trajectories that are associated with quadratic HAMILTON functions have been used extensively to describe semi-classical propagation of matter-waves [57, 58].

In its most general form, a quadratic single-particle Hamiltonian is written

$$H(\mathbf{z}) = \tfrac{1}{2}\,\mathbf{z}^{\mathsf{T}}\Lambda\,\mathbf{z} + \boldsymbol{\lambda}^{\mathsf{T}}\mathbf{z}. \tag{2.58}$$

The symmetric matrix Λ has real elements. Its associated bilinear form $\mathbf{z}^{\mathsf{T}}\Lambda\,\mathbf{z}$ can be divided into three parts, one that is quadratic in position, $\mathbf{x}^{\mathsf{T}}\Lambda_{xx}\,\mathbf{x}$, one that is quadratic in momentum, $\mathbf{p}^{\mathsf{T}}\Lambda_{pp}\,\mathbf{p}$, and one that contains both to linearly, $\mathbf{p}^{\mathsf{T}}\Lambda_{xp}\,\mathbf{p}$. Clearly, Λ_{pp} corresponds to the kinetic energy implying $\Lambda = \mathbb{1}/M$. Similarly, Λ_{xx} can be easily deduced from the quadratic potential. Moreover, the linear term that is proportional to the real vector $\boldsymbol{\lambda}$ covers linear potentials causing constant acceleration of particles. With these definitions, HAMILTON's equations can be expressed as

$$\dot{\mathbf{z}} = \mathsf{J}\,\Lambda\,\mathbf{z} + \mathsf{J}\,\boldsymbol{\lambda}. \tag{2.59}$$

It is a linear inhomogeneous ordinary differential equation of first order. With initial condition $\mathbf{z}(t_0) = \mathbf{z}_0$, equation (2.59) is solved [59] by an affine transformation

$$\mathbf{z}(t) = \hat{\mathscr{U}}_{(t-t_0)}\,\mathbf{z}_0 = \mathsf{U}_{(t-t_0)}\,\mathbf{z}_0 + \overline{\mathbf{z}}_{(t-t_0)}. \tag{2.60}$$

The first part, $\mathsf{U}\mathbf{z}_0$, is a solution of the homogeneous equation $\dot{\mathbf{z}} = \mathsf{J}\Lambda\mathbf{z}$ while the second part, $\bar{\mathbf{z}}$, is a particular solution of the inhomogeneous equation. Plugging this ansatz into (2.59) yields evolution equations for the time-dependent transformation matrix and offset vector,

$$\frac{\mathrm{d}}{\mathrm{d}t}\mathsf{U} = \mathsf{J}\Lambda\mathsf{U} \tag{2.61}$$

$$\frac{\mathrm{d}}{\mathrm{d}t}\left(\mathsf{U}^{-1}\bar{\mathbf{z}}\right) = \mathsf{U}^{-1}\mathsf{J}\boldsymbol{\lambda}. \tag{2.62}$$

For finding the second equation, one has to exploit the symplectic relation (2.20) to write the inverse propagation matrix as $\mathsf{U}^{-1} = \mathsf{J}^{\mathsf{T}}\mathsf{U}^{\mathsf{T}}\mathsf{J}$ having the time derivative $(\mathrm{d}/\mathrm{d}t)\mathsf{U}^{-1} = -\mathsf{U}^{-1}\dot{\mathsf{U}}\mathsf{U}^{-1}$. The first equation is readily solved by

$$\mathsf{U}(t-t_0) = e^{(t-t_0)\mathsf{J}\Lambda}, \tag{2.63}$$

while the second yields

$$\bar{\mathbf{z}}(t-t_0) = \mathsf{U}(t-t_0)\int_0^{t-t_0}\mathrm{d}t'\,\mathsf{U}^{-1}(t')\,\mathsf{J}\boldsymbol{\lambda} \tag{2.64}$$

In analogy to the abcd-formalism in geometrical optics [60], any propagation matrix can be separated into four blocks, two that exclusively act on positions and momenta, respectively, and two that mix position and momentum coordinates. One writes explicitly

$$\mathsf{U} \equiv \begin{pmatrix} \mathsf{a} & \mathsf{b} \\ \mathsf{c} & \mathsf{d} \end{pmatrix}. \tag{2.65}$$

Going from the Heisenberg to the Schrödinger picture of classical mechanics, one also needs to know the inverse of the propagation matrix,

$$\mathbf{z}(t_i) = \mathsf{U}^{-1}(t_{ij})\left(\mathbf{z}(t_j) - \Delta\mathbf{z}(t_{ij})\right). \tag{2.66}$$

Using the symplectic relation (2.20) and the abcd-matrix expression according to equation (2.65), the inverse propagation matrix can be written as

$$\mathsf{U}^{-1} = \mathsf{J}^{\mathsf{T}}\mathsf{U}^{\mathsf{T}}\mathsf{J} = \begin{pmatrix} \mathsf{d}^{\mathsf{T}} & -\mathsf{b}^{\mathsf{T}} \\ -\mathsf{c}^{\mathsf{T}} & \mathsf{a}^{\mathsf{T}} \end{pmatrix}. \tag{2.67}$$

Evolution of distribution functions

Since we assumed our quadratic Hamiltonian to be free of interactions between particles, we may consider the effective single-particle distribution f as a representation for the system's dynamics. Knowing the initial distribution function f_0 at time instance $t_0 = 0$, according to the HEISENBERG picture, its time-evolved version is given by

$$f(\mathbf{z}, t) = f_0\left(\hat{\mathcal{U}}^{-1}(t)\,\mathbf{z}\right) = f_0\Big(\mathsf{U}^{-1}(t)\,(\mathbf{z} - \bar{\mathbf{z}}(t))\Big). \tag{2.68}$$

Although this relation is true for any distribution function, it is most convenient to consider Gaussians. Suppose we write the initial distribution as

$$f_0(\mathbf{z}) = N\,\frac{\exp\left(-\mathbf{z}^{\mathsf{T}}\,\mathsf{C}_{z0}^{-1}\,\mathbf{z}\right)}{\sqrt{\pi^6 \det \mathsf{C}_{z0}}}, \tag{2.69}$$

with C_{z0} being the correlation matrix (2.44). By virtue of the evolution being described by an affine transformation, the distribution will remain Gaussian after propagating for a time span t,

$$f(\mathbf{z}, t) = N\,\frac{\exp\left[-(\mathbf{z} - \bar{\mathbf{z}}(t))^{\mathsf{T}}\,\mathsf{C}_z^{-1}(t)\,(\mathbf{z} - \bar{\mathbf{z}}(t))\right]}{\sqrt{\pi^6 \det \mathsf{C}(t)}}. \tag{2.70}$$

The inverse of the time-evolved correlation matrix is given by

$$\mathsf{C}_z^{-1}(t) = \mathsf{U}^{-1\mathsf{T}}(t)\,\mathsf{C}_{z0}^{-1}\,\mathsf{U}^{-1}(t). \tag{2.71}$$

Knowing the propagated distribution, one can calculate physical observables as integrals over f times a dynamical function. Permanently reoccurring examples are position and momentum density, $n(\mathbf{x}) = \int \mathrm{d}^3p\ 1\,f(\mathbf{z})$, $n(\mathbf{p}) = \int \mathrm{d}^3x\ 1\,f(\mathbf{p})$ or distribution momenta $\langle \mathbf{x}^m \rangle = \int \mathrm{d}^6z\ \mathbf{x}^m f(\mathbf{z})$. In case of Gaussian distributions, the result of integration over some (not all) axes can again be expressed with a Gaussian having an effective correlation matrix. The latter lives in the subspace that has not been integrated. For example, being interested in the position density, we divide the inverse phase space correlation matrix into four blocks,

$$\mathsf{C}_z^{-1} = \begin{pmatrix} \mathsf{A}_{xx} & \mathsf{A}_{xp} \\ \mathsf{A}_{px} & \mathsf{A}_{pp} \end{pmatrix}, \tag{2.72}$$

acting on position and momentum subspaces and mixing them, respectively. From $\mathsf{C}_z^{\mathsf{T}} = \mathsf{C}$ follows $\mathsf{A}_{xx} = \mathsf{A}_{xx}^{\mathsf{T}}$, $\mathsf{A}_{pp} = \mathsf{A}_{pp}^{\mathsf{T}}$, and $\mathsf{A}_{px} = \mathsf{A}_{xp}^{\mathsf{T}}$. According to section A.2, the density can then be written as

$$n(\mathbf{x}) = N\,\frac{\exp\left[(\mathbf{x} - \bar{\mathbf{x}})^{\mathsf{T}}\,\mathsf{C}_x^{-1}\,(\mathbf{x} - \bar{\mathbf{x}})\right]}{\sqrt{\pi^3 \det \mathsf{C}_x}}, \tag{2.73}$$

with the inverse effective correlation matrix

$$\mathsf{C}_x^{-1} \equiv \mathsf{A}_{xx} - \mathsf{A}_{xp}\,\mathsf{A}_{pp}^{-1}\,\mathsf{A}_{px}. \tag{2.74}$$

A prominent example for Gaussian distributions is the preparation of a thermal state in a harmonic trap potential $V_{\text{ext}}(\mathbf{x}) = (M/2)\,\mathbf{x}^{\mathsf{T}}\Omega^{\mathsf{T}}\mathbf{x}$ with temperature T. In this case, the initial condition is given by the canonical ensemble (2.26) in a harmonic oscillator, obtaining

$$f_0(\mathbf{z}) = N\left(\frac{\det\Omega^2}{2\pi k_B T}\right)^3 \exp\left[-\tfrac{1}{2k_B T}\left(M\,\mathbf{x}^{\mathsf{T}}\Omega^2\mathbf{x} + \tfrac{1}{M}\mathbf{p}^2\right)\right]. \tag{2.75}$$

Obviously, the phase space correlation matrix is

$$\mathsf{C}_{z0} = \begin{pmatrix} \frac{2k_B T}{M}\,\Omega^{-2} & \mathbb{0} \\ \mathbb{0} & 2Mk_B T\,\mathbb{1} \end{pmatrix} = \begin{pmatrix} \mathsf{C}_{x0} & \mathbb{0} \\ \mathbb{0} & \mathsf{C}_{p0} \end{pmatrix}. \tag{2.76}$$

The matrices that define distribution in the position and momentum subspaces are not independent from each other. They are related by $\mathsf{C}_{p0} = (M\,\Omega)^2\,\mathsf{C}_{x0}$. Calculation of the density profile, associated to the distribution (2.75), is straightforward. One obtains

$$n_0(\mathbf{x}) = N\,\left(\tfrac{M\det\Omega^2}{2\pi k_B T}\right)^{3/2}\, e^{-\frac{M}{2k_B T}\,\mathbf{x}^{\mathsf{T}}\Omega^2\mathbf{x}}. \tag{2.77}$$

Having a phase space correlation matrix of the form (2.76), we can directly use its “position block” C_{x0} to express the position density.

Expression (2.75) is referred to as MAXWELL-BOLTZMANN distribution. Consequently, we call (2.77) the MAXWELL-BOLTZMANN density.

2.3.1 Free propagation

The most simple system is realized by a freely moving particle without inner structure. In the absence of external potentials, the Hamiltonian is merely the kinetic energy, $H = \mathbf{p}^2/(2M)$, and consequently, HAMILTON’s equations read

$$\dot{\mathbf{x}} = \frac{\mathbf{p}}{M}, \qquad \dot{\mathbf{p}} = \mathbf{0}. \tag{2.78}$$

In terms of the general quadratic Hamiltonian expressed in (2.58), we have

$$\Lambda = \begin{pmatrix} \mathbb{0} & \mathbb{0} \\ \mathbb{0} & \frac{\mathbb{1}}{M} \end{pmatrix}, \qquad \boldsymbol{\lambda} = \begin{pmatrix} \mathbf{0} \\ \mathbf{0} \end{pmatrix}, \tag{2.79}$$

with $\mathbb{1}$ and $\mathbb{O}$ denoting 3×3 unity and zero matrix, respectively, and $\mathbf{0}$ being a vector of zeros. Consequently, evolution is described by a matrix multiplication $\mathbf{z}(t_j) = \mathsf{U}(t_{ij})\,\mathbf{z}(t_i)$ with $t_{ij} = t_j - t_i$ for which one finds

$$\mathsf{U}(t) = \begin{pmatrix} \mathbb{1} & \frac{\mathbb{1}}{M} t \\ \mathbb{O} & \mathbb{1} \end{pmatrix}. \tag{2.80}$$

This matrix displaces only the position coordinate, with the displacement distance depending on the momentum coordinate. The latter remain constant during evolution. Inverting the free propagator $\mathsf{U}(t)$ means changing the sign of the time parameter,

$$\mathsf{U}^{-1}(t) = \mathsf{U}(-t) = \begin{pmatrix} \mathbb{1} & -\frac{\mathbb{1}}{M} t \\ \mathbb{O} & \mathbb{1} \end{pmatrix}. \tag{2.81}$$

Thus, finding the evolved distribution is quite simple. We obtain

$$f(\mathbf{x}, \mathbf{p}, t) = f_0\left(\mathbf{x} - \tfrac{1}{M}\mathbf{p}\, t,\ \mathbf{p}\right). \tag{2.82}$$

Geometrically speaking, it has been sheared in comparison to its preceding version. The phase space flow is illustrated in figure 2.1.

Concerning the correlation matrix of Gaussians, we assume the initial distribution to be described by C_{z0} as given in (2.76). Consequently, applying prescription (2.71), the inverse of the propagated phase space correlation matrix reads

$$\mathsf{C}_z^{-1}(t) = \begin{pmatrix} \mathsf{C}_{x0}^{-1} & -\frac{1}{M}\mathsf{C}_{x0}^{-1}\, t \\ -\frac{1}{M}\mathsf{C}_{x0}^{-1}\, t & \mathsf{C}_{p0}^{-1} + \frac{1}{M^2}\mathsf{C}_{x0}^{-1}\, t^2 \end{pmatrix}. \tag{2.83}$$

The corresponding effective correlation matrix in position space is found to be

$$\begin{aligned} \mathsf{C}_x(t) &= \mathsf{C}_{x0} + \mathbb{1}\frac{2k_\mathrm{B}T}{M}\, t^2 \\ &= \mathsf{C}_{x0} + \tfrac{1}{M^2}\mathsf{C}_{p0}\, t^2 \\ &= \left(\mathbb{1} + \Omega^2 t^2\right)\mathsf{C}_{x0}. \end{aligned} \tag{2.84}$$

It describes an isotropically spreading position density profile. This means that any initially anisotropic distribution becomes isotropic as $t \to \infty$. The spreading of a freely evolving density profile can be conveniently pictured for one dimension. In this case, one replaces the correlation matrix C_x and the potential matrix Ω by the squared scalar-valued width σ_x^2 and the squared scalar-valued frequency ω^2, respectively. The time-dependent width,

$$\sigma_x(t) = \sqrt{1 + \omega^2 t^2}\, \sigma_{x0}, \tag{2.85}$$

is plotted in figure 2.2. On the other hand, the distribution in momentum space remains the same. This means correlation matrix as well as center of mass are unaltered in momentum subspace by free propagation, $\mathsf{C}_p(t) = \mathsf{C}_{p0}$ and $\overline{\mathbf{p}}(t) = \overline{\mathbf{p}}(0)$.

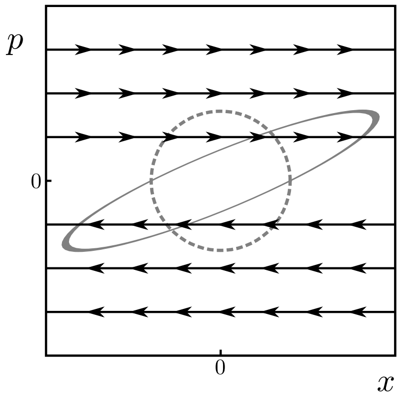

Figure 2.1.: Phase portrait of free propagation. Trajectories are parallel to the position axis. Distributions, sketched with gray lines, are sheared.

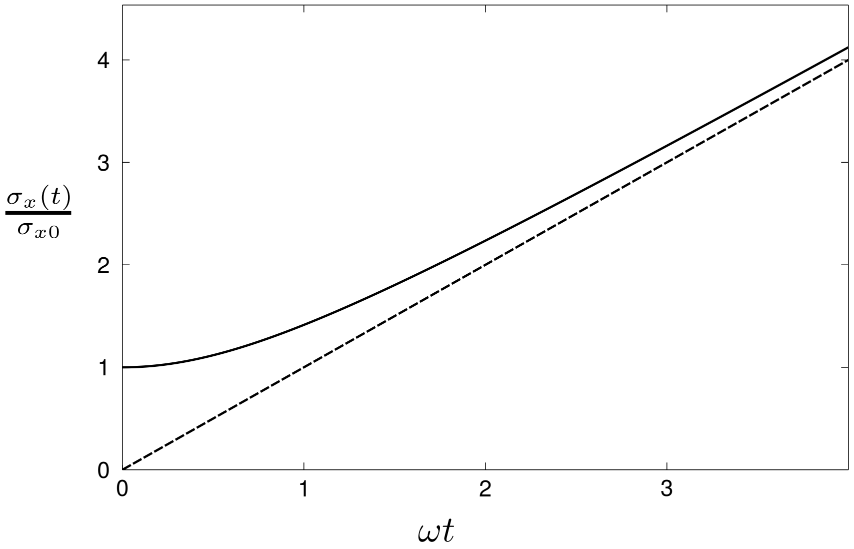

Figure 2.2.: Time-dependent width of a one-dimensional Gaussian distribution in position space according to equation (2.85). The initial state is confined in a harmonic potential with frequency ω. Dashed lines indicate the asymptotic limit $\sigma_{x(t\to\infty)} = \sigma_{x0}\,\omega t$.

2.3.2 Linear gravity

Most systems that evolve without spatial confinement are not truly free but experience constant acceleration by the earth's gravity. Being sufficiently far from the gravity center, say at least the radius of the earth, the potential is very well approximated by a linear term and the Hamiltonian reads $H = \mathbf{p}^2/(2M) + Mg\,x_3$. Here we have chosen a typical coordinate system in which the gravitational acceleration is aligned with the x_3 component. Ignoring the first two components, we can discuss an effective one-dimensional system being described by

$$\dot{x} = \frac{p}{M}, \qquad \dot{p} = -Mg. \tag{2.86}$$

Thus, instead of a six-dimensional phase space we consider a two-dimensional one with elements $\mathbf{z} = (x, p)^\mathsf{T}$. In terms of general quadratic Hamiltonians, we assign

$$\Lambda = \begin{pmatrix} 0 & 0 \\ 0 & \frac{1}{M} \end{pmatrix}, \qquad \boldsymbol{\lambda} = \begin{pmatrix} 0 \\ Mg \end{pmatrix}, \tag{2.87}$$

which implies the evolution transformation $\mathbf{z}(t) = \mathsf{U}(t)\,\mathbf{z}(0) + \overline{\mathbf{z}}(t)$, including

$$\mathsf{U}(t) = \begin{pmatrix} 1 & \frac{t}{M} \\ 0 & 1 \end{pmatrix}, \qquad \overline{\mathbf{z}}(t) = \begin{pmatrix} -\frac{g}{2}t^2 \\ -Mg\,t \end{pmatrix}. \tag{2.88}$$

Obviously the matrix part of the transformation is identical to free evolution. Consequently, initial distributions are also sheared in the course of propagation. In addition to that, all points are shifted along quadratic curves in phase space. An illustration of the phase space flow is found in figure 2.3. Assuming an initial condition f_0 at $t_0 = 0$ that is centered in phase space around $(x, p) = (0, 0)$, the time-evolved distribution becomes

$$f(x, p, t) = f_0\left(x - \frac{p}{M}t - \tfrac{1}{2}gt^2,\ p + Mgt\right). \tag{2.89}$$

Its mean momentum is $\overline{p} = -Mgt$ while its mean position is $\overline{x} = -gt^2/2$. The shape and center of evolved distribution function becomes more apparent when transforming to coordinates that are centered at its mean position and momentum,

$$X(t) \equiv x - \overline{x}(t) = x + \tfrac{1}{2}gt^2, \tag{2.90a}$$

$$P(t) \equiv p - \overline{p}(t) = p + Mgt. \tag{2.90b}$$

In this freely falling frame that is co-moving with the distribution's center in phase space, one writes

$$f\big(X(t), P(t), t\big) = f_0\left(X(t) - \frac{P(t)}{M}t,\ P(t)\right), \tag{2.91}$$

exhibiting only shearing of the initial distribution. Consequently, the time-dependent phase space correlation matrix $\mathsf{C}_{z}(t)$ is the same as in case of free propagation. That is, the width of the distribution in position space expands, while its shape in momentum space remains constant. The only difference to free propagation is translation of the center in phase space.

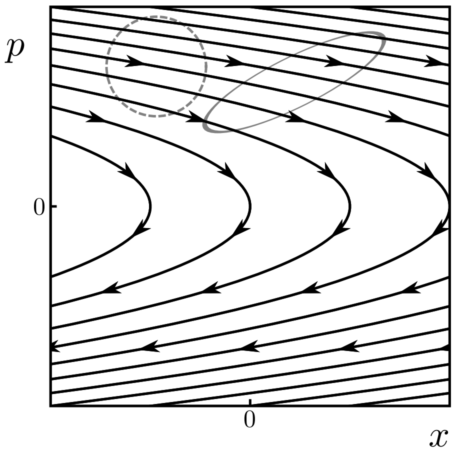

Figure 2.3.: Phase portrait of linear gravity. Trajectories are parabolas. Distributions, sketched with gray lines, are sheared.

2.3.3 Harmonic oscillator

A very important system which is suitable for describing many confided systems is the harmonic oscillator. Its Hamiltonian

$$H(\mathbf{x},\mathbf{p}) = \frac{\mathbf{p}^2}{2M} + \frac{M}{2}\mathbf{x}^\mathsf{T}\Omega^2\mathbf{x} \tag{2.92}$$

comprises a quadratic potential, quantified by the real symmetric matrix Ω. In this case, Hamilton's equations are

$$\dot{\mathbf{x}} = \frac{\mathbf{p}}{M}, \qquad \dot{\mathbf{p}} = -M\Omega^2\mathbf{x}. \tag{2.93}$$

In terms of expression (2.58) we write

$$\Lambda = \begin{pmatrix} M\Omega^2 & \mathbb{O} \\ \mathbb{O} & \frac{\mathbb{1}}{M} \end{pmatrix}, \qquad \boldsymbol{\lambda} = \begin{pmatrix} \mathbf{0} \\ \mathbf{0} \end{pmatrix}. \tag{2.94}$$

Like in the equations of free evolution, we have no inhomogeneities $\boldsymbol{\lambda}$, and thus propagation is described only by matrix multiplication, $\mathbf{z}(t_j) = \mathsf{U}(t_{ij})\,\mathbf{z}(t_i)$. Here, U is a rotation matrix in phase space,

$$\mathsf{U}(t) = \begin{pmatrix} \cos(\Omega t) & (M\Omega)^{-1}\sin(\Omega t) \\ -M\Omega\sin(\Omega t) & \cos(\Omega t) \end{pmatrix} \tag{2.95}$$

Hence, a propagated distribution that emanates from an initial function f_0 reads

$$f(x,p,t) = f_0\Big(\cos(\Omega t)\mathbf{x} - (M\Omega)^{-1}\sin(\Omega t)\mathbf{p},\; M\Omega\sin(\Omega t)\mathbf{x} + \cos(\Omega t)\mathbf{p}\Big), \tag{2.96}$$

again assuming the initial time instance to be $t_0 = 0$. The phase space flow is depicted in figure 2.4.

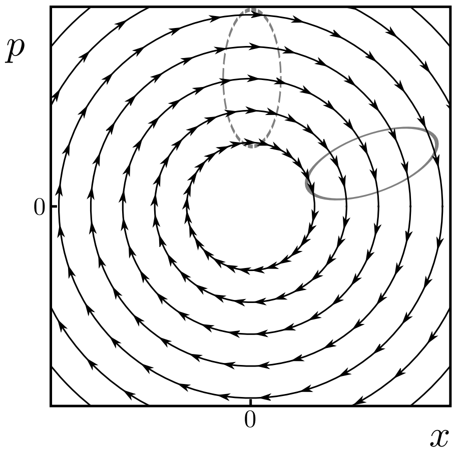

Figure 2.4.: Phase portrait of harmonic oscillator. Trajectories are circles. Distributions, sketched with gray lines, are rotated.

2.4 Effective few-particle distributions

In order to formulate a model which contains interaction between particles but is as simple as possible, we add a two-particle interaction term to the Hamiltonian of trapped particles (2.48). In doing so, one ignores processes with more than three particles involved. It is thus only valid if the probability of such more-particle encounters can be safely neglected in comparison to the occurrence of two-particle encounters. This is certainly true for very dilute systems. In contrast to ideal gases discussed above, two-particle interaction shall have significant influence on equilibrium distributions and dynamics. Turning to mathematical expressions, the Hamiltonian of binarily interacting particles comprises three terms,

$$H = H_{\text{kin}} + H_{\text{trap}} + H_{\text{int}}. \tag{2.97}$$

The first two terms are the kinetic and the trap potential energy, respectively, known from the Hamiltonian (2.48) of the noninteracting model. As we mentioned above, they are simply sums of single-particle contributions. On the contrary, the interaction term depends on all possible pairs of position coordinates,

$$H_{\text{int}} = \frac{1}{2} \sum_{i=1}^{N} \sum_{i \neq j=1}^{N} V_{\text{int}}(\mathbf{x}_i, \mathbf{x}_j). \tag{2.98}$$

Of course, binary interaction between classical identical particles is symmetric under particle permutation, $V_{\text{int}}(\mathbf{x}_1, \mathbf{x}_2) = V_{\text{int}}(\mathbf{x}_2, \mathbf{x}_1)$. Moreover we require $\nabla_1 V_{\text{int}}(\mathbf{x}_1, \mathbf{x}_2) = -\nabla_2 V_{\text{int}}(\mathbf{x}_1, \mathbf{x}_2)$, where ∇_i denotes the derivative with respect to the i-th particle's position. This is an expression of Newton's third law, 'actio equals reactio'. Both of these symmetry requirements are met by constricting possible interaction potentials to $V_{\text{int}}(\mathbf{x}_1, \mathbf{x}_2) = V_{\text{int}}(|\mathbf{x}_1 - \mathbf{x}_2|)$. All contributions to the Hamiltonian (2.97) are symmetric under permutation of particles.

Having defined the basic model Hamiltonian, we are now interested in the time evolution it generates. The Liouvillian of equation (2.33) can be expressed as $\hat{\mathscr{L}} = \sum_i \left((\nabla_i H)\partial_i - (\partial_i H)\nabla_i\right)$. Since $\hat{\mathscr{L}}$ is a linear operator, it can be decomposed into a sum of terms, $\hat{\mathscr{L}} = \hat{\mathscr{L}}_{\text{kin}} + \hat{\mathscr{L}}_{\text{ext}} + \hat{\mathscr{L}}_{\text{int}}$, associated with the several Hamiltonians, H_{kin}, H_{trap}, and H_{int}, respectively. First of all, the single-particle contributions were already given above when discussing noninteracting particles. In the following, they are abbreviated as

$$\hat{\mathscr{L}}_{\text{kin}} + \hat{\mathscr{L}}_{\text{ext}} = \sum_{i=1}^{N} \left(-\frac{\mathbf{p}_i}{M} \nabla_i + (\nabla_i V_{\text{ext}})\, \partial_i \right) \equiv \sum_{i=1}^{N} \hat{\ell}_i. \tag{2.99}$$

Moreover, one can exploit the symmetry of the binary interaction to write the two particle contribution to the Liouvillian as

$$\begin{aligned} \hat{\mathscr{L}}_{\text{int}} &= \frac{1}{2} \sum_{i=1}^{N} \sum_{i \neq j=1}^{N} (\nabla_i V_{\text{int}})(\partial_i - \partial_j) \\ &= \frac{1}{2} \sum_{i=1}^{N} \sum_{i \neq j=1}^{N} \hat{\ell}_{ij}^{(\text{int})}. \end{aligned} \tag{2.100}$$

In summary, the dynamics of a system of binarily interacting trapped particles can be expressed as

$$\partial_t f^{(N)} = \sum_{i=1}^{N} \left(\hat{\ell}_i + \frac{1}{2} \sum_{i \neq j=1}^{N} \hat{\ell}_{ij}^{(\text{int})} \right) f^{(N)}, \tag{2.101}$$

where the indices i and j denote on which particle the operators $\hat{\ell}$ and $\hat{\ell}^{(\text{int})}$ act. At first sight, equation (2.101) is merely a rather cumbersome way to re-express LIOUVILLE's equation (2.33). Its profitableness lies in providing a good starting point for obtaining useful approximations to the full N-particle LIOUVILLE equation.

2.4.1 Reduced distributions

We already showed that if the Hamiltonian comprises only single-particle terms, the N-particle distribution is an effective single-particle function, given the initial distribution is also a single-particle function. In the following, we present the systematic generalization of this idea to effective few-particle distribution. First of all, note that any N-particle dynamical function a can be expressed as

$$\begin{aligned} a(\mathbf{z}_1,...,\mathbf{z}_N) =& a^{(0)} + \sum_{i=1}^{N} a^{(1)}(\mathbf{z}_i) + \frac{1}{2}\sum_{i_1=1}^{N}\sum_{i_1\neq i_2=1}^{N} a^{(2)}(\mathbf{z}_{i_1},\mathbf{z}_{i_2}) + ... \\ & ... + \frac{1}{s!}\sum_{i_1=1}^{N} ... \sum_{i_1\neq ...\neq i_s=1}^{N} a^{(s)}(\mathbf{z}_{i_1},...,\mathbf{z}_{i_s}) + ... \\ & ... + \frac{1}{N!} a^{(N)}(\mathbf{z}_1,...,\mathbf{z}_N), \end{aligned} \tag{2.102}$$

such that for every $s = 1,...,N$, the object $a^{(s)}$ is a function of no more than s phase space coordinates and cannot be expressed in terms of functions depending on lesser variables. By virtue of particle permutation symmetry, the s-th order term is a sum over the same function $a^{(s)}$ evaluated at different arguments $\mathbf{z}_1,...,\mathbf{z}_s$. Therefore, the above decomposition is merely another (at first sight more complicated) way to express a. The true power of this approach becomes evident when using it for the computation of expectation values. The latter are written

$$\begin{aligned} \langle a\rangle &= \int \mathrm{d}^{2N}z\, a(\underline{z}) f^{(N)}(\underline{z}) \\ &= \int \mathrm{d}^6 z_1 ... \mathrm{d}^6 z_N\, a(\mathbf{z}_1,...,\mathbf{z}_N) f^{(N)}(\mathbf{z}_1,...,\mathbf{z}_N) \\ &= \int \mathrm{d}^6 z_1 ... \mathrm{d}^6 z_N \\ & \qquad \left[a^{(0)} + \sum_{i=1}^{N} a^{(1)}(\mathbf{z}_i) + ... + \frac{1}{s!}\sum_{i_1=1}^{N} ... \sum_{i_1\neq ...\neq i_s=1}^{N} a^{(s)}(\mathbf{z}_{i_1},...,\mathbf{z}_{i_s}) + ... \right] \\ & \qquad \times f^{(N)}(\mathbf{z}_1,...,\mathbf{z}_N). \end{aligned} \tag{2.103}$$

Exploiting again permutation symmetry of all terms, the integrals of the sums simplify to

$$\begin{aligned} \langle a\rangle =& a^{(0)} \int \mathrm{d}^6 z_1 ... \mathrm{d}^6 z_N\, f^{(N)}(\mathbf{z}_1,...,\mathbf{z}_N) \\ & + N \int \mathrm{d}^6 z_1 ... \mathrm{d}^6 z_N\, a^{(1)}(\mathbf{z}_1) f^{(N)}(\mathbf{z}_1,...,\mathbf{z}_N) + ... \\ & + \frac{N!}{(N-s)!s!} \int \mathrm{d}^6 z_1 ... \mathrm{d}^6 z_N\, a^{(s)}(\mathbf{z}_1,...,\mathbf{z}_s) f^{(N)}(\mathbf{z}_1,...,\mathbf{z}_N) + ... \quad . \end{aligned} \tag{2.104}$$

In the very first term, the integral is just the normalization condition of the distribution function, which is chosen to be unity here, $\int \mathrm{d}^{6N}z\, f = 1$. The higher terms can be written more compactly by defining effective s-particle distribution functions,

$$f^{(s)}(\mathbf{z}_1, \dots, \mathbf{z}_s) = \frac{N!}{(N-s)!} \int \mathrm{d}^6 z_{s+1} \dots \mathrm{d}^6 z_N\, f^{(N)}(\mathbf{z}_1, \dots, \mathbf{z}_N). \tag{2.105}$$

We are now able to rewrite the expectation value of $a(\underline{z})$ in a simple form that is reminiscent of a scalar product [47],

$$\begin{aligned} \langle a \rangle &= \sum_{s=0}^{N} \frac{1}{s!} \int \mathrm{d}^6 z_1 \dots \mathrm{d}^6 z_s\, a^{(s)}(\mathbf{z}_1, \dots, \mathbf{z}_s) f^{(s)}(\mathbf{z}_1, \dots, \mathbf{z}_s) \\ &= a^{(0)} + \int \mathrm{d}^6 z_1\, a^{(1)}(\mathbf{z}_1) f^{(1)}(\mathbf{z}_1) + \tfrac{1}{2} \int \mathrm{d}^6 z_1 \mathrm{d}^6 z_2\, a^{(2)}(\mathbf{z}_1, \mathbf{z}_2) f^{(2)}(\mathbf{z}_1, \mathbf{z}_2) + \dots . \end{aligned} \tag{2.106}$$

Being interested in single- or few-particle observables, one can terminate this expansion at some order s. This idea is used again in the next subsection in order to simplify the equation of motion.

2.4.2 Time evolution and the BBGKY-hierarchy

Loosely speaking, the BBGKY-hierarchy [47, 61], named after BOGOLIUBOV, BORN GREEN, KIRKWOOD, and YVON, is used to substitute a single equation of motion in a complex microscopic function, like the LIOUVILLE equation (2.33), by a series of equations in less complex functions. In the current case of classical phase space distributions, the complex microscopic function is the full N-particle distribution $f^{(N)}$, and the less complex ones will be the reduced distributions $f^{(s)}$ defined in (2.105).

Again, we assume a system of binarily interacting particles in external potentials described by equation (2.101). Clearly, Hamiltonian dynamics leaves the norm of distribution functions unaltered, $\partial_t \int \mathrm{d}^{6N}z\, f^{(N)}(\underline{z}, t) = 0$. Furthermore, one can also show that the phase space integral over the individual terms of (2.101) vanish, i.e.

$$\int \mathrm{d}^6 z_i\, \hat{\ell}_i f^{(N)}(\mathbf{z}_1, \dots, \mathbf{z}_N, t) = 0, \tag{2.107a}$$

$$\int \mathrm{d}^6 z_i\, \mathrm{d}^6 z_j\, \hat{\ell}_{ij}^{(\mathrm{int})} f^{(N)}(\mathbf{z}_1, \dots, \mathbf{z}_N, t) = 0. \tag{2.107b}$$

These relations follow from GREEN's theorem neglecting boundary terms. Mind that we can safely neglect contributions from integration borders because we integrate over the entire phase space and consider normalizable distributions only. With this result, the time dependence of the reduced distribution function can be expressed as

$$\partial_t f^{(s)}(\mathbf{z}_1, \dots, \mathbf{z}_s) = \frac{N!}{(N-s)!} \int \mathrm{d}^6 z_{s+1} \dots \mathrm{d}^6 z_N \sum_{i=1}^{N} \left[\hat{\ell}_i + \frac{1}{2} \sum_{i \neq j=1}^{N} \hat{\ell}_{ij}^{(\mathrm{int})} \right] f^{(N)}(\mathbf{z}_1, \dots, \mathbf{z}_N). \tag{2.108}$$

The first term, being a sum of single-particle expressions, is calculated straightforwardly. Utilizing equation (2.107a) and the definition of reduced distributions (2.105), one finds

$$(\text{1st term}) = \sum_{i=1}^{s} \hat{\ell}_i f^{(s)}(\mathbf{z}_1, \ldots, \mathbf{z}_s). \tag{2.109a}$$

The second term contains the two-particle interaction Liouvillians. It can be further decomposed with respect to indices.

- Both, i and j, are in $\{1, \ldots, s\}$. In this case, the associated contribution to the total Liouvillian is calculated similar to the first term (2.109a). Using relations (2.107b) and (2.105), we obtain

$$(\text{I}) = \frac{1}{2} \sum_{i=1}^{s} \sum_{i \neq j=1}^{s} \hat{\ell}_{ij}^{(\text{int})} f^{(s)}(\mathbf{z}_1, \ldots, \mathbf{z}_N). \tag{2.109b}$$

- The index i is in $\{1, \ldots, s\}$ while j is in $\{s+1, \ldots, N\}$ and vice versa. This implies

$$\begin{aligned}
(\text{II}) &= \sum_{i=1}^{s} \sum_{j=s+1}^{N} \frac{N!}{(N-s)!} \int \mathrm{d}^6 z_{s+1} \ldots \mathrm{d}^6 z_N \; \hat{\ell}_{ij}^{(\text{int})} f^{(N)}(\mathbf{z}_1, \ldots, \mathbf{z}_N) \\
&= \sum_{i=1}^{s} \frac{N!}{(N-s)!} (N-s) \int \mathrm{d}^6 z_{s+1} \ldots \mathrm{d}^6 z_N \; \hat{\ell}_{i,s+1}^{(\text{int})} f^{(N)}(\mathbf{z}_1, \ldots, \mathbf{z}_N) \\
&= \sum_{i=1}^{s} \int \mathrm{d}^6 z_{s+1} \; \hat{\ell}_{i,s+1}^{(\text{int})} \left[\frac{N!}{(N-(s+1))!} \int \mathrm{d}^6 z_{s+2} \ldots \mathrm{d}^6 z_N \; f^{(N)}(\mathbf{z}_1, \ldots, \mathbf{z}_N) \right] \\
&= \sum_{i=1}^{s} \int \mathrm{d}^6 z_{s+1} \; \hat{\ell}_{i,s+1}^{(\text{int})} \; f^{(s+1)}(\mathbf{z}_1, \ldots, \mathbf{z}_{s+1}).
\end{aligned} \tag{2.109c}$$

  Going from first to the second line, we have again exploited the particle permutation symmetry of $f^{(N)}$.

- Both, i and j are in $\{s+1, \ldots, N\}$. Here, the associated contribution vanishes due to relation (2.107b),

$$(\text{III}) = \sum_{i=s+1}^{N} \sum_{i \neq j=s+1}^{N} \frac{N!}{(N-s)!} \int \mathrm{d}^6 z_{s+1} \ldots \mathrm{d}^6 z_N \; \hat{\ell}_{ij}^{(\text{int})} f^{(N)}(\mathbf{z}_1, \ldots, \mathbf{z}_N) = 0. \tag{2.109d}$$

Summing up all terms, the equation of motion for the reduced s-particle distribution is expressed as

$$\partial_t f^{(s)} - \sum_{i=1}^{s} \left[\hat{\ell}_i + \frac{1}{2} \sum_{i \neq j=1}^{s} \hat{\ell}_{ij}^{(\text{int})} \right] f^{(s)} \quad = \sum_{i=1}^{s} \int \mathrm{d}^6 z_{s+1} \; \hat{\ell}_{i,s+1}^{(\text{int})} f^{(s+1)}. \tag{2.110}$$

So far, no approximation has entered the theory since the formulation of the Hamiltonian (2.97). The evolution equation in terms of the reduced distribution (2.110) is fully equivalent to the general LIOUVILLE equation (2.33). The former is, however, not a single closed equation but a hierarchy of N equations. The evolution of the reduced distribution of any order $f^{(s)}$ is coupled to the next higher order $f^{(s+1)}$ except, of course, on the highest rung of the ladder when $s = N$. The explicit form of the three lowest orders are

$$\partial_t f^{(0)} = 0 \tag{2.111a}$$

$$\left[\partial_t - \hat{\ell}_1\right] f^{(1)}(\mathbf{z}_1) = \int \mathrm{d}^6 z_2\, \hat{\ell}^{(\mathrm{int})}_{12}\, f^{(2)}(\mathbf{z}_1, \mathbf{z}_2) \tag{2.111b}$$

$$\left(\partial_t - \hat{\ell}_1 - \hat{\ell}_2 - \hat{\ell}^{(\mathrm{int})}_{12}\right) f^{(2)}(\mathbf{z}_1, \mathbf{z}_2) = \int \mathrm{d}^6 z_3\, \left(\hat{\ell}^{(\mathrm{int})}_{13} + \hat{\ell}^{(\mathrm{int})}_{23}\right) f^{(3)}(\mathbf{z}_1, \mathbf{z}_2, \mathbf{z}_3) \tag{2.111c}$$

The zeroth order equation (2.111a) is simply the norm conservation. Now, the subsequent low order equations are truly beneficial if one is not interested in tiny details of the system or many-particle correlation. This is especially true when discussing mainly macroscopic aspects of a system. Consequently, one breaks the hierarchy by neglecting all orders except the lowest few, say $s \leq 2$. This way, one obtains a closed system of equations in effective few particle distribution functions $f^{(s)}$, containing all relevant information.

2.4.3 Effective single-particle distributions

A very fruitful application of the procedure presented above is the description of interacting weakly correlated many-particle systems with single-particle function. This implies a breaking of the hierarchy after the first (non-trivial) equation, neglecting orders $s \geq 2$. If we simply set the next-higher order distribution $f^{(2)}$ zero, however, we ignore interactions completely and would merely reproduce the result we have obtained for noninteracting systems in section 2.2.4. A more thorough examination of $f^{(2)}$ leads to proper inclusion of interaction effects into the single-particle distribution $f^{(1)}$. Therefore we note that two-particle distribution can in general be decomposed into a factorization of single-particle functions on one hand, and a two-particle correlation function $g^{(2)}$ on the other,

$$f^{(2)}(\mathbf{z}_1, \mathbf{z}_2) = f^{(1)}(\mathbf{z}_1) f^{(1)}(\mathbf{z}_2) + g^{(2)}(\mathbf{z}_1, \mathbf{z}_2). \tag{2.112}$$

Likewise, three-particle distributions can be expressed in terms of single-particle functions, two-particle, and three-particle correlation, as

$$\begin{aligned} f^{(3)}(\mathbf{z}_1, \mathbf{z}_2, \mathbf{z}_3) = \;& f^{(1)}(\mathbf{z}_1) f^{(1)}(\mathbf{z}_2) f^{(1)}(\mathbf{z}_3) \\ & + f^{(1)}(\mathbf{z}_1) g^{(2)}(\mathbf{z}_2, \mathbf{z}_3) + f^{(2)}(\mathbf{z}_2) g^{(2)}(\mathbf{z}_1, \mathbf{z}_3) + f^{(1)}(\mathbf{z}_3) g^{(2)}(\mathbf{z}_1, \mathbf{z}_2) \\ & + g^{(3)}(\mathbf{z}_1, \mathbf{z}_2, \mathbf{z}_3), \end{aligned} \tag{2.113}$$

and so forth. An effective single-particle description is adequate if correlations between particles, quantified by $g^{(2)}$, are negligible. This way, we can write

$$f^{(2)}(\mathbf{z}_1,\mathbf{z}_2) \approx f(\mathbf{z}_1)f(\mathbf{z}_2), \tag{2.114}$$

which indeed breaks the BBGKY-hierarchy. Aiming for expressions exclusively in terms of single-particle distributions $f^{(1)}$, we have omitted again the superscript, catering to our laziness. Only for higher orders $s \geq 2$, we explicitly write $f^{(s)}$. The right-hand side of the remaining evolution equation (2.111b) can now be written as

$$\begin{aligned}
&\int \mathrm{d}^6 z_2\, \hat{\ell}_{12}^{(\mathrm{int})} f^{(2)}(\mathbf{z}_1,\mathbf{z}_2) \\
&\quad = \int \mathrm{d}^6 z_2\, \hat{\ell}_{12}^{(\mathrm{int})} f(\mathbf{z}_1)f(\mathbf{z}_2) \\
&\quad = \int \mathrm{d}^6 z_2\, (\nabla_2 V_{\mathrm{int}})(\partial_2 - \partial_1) f(\mathbf{z}_1)f(\mathbf{z}_2) \\
&\quad = \left[\int \mathrm{d}^6 z_2\, (\nabla_2 V_{\mathrm{int}})\,\partial_2 f(\mathbf{z}_2)\right] f(\mathbf{z}_1) - \left[\int \mathrm{d}^6 z_2\, (\nabla_2 V_{\mathrm{int}}) f(\mathbf{z}_2)\right] \partial_1 f(\mathbf{z}_1).
\end{aligned} \tag{2.115}$$

Utilizing Green's theorem and neglecting boundary terms, one can see that the first term of the last line vanishes. The second term, on the other hand, can be expressed as $(\nabla_1 V_{\mathrm{mf}})\partial_1 f$, introducing the mean field potential

$$V_{\mathrm{mf}}(\mathbf{x}) = \int \mathrm{d}^3 x_2\, V_{\mathrm{int}}(\mathbf{x}_1,\mathbf{x}_2) f^{(1)}(\mathbf{z}_2). \tag{2.116}$$

It is a functional on the single-particle function f which results in a position dependent potential that adds to the external potential V_{ext}. Thus, recalling the explicit form of the single-particle Liouvillian $\hat{\ell}$, written in expression (2.99), the evolution equation for single-particle distribution (2.111b) becomes a closed partial differential equation,

$$\left[\partial_t + \frac{\mathbf{p}}{M}\nabla - \nabla\left(V_{\mathrm{ext}} + V_{\mathrm{mf}}[f]\right)\right] f = 0. \tag{2.117}$$

In contrast to its microscopic pendant (2.33), it possesses a non-linearity. One may say that for arriving at a closed equation, we had to pay the price of abandoning the linearity of microscopic description. Equation (2.117) is well-known in the context of plasma physics as Vlasov equation [47, 61, 62]. In that case, the two-particle interaction V_{int} is given by the long-ranged Coulomb potential. In case of neutral atoms, typical interaction potentials decay on very short length scales. Below, we specify mean field evolution in the limit of infinity short-ranged interaction potential.

Energy functional

To every solution f of equation (2.117) corresponds a total energy

$$E[f] = \int \mathrm{d}^3x \int \mathrm{d}^3p \left(\frac{\mathbf{p}^2}{2M} + V_{\mathrm{ext}} + \tfrac{1}{2} V_{\mathrm{mf}}[f] \right) f. \tag{2.118}$$

It is straightforward to check that it remains constant during evolution.

$$\begin{aligned}
\partial_t E[f] &= \int \mathrm{d}^3x \int \mathrm{d}^3p \left(\frac{\mathbf{p}^2}{2M} + V + V_{\mathrm{mf}} \right) \partial_t f \\
&= \int \mathrm{d}^3x \int \mathrm{d}^3p \left(\frac{\mathbf{p}^2}{2M} + V + V_{\mathrm{mf}} \right) \left(-\frac{\mathbf{p}}{M} \cdot \nabla f + \nabla(V + V_{\mathrm{mf}}) \cdot f \right) \\
&= \int \mathrm{d}^3x \int \mathrm{d}^3p \left(\nabla(V + V_{\mathrm{mf}}) \cdot \frac{\mathbf{p}}{M} - \frac{\mathbf{p}}{M} \cdot \nabla(V + V_{\mathrm{mf}}) \right) f \\
&= 0,
\end{aligned} \tag{2.119}$$

where we have used again GREEN's theorem poing from the second line to the third. Moreover, the factor 1/2 that is attached to the mean field potential in expression (2.118) is compensated in the first line of equation (2.119) by differentiating the squared distribution.

Contact interaction

We now discuss a very useful approximation of the interaction potential V_{int}. Considering a gas of neutral interacting atoms, as is done in the main part of this work, two-particle interactions are short-ranged. That is, particles only interact with each other if their distance is below a certain value and are free, or subject to external forces only, otherwise. If, moreover, the typical interaction length is sufficiently small, the exact inter-particle potential is well approximated by a contact interaction,

$$V_{\mathrm{int}}(\mathbf{x}_1, \mathbf{x}_2) = 2g\, \delta(\mathbf{x}_1 - \mathbf{x}_2), \tag{2.120}$$

quantified by a single parameter, the interaction strength g. The factor of 2 which may appear somewhat arbitrary here is introduced to be consistent with the quantum mechanical evolution equations, that are discussed in the next chapter. Assumption (2.120) leads to a simple mean field interaction potential,

$$V_{\mathrm{mf}}(\mathbf{x}) = 2g\, n(\mathbf{x}) \tag{2.121}$$

where the spatial density is the momentum integral over the distribution function, $n(\mathbf{x}) = \int \mathrm{d}^3p\, f(\mathbf{x}, \mathbf{p})$. Hence equation (2.117) can then be written explicitly as

$$\partial_t f = -\frac{\mathbf{p}}{M} \cdot \nabla f + \nabla U \cdot \boldsymbol{\partial} f. \tag{2.122}$$

We have combined the external potential and the mean field interaction into a single self-consistent potential function,

$$U(\mathbf{x}) = V_{\text{ext}}(\mathbf{x}) + 2gn(\mathbf{x}). \tag{2.123}$$

The associated energy functional reads

$$E[f] = \int \mathrm{d}^3x \int \mathrm{d}^3p \left(\frac{\mathbf{p}^2}{2M} + V_{\text{ext}} + gn \right) f. \tag{2.124}$$

3 Quantum-mechanical description of atomic gases

In many cases it is totally sufficient to describe the dynamics of a thermal atomic gas in terms of classical mechanics, as we did in the preceding chapter. Above the critical temperature, the thermal DE-BROGLIE wave length of the particles is well below the mean particle distance [17,53,63]. Thus, quantum-mechanical aspects can be safely neglected. In contrast to that, the condensed atoms, possessing long-range phase coherence [64,65], are collectively described by a macroscopic wave function.

In the classical discussion, we quantified the system's state with a phase space distribution function. A quantum-mechanical equivalent to this entity is the WIGNER function [66, 67]; a phase space representation of quantum-mechanical states that yields the classical distribution function in the high temperature limit. Furthermore, under certain conditions, its evolution is subject to the same equations as the classical distribution which allows us to reuse many results of the preceding chapter.

We begin the current chapter with a brief reminder of single-particle quantum mechanics [55, 56, 68]. Although assuming the reader is quite familiar with this topic, we give some basic relations, particularly showing similarities and differences to the classical formalism [47]. Based on these refreshed basics, we introduce the single-particle WIGNER function and corresponding equations of motion. Finally, we show how inter-particle interactions enter the formalism, especially concentrating on mean field approximations.

3.1 Brief reminder of basic single-particle quantum mechanics

The key difference between classical and quantum mechanics is the mathematical representation of observables by self-adjoint operators in HILBERT space, $\hat{a}^\dagger = \hat{a}$, rather than dynamical functions $a(\underline{q}, \underline{p}, t)$. Additionally, the state of the system is described by an element $|\psi\rangle$ of that HILBERT space. At the very basis of quantum mechanics is the relation

$$\left[\hat{x}_j, \hat{p}_{j'}\right] = i\hbar\,\delta_{jj'}, \tag{3.1}$$

fixing the algebra between position and momentum operator. Defining now the eigenvectors of $\hat{\mathbf{x}}$ and $\hat{\mathbf{p}}$ as $\hat{\mathbf{x}}\,|\mathbf{x}\rangle = \mathbf{x}\,|\mathbf{x}\rangle$ and $\hat{\mathbf{p}}\,|\mathbf{p}\rangle = \mathbf{p}\,|\mathbf{p}\rangle$, respectively, one obtains the wave function in position space, $\psi(\mathbf{x}) = \langle\mathbf{x}|\psi\rangle$, and in momentum space, $\tilde{\psi}(\mathbf{p}) = \langle\mathbf{p}|\psi\rangle$. They can be considered as tangible representations of the abstract HILBERT space element $|\psi\rangle$. The position representation of the momentum operator is obtained by exploiting its role as the generator of position displacements,

$$\langle \mathbf{x}+\Delta\mathbf{x}|\psi\rangle = \langle \mathbf{x}|e^{i\Delta\mathbf{x}\mathbf{p}/\hbar}|\psi\rangle.$$

A comparison with the TAYLOR expansion of $\psi(\mathbf{x}+\Delta\mathbf{x})$ yields the useful identity

$$\langle \mathbf{x}|\hat{\mathbf{p}}|\psi\rangle = -i\hbar\nabla\psi(\mathbf{x}). \tag{3.2}$$

From the elementary operators, $\hat{\mathbf{x}}$ and $\hat{\mathbf{p}}$, more complicated observables can be constructed. Having a classical dynamical function $a(\mathbf{x},\mathbf{p})$, its quantum-mechanical pendant is given by replacing position ond momentum coordinates with operators $\hat{\mathbf{x}}$ and $\hat{\mathbf{p}}$. For example, the angular momentum operator reads $\hat{\mathbf{L}} = \hat{\mathbf{x}} \times \hat{\mathbf{p}}$. Nevertheless, there are quantum-mechanical observables which do not have a classical counterpart. One prominent example is the spin of atomic or sub-atomic particles.

Time evolution

Evolution of states is described as the action of a unitary operator,

$$|\psi(t)\rangle = \hat{U}(t-t_0)\,|\psi(t_0)\rangle\,. \tag{3.3}$$

Unitary, $\hat{U}^\dagger = \hat{U}^{-1}$, ensures the norm conservation of evolving states. Like the classical propagators $\hat{\mathscr{U}}$, introduced in chapter 2, these time-translation operators constitute a single-parameter LIE group. Consequently, two successive evolutions about the intervals $t_2 - t_1$ and $t_1 - t_0$, respectively, are equal to a single evolution about the combined interval $t_2 - t_0$. These conditions constrain the form of $\hat{U}$ to

$$\hat{U}(t) = e^{-i\hat{H}t/\hbar}. \tag{3.4}$$

The privileged observable $\hat{H}$ is the HAMILTON operator. Similar to the HAMILTON function in classical mechanics, it is the generator of time translations. Equivalently, the evolution operator is a solution of the differential equation

$$i\hbar\,\partial_t\,|\psi\rangle = \hat{H}\,|\psi\rangle\,, \tag{3.5}$$

which is known as SCHRÖDINGER equation. Splitting the Hamiltonian into kinetic and potential part and adopting position representation, one writes

$$i\hbar\,\partial_t\psi(\mathbf{x}) = \left(-\frac{\hbar^2\nabla^2}{2M} + V(\mathbf{x})\right)\psi(\mathbf{x}). \tag{3.6}$$

The stationary form is obtained with the help of the Hamiltonian's eigenstates $|m\rangle$ which satisfy $\hat{H}\,|m\rangle = \epsilon_m\,|m\rangle$. Making the ansatz $\psi(\mathbf{x}) = \phi_m(\mathbf{x})e^{-i\epsilon_m t/\hbar}$, where $\phi(\mathbf{x}) = \langle \mathbf{x}|m\rangle$ is the position representation of the eigenstate, yields

$$\left(-\frac{\hbar^2\nabla^2}{2M} + V(\mathbf{x}) - \epsilon_m\right)\phi_m(\mathbf{x}) = 0. \tag{3.7}$$

Expression (3.6) implies that time dependence is carried by the states, while observables are constant operators. This is known as the SCHRÖDINGER picture of quantum mechanics. Looking at the expectation value of an observable in a time-dependent state,

$$\hat{a}(t) = \langle\psi(t_0)|\,\hat{U}^\dagger(t-t_0)\,\hat{a}\,\hat{U}(t-t_0)\,|\psi(t_0)\rangle, \tag{3.8}$$

it is obvious that one may equivalently define time-dependent observables,

$$\hat{a}(t) = \hat{U}^\dagger(t-t_0)\,\hat{a}\,\hat{U}(t-t_0), \tag{3.9}$$

while keeping the states constant. This approach is known as the HEISENBERG picture of quantum mechanics. It implies the evolution of observables to be subject to the HEISENBERG equation,

$$i\hbar\,\partial_t\hat{a} = -[\hat{H},\hat{a}]. \tag{3.10}$$

Apart from the factor $i\hbar$, it is formally similar to the equation of motion in classical dynamical functions (2.6), replacing the POISSON brackets with the commutator.

Mixed states

Whenever one has not complete knowledge of the system's state, it has to be described by a density matrix (or density operator) $\hat{\rho}$. Suppose the probability for the m-th eigenstate of the system, $|\phi_m\rangle$, to be populated is $\mathscr{P}_m$. The density matrix is defined as the sum over projectors on all involved states, weighted with the associated probability,

$$\hat{\rho} = \sum_n \mathscr{P}_m\,|\phi_m\rangle\,\langle\phi_m|\,. \tag{3.11}$$

In this formulation, observable values are given as traces of the product of the density matrix and the operator of interest,

$$\langle\hat{a}\rangle = \mathrm{Tr}\,\hat{\rho}\,\hat{a}. \tag{3.12}$$

The equation of motion for the density matrix is calculated straightforwardly. By differentiating (3.11) with respect to time and plugging in the SCHRÖDINGER equation (3.6), one obtains the VON-NEUMANN equation,

$$i\hbar\,\partial_t\hat{\rho} = [\hat{H},\hat{\rho}]. \tag{3.13}$$

One can recognize its formal resemblance to the classical LIOUVILLE equation (2.33). Solutions to (3.13) read

$$\hat{\rho}(t) = \hat{U}(t-t_0)\,\hat{\rho}(t_0)\,\hat{U}^\dagger(t-t_0). \tag{3.14}$$

Writing this expression, we have chosen again the SCHRÖDINGER picture. Translation to the HEISENBERG picture is achieved by writing down the time-dependent expectation value of an observable in terms of the density matrix,

$$\langle\hat{a}(t)\rangle = \mathrm{Tr}\ \hat{U}\,\hat{\rho}_0\,\hat{U}^\dagger\hat{a} = \mathrm{Tr}\ \hat{\rho}_0\,\hat{U}^\dagger\hat{a}\,\hat{U}, \tag{3.15}$$

exploiting the trace's invariance under cyclic permutations of subjected operator products. One identifies the time-dependent observable

$$\hat{a}(t) = \hat{U}^\dagger(t-t_0)\,\hat{a}(t_0)\,\hat{U}(t-t_0) \tag{3.16}$$

in the HEISENBERG picture, being a solution of the HEISENBERG equation (3.10). Thus, states and observables are subject to similar equations of motion. Mind however the different signs. Like in the classical case, it can be said that observables propagate forward in time using the HEISENBERG picture while states propagate backwards in time in the SCHRÖDINGER picture.

3.1.1 Example: Release from harmonic trap

As a simple example, we consider the free propagation of a quantum state after being released from a harmonic trap. The latter is described by the potential function

$$V(\mathbf{x}) = \tfrac{M}{2}\mathbf{x}^\mathsf{T}\Omega^2\mathbf{x}. \tag{3.17}$$

Pure ground state

The ground state's wave function [56] is a Gaussian,

$$\phi_0(\mathbf{x}) = \frac{\exp\left[-\frac{M}{2\hbar}\,\mathbf{x}^\mathsf{T}\,\Omega\,\mathbf{x}\right]}{\left[\left(\frac{\pi\hbar}{M}\right)^3\det\Omega^{-1}\right]^{1/4}}. \tag{3.18}$$

Its correlation matrix is given by $\mathsf{C}_{x0} = \hbar/(M\Omega)^{-1}$. In case of one dimension, having a scalar-valued oscillation frequency ω, the correlation matrix is merely the square of the distribution's width $a_{\mathrm{ho}}^2 = \hbar/(M\omega)$. The parameter a_{ho} is called oscillation length of the quantum-mechanical harmonic oscillator. In three dimensions, one can define the geometrical mean of the oscillator length as $\overline{a}_{\mathrm{ho}}^2 = \hbar/(M\overline{\omega})$, where $\overline{\omega} = (\prod_{i=1}^3 \omega_i)^{1/3}$ is the geometrical mean of the eigenfrequencies of Ω. The ground state's position density is

$$
\begin{aligned}
n_0(\mathbf{x}) &= \phi_0^*(\mathbf{x})\,\phi_0(\mathbf{x}) \\
&= \frac{\exp\left[-\mathbf{x}^{\mathsf{T}}\mathsf{C}_{x0}^{-1}\mathbf{x}\right]}{\left[\pi^3 \det \mathsf{C}_{x0}\right]^{1/2}}.
\end{aligned}
\tag{3.19}
$$

Free evolution, wave packet spreading

Now, switching off the harmonic confining potential at $t = 0$ we let the state evolve freely thereafter. At any later time instance $t > 0$, the time-evolved state is given by

$$
\begin{aligned}
\psi(\mathbf{x}, t) &= \langle \mathbf{x}| e^{-i\frac{\hat{\mathbf{p}}^2}{2M\hbar}t} |\phi_0\rangle \\
&= \frac{1}{\det \mathsf{s}(t)}\phi_0\left(\mathsf{s}^{-1}(t)\,\mathbf{x}\right).
\end{aligned}
\tag{3.20}
$$

We have expressed the result in a compact form, defining the matrix

$$
\mathsf{s}(t) = \left(\mathbb{1} + i\tfrac{\hbar}{M}\mathsf{C}_{x0}^{-1}\,t\right)^{1/2},
\tag{3.21}
$$

which acts on position vectors. Time evolution is thus described in terms of the initial function $\phi_0(\mathbf{x})$ and a complex coordinate transformation applied to its argument. The wave function (3.20) is spreading in position space but it also develops a quadratic phase as time progresses.

Based on the wave function (3.20), the density profile of the evolved state becomes

$$
\begin{aligned}
n(\mathbf{x}, t) &= \psi^*(\mathbf{x}, t)\,\psi(\mathbf{x}, t) \\
&= \frac{1}{\det(\mathsf{s}^\dagger(t)\,\mathsf{s}(t))} n_0\left((\mathsf{s}^\dagger(t)\,\mathsf{s}(t))^{-1}\,\mathbf{x}\right).
\end{aligned}
\tag{3.22}
$$

It is also written in terms of the initial density n_0 and a coordinate transformation. The latter is represented by a real matrix

$$
\begin{aligned}
\mathsf{s}^\dagger(t)\,\mathsf{s}(t) &= \left[\mathbb{1} + \left(\tfrac{\hbar}{M}\mathsf{C}_{x0}^{-1}\right)^2 t^2\right]^{1/2} \\
&= \left[\mathbb{1} + \Omega^2 t^2\right]^{1/2}.
\end{aligned}
\tag{3.23}
$$

Hence, the evolved density can be expressed more explicitly as

$$n(\mathbf{x},t)=\frac{\exp\left[-\mathbf{x}^{\mathrm{T}}\,\mathsf{C}_{x}^{-1}(t)\,\mathbf{x}\right]}{[\pi^{3}\det\mathsf{C}_{x}(t)]^{1/2}}, \tag{3.24}$$

utilizing the time dependent correlation matrix

$$\mathsf{C}_{x}(t)=\left(\mathbb{1}+\Omega^{2}t^{2}\right)\mathsf{C}_{x0}. \tag{3.25}$$

This equation is identical to the time-dependent correlation matrix of a freely expanding classical density distribution (2.84) in terms of the potential frequency matrix Ω. Here, the only difference between classical and quantum case is the initial correlation matrix C_{x0}. In the former, it is determined by the competition between thermal energy $k_B T$ and potential energy $V(\mathbf{x})$ of the initial state. In the latter, being the quantum-mechanical ground state, the correlation matrix is the ratio of zero-point energy and potential energy.

Thermal state

A model that is more suitable to many practical situations involves a thermalized initial state. It is described by the density matrix in the canonical ensemble [53]

$$\hat{\rho}_0=\frac{\exp\left(-\frac{\hat{H}}{k_B T}\right)}{\mathrm{Tr}\,\exp\left(-\frac{\hat{H}}{k_B T}\right)}. \tag{3.26}$$

Assuming the trapping potential again to be a harmonic oscillator, the position representation of the initial state, $\rho_0(\mathbf{x},\mathbf{x}')=\langle\mathbf{x}'|\,\hat{\rho}_0\,|\mathbf{x}\rangle$, is obtained by inserting the identity operator in terms of harmonic oscillator eigenfunctions, $1=\sum_{\underline{m}}\left|\underline{m}\right\rangle\left\langle\underline{m}\right|$. In three dimensions, these are numerated by a triple of quantum numbers, $\left|\underline{m}\right\rangle=|m_1,m_2,m_3\rangle$. Without loss of generality, we chose a coordinate frame that aligns with the harmonic oscillator axes. Hence, the frequency matrix of the potential is a diagonal, $\Omega=\mathrm{diag}(\omega_1,\omega_2,\omega_3)$. The Hamiltonian in its eigenbasis reads

$$\langle\underline{m}'|\hat{H}|\underline{m}\rangle=\hbar\sum_{i=1}^{3}\left(m_i\omega_i+\tfrac{1}{2}\right).$$

The position representation of the eigenstates is

$$\langle\xi|\underline{m}\rangle=\prod_i\frac{1}{\pi^{1/4}(2m_i)^{1/2}}H_{m_i}(\xi_i)\,e^{-\xi^2/2},$$

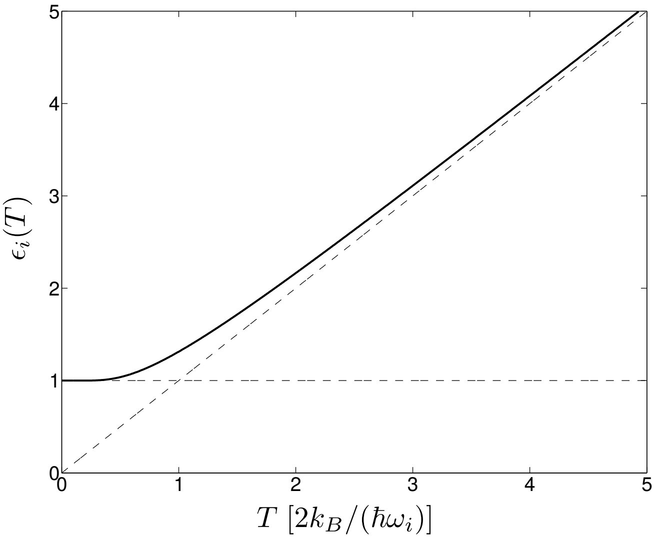

Figure 3.1.: Temperature dependence of the factor ϵ_i defined in equation (3.28). It determines the shape of the thermal harmonic oscillator along the i-th axis.

with dimensionless coordinates $\xi_i = (M\omega_i/\hbar)^{1/2} x_i$. Furthermore, H_m is the m-th order HERMITE polynomial (see A.3). Exploiting some basic relations in H_m (A.19, A.20, A.21), one finally obtains

$$\rho_0(\mathbf{x},\mathbf{x}') = \prod_{i=1}^{3} \sqrt{\frac{M\omega_i}{\pi\hbar\,\epsilon_{i(T)}}}\ \exp\left\{-\tfrac{1}{4}\,\frac{M\omega_i}{\hbar}\left[\frac{1}{\epsilon_{i(T)}}(x_i+x_i')^2 + \epsilon_{i(T)}(x_i-x_i')^2\right]\right\}. \tag{3.27}$$

For ease of notation, we have defined a dimensionless factor

$$\epsilon_i(T) = \frac{1}{\tanh\left(\frac{\hbar\omega_i}{2k_B T}\right)}. \tag{3.28}$$

Being a strictly monotonic function of T, it quantifies the influence of temperature on the initial state $\rho_0(\mathbf{x},\mathbf{x}')$. A plot of the function $\epsilon_i(T)$ is displayed in 3.1.

It is interesting to consider the extreme temperature limits of expression (3.27). On one hand, for $T = 0$ we have $\epsilon_i = 1$. This way, we indeed recover the density matrix of the pure ground state,

$$\rho_0(\mathbf{x},\mathbf{x}') = \phi_0^*(\mathbf{x}')\,\phi_0(\mathbf{x}), \tag{3.29}$$

where ϕ_0 is given in (3.18). In this limit, ρ_0 is a spherically symmetric function in the $\mathbf{x}$-$\mathbf{x}'$-space, which implies significant off-diagonal contributions, $\rho(\mathbf{x},\mathbf{x}') \neq 0$ for $\mathbf{x} \neq \mathbf{x}'$. The state is said to have non-diagonal long-range order [64, 65]. Physically, this indicates phase coherence across the complete spatial extent of the state. In contrast, turning to high temperatures, we obtain $\epsilon_i \to 2k_\mathrm{B}T/(\hbar\omega_i)$ as $T \to \infty$. This asymptotically leads to

$$\rho_0(\mathbf{x},\mathbf{x}') = \left(\frac{M\det\Omega^2}{2\pi k_B T}\right)^{3/2}\ \exp\left(-\frac{M}{2k_B T}\,\mathbf{x}^\mathsf{T}\,\Omega^2\,\mathbf{x}\right)\ \delta(\mathbf{x}-\mathbf{x}'). \tag{3.30}$$

The position representation of the density matrix extends along the diagonal for rising temperature, reproducing the density profile of the MAXWELL-BOLTZMANN distribution (2.77). Meanwhile, it shrinks along the anti-diagonal, leaving only non-zero contributions for $\mathbf{x} = \mathbf{x}'$. This corresponds to a total loss of phase coherence between different positions.

Although it is straightforward to calculate the time-evolved density matrix,

$$\rho(\mathbf{x}, \mathbf{x}', t) = \langle \mathbf{x}' | \hat{U}(t) \hat{\rho}_0 \hat{U}^\dagger(t) | \mathbf{x} \rangle, \tag{3.31}$$

we postpone discussing the evolution of thermal states after their release until we have introduced the WIGNER function in the following section.

3.2 Quantum mechanical phase space distributions

Although there have already appeared some formal similarities between quantum and classical formalism, like the LIE group structure of time evolution, the most striking correspondence emerges when introducing phase space representations of quantum states. This way, one is able to obtain expressions which, under certain conditions, exactly reproduce the equations governing classical statistical ensembles. To begin with, since there exist many phase space representation in quantum mechanics [66], we have to chose a representation that fits our needs best. As far as classical mechanics is concerned, phase space distributions have two useful features. First, they are positive everywhere. This allows for identifying them as probability densities. Second, integrals over momentum coordinates yield the position density, while those over position coordinates yield the momentum density.

Unfortunately, there does not exist a phase space representation of quantum-mechanical states that fulfills both of these requirements. Discarding positivity in favor of direct connection to density profiles, we chose to represent our state by the WIGNER function. As we show below, one can obtain position and momentum densities directly by integration, while negative values are possible. Rather than judging the non-positivity of the WIGNER function as shortcoming, it can be exploited to study the departure of the "true" quantum formalism from classical and semi-classical formulations.

A comprehensive discussion of WIGNER functions is found in the book of SCHLEICH [67].

3.2.1 Single-particle Wigner function

The WIGNER function can be motivated starting with WEYL's correspondence rule [47]. The latter is a prescription for associating quantum-mechanical observables $\hat{a}$ to complex functions in phase space coordinates [69, 70],

$$\hat{a} = \int \mathrm{d}^3 k \int \mathrm{d}^3 j \; \alpha(\mathbf{k}, \boldsymbol{j}) \, e^{i(\mathbf{k}\hat{\mathbf{x}} + \boldsymbol{j}\hat{\mathbf{p}})}. \tag{3.32}$$

Using this relation, the expectation values of $\hat{a}$ can be expressed as

$$\langle \hat{a} \rangle = \int \mathrm{d}^3 k \int \mathrm{d}^3 j \; \alpha(\mathbf{k}, \boldsymbol{j}) \, \mathrm{Tr} \left\{ \hat{\rho} \, e^{i(\mathbf{k}\hat{\mathbf{x}} + \boldsymbol{j}\hat{\mathbf{p}})} \right\}. \tag{3.33}$$

Now, the traced term can already be considered a distribution function that relates to a particular state $\hat{\rho}$ and determines the expectation value $\langle \hat{a} \rangle$. However, it is a function of rather abstract coordinates, $\mathbf{k}$ and $\boldsymbol{j}$. We can translate it nevertheless into a function in terms of position and momentum via Fourier-transformation,

$$\mathrm{Tr} \left\{ \hat{\rho} \, e^{i(\mathbf{k}\hat{\mathbf{x}} + \boldsymbol{j}\hat{\mathbf{p}})} \right\} = \int \mathrm{d}^3 x \int \mathrm{d}^3 p \; e^{i(\mathbf{k}\mathbf{x} + \boldsymbol{j}\mathbf{p})} f(\mathbf{x}, \mathbf{p}). \tag{3.34}$$

Based on this relation, the Wigner function f in terms of the density matrix $\hat{\rho}$ can be expressed as

$$f(\mathbf{x}, \mathbf{p}) = \frac{1}{(2\pi\hbar)^3} \int \mathrm{d}^3 \xi \; e^{-i\xi \cdot \mathbf{p}/\hbar} \, \langle \mathbf{x} + \tfrac{\xi}{2} | \, \hat{\rho} \, | \mathbf{x} - \tfrac{\xi}{2} \rangle. \tag{3.35}$$

This equation can be paraphrased as following. The Wigner function along the position axes is given by the diagonal of the matrix element $\langle \mathbf{x} | \hat{\rho} | \mathbf{x}' \rangle$. On the other hand, the distribution along the momentum axes is obtained by Fourier-transforming $\langle \mathbf{x} | \hat{\rho} | \mathbf{x}' \rangle$ over its anti-diagonal matrix elements which are parametrized in expression (3.35) as ξ. Note that we use the same letter f to denote the Wigner functions as well as classical phase space distributions. We do this not by accident but rather to emphasize the similarities between both descriptions that will become apparent in the course of this discussion.

Integrating definition (3.1.1) over momentum or position coordinates, one indeed obtains the position density or the momentum density,

$$\int \mathrm{d}^3 p \; f(\mathbf{x}, \mathbf{p}) = |\langle \mathbf{x} | \psi \rangle|^2, \qquad \int \mathrm{d}^3 x \; f(\mathbf{x}, \mathbf{p}) = |\langle \mathbf{p} | \psi \rangle|^2, \tag{3.36}$$

respectively. Moreover, the above calculations imply that the expectation value of any observable can be expressed as

$$\langle \hat{a} \rangle = \int \mathrm{d}^3 x \int \mathrm{d}^3 p \; f(\mathbf{x}, \mathbf{p}) \, a(\mathbf{x}, \mathbf{p}), \tag{3.37}$$

where the phase space representation of $\hat{a}$ is given by

$$a(\mathbf{x}, \mathbf{p}) = \frac{1}{(2\pi\hbar)^3} \int \mathrm{d}^3 \xi \; e^{-i\xi \cdot \mathbf{p}/\hbar} \, \langle \mathbf{x} + \tfrac{\xi}{2} | \, \hat{a} \, | \mathbf{x} - \tfrac{\xi}{2} \rangle. \tag{3.38}$$

As we noted above, the WIGNER function can have negative values. This can be seen by considering two orthogonal states satisfying $\mathrm{Tr}\,\hat{\rho}_1\hat{\rho}_2 = 0$. In terms of WIGNER functions, it can be written

$$\int \mathrm{d}^3x\,\mathrm{d}^3p\; f_1(\mathbf{x},\mathbf{p}) f_2(\mathbf{x},\mathbf{p}) = 0.$$

Assuming the distributions to have overlapping support in phase space, this expression can only be true if either f_1, or f_2, or both are allowed to become negative. Nevertheless, the position as well as the momentum density, calculated on basis of f are positive everywhere.

3.2.2 Time evolution

For finding an equation that governs the evolution of quantum-mechanical phase space distributions in phase space, one can simply translate the VON NEUMANN equation (3.13) into an equation of motion in the WIGNER function. Let the Hamiltonian, that governs the system's dynamics, comprise a kinetic and a potential term. Plugging relation (3.13) into definition (3.35) yields the time derivative of the WIGNER function,

$$\partial_t f = \frac{1}{(2\pi\hbar)^3}\int \mathrm{d}^3\xi\; e^{-i\xi\cdot\mathbf{p}/\hbar}\,\langle \mathbf{x}+\tfrac{\xi}{2}|\,[-\tfrac{\hbar^2}{2M}\nabla^2,\hat{\rho}\,] + [\hat{V},\hat{\rho}\,]\,|\mathbf{x}-\tfrac{\xi}{2}\rangle. \tag{3.39}$$

The potential $\hat{V}$ has to be evaluated at different position arguments, depending on whether it acts on the bra $\langle \mathbf{x}+\xi/2|$ or the ket vector $\langle \mathbf{x}-\xi/2|$. Assuming $V(\mathbf{x})$ to be sufficiently smooth in position space, one may TAYLOR-expand the displaced function $V(\mathbf{x}\pm\xi/2)$ in order to express the potential contribution in terms of the undisplaced function $V(\mathbf{x})$. Furthermore, the displaced Laplacians $\nabla^2_{\mathbf{x}\pm\xi/2}$ can be expressed in terms of $\nabla_{\mathbf{x}}$ and ∇_{ξ}. For compactly writing spatial derivatives in position and mometum subspace, we reuse the notation $\nabla = \partial/\partial\mathbf{x}$ and $\boldsymbol{\partial} = \partial/\partial\mathbf{p}$, introduced in section 2.2.4. After all, one arrives at

$$\left(\partial_t + \frac{1}{M}\mathbf{p}\cdot\nabla - (\nabla V)\cdot\boldsymbol{\partial}\right) f = \sum_{l=1}^{\infty}\frac{(-1)^l}{(2l+1)!}\left(\frac{\hbar}{2}\right)^{2l}\sum_{|\underline{m}|=2l+1}(\nabla^{\underline{m}}V)\,\boldsymbol{\partial}^{\underline{m}} f, \tag{3.40}$$

abbreviating the tuples $\underline{m} = (m_1, m_2, m_3)$, their norm $|\underline{m}| = m_1 + m_2 + m_3$, and higher derivatives

$$\nabla^{\underline{m}} \equiv \left(\frac{\partial}{\partial x_1}\right)^{m_1}\left(\frac{\partial}{\partial x_2}\right)^{m_2}\left(\frac{\partial}{\partial x_3}\right)^{m_3}, \tag{3.41}$$

$$\boldsymbol{\partial}^{\underline{m}} \equiv \left(\frac{\partial}{\partial p_1}\right)^{m_1}\left(\frac{\partial}{\partial p_2}\right)^{m_2}\left(\frac{\partial}{\partial p_3}\right)^{m_3}. \tag{3.42}$$

Expression (3.40) is termed the quantum-LIOUVILLE equation. The second term on the left-hand side relates to the kinetic contribution of the Hamiltonian. The third one is just the first-order term of the TAYLOR expansion of the potential. The higher-order terms, involving multiple momentum derivatives, have all been arranged on the right-hand side. This way, we have separated all terms which carry a non-zero power of $\hbar$ from the classical terms without $\hbar$. Neglecting the right-hand side of the quantum-LIOUVILLE equation (3.40), we obviously recover the classical LIOUVILLE equation (2.53) for non-interacting particles (2.50). This approximation is justified if spatial derivatives of V of the order $l = 3$ and higher are negligible, which is certainly true for a harmonic oscillator but also for sufficiently smooth potentials. Although phase space dynamics is ruled by a classical equation in this case, the function f still represents a quantum state, which may depart from classical distributions, for example by being partially negative. This semi-classical approximation is also called the truncated WIGNER approach.

The fact that the evolution of the quantum-mechanical phase space distribution is – under certain conditions – subject to the classical LIOUVILLE equation has truly advantageous consequences. We can reuse results from the evolution of classical distributions. In particular, time-evolved WIGNER functions are connected to their preceding versions via a coordinate transformation,

$$f(\mathbf{z}, t_j) = f\Big(\hat{\mathscr{U}}^{-1}(t_{ij})\,\mathbf{z},\ t_i\Big). \tag{3.43}$$

The classical propagator $\hat{\mathscr{U}}(t)$ is introduced in chapter 2. The trajectories it generates are solutions to HAMILTON's equations (2.3). In case relation (3.43) is valid, one speaks of *classical transport*. It is of central importance for developing a ray tracing formalism that describes matter wave propagation. In order to evaluate the WIGNER function at certain phase space coordinates, on has to trace back this point along the classical phase space flow to a preceding time instance and query the distribution value there.

3.2.3 Example: Release from harmonic trap II

In order to give an example for evolving WIGNER functions, we continue the discussion of the release of atom clouds from harmonic traps which we have adjourned at the end of subsection 3.1.1. We have presented an expression for the thermal density matrix in coordinate representation (3.27). The formulation of time-dependence is quite convenient in terms of the WIGNER function and, moreover, similar to classical expressions.

Thermal equilibrium in trap

Plugging expression (3.27) into the definition (3.35) yields, as initial distribution, the quantum-mechanical phase space distribution of a thermal harmonic oscillator,

$$f_0(\mathbf{x}, \mathbf{p}) = \prod_{i=1}^{3} \frac{1}{\sqrt{\pi\hbar\epsilon_i(T)}} \exp\left[-\frac{1}{\epsilon_i(T)}\left(\frac{M\omega_i}{\hbar}x_i^2 + \frac{1}{M\hbar\omega_i}p_i^2\right)\right]. \tag{3.44}$$

In order to obtain a more compact notation which also reveals the correlation matrix of the phase space distribution more clearly, we define the diagonal matrix

$$\begin{aligned}\bar{\mathsf{b}}_{ij} &= \tanh\left(\frac{\hbar\omega_i}{2k_\mathrm{B}T}\right)\frac{2}{\hbar\omega_i}\delta_{ij} \\ &= \frac{2}{\hbar\omega_i\epsilon_i(T)}\delta_{ij}.\end{aligned} \tag{3.45}$$

Now, going to coordinate frames that do not align with the symmetry axes of the harmonic potential, the above defined diagonal matrix becomes a symmetric non-diagonal matrix. Similar to the transformation of the frequency matrix,

$$\Omega = \mathsf{R}^\mathsf{T}\begin{pmatrix}\omega_1 & 0 & 0\\ 0 & \omega_2 & 0\\ 0 & 0 & \omega_3\end{pmatrix}\mathsf{R}, \tag{3.46}$$

where R is a rotation, the non-diagonal b-matrix is

$$\mathsf{b} = \mathsf{R}^\mathsf{T}\,\bar{\mathsf{b}}\,\mathsf{R} \to \begin{cases}2(\hbar\Omega)^{-1}, & T\to 0\\ \frac{1}{k_BT}\mathbb{1}, & T\to\infty\end{cases}. \tag{3.47}$$

The quantum-mechanical ground state and the classical case are included as extreme temperature limits. With this, the WIGNER function for a thermal harmonic oscillator for arbitrary coordinate systems is written

$$f_0(\mathbf{x},\mathbf{p}) = \frac{\det\mathsf{b}}{(2\pi\hbar)^3}\,\exp\left(-\tfrac{M}{2}\mathbf{x}^\mathsf{T}\mathsf{b}\Omega^2\mathbf{x} - \tfrac{1}{2M}\mathbf{p}^\mathsf{T}\mathsf{b}\mathbf{p}\right). \tag{3.48}$$

In this form, the quantum-mechanical distribution has great resemblance to its classical counterpart (2.75). However, the scalar factor $1/(k_\mathrm{B}T)$ is replaced by the matrix b, which includes compliance with HEISENBERG's uncertainty relation in the zero-temperature limit. The most compact phase space notation is obtained by defining the six-dimensional block matrix

$$\mathsf{B} = \begin{pmatrix}\mathsf{b} & \mathbb{0}\\ \mathbb{0} & \mathsf{b}\end{pmatrix}. \tag{3.49}$$

Reusing the matrix of the bilinear harmonic oscillator Hamiltonian,

$$\Lambda = \begin{pmatrix}M\Omega^2 & \mathbb{0}\\ \mathbb{0} & \frac{1}{M}\mathbb{1}\end{pmatrix}, \tag{3.50}$$

we can write the quantum-mechanical Wigner function of a harmonic oscillator with finite temperature as

$$f_0(\mathbf{z}) = \frac{\sqrt{\det \mathsf{B}\Lambda}}{(2\pi)^3} \exp\left(-\tfrac{1}{2}\, \mathbf{z}^{\mathsf{T}}\, \mathsf{B}\,\Lambda\, \mathbf{z}\right). \tag{3.51}$$

The associated density profile in position space is

$$n_0(\mathbf{x}) = \left(\tfrac{M}{2\pi}\right)^{3/2} \sqrt{\det(\mathsf{b}\,\Omega^2)}\, \exp\left(-\tfrac{1}{2M}\, \mathbf{x}^{\mathsf{T}}\, \mathsf{b}\,\Omega^2\, \mathbf{x}\right). \tag{3.52}$$

Consider again the extreme temperature limits. At first, the zero-temperature limit means $k_{\mathrm{B}}T$ is negligible compared to all three energies $\hbar\omega_1$, $\hbar\omega_2$, and $\hbar\omega_3$. In this case, the position correlation matrix is $\langle\!\langle x_i x_j \rangle\!\rangle = \hbar/(2M)(\Omega^{-1})_{ij}$. Meanwhile, for momentum coordinates we have $\langle\!\langle p_i p_j \rangle\!\rangle = M\hbar\Omega_{ij}/2$. Both, the position and the momentum density, are shaped by the harmonic potential. The fact that increased frequencies Ω_{ij} leads to smaller widths in position space but to extended widths in momentum space is a manifestation of Heisenberg's uncertainty principle. In contrast, the high temperature limit implies neglecting all energies $\hbar\omega_i$ $(i = 1, 2, 3)$, which leads to $\langle\!\langle x_i x_j \rangle\!\rangle = k_{\mathrm{B}}T/M(\Omega^{-2})_{ij}$ and $\langle\!\langle p_i p_j \rangle\!\rangle = Mk_{\mathrm{B}}T$. The increase in temperature entails a significantly broadened phase space distribution. In particular, the momentum density is now isotropic and solely determined by temperature, while the position density's shape is subject to the potential as well as temperature. Clearly, the high temperature limit of the Wigner function is exactly identical to the classical phase space distribution given in (2.75).

Free expansion after release

Again, we release the harmonically trapped cloud by switching off the potential at $t = 0$. In the absence of external forces, $V = 0$, the right-hand side of (3.40) vanishes exactly. We are thus in the comfortable situation of using the classical equation of motion without the need of semi-classical approximations. Consequently, the expressions we seek have already been calculated in section 2.3.1 when we discussed the free expansion of a classical distribution. We briefly recapitulate on the results.

The initial distribution f_0, be it Gaussian or not, evolves according to

$$f(\mathbf{x}, \mathbf{p}, t) = f_0\left(\mathbf{x} - \tfrac{1}{M}\mathbf{p}\, t,\ \mathbf{p}\right). \tag{2.82}$$

The difference to the classical discussion is that in the current context, f and f_0 are Wigner functions. This means they can not only be non-Gaussian but also assume negative values. The evolution, nevertheless, follows classical phase space flow.

The inverse correlation matrices in position and momentum subspace that correspond to the initial distribution (3.48), are

$$\mathsf{C}_{x0}^{-1} = \tfrac{M}{2}\, \mathsf{b}\,\Omega^2, \qquad\qquad \mathsf{C}_{p0}^{-1} = \tfrac{1}{2M}\, \mathsf{b}, \tag{3.53}$$

respectively. Like in the classical discussion in section 2.3.1, these two matrices are related by $\mathsf{C}_{p0} = (M\Omega^2)\mathsf{C}_{x0}$. Now, being subject to free propagation, the phase space correlation matrix becomes

$$\mathsf{C}_z^{-1}(t) = \begin{pmatrix} \mathsf{C}_{x0}^{-1} & -\frac{1}{M}\mathsf{C}_{x0}^{-1}\,t \\ -\frac{1}{M}\mathsf{C}_{x0}^{-1}\,t & \mathsf{C}_{p0}^{-1} + \frac{1}{M^2}\mathsf{C}_{x0}^{-1}\,t^2 \end{pmatrix}. \tag{2.83}$$

This implies a time-dependent position correlation matrix

$$\mathsf{C}_x(t) = \left(\mathbb{1} + \Omega^2 t^2\right)\mathsf{C}_{x0}. \tag{2.84}$$

Meanwhile, the momentum correlation matrix, on the other hand, remains unaltered in the course of propagation, $\mathsf{C}_p(t) = \mathsf{C}_{p0}$. Expression (2.84) describes the spreading of the initial state. It can be conveniently pictured in the one-dimensional case, as we have done in figure (2.2).

3.3 Interacting boson gases

Neglecting interaction between particles, we can use the single-particle formulation presented in this chapter so far to describe the physics of atomic clouds. Taking into account interaction effects, however, one has to extent the formalism to many-particle quantum mechanics for realistic models [71, 72].

The transition from single to many-particle physics is already challenging in classical mechanics (cf. section 2.4). In quantum mechanics, it is additionally complicated by the indistinguishably of identical particles. This gives rise to many-particle wave functions which are either symmetric (bosons) or anti-symmetric (fermions) under particle permutation. Typical textbook discussions of many-body quantum mechanics split into two separate parts for bosons and fermions. However, since this work exclusively considers boson gases, we assume all states to possess even permutation symmetry from now on.

3.3.1 Reduced distributions for binarily interacting gas of bosons

A concise derivation of effective single-particle equations that describe the physics of quantum gases is given by Castin [73]. In analogy to our discussion of classical interacting gases in section 2.4, we assume inter-particle interactions to be binary. Consequently, the Hamiltonian comprises single- and two-particle terms,

$$\hat{H} = \sum_{i=1}^{N} \hat{h}_i + \tfrac{1}{2} \sum_{i \neq j = 1}^{N} \hat{V}_{ij}. \tag{3.54}$$

The former contains the kinetic contribution as well as the energy in the external potential of each particle. The latter corresponds to the energy of particle pairs in their inter-atomic scattering potential. Particularly useful are the matrix elements of these contributions in position representation,

$$\langle \mathbf{x}_i|\hat{h}_i|\mathbf{x}_i'\rangle = \delta(\mathbf{x}_i - \mathbf{x}_i') \left(-\frac{\hbar^2\nabla_i^2}{2M} + V_{\text{ext}}(\mathbf{x}_1)\right), \tag{3.55}$$

$$\langle \mathbf{x}_1\mathbf{x}_2|\hat{V}_{12}|\mathbf{x}_1'\mathbf{x}_2'\rangle = \delta(\mathbf{x}_1 - \mathbf{x}_1')\,\delta(\mathbf{x}_2 - \mathbf{x}_1')\,V_{\text{int}}(|\mathbf{x}_1 - \mathbf{x}_2|). \tag{3.56}$$

The function V_{int} possesses the same properties as the one introduced in equation (2.98). That is, V_{int} is symmetric and $\nabla_1 V_{\text{int}}$ is antisymmetric under particle permutation. The time evolution of the N-body density matrix $\hat{\rho}^{(N)}$, describing the complete many-particle state, is given by the VON-NEUMANN equation

$$i\hbar\partial_t\hat{\rho}^{(N)} = [\hat{H}, \hat{\rho}^{(N)}]. \tag{3.57}$$

Needless to say, despite the formal simplicity of this equation, the object $\hat{\rho}^{(N)}$ is extremely unpractical. Similar to section 2.4, we aim for an effective formalism in terms of few-body distributions. These are obtained from the N-body density matrix by tracing over the "rest particles",

$$\hat{\rho}_1 = \mathrm{Tr}_{\,2,\ldots,N}\,\hat{\rho}^{(N)}, \tag{3.58a}$$

$$\hat{\rho}_{12} = \mathrm{Tr}_{\,3,\ldots,N}\,\hat{\rho}^{(N)}, \tag{3.58b}$$

$$\cdots \quad .$$

Similar to the classical case discussed in section 2.4, these few-body representations give rise to a hierarchy of equations called BBGKY hierarchy [47, 61, 73]. Its first order equation reads

$$i\hbar\,\partial_t\hat{\rho}_1 - [\hat{h}_1, \hat{\rho}_1] = \mathrm{Tr}_{\,2}\,[\hat{V}_{12}, \hat{\rho}_{12}], \tag{3.59}$$

being the quantum-mechanical analog to equation (2.111b). Our goal is to break the hierarchy by approximating $\hat{\rho}_{12}$ in terms of $\hat{\rho}_1$, ignoring many-particle correlations of the atoms.

Hartree-Fock approximation for the pure condensate

An exclusive feature of boson gases is a phase transition to BOSE-EINSTEIN condensates below a critical temperature T_c. This condensation implies a macroscopic occupation of a single state which we assume, for instance, to be the system's ground state. Thus, the single-particle density matrix can be written [53, 63, 72]

$$\hat{\rho}_1 = N_0\,|\phi_0\rangle\langle\phi_0| + \sum_{k>0} \nu_k\,|\phi_k\rangle\langle\phi_k|, \tag{3.60}$$

with $N_0 \gg \nu_k$. The macroscopic occupation number is a consequence of BOSE-EINSTEIN statistics which, in turn, follows from the symmetry of bosonic many-particle functions. We consider the extreme case $T = 0$ and additionally ignore excited states completely. The single-particle density matrix can then be written as

$$\hat{\rho}_1 \approx N\, |\phi_0\rangle\langle\phi_0|, \tag{3.61}$$

implying $N \approx N_0$. The state $\hat{\rho}_1$ possesses off-diagonal long-range order [64, 65], i.e. it is phase-coherent across the entire cloud. Moreover, the HARTREE approximation for the two-body density matrix reads

$$\hat{\rho}_{12} \approx \hat{\rho}_1 \otimes \hat{\rho}_1 = N^2\, |\phi_0, \phi_0\rangle\langle\phi_0, \phi_0|. \tag{3.62}$$

Note that this two-particle state is already symmetrized. With these approximations, the BBGKY hierarchy is broken, yielding the closed equation

$$i\hbar\, \partial_t \hat{\rho}_1 = \left[\hat{h}_1 + \left(\int \mathrm{d}^3x_2\; V_{\text{int}}(|\mathbf{x}_1 - \mathbf{x}_2|)\, n(\mathbf{x}_2)\right) |\mathbf{x}_1\rangle\langle\mathbf{x}_1|,\; \hat{\rho}_1\right] \tag{3.63}$$

where we have used the matrix element of V_{int} in position representation as introduced in equation (3.56).

Hartree-Fock approximation for thermal gas

The second case we consider is a thermal gas with a temperature well above T_c. In this limit, the single-particle density $\hat{\rho}_1$ does not possess off-diagonal long-range order since phase coherence is destroyed by thermal fluctuations. Furthermore, as an opposite to the pure condensate limit, we assume the occupation numbers of all states to be on the order of one. We can then apply the HARTREE-FOCK approximation to the two-body density matrix [61, 73] as

$$\hat{\rho}_{12} \approx (1 + \hat{P}_{12})\, \hat{\rho}_1 \otimes \hat{\rho}_1. \tag{3.64}$$

Remembering to symmetrize the bosonic many-particle state, we have utilized the operator $\hat{P}_{12}$, permutating particles 1 and 2. The contribution $\hat{\rho}_1 \otimes \hat{\rho}_1$ is called direct or HARTREE term, while $\hat{P}_{12}\, \hat{\rho}_1 \otimes \hat{\rho}_1$ is called exchange or FOCK term. Breaking the BBGKY hierarchy with relation (3.64), the evolution equation for the thermal single-particle density matrix becomes

$$i\hbar\, \partial_t \hat{\rho}_1 = \left[\hat{h}_1 + 2\left(\int \mathrm{d}^3x_2\; V_{\text{int}}(|\mathbf{x}_1 - \mathbf{x}_2|)\, n(\mathbf{x}_2)\right) |\mathbf{x}_1\rangle\langle\mathbf{x}_1|,\; \hat{\rho}_1\right]. \tag{3.65}$$

Obviously, this expression is quite similar to its counterpart (3.63) in case of a pure condensate. The only difference is a factor of 2 in the interaction term of equation (3.65). It is a manifestation of the different occupation statistics in both cases.

3.3.2 Mean field theory at zero temperature

We now take a closer look at some features of a pure condensate ($T = 0$) with binary interactions. To this end, we define the macroscopic wave function in terms of the macroscopically occupied single-particle state as

$$\Psi(\mathbf{x}) = \sqrt{N}\,\langle \mathbf{x}|\phi_0\rangle. \tag{3.66}$$

Moreover, the inter-atomic interaction shall be approximated by a contact potential

$$V_{\text{int}}(\mathbf{x}-\mathbf{x}') = g\,\delta(\mathbf{x}-\mathbf{x}'). \tag{3.67}$$

The corresponding equation of motion is then given by a nonlinear SCHRÖDINGER equation,

$$i\hbar\,\partial_t\Psi = \left(-\frac{\hbar^2\nabla^2}{2M} + V_{\text{ext}} + g|\phi|^2\right)\Psi, \tag{3.68}$$

known as GROSS-PITAEVSKII equation. The macroscopic wave function is normalized to the total particle number,

$$\int \mathrm{d}^3x\,|\Psi|^2 = N. \tag{3.69}$$

In this work, we only consider repulsive interaction, $g > 0$. In analogy to the classical mean field theory, one attains a macroscopic description of an interacting many-body system involving a single equation at the expense of giving up the linearity of the microscopic equations. Mind that the influence of the nonlinear term $g|\phi|^2$ does not only depend on the value of g but also on the particle number N which is hidden in the wave function's normalization.

Hydrodynamic formulation

Describing the atom cloud in terms of two real fields instead of a single complex function ϕ, yields two equations of motion that are equivalent to the GROSS-PITAEVSKII equation (3.68). Therefore, the complex wave function is explicitly written in terms of its modulus and phase,

$$\Psi(\mathbf{x},t) = n^{1/2}(\mathbf{x},t)\,e^{\frac{i}{\hbar}S(\mathbf{x},t)}. \tag{3.70}$$

This is known as the MADLUNG ansatz. Inserting it into the GROSS-PITAEVSKII equation, we can separate two coupled equations in two real fields,

$$\partial_t n + \tfrac{1}{M}\nabla\cdot(n\,\nabla S) = 0, \tag{3.71a}$$

$$\partial_t S + \tfrac{1}{2M}(\nabla S)^2 + V_{\text{ext}} + gn + U_q[n^{1/2}] = 0. \tag{3.71b}$$

We have abbreviated the quantum pressure term as

$$U_q[n^{1/2}] = \frac{\hbar^2}{2M}\frac{-\nabla^2 n^{1/2}}{n^{1/2}}. \tag{3.72}$$

Equations (3.71b) is, apart from interaction gn and quantum pressure U_q similar to the classical HAMILTON-JACOBI equation. This implies that we can identify S, i.e. the phase in units if $\hbar$, with the classical action. An alternative formulation is obtained by using the velocity field $v(\mathbf{x}, t)$ instead of S. It is given by

$$v = \frac{\hbar}{2iM}\frac{\Psi^*(\nabla\Psi) - (\nabla\Psi^*)\Psi}{|\Psi|^2} = \frac{1}{M}\nabla S. \tag{3.73}$$

Exploiting this relation, we derive the *continuity equation* from expression (3.71a). It reads

$$\partial_t n + \nabla \cdot (n\, v) = 0, \tag{3.74}$$

describing the norm conservation of the particle flow. Moreover, equation (3.71b) can be reformulated in terms of the velocity field, yielding

$$M\,\partial_t \mathbf{v} + \nabla\left[\frac{1}{2}M\mathbf{v}^2 + V_{\text{ext}} + gn + U_q[n]\right] = 0. \tag{3.75}$$

This is, apart from the quantum pressure U_q, the EULER equation, describing the dynamics of a classical fluid without viscosity. Inclusion of U_q leads to quantum dispersion of the macroscopic wave function Ψ. The occurrence of the (quantum-) EULER equation suggests conceiving the condensate as a quantum fluid.

Although we present the hydrodynamic formulation here in the context of condensates of interacting atoms, it is not limited to this case. Clearly, starting with the SCHRÖDINGER equation, which is formally obtained from the GROSS-PITAEVSKII equation by setting $g = 0$, one obtains the continuity, the HAMILTON-JACOBI, and the EULER equation just as well.

Stationary state

For the stationary state, we make the ansatz

$$\Psi_0(\mathbf{x}, t) = n_0^{1/2}(\mathbf{x})\, e^{-i\mu t/\hbar}, \tag{3.76}$$

comprising a phase that is constant in space and linear in time. The stationary wave function modulus satisfies the stationary Gross-Pitaevskii equation

$$\left(-\frac{\hbar^2\nabla^2}{2M} + V_{\text{ext}} + gn_0 - \mu\right) n_0^{1/2}(\mathbf{x}) = 0. \tag{3.77}$$

The above ansatz implies $S_0(t) = -\mu t$ which can be plugged into equation (3.71b) to obtain a relation that determines the shape of the ground state density,

$$g n_0 = \mu - V_{\text{ext}} - U_q[n_0^{1/2}]. \tag{3.78}$$

It can be shown that μ is indeed the chemical potential $\partial E/\partial N$. The actual shape of the ground state is subject to the competition of three energy contributions. The quantum dispersion U_q and the repulsive interaction $g n_0$ favor a widely spread wave function, while the external potential V_{ext} counteracts these forces and confines the wave function.

The energy of the condensate [17, 73] is given by a functional in the mean field,

$$E[\Psi, \Psi^*] = \int \mathrm{d}^3 x \left(\frac{\hbar^2 |\nabla \Psi|^2}{2M} + V_{\text{ext}} |\Psi|^2 + \frac{1}{2} g |\Psi|^4 \right). \tag{3.79}$$

Based on this expression, the stationary Gross-Pitaevskii equation is obtained via a variational approach. The condition for Ψ making the functional $E[\Psi, \Psi^*]$ extremal under the constrain of constant particle number is just expression (3.77). Thereby, the chemical potential μ enters the equation as a Lagrange multiplier, ensuring compliance with the constraint (3.69).

In the limit of vanishing interaction $g = 0$, one recovers the non-interacting Schrödinger equation from expression (3.78). The corresponding ground state density n_0 becomes a smooth function of the position variables since quantum dispersion U_q penalizes rapid variations with an energy cost. The only relevant length scales are fixed by the competition between quantum dispersion and potential energy. In one-dimensional or radially symmetric systems, it is given by single parameter a, being the distance from the potential minimum where quantum dispersion equals potential energy. It is thus a solution of $V_{\text{ext}}(x = a) = \hbar^2/(2Ma^2)$. For more complicated geometries, this equilibrium condition is satisfied for a iso-surface of the potential, requiring more parameters for proper description. Considering a harmonic oscillator, for example, the typical length scale is given by the harmonic oscillator length $a_{\text{ho}}^2 = \hbar/(M\omega)$.

Having non-negligible mean field interaction $g n_0 \neq 0$, the ground state is no longer described by a single energy ratio but rather by two independent ratios. These are repulsion versus quantum dispersion on one hand, and repulsion versus external potential on the other. The former is characterized by the so-called Healing length

$$\xi(\mathbf{x}) = \frac{\hbar}{\sqrt{2M g\, n_0(\mathbf{x})}}. \tag{3.80}$$

Physically, it can be described as follows. The presence of interaction energy facilitates the creation of spatial density variations on length scales shorter than the harmonic oscillator width. The length scale on which the interaction energy gn exactly balances the quantum dispersion energy U_q is given by the Healing length. Note that ξ, depending on the density $n_0(\mathbf{x})$, is a local feature of the trapped cloud. Hence, at the edge of the atom cloud, lower density entails an increased Healing length.

In terms of ξ, the quantum pressure can compactly be written as

$$U_q[n_0^{1/2}] = \xi^2\, n_0^{1/2}\, \nabla^2 n_0^{1/2}. \tag{3.72'}$$

Inside the interaction dominated regime $gn \gg U_q$, the healing length ξ becomes negligibly small. The ground state's shape is then solely determined by interaction and potential energy. In this case,it is a solution of

$$g\, n(\mathbf{x}) = \mu_{\mathrm{TF}} - V_{\mathrm{ext}}(\mathbf{x}), \tag{3.81}$$

being called the THOMAS-FERMI density [10, 18]. Note that the n is calculated with equation (3.81) only where $\mu > V_{\mathrm{ext}}(\mathbf{x})$ and is zero otherwise.

Analytical insight into the solution of equation (3.81) is greatly facilitated by choosing a definite potential form. In order to not over-complicate the discussion, we assume to have an isotropic harmonic oscillator, $V_{\mathrm{ext}}(\mathbf{x}) = M\omega^2 x^2/2$. Remember that every anisotropic harmonic oscillator can be made isotropic via a coordinate transformation (see appendix A). With this choice of V_{ext}, the THOMAS-FERMI density is written

$$n(\mathbf{x}) = \begin{cases} \frac{M\omega^2}{2g}\left(R_{\mathrm{TF}}^2 - \mathbf{x}^2\right), & \mathbf{x}^2 < R_{\mathrm{TF}}^2 \\ 0, & \mathbf{x}^2 > R_{\mathrm{TF}}^2 \end{cases}. \tag{3.82}$$

It has the shape of an inverted parabola. The THOMAS-FERMI radius

$$R_{\mathrm{TF}} = \sqrt{\frac{2\mu_{\mathrm{TF}}}{M\omega^2}} \tag{3.83}$$

quantifies the spatial extent of the strongly interacting atom cloud. Moreover, R can be expressed in terms of the particle number by virtue of the normalization condition. Integrating the THOMAS-FERMI density (3.82) over a sphere of radius R_{TF} yields

$$N = \frac{\pi^{D/2}}{\Gamma(\frac{D}{2}+2)}\,\frac{M\omega^2}{2g}\,R_{\mathrm{TF}}^{D+2}. \tag{3.84}$$

And finally, the chemical potential in terms of the particle number can be expressed as

$$\mu_{\mathrm{TF}} = \left[\Gamma\left(\tfrac{D}{2}+2\right)\left(\frac{M\omega^2}{2\pi}\right)^{D/2} N g\right]^{2/(D+2)}. \tag{3.85}$$

Thus, for interaction dominated systems, μ_{TF} is related to N by a power law. For noninteracting systems, in contrast, it is independent of the particle number, $\mu = \hbar\omega/2$. In figure 3.2, the density of the GROSS-PITAEVSKII solution is compared to the THOMAS-FERMI density for an one-dimensional harmonic oscillator.

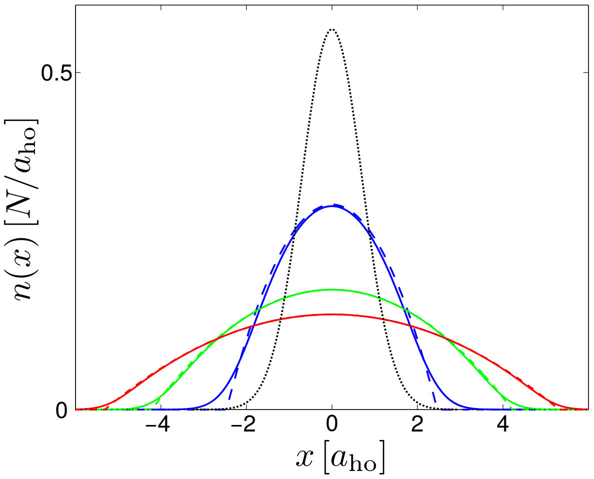

Figure 3.2.: Comparison of numerical solution of the GROSS-PITAEVSKII (solid lines) to the THOMAS-FERMI limit (dashed lines) in a one-dimensional harmonic oscillator. The latter is given in expression (3.82). The colors blue, green, and red indicate interaction strengths Ng of $10\hbar\omega/a_{\rm ho}$, $50\hbar\omega/a_{\rm ho}$, and $100\hbar\omega/a_{\rm ho}$, respectively. The dotted curve is for zero interaction (Gaussian, according to e.g. (3.19)).

Sound wave excitations

Suppose we have prepared a condensate in a trapping potential. How does this state respond to small perturbations? To answer this question, one linearizes the equilibrium density and phase,

$$n(\mathbf{x},t) = n_0(\mathbf{x}) + \lambda n_1(\mathbf{x},t), \tag{3.86a}$$

$$S(\mathbf{x},t) = S_0(t) + \lambda S_1(\mathbf{x},t). \tag{3.86b}$$

The dimensionless auxiliary factor λ is useful for keeping track of the order of perturbation. Linear perturbation theory implies ignoring all terms containing λ^2 or higher powers. Thereafter, one sets $\lambda = 1$. According to the ground state we defined above, the zeroth order modulus n_0 is time independent, while the zeroth order phase $S_0(t) = -\mu t$ is spatially constant. In order to obtain a single equation of motion in the linearized perturbations, one differentiates the continuity equation (3.74) with respect to time, inserts the ansatz (3.86). After neglecting all higher order terms one has

$$\partial_t^2 n_1 - \nabla\left(\frac{gn_0}{M}\nabla n_1\right) = 0. \tag{3.87}$$

This equation describes the propagation of sound waves in an inhomogeneous medium. One can identify the speed of sound as $c^2(\mathbf{x}) = gn_0(\mathbf{x})/M$, which is spatially varying. The inhomogeneity results from the ground state density n_0. In this spirit, we can identify the position dependent speed of sound $c(\mathbf{x})$, satisfying

$$c^2 = \frac{gn_0}{M}. \tag{3.88}$$

In the THOMAS-FERMI limit and in case of a three-dimensional harmonic potential, the above equation can be solved applying a power series ansatz [74]. In the simple case of a one-dimensional harmonic oscillator with frequency ω, sound wave propagation in the strongly interacting regime is subject to

$$\partial_t n_1 - \frac{\omega}{2}\partial_x\Big((R^2 - x^2)\,\partial_x n_1\Big) = 0. \tag{3.89}$$

Introducing dimensionless coordinates $z = x/R$ and making the ansatz $n_1(z,t) = \overline{n}(z)\,e^{-i\nu t}$, it can be expressed as

$$(1-z)^2\,\partial_z^2\overline{n} - 2z\,\partial_z\overline{n} + 2\frac{\nu^2}{\omega^2}\overline{n} = 0 \tag{3.90}$$

This is just LEGENDRE's differential equation, which is solved by LEGENDRE polynomials, $\overline{n}_\ell(z) = P_\ell(z)$ [75]. The frequencies of the solutions must satisfy $\nu_\ell = \omega\,\big(\ell(\ell-1)/2\big)$. Consequently, the general solution for sound waves in one dimension is

$$n_1(x,t) = \sum_\ell a_\ell P_\ell\left(\frac{x}{R_{\mathrm{TF}}}\right) e^{-i\frac{\ell(\ell-1)}{2}\,\omega t}. \tag{3.91}$$

3.3.3 Wigner functions with mean field interaction

WIGNER functions, introduced in the context of single-particle physics in section 3.2.1, are easily generalized to describe many-body states. The N-particle WIGNER function is defined as

$$\begin{aligned} f^{(N)}(\mathbf{x}_1,\mathbf{p}_1;\ldots;\mathbf{x}_N,\mathbf{p}_N) = \frac{1}{(2\pi\hbar)^{3N}} \int_{\mathbb{R}^{3N}} \mathrm{d}^3\xi_1\ldots\mathrm{d}^3\xi_N\; e^{-i(\xi_1\mathbf{p}_1+\ldots+\xi_N\mathbf{p}_N)/\hbar} \\ \times\,\langle \mathbf{x}_1 + \tfrac{\xi_1}{2},\ldots,\mathbf{x}_1 + \tfrac{\xi_N}{2} |\,\hat{\rho}^{(N)}\,| \mathbf{x}_1 - \tfrac{\xi_1}{2},\ldots,\mathbf{x}_1 - \tfrac{\xi_N}{2}\rangle. \end{aligned} \tag{3.92}$$

It is a phase space representation of the full N-body density matrix $\hat{\rho}^{(N)}$. Similar to the discussion of classical phase space distributions in section 2.4.1, we can define reduced WIGNER functions as

$$f^{(s)}(\mathbf{z}_1,\ldots,\mathbf{z}_N) = \frac{N}{(N-s)!}\int \mathrm{d}^6 z_{s+1}\ldots\mathrm{d}^6 z_N\, f^{(N)}(\mathbf{z}_1,\ldots,\mathbf{z}_N), \tag{2.105}$$

being an effective few-particle representation of the N-particle state. We have combined position and momentum into phase space coordinates, $\mathbf{z}_i = (\mathbf{x}_i, \mathbf{p}_i)$. Again, one finds a closed evolution equation for the effective single-particle WIGNER function $f = f^{(s=1)}$ by breaking the BBGKY hierarchy [47, 61]. We can also directly WIGNER-transform equations that resulted from the

Hartree-Fock approximation in section 3.3.1. This way, the effective single-particle Wigner function, describing an interacting gas, is subject to

$$\left(\partial_t + \frac{1}{M}\mathbf{p}\cdot\nabla - (\nabla U)\cdot\partial\right) f = \sum_{l=1}^{\infty} \frac{(-1)^l}{(2l+1)!}\left(\frac{\hbar}{2}\right)^{2l} \sum_{|\underline{m}|=2l+1} (\nabla^{\underline{m}} U)\, \partial^{\underline{m}} f. \tag{3.93}$$

Here, the position dependent function U comprises a contribution from the external potential V_{ext}, as well as mean field interaction. Assuming again contact interaction (3.67), the explicit form of U that follows from equation (3.63) is

$$U = V_{\text{ext}} + gn, \tag{3.94}$$

in case f describes a pure condensate. Its dependence on the density makes (3.93) a non-linear equation in the Wigner function. Meanwhile, in case f is the phase space representation of a thermal gas, we can Wigner-transform equation (3.65), to obtain an evolution equation that contains

$$U = V_{\text{ext}} + 2gn. \tag{3.95}$$

As already mentioned, the different factors of the mean field terms are due to particle statistics. Identifying the semi-classical limit of equation (3.93), where we can ignore all contribution with $\hbar$, is slightly more involved than in the noninteracting case. Since the Wigner function is subject to a self-consistent potential, we require both, the external potential V_{EXT} as well as the density profile of the cloud itself to be slowly varying in position space. If these conditions are fulfilled we can again apply the truncated Wigner approach. In this case, evolution of Wigner functions is approximately described by

$$\partial_t f + \frac{\mathbf{p}}{M}\nabla f - (\nabla U)\,\partial f = 0. \tag{3.96}$$

Being identical to its classical counterpart (2.122), we can utilize classical phase space propagation to describe the evolution of interacting Wigner functions in the semi-classical limit. The energy content of a pure condensate is calculated by the expression

$$E[f] = \int \mathrm{d}^3x\, \mathrm{d}^3p \left(\frac{\mathbf{p}^2}{2M} + V_{\text{ext}} + \frac{1}{2}gn\right) f, \tag{3.97}$$

being a non-linear functional of the Wigner function. For a thermal gas, the energy functional $E[f]$ is identical to (3.97) except that the mean field term gn enters without a factor $1/2$.

Part II.

Applications

4 The Lambert density solution

A particular stationary solution of the nonlinear LIOUVILLE equation, which we call LAMBERT density, is studied in the this chapter. As we will see, it reproduces approximations to the density profile of a trapped gas in the strongly and weakly interacting limit. For intermediate interaction strengths, it interpolates continuously between the extreme parameter regimes.

In the first section, we directly give the separating ansatz solution and study its extreme parameter limits. We then compare it to numerical solutions of the GROSS-PITAEVSKII equation. After that, going away from the assumption of harmonic potentials that facilitate analytical treatment, we calculate the LAMBERT density and corresponding results for a chip-trap potential.

4.1 Seperating anstatz solution to stationary Liouville equation with interaction

The stationary solution $f_0(\mathbf{x},\mathbf{p})$ of the interacting classical LIOUVILLE equation (2.122) or the semi-classical limit of the interacting quantum-LIOUVILLE equation (3.96) is found by solving,

$$\{H, f\} = 0. \tag{4.1}$$

As we saw in chapters 2 and 3, we can use equation (4.1) to describe classical gases as well as condensates. In case of the latter, we have to assume the truncated WIGNER approach to be valid. In both scenarios, the HAMILTON function of a trapped gas with mean field interactions can be expressed as

$$H = \frac{\mathbf{p}^2}{2M} + U(\mathbf{x}), \tag{4.2}$$

where the function U comprises the external potential and the mean field interaction,

$$U(\mathbf{x}) = V_{\text{ext}}(\mathbf{x}) + \kappa \frac{n(\mathbf{x})}{N}. \tag{4.3}$$

The main difference between considering a thermal gas and a condensate is the interaction parameter κ. Assuming a contact interaction potential of the form $V_{\text{int}}(\mathbf{x},\mathbf{x}') = g\,\delta(\mathbf{x}-\mathbf{x}')$, one obtains the mean field contribution

$$\kappa\, n(\mathbf{x}) = \begin{cases} N\, g\, n(\mathbf{x}), & \text{condensate} \\ 2N\, g\, n(\mathbf{x}), & \text{class. gas} \end{cases} \tag{4.4}$$

to the Hamilton function. Aiming for a formulation that suits both cases, we will just write κ in the following. Meanwhile, we keep in mind expression (4.4) if we have to decide whether we describe a condensate or a thermal gas.

The way we have written the mean field interaction term here may seem a little cumbersome compared to $2gn$ in equation (2.121) or gn in (3.94). It has nonetheless some advantages. On one hand, the parameter κ properly quantifies the mean field interaction strength which depends on both, the interaction parameter g and the total particle number N. In most cases, the former is fixed by the choice of atom type. On the other, the ratio $n(\mathbf{x})/N$ is an intrinsic observable.

Clearly, equation (4.1) is satisfied by any function of the classical Hamiltonian $f(H)$. A simple ansatz to solve the stationary Liouville equation is to split position and momentum dependence into separate functions that enter the stationary Wigner distribution as a product,

$$f_0(\mathbf{x},\mathbf{p}) = n(\mathbf{x})\,u(\mathbf{p}). \tag{4.5}$$

The position density is normalized to the particle number

$$\int \mathrm{d}^3x\; n(\mathbf{x}) = N. \tag{4.6}$$

Since the Wigner function is also normalized to N, the momentum distribution has to be normalized to unity,

$$\int \mathrm{d}^3p\; u(\mathbf{p}) = 1. \tag{4.7}$$

Now, with the separating ansatz (4.5), the stationary Liouville (4.1) equation becomes

$$\frac{\mathbf{p}}{M}\,\frac{\partial_{\mathbf{x}} n(\mathbf{x})}{n(\mathbf{x})} = \partial_{\mathbf{x}} U(\mathbf{x})\,\frac{\partial_{\mathbf{p}} u(\mathbf{p})}{u(\mathbf{p})}. \tag{4.8}$$

It is readily solved by density functions being exponentials of the position- and the momentum-dependent term of the Hamiltonian, respectively,

$$n(\mathbf{x}) \propto e^{-b\,U(\mathbf{x})}, \qquad\qquad u(\mathbf{p}) \propto e^{-b\mathbf{p}^2/(2M)}. \tag{4.9}$$

Their proportionality factors are subject to the normalization of the phase space distribution $f_0(\mathbf{x},\mathbf{p})$. The factorizing stationary solution in the D-dimensional case can thus be written as

$$u(\mathbf{p}) = \left(\frac{b}{2\pi M}\right)^{D/2} e^{-b\,\mathbf{p}^2/(2m)}, \tag{4.10}$$

$$n(\mathbf{x}) = N\,\overline{n}(b,\kappa)\,e^{-b\,U(\mathbf{x})}, \tag{4.11}$$

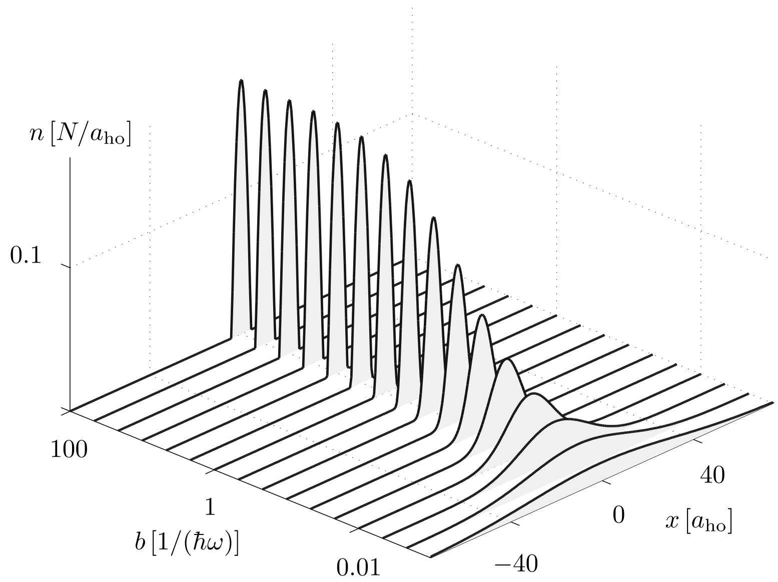

Figure 4.1.: Lambert density profile for different values of b in a one-dimensional harmonic oscillator. Length scale is $a_{\text{ho}} = [\hbar/(M\omega)]^{1/2}$. Interaction strength is $\kappa = 50\,\hbar\omega l_{\text{ho}}$. The b-axis is scaled logarithmically.

where $\overline{n}(b, N)$ is determined by the normalization condition

$$\int_{\mathbb{R}^D} \mathrm{d}^D x\; \overline{n}(b,\kappa)\, e^{-b\,U(\mathbf{x})} = 1. \tag{4.12}$$

Expression (4.11) is a self-consistent equation in the position density n. It can be solved by a closed relation,

$$n(\mathbf{x}) = \frac{N}{b\kappa}\, W\left[\, b\kappa\, \overline{n}(b,\kappa)\, e^{-bV_{\text{ext}}(\mathbf{x})}\right], \tag{4.13}$$

utilizing the LAMBERT function $W(z)$ (see appendix B). We will refer to it as LAMBERT density.

Solution (4.13) as well as the momentum density (4.10) depend on a parameter b, which needs a physical interpretation assigned to it. Its influence on the position density profile is depicted in figure 4.1 in case of an one-dimensional harmonic oscillator with fixed interaction strength. On one side, we can observe how the width of the Gaussian-like density profile decreases while b is increased starting from small values. This is akin to a thermal gas of trapped classical particles that localizes at the trap center for higher $\beta = (k_{\text{B}}T)^{-1}$ (i.e. lower temperature). On the other side of the parameter range, the density profile approaches a shape with finite width – akin to the THOMAS-FERMI limit (3.82) – rather than producing arbitrarily sharp distributions. It is tempting to interpret b as a variation parameter that assumes an optimal value when minimizing the system's energy. We will see in the following subsections, however, that $E(b)$ does not have a minimum for finite values of b. Alternatively, since b also appears in the Gaussian momentum density profile (4.10), its proper value can be deduced by estimating the momentum variance $\Delta p^2 = b/M$. This estimation can either involve thermal movement, quantum pressure or both.

4.1.1 Energy and particle number of D-dimensional isotropic, harmonic systems

Discussing the Lambert density solution (4.13) is greatly facilitated by considering isotropic harmonic oscillators as trapping potentials, $V_{\text{ext}}(\mathbf{x}) = M\omega^2\mathbf{x}^2/2$. In this way, the radial extend of the corresponding ground state, $a_{\text{ho}} = [\hbar/(M\omega)]^{1/2}$, is a manifest length scale. Note that even for anisotropic harmonic oscillators, coordinates can be rotated and rescaled to render the potential isotropic. For convenience, we also define the parameter $\nu(b,\kappa) = \ln[b\kappa\overline{n}(b,\kappa)]$, so the position density (4.13) can be written as

$$n(\mathbf{x}) = \frac{N}{b\kappa} W\left[e^{\nu(b,\kappa)-bM\omega^2\mathbf{x}^2/2}\right]. \tag{4.14}$$

First of all, we take a look at the parameter ν which depends on b and κ. Using definition (B.6), the normalization condition (4.12) may be rearranged to

$$\left(\frac{M\omega^2}{2\pi}\right)^{D/2} \kappa b^{D/2+1} = \tfrac{1}{(2\pi)^{D/2}} \int \mathrm{d}^D x \, W\left(e^{\nu - x^2/2}\right) = \mathscr{I}_D^{(1)}(\nu). \tag{4.15}$$

By virtue of $\mathscr{I}_D^{(1)}(\nu)$ being strictly monotonically increasing (see appendix B.2), for fixed trap parameters M and ω, we have a one-to-one relation between the normalization parameter ν and the product $\kappa\, b^{D/2+1}$. In particular, the conditions for weakly interacting ($\kappa \to 0$) and strongly interacting ($\kappa \to \infty$) regimes translate to $\nu \to -\infty$ and $\nu \to \infty$, respectively. A key-observable of the gas is the total energy which comprises three additive contributions,

$$\begin{aligned} E[f] &= E_{\text{kin}} + E_{\text{ext}} + E_{\text{mf}} \\ &= \int \mathrm{d}^D x \, \mathrm{d}^D p \left[\frac{\mathbf{p}^2}{2M} + \frac{M\omega^2\mathbf{x}^2}{2} + \tfrac{1}{2}\kappa \frac{n(\mathbf{x})}{N}\right] u(\mathbf{p})\, n(\mathbf{x}). \end{aligned} \tag{4.16}$$

Firstly, calculation of the kinetic term is straightforward. The position integral is just the normalization condition on $n(\mathbf{x})$ and the momentum integral is the variance of the Gaussian $u(\mathbf{p})$. We obtain

$$E_{\text{kin}}(N,b,\kappa) = N \int \mathrm{d}^D p \, \frac{\mathbf{p}^2}{2M} u(\mathbf{p}) = N\frac{D}{2b}. \tag{4.17}$$

The second contribution accounts for the potential energy of the atoms inside the trap. Since the integral over the momentum distribution merely yields unity, we are left with

$$\begin{aligned} E_{\text{ext}}(N,b,\kappa) &= \frac{N}{b^2\kappa} \int \mathrm{d}^D x \, \frac{bM\omega^2}{2} x^2 \, W\left[e^{\nu(b,\kappa) - bM\omega^2 x^2/2}\right] \\ &= \tfrac{1}{2} DN \left(\frac{2\pi}{M\omega^2}\right)^{D/2} \frac{\mathscr{I}_{D+2}^{(1)}[\nu(b,\kappa)]}{b^{D/2+2}\kappa}, \end{aligned} \tag{4.18}$$

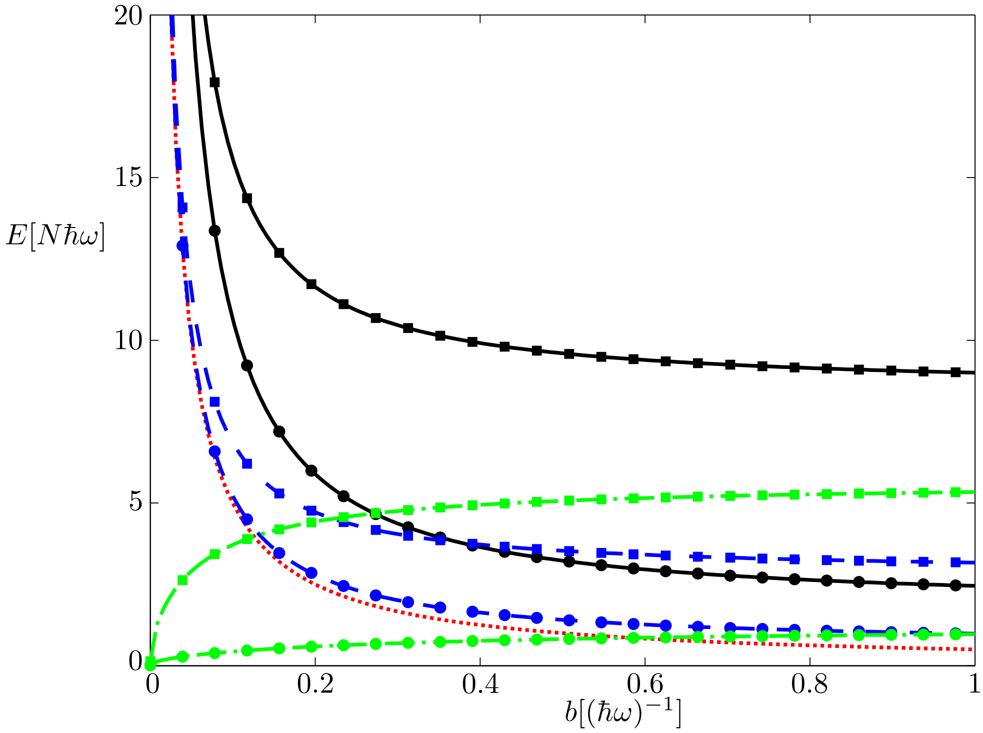

Figure 4.2.: Comparison of contributions to the total energy functional $E[f]$ for different interaction strengths, $\kappa = 100\,\hbar\omega a_{\text{ho}}$ (■) and $\kappa = 10\,\hbar\omega a_{\text{ho}}$ (•) in case of an one-dimensional harmonic oscillator potential. Colors and line styles are used to distinguish between energy contribution in the following way. Total energy is black solid, kinetic part is red dotted, trap part is blue dashed, and mean-field part is green dash-dotted. Expressions for the energy comntributions E_{kin}, E_{ext}, and E_{mf} are given in (4.17), (4.18), and (4.19), respectively.

where we have used definition (B.6) in the last step. Similarly, the meanfield term with its quadratic density dependence can be written as

$$\begin{aligned} E_{\text{mf}}(N,b,\kappa) &= \frac{N}{2b^2\kappa}\int \mathrm{d}^D x\, W^2\left[e^{\nu(b,\kappa)-bM\omega^2x^2/2}\right] \\ &= \frac{1}{2}N\left(\frac{2\pi}{M\omega^2}\right)^{D/2}\frac{\mathscr{I}_D^{(2)}\left[\nu(b,\kappa)\right]}{b^{D/2+2}\kappa}. \end{aligned} \tag{4.19}$$

The influence of the parameters b and κ on these contributions is depicted in FIG. 4.2. Apparently, in the limit $b \to \infty$, all energy terms either vanish or assume a finite value. The limit values for E_{ext} and E_{mf}, which increase for stronger interactions, are calculated in section 4.1.2. As expected, the kinetic energy is independent of the interaction strength. Remarkably, the total energy does not possess a minimum at finite b, which could have given rise to an optimal b-value. Moreover, figure 4.2 compares the total energy for medium and strong interaction, i.e., $\kappa = 10\,\hbar\omega l_{\text{ho}}$ and $\kappa = 100\,\hbar\omega l_{\text{ho}}$. We observe that for zero interaction, the kinetic and the trap contribution to the total energy coincide, which is typical for harmonic oscillators. Trivially, the mean field energy vanishes in this case. For increasing interaction, however, the mean field part assumes non-zero values growing with b while the trapping energy rises above E_{kin}. The latter remains independent of the interaction strength (at least in our model).

4.1.2 Extreme parameter regimes of the Lambert density

We are now able to calculate the Lambert density and corresponding observables for arbitrary mean field interactions κ. Nevertheless, much analytical insight into solution (4.13) is gained by considering extreme parameter regimes. In this way, we can also check for consistency with well-established theories for both, noninteracting classical gases and interacting condensates. The density expressions for strongly and weakly interacting gases given below hold for arbitrary external potentials. For the sake of calculating observables that involve integrals of the Lambert density (e.g. particle number, energy) analytically, we assume again a harmonic trapping potential $V_{\mathrm{ext}}(\mathbf{x}) = M\omega^2\mathbf{x}^2/2$. This way, we can use the results ot the preceding subsection. It should be noted, however, that these calculations can be performed for arbitrary confining potentials as well.

Strongly interacting limit

In the case of strongly interacting gases in atom traps, $\kappa \to \infty$, areas of different particle densities demand different approximation schemes. Near the cloud center (I), mean-field effects are dominant. In terms of Eq. (4.14), this condition is reflected in ν largely overwhelming the potential term which allows us to apply the asymptotic expression of the LAMBERT function (B.4). Far beyond the cloud edge (III), the trapping potential V_{ext} dominates the cloud's behavior. Densities become very small, and thus we may expand W in a series as instructed in (B.3). However, in the intermediate region at the cloud edge (II) where the argument of the Lambert function in expression (4.14) is around one, neither approximation scheme is appropriate (see appendix). The transit between the asymptotic regimes in regions I and III is roughly characterized by $\nu \approx bV(\mathbf{x})$. This condition – in case of radially symmetric potentials – gives rise to the definition of a radius,

$$R^2 = \frac{2\nu}{b\,M\omega^2}, \tag{4.20}$$

assuming a harmonic trap. Close to the trap minimum, $|\mathbf{x}| \ll R$ (region I), the density profile is subject solely to the competition between potential energy and mean field interactions. Outside the bulk center, densities at and beyond the cloud edge (region II and III) are comparatively small and assumed to be negligible. Moreover, we keep only the $\ln(z)$ term of the asymptotic expression (B.4) as it is the most dominant one for large z. Altogether, the above assumptions lead to

$$n(\mathbf{x}) \approx \frac{N}{\kappa}\left[\frac{\nu(b,\kappa)}{b} - V(\mathbf{x})\right], \tag{4.21}$$

for $|\mathbf{x}| < R$. This is exactly the density profile of the THOMAS-FERMI approximation, introduced in section 3.3.2. This way, we can identify the ratio of the parameters ν and b as chemical potential,

$$\mu_{\mathrm{TF}} = \frac{\nu(b,\kappa)}{b}. \tag{4.22}$$

Note that expression (4.21) is constricted to a sphere with radius R, given in (4.20), while $n(\mathbf{x}) \approx 0$ for $|\mathbf{x}| > R$. With identity (4.22), expression (4.20) exactly reproduces the THOMAS-FERMI radius R_{TF} defined in equation (3.83). Calculating ν in terms of κ and b as given in relation (4.15), we use approximation (B.10) for the integral $I_D^{(1)}(\nu)$ to find

$$\mu_{\mathrm{TF}}(\kappa) = \left[\Gamma\left(\tfrac{D}{2}+2\right)\left(\tfrac{M\omega^2}{2\pi}\right)^{D/2} \kappa\right]^{2/(D+2)}. \tag{4.23}$$

Note that this expression has lost any b-dependence. In case of $D = 3$, result (4.23) is well-known from studies of the THOMAS-FERMI limit of ultra cold gases [17, 19] where one finds $\mu_{\mathrm{TF}} \propto N^{2/5}$. Being interested in the total energy of the gas, we use again the asymptotic expression (B.10) to simplify the energy contributions (4.17)-(4.19) and sum them up to

$$E(N,b,\kappa) = \frac{DN}{2b} + \frac{D+2}{D+4} N\, \mu_{\mathrm{TF}}(\kappa). \tag{4.24}$$

Furthermore, the chemical potential can be calculated as

$$\mu(b,\kappa) = \frac{\partial E}{\partial N} = \frac{D}{2b} + \mu_{\mathrm{TF}}(\kappa). \tag{4.25}$$

In contrast to expression (3.85), the chemical potential given in equation (4.25) comprises an additional term that accounts for the finite spread of the distribution function in momentum space. Since μ_{TF} is independent of b, neither the energy nor the chemical potential posses a minimum for finite b, as we have mentioned in the last subsection. Nevertheless, the results of the THOMAS-FERMI are reproduced exactly in the limit $b \to \infty$, making the kinetic energy contribution vanish completely. Figure 4.3 shows a comparison of the Lambert density and the THOMAS-FERMI density for several values of the interaction strength. Obviously, the arbitrarily chosen b-value of $1000\,\hbar^{-1}\omega^{-1}$ is sufficiently large to make the Lambert density visually indistinguishable from n_{TF}. Although it is satisfactory to see that familiar results are obtained for $b \to \infty$, this limit implies zero momentum variance. The conflict of $\Delta p = 0$ with the uncertainty principle may be solved by postulating a minimal Δp and thus an upper bound on b. We further elaborate on this aspect when comparing the Lambert density solution with numerical results of the Gross-Pitaevskii equation in Section 4.2.

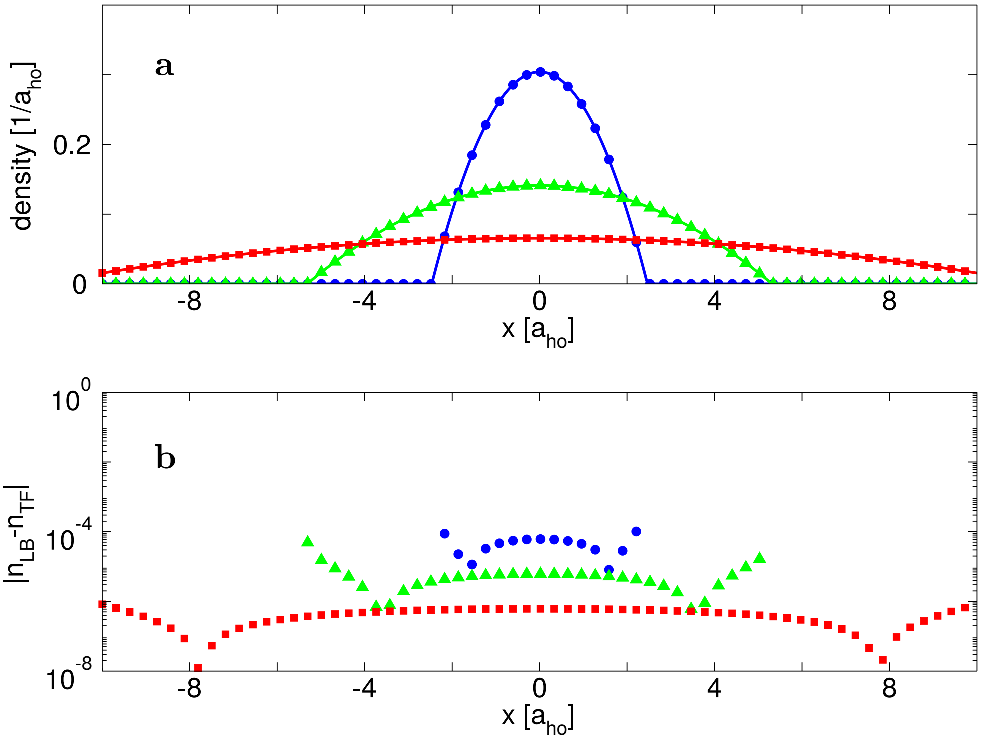

Figure 4.3.: Comparison of Lambert density (n_{LB}) to Thomas-Fermi density (n_{TF}) for strong interaction in a one-dimensional harmonic oscillator with constant parameter $b = 1000\,(\hbar\omega)^{-1}$. Part **a:** Direct comparison of n_{LB} (markers) and n_{TF} (solid lines). Part **b:** Absolute value of difference between n_{LB} (markers) and n_{TF}. Various interaction parameter values are $\kappa = 10\,\hbar\omega a_{\mathrm{ho}}$ (blue •), $\kappa = 100\,\hbar\omega a_{\mathrm{ho}}$ (green ▲), and $\kappa = 1000\,\hbar\omega a_{\mathrm{ho}}$ (red ■).

Weakly interacting limit

For the case of weak interactions, we may use the series expansion of W (B.3) to approximate the LAMBERT density (4.13). In order to develop a formalism which comprises interaction effects to the lowest non-trivial order, we linearize the Lambert density (4.13) in κ,

$$n(\mathbf{x}) = \overline{n}\, e^{-b\,V_{\text{ext}}(\mathbf{x})} - b\kappa\,\overline{n}^2\, e^{-2b\,V_{\text{ext}}(\mathbf{x})}. \tag{4.26}$$

Clearly, the effect of the perturbation term is to flatten the density profile in the cloud center. Mind that the factor $\overline{n}$ ensures normalization of $n(\mathbf{x})$ to N and thus also depends on κ and b. Stipulating again harmonic oscillator potentials, the linear approximation of the normalization condition (4.15) takes the form

$$\overline{n} - 2^{-D/2}\, b\kappa\,\overline{n}^2 = \left(\tfrac{bM\omega^2}{2\pi}\right)^{D/2}, \tag{4.27}$$

which is solved by

$$\overline{n} = \left(\tfrac{bM\omega^2}{2\pi}\right)^{D/2}\left[1 + \left(\tfrac{bM\omega^2}{4\pi}\right)^{D/2} b\kappa + \mathcal{O}(\kappa^2)\right]. \tag{4.28}$$

Hence, expression (4.26) is written

$$n(\mathbf{x}) = \left(\tfrac{bM\omega^2}{2\pi}\right)^{D/2} e^{-\frac{bM\omega^2}{2}x^2} + b\kappa\left(\tfrac{bM\omega^2}{2\pi}\right)^{D}\left[2^{-D/2}\, e^{-\frac{bM\omega^2}{2}x^2} - e^{-bM\omega^2x^2}\right] + \mathcal{O}(\kappa^2) \tag{4.29}$$

Comparing this expression to (2.77), it is satisfactory to see that one recovers the classical noninteracting density profile in harmonic potentials when setting $\kappa = 0$ exactly and identifying $b = (k_{\text{B}}T)^{-1}$. In order to evaluate the linear approximation of the several energy contributions we utilize the series expansions (B.8) and (B.9) of the overlap integral $\mathcal{I}_D^{(m)}(\nu)$. Consequently, the contributions from the trap energy,

$$E_{\text{ext}}(N,b,\kappa) = \frac{DN}{2b}\left[1 + \frac{1}{2}\left(\frac{bM\omega^2}{4\pi}\right)^{D/2} b\kappa + \mathcal{O}(\kappa^2)\right], \tag{4.30}$$

the mean-field energy

$$E_{\text{mf}}(N,b,\kappa) = \frac{N}{2}\left(\frac{bM\omega^2}{4\pi}\right)^{D/2} \kappa + \mathcal{O}(\kappa^2), \tag{4.31}$$

and the interaction independent kinetic energy of the gas,

$$E_{\text{kin}}(N,b) = \frac{DN}{2b}, \tag{4.32}$$

sum up to yield the total energy

$$E(N,b,\kappa) = \frac{D}{b}N + \frac{D+4}{4}N\left(\frac{bM\omega^2}{4\pi}\right)^{D/2}\kappa. \tag{4.33}$$

The corresponding chemical potential in this limit reads

$$\mu(b,\kappa) = \frac{D}{b} + \frac{D+4}{2}\left(\frac{bM\omega^2}{4\pi}\right)^{D/2}\kappa. \tag{4.34}$$

The formal correspondence between the parameter b and the inverse temperature, which becomes apparent in the weakly interacting limit, can be justified more rigorously by regarding expression (4.33) in the context of the equipartition theorem. Assuming each degree of freedom to carry the energy $k_{\mathrm{B}}T/2$, leads to the identity

$$E(N,b,\kappa) = DN\,k_{\mathrm{B}}T. \tag{4.35}$$

This equation can be solved iteratively by

$$\frac{1}{b} \approx k_{\mathrm{B}}T - \frac{D+4}{4D}\left(\frac{M\omega^2}{4\pi k_{\mathrm{B}}T + \ldots}\right)^{D/2}\kappa. \tag{4.36}$$

Hence, for weak mean field interactions in combination with high temperatures, we can estimate

$$\left(\tfrac{M\omega}{4\pi k_{\mathrm{B}}T}\right)^{D/2}\tfrac{\kappa}{k_{\mathrm{B}}T} \ll 1. \tag{4.37}$$

In this case, we can ignore the interaction corrections in equation (4.36) and simply use

$$b = \frac{1}{k_{\mathrm{B}}T}. \tag{4.38}$$

A comparison between the classical noninteracting density (2.77) and the weakly interacting Lambert density is shown in figure 4.4. The former is plotted for several values of $(k_{\mathrm{B}}T)^{-1}$ and the latter is plotted for corresponding values of b. The Lambert density matches the noninteracting Gaussian solution quite well, especially for high temperatures. For low temperatures, however, mean field effects become more important, lowering central densities of the interacting Lambert density solution compared to expression (2.77).

When trying to assign a physical meaning to the parameter b, we concentrated exclusively on the correspondence of the Lambert density to the Maxwell-Boltzmann theory in case of hot weakly interacting gases. Nevertheless, the Lambert density is also consistent with the noninteracting quantum mechanical ground-state of the harmonic oscillator at zero temperature. In this

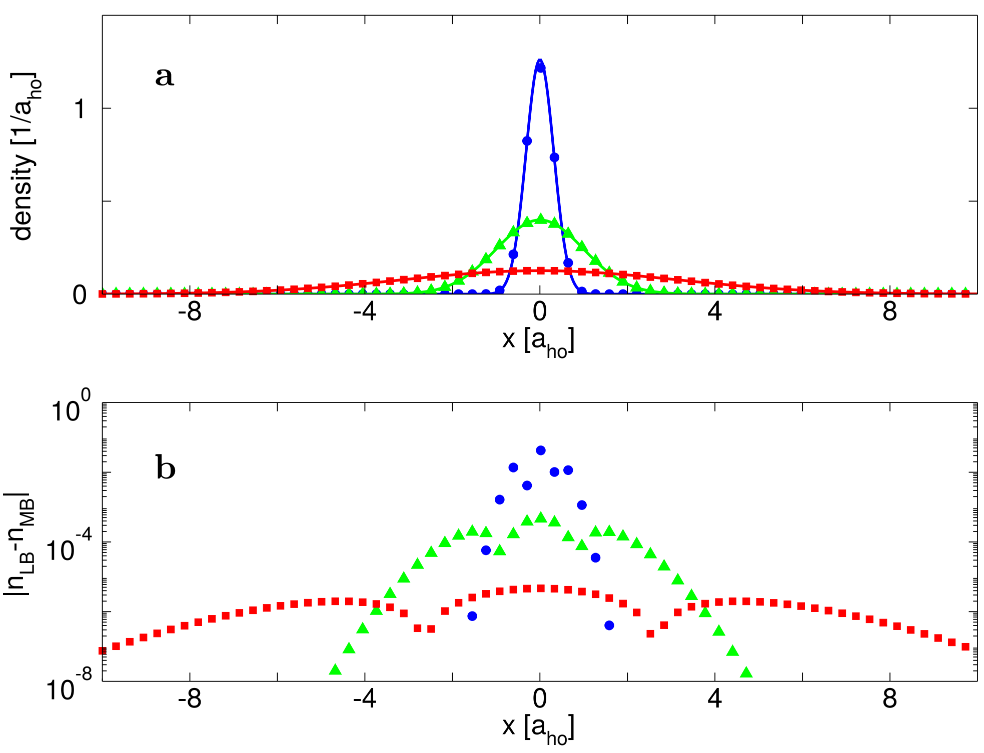

Figure 4.4.: Comparison of Lambert density (n_{LB}) to the noninteracting MAXWELL-BOLTZMANN density (n_{MB}) in an one-dimensional harmonic oscillator, identifying $b = (k_{\text{B}}T)^{-1}$, with constant interaction strength $\kappa = 0.01\,\hbar\omega a_{\text{ho}}$. Part **a**: Direct comparison of n_{LB} and n_{MB}. Part **b**: Absolute value of difference between n_{LB} and n_{MB}. Values for b-parameters are $b = 10\,(\hbar\omega)^{-1}$ (blue •), $b = 1\,(\hbar\omega)^{-1}$ (green △), and $b = 0.1\,(\hbar\omega)^{-1}$ (red ■).

case, one simply has $b = 2/(\hbar\omega)$. The WIGNER function that describes a quantum-mechanical thermal state in a harmonic oscillator was given in expression (3.44). Its extend in phase space along a particular axis scales with the temperature dependent factor

$$\epsilon(T) = \frac{1}{\tanh\left(\frac{\hbar\omega}{2k_\mathrm{B}T}\right)}.$$

Consequently, these results for noninteracting gases are obtained from the LAMBERT denisty in the limit $\kappa \to 0$, if we identify

$$b = \frac{1}{\epsilon(T)} = \begin{cases} 2/(\hbar\omega), & k_\mathrm{B}T \ll \hbar\omega/2 \\ 1/(k_\mathrm{B}T), & k_\mathrm{B}T \gg \hbar\omega/2 \end{cases}. \tag{4.39}$$

4.2 Comparison of the Lambert density to the Gross-Pitaevskii solution

So far, we have shown that approximations of the Lambert density for extremely strong or extremely weak interactions are consistent with well-established theories concerning those regimes. To check its validity for condensates at zero temperature with arbitrary interactions, we compare solution (4.13) to the numerical solution of the stationary Gross-Pitaevskii equation,

$$\left[\mu + \frac{\hbar^2\nabla^2}{2M} - V_\mathrm{ext}(\mathbf{x}) - \kappa\frac{|\phi(x)|^2}{N}\right]\phi(x) = 0, \tag{4.40}$$

with varying interaction strength κ. To keep mathematical expressions and visualizations simple, we consider again an one-dimensional harmonic oscillator.

Looking for the ground state of a quantum-mechanical system, we require a b-value that minimizes the energy but respects the uncertainty principle at the same time. By virtue of the momentum distribution (4.10), a particular value of b fixes the momentum variance Δp. Since we have neglected quantum pressure on the way to find the Lambert density solution (4.13), we have to postulate a minimal Δp if we want the uncertainty principle to re-enter our model. On one side, in the interaction dominated THOMAS-FERMI limit, the position variance Δx^2 is on the order of $2\mu/(M\omega)$. Consequently, the uncertainty principle leads to $b = 2\mu/(\hbar\omega)^2$. On the other side, neglecting interaction effects, the ground-state momentum variance is well-known to be $\Delta p = M\hbar\omega/2$ and consequently $b = 2/(\hbar\omega)$. As a rough estimate, we patch together those distinct regimes as follows.

$$\mu(\kappa) = \frac{\hbar\omega}{2} + \mu_\mathrm{TF}(\kappa), \tag{4.41}$$

$$b(\kappa) = \frac{2}{\hbar\omega}\begin{cases} \mu(\kappa)/(\hbar\omega) & , \quad \mu > \hbar\omega \\ 1 & , \quad \mu < \hbar\omega \end{cases}, \tag{4.42}$$

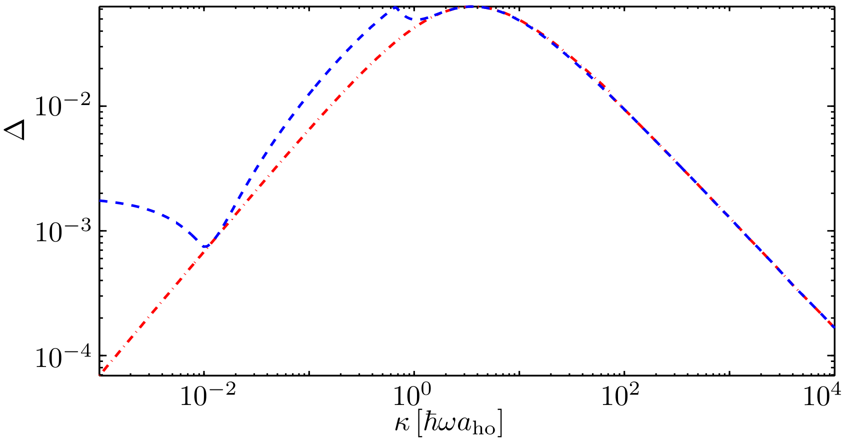

Figure 4.5.: Comparison of the LAMBERT density to the numerical solution I: Integrated deviation of n_{est} (blue dashed) and n_{fit} (red dash-dotted) to n_{GP} over varying interaction strength κ.

where μ_{TF} is given in equation (4.23). The Lambert density that corresponds to this estimated b-value is denoted n_{est}. The ground state mean field of the GROSS-PITAEVSKII equation, $\phi(x)$, is calculated numerically, using imaginary time propagation. The associated density distribution is called $n_{\text{GP}} = |\phi|^2$. Suspecting the estimate (4.42) to diverge from the "true" value of b in the intermediate parameter regime, $\kappa \approx \hbar\omega a_{\text{ho}}$, we calculate another Lambert density function by fitting the b-parameter to match n_{GP}. We denote this solution by n_{fit}.

In order to compare the various solutions for different interaction strengths in a comprehensible way, figure 4.5 shows the integrated absolute deviation of n_{est} and n_{fit}. We define these deviations as

$$\Delta_{\text{est}} = \int \mathrm{d}x\ |n_{\text{GP}} - n_{\text{est}}|, \qquad\qquad \Delta_{\text{fit}} = \int \mathrm{d}x\ |n_{\text{GP}} - n_{\text{fit}}|. \tag{4.43}$$

According to figure 4.5, both, Δ_{est} and Δ_{fit}, become negligible in the limits of weak and strong interaction, meaning very good agreement of the LAMBERT density to the numerical solution n_{GP}. For intermediate interaction strengths $\kappa \approx \hbar\omega a_{\text{ho}}$, however, the agreement becomes worse. Although n_{fit} is slightly closer to n_{GP} in this regime, both realizations of the Lambert density fail to match the GROSS-PITAEVSKII density as close as in the case of extreme values of κ. Figure 4.6 shows a comparison of the three density functions for a specific interaction strength of $\kappa = 0.5\ \hbar\omega a_{\text{ho}}$. The relatively good agreement of n_{fit} to n_{GP} in the center of the trap (part **a**) comes at the cost of higher deviation far from the cloud center. The estimated LAMBERT density, on the other hand, matches the far-from-center behavior of the GROSS-PITAEVSKII solution quite well but deviates in the center.

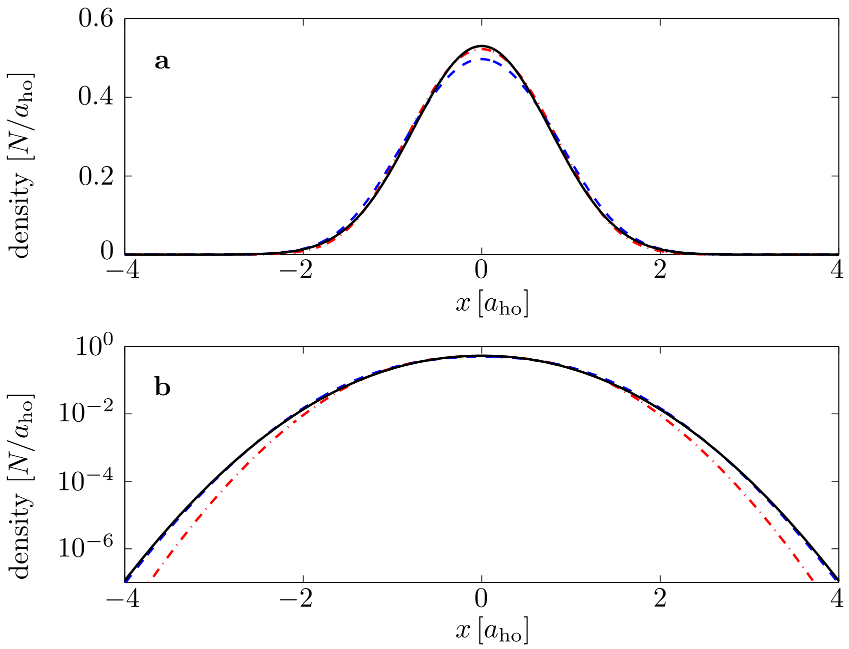

Figure 4.6.: Comparison of the LAMBERT density to the numerical solution II: density shape. Density distributions n_{GP} (black solid), n_{est} (blue dashed), and n_{fit} (red dash-dotted) are compared in the center of the trap (**a**) and at the cloud edge (**b**). Interaction strength is $\kappa = 0.5\,\hbar\omega l_{\text{ho}}$.

Finally, we compare the energy contents that are calculated using the three different density profiles. The energy functional of the GROSS-PITAEVSKII wave function solution is given by expression (3.79). In terms of the LAMBERT density solution, the energy of the condensate reads

$$E[n,u] = N\int \mathrm{d}^3p\,\frac{\mathbf{p}^2}{2M}\,u(\mathbf{p}) + \int \mathrm{d}^3x\,\left(V_{\text{ext}}(\mathbf{x}) + \frac{1}{2}\kappa\,\frac{n(\mathbf{x})}{N}\right)n(\mathbf{x}) \tag{4.44}$$

Figure 4.7 shows the energy curves associated with the various solutions. Once again, values of E belonging to the Lambert density agree best with those belonging to n_{GP} in extreme parameter regimes, while exhibiting some deviation for intermediate interaction strengths. The linear slope of $E(\kappa)$ in the limit $\kappa \to \infty$ is given by the exponent of μ_{TF} in equation (4.23). It is $2/3$ in the three-dimensional case.

4.3 The Lambert density of a thermal gas in a chip trap potential

In order to demonstrate the usability of the Lambert density solution beyond the simplifying assumption of harmonic potentials, we calculate the density profile of an interacting thermal gas in a realistic trap. Therefore, we consider a trapping potential created by a z-shaped wire, which is often found on atom chips (z-trap). Figure 4.8 shows a sketch of the atom chip, the BEC,

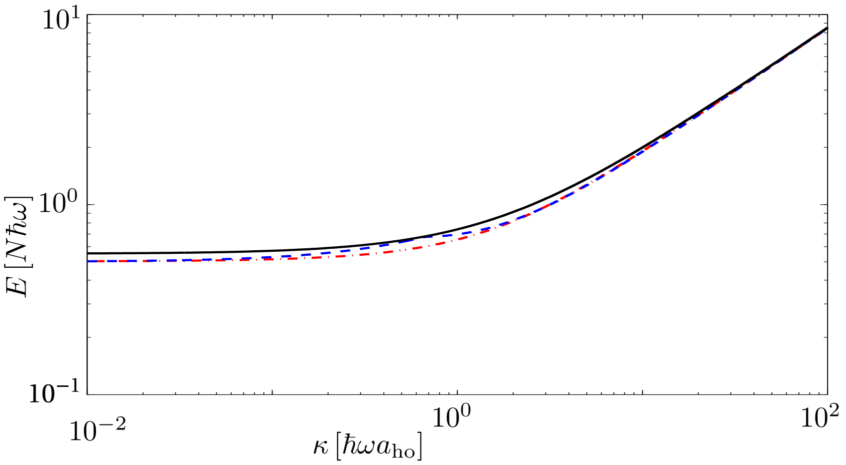

Figure 4.7.: Comparison of the Lambert density to the numerical solution III: Energy of density profiles n_{GP} (black solid), n_{est} (blue dashed), and n_{fit} (red dash-dotted) plotted against interaction strength κ.

and the reference frame's orientation. The current inside the wire, I, creates an inhomogeneous magnetic field which can be calculated with Biot-Savart's law,

$$\mathbf{B}(\mathbf{x}) = \frac{\mu_0 I}{4\pi}\int_{\mathrm{wire}} \mathrm{d}\mathbf{s} \times \frac{\mathbf{x}-\mathbf{s}}{|\mathbf{x}-\mathbf{s}|^3}, \tag{4.45}$$

where $\mathbf{s}$ is a line element along the wire. The shape of the wire leads to a local minimum of the magnetic field corresponding to a minimal Zeemann energy shift $\Delta E = \mu|\mathbf{B}|$ of atoms near the chip. Consequently, this potential minimum constitutes an atom trap. In our specific example, the center of the trap is situated at $(x_0, y_0, z_0) = (100.50, -1.66, 227.06)\mu$m, where the z-component indicates the distance to the chip surface. Close to the potential minimum, the harmonic approximation agrees very well with the real potential, as can be seen in the visualization of the chip trap potential in figure 4.9. Along the z-direction (parts **c**, **f**), we observe the largest deviation of the harmonic approximation from the real potential. Roughly speaking, the weakly bound direction of the cigar shaped trap geometry is aligned to the x-axis. In the y-z-plane, the potential is radially symmetric. The eigenfrequencies of the harmonic approximation are $(\omega_1, \omega_2, \omega_3) = 2\pi \cdot (19, 325, 328)\,$Hz which entail a geometric mean frequency of $\overline{\omega} = 2\pi \cdot 127\,$Hz.

For a thermal cloud of trapped ^{87}Rb atoms, we want to compare observables associated with the Lambert density solution to results from Maxwell-Boltzmann theory. Considering ^{87}Rb atoms, the binary interaction is $g = 0.076\hbar\overline{\omega}a_{\mathrm{ho}}^3$. As mentioned in the beginning of this chapter, we have to recall that in case of thermal gases, the mean field interaction gives rise to a contribution $2gn$ to the Hamilton function which is twice as high as in the case of a condensate. Varying the particle number N in order to realize several values of κ, we must be careful to stay above the

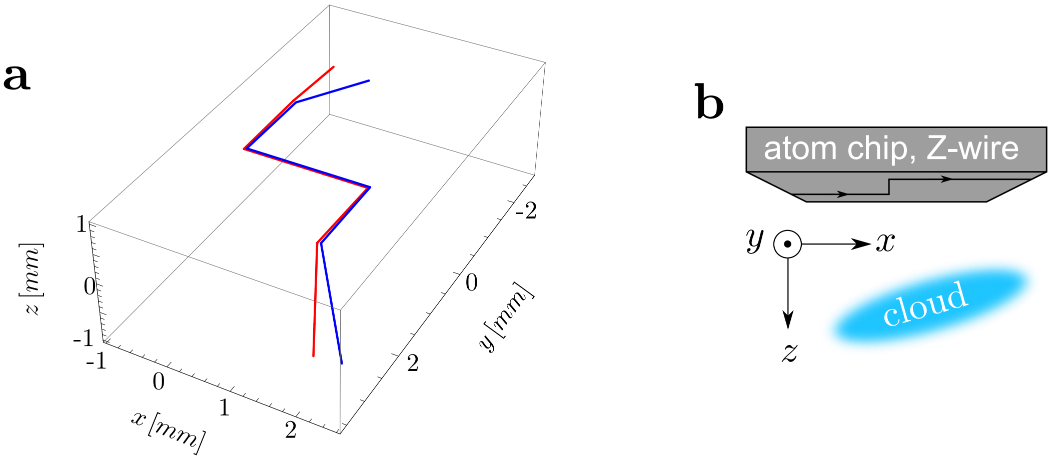

Figure 4.8.: Part **a**: Model of the wire geometry of the chip trap. Part **b**: Illustration of the cloud's postition relative to the atom chip and reference frame orientation.

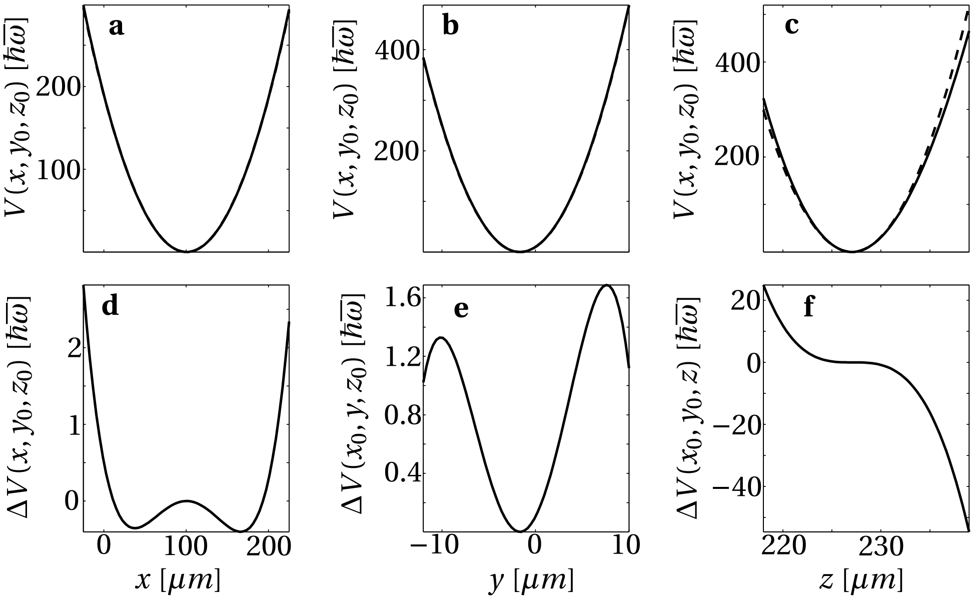

Figure 4.9.: Visualization of potential energies of Z-trap. **a-c**: Potential along x-, y-, and z-axis, respectively, around the potential minimum. Numerically calculated Z-trap potential (solid line) and harmonic approximation (dashed line). **d-f**: Difference between Z-trap potential and harmonic approximation.

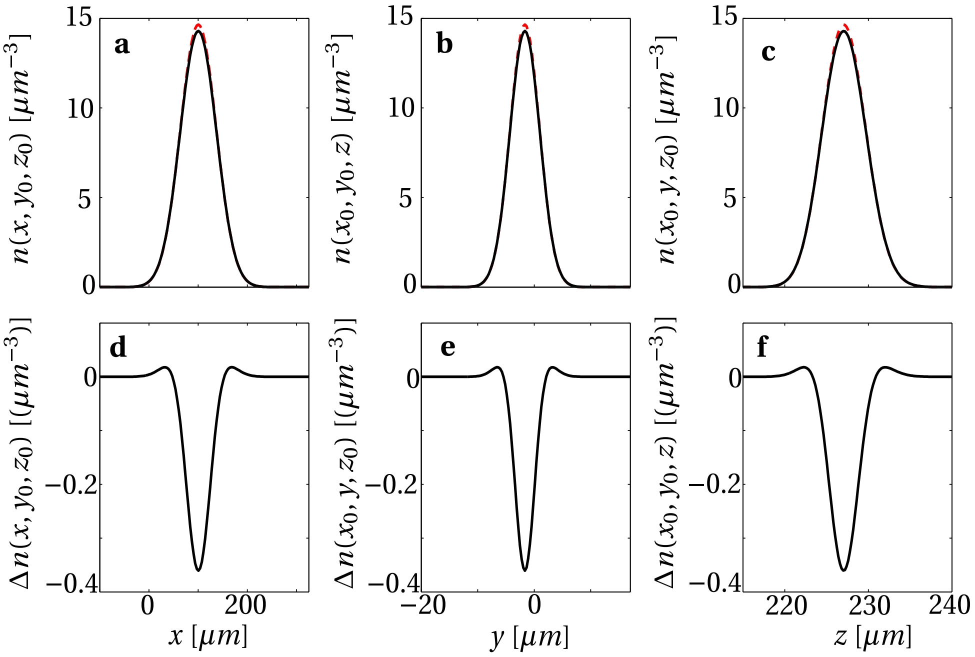

Figure 4.10.: Visualization of densities along coordinate axes as one-dimensional excerpts of the three-dimensional density. The latter was evaluated on a position grid with 32^3 points. Parameters are $T = 300$ nK, $N = 7 \cdot 10^4$, and $g = 0.076\hbar\overline{\omega}a_{ho}^3$. Upper row, **a-c**: Lambert density (black solid line) and Maxwell-Boltzmann density (red dashed line) along x-, y-, and z-axis, respectively, around the potential minimum. Lower row, **d-f**: Difference between Lambert density and Maxwell-Boltzmann density. The trapping potential is visualized in figure 4.9.

critical temperature T_c of the BEC phase transition. Its relation to the particle number of the trapped gas [19] is given by

$$\frac{k_B T_c}{\hbar\overline{\omega}} = \left(\frac{N}{\zeta(3)}\right)^{1/3} . \tag{4.46}$$

Assuming for instance $N \leq 7 \cdot 10^4$, all temperatures must satisfy $T \geq 236$ nK to exclude the existence of a condensate. Furthermore, restricting the discussion to particle numbers below $7 \cdot 10^4$ and temperatures above 240 nK, the ratio of interaction to thermal energy, $(M\omega/(4\pi k_B T))^{D/2}\kappa/(k_B T)$, remains below 0.0246. Thus, by virtue of relation (4.36), we can simply identify $b = (k_B T)^{-1}$.

As a first step, for any combination of values for b and κ, one has to determine the normalization factor $\overline{n}$. Unlike the previously discussed case of harmonic potentials, where the normalization condition is a closed equation (4.15), we have to solve Eq. (4.12) for ν numerically. Figure 4.10 shows the Lambert density, the Maxwell-Boltzmann density (parts **a-c**), as well as their difference (parts **d-f**) for $T = 300$ nK. In the considered regime, where the spatial extent of the cloud is determined by thermal fluctuations rather than interatomic interactions,

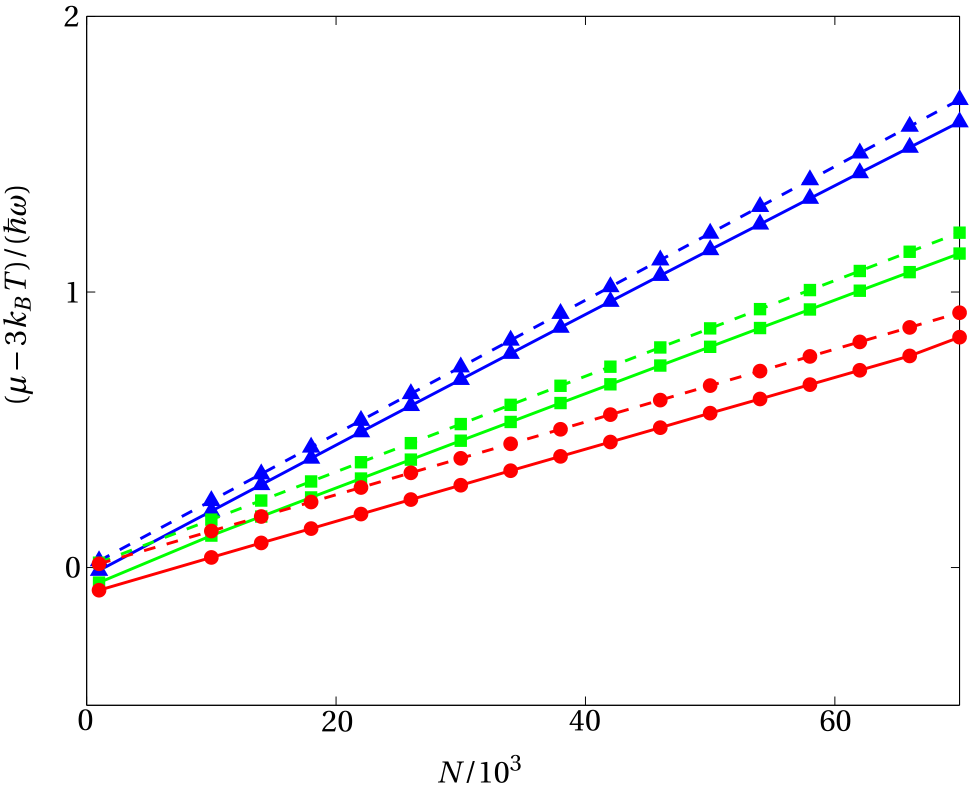

Figure 4.11.: Comparison of energy calculation methods. We have subtracted the energy non-interacting classical gas, $3Nk_BT$, from each contribution. Solid lines: energy of LAMBERT density in the z-trap. Dotted lines: energy of LAMBERT density in harmonically approximated trap. Dashed lines: energy of density with linearized weak interaction in harmonically approximated trap according to (4.33). Different temperatures are $T = 240\ nK$ (blue ▲), $T = 300\ nK$ (green ■), and $T = 360\ nK$ (red •).

the Lambert density differs only up to ~0.2% in the center of the trap and is thus a negligible correction to the MAXWELL-BOLTZMANN result. However, the weakly interacting regime is well suited for studying the behavior of first-order corrections to global observables like total energy, derived in section 4.1.2.

In figure 4.11, we show the result from directly integrating the energy functional (4.16) numerically. Therefore, we compare the energy we obtain from using the LAMBERT density to that resulting from the noninteracting MAXWELL-BOLTZMANN density. This reveals the influence of weak interaction onto the total energy. In addition, we also plot the energy curve according to the analytical relation (4.33) that gives a linear approximation to the energy of a weakly interacting gas. Comparing it to the above calculations that utilize the z-trap potential, we can see how anharmonicities affect the results.

5 Condensates in hybrid systems

Hybrid systems, like microscopical objects immersed into BECs, are an active field of research. Prominent examples are the resonant coupling of ultra-cold atoms to micro-mechanical cantilevers [22, 23]. Recent experiments focused on the interaction of a BEC cloud to even smaller objects like carbon nanotubes [24–28] or single ions [76, 77]. Motivations for studying hybrid systems are manifold and include advances in quantum information technology as well as precision measurement of microscopical forces.

In the following, we investigate the influence of a microscopical object (MO) on a cloud of ultra-cold atoms which we describe with the mean field approach utilizing hydrodynamic equations. The MO may be a carbon nanotube, a fullerene, or the like. To this end, we formulate a simple model for the local response of the atomic cloud on the perturbation with an MO. Furthermore, we examine the dynamics of the global number of condensed atoms.

5.1 Model

In order to obtain an effective equation of motion for a BEC being in contact with a MO, we identify the main effects, the immersed body has on the condensed atoms. These are attraction of neutral atoms towards the MO on one hand, and the loss of condensed atoms on the other. The former results from the interaction between neutral objects that carry dipoles which are induced by vacuum fluctuations. This phenomenon is known as CASIMIR-POLDER effect [78, 79]. Its influence on the BEC's dynamics is described simply by an additional potential, $V_{\mathrm{CP}}(\mathbf{x})$. The latter effect, the loss of condensed atoms, is due to their inelastic scattering at the surface of the MO. Without considering microscopic details, we assume a local single-particle loss rate for the condensate $\Gamma(\mathbf{x})$ to effectively cover these processes. Clearly, the space dependence of Γ is supposed to resemble the spatial shape of the MO. Moreover, both entities, V_{CP} and Γ, can be equipped with time dependence in order to describe the immersion of the initially seperated systems into each other.

5.1.1 Modified hydrodynamic equations

For describing the condensate's dynamics, we start with the time dependent GROSS-PITAEVSKII equation (3.68), assuming the cloud's behavior to be dominated by mean field interactions. Thus, we neglect thermal excitations as well as two-particle correlations. Based on that, the two effects of MO immersion described above (attraction and loss) are reflected by two extra terms in the equation of motion. Assuming the cloud is held in an external trap V_{ext}, the CASIMIR-POLDER potential adds up to a total potential, $V_{\text{ext}}+V_{\text{CP}}$. At the same time, the inelastic scattering of condensed atoms leads to a damping of the macroscopic wave function of the condensate. This can be modeled by adding an imaginary term $-i\hbar\Gamma/2$ to the real potentials. All in all, our modified macroscopic wave equation reads

$$\left[i\hbar\,\partial_t + \tfrac{\hbar^2}{2M}\nabla^2 - V_{\text{ext}}(\mathbf{x}) - g|\phi(\mathbf{x},t)|^2\right]\Psi(\mathbf{x},t) = \left[V_{\text{CP}}(\mathbf{x},t) - \tfrac{i\hbar}{2}\Gamma(\mathbf{x},t)\right]\Psi(\mathbf{x},t), \tag{5.1}$$

arranging the terms of the original GROSS-PITAEVSKII equation (3.68) on the left-hand side and those describing the MO interaction on the right-hand side. Re-applying now the steps that led to the hydrodynamic formulation in section 3.3.2, we obtain the modified hydrodynamic equations in density n action S,

$$\partial_t S + \tfrac{1}{2M}(\nabla S)^2 + V_{\text{ext}} + U_q[n] + gn = -V_{\text{CP}}, \tag{5.2}$$

$$\partial_t n + \tfrac{1}{M}\nabla\cdot(n\nabla S) = -\Gamma\, n, \tag{5.3}$$

which are fully equivalent to the modified wave equation (5.1). In the following, we assume the cloud's dynamics to be dominated by its mean field interaction gn so that quantum pressure U_q can be neglected and the density profile of the unperturbed atom cloud, n_0 shall be well approximated by the THOMAS-FERMI density (3.81).

5.1.2 Time and space dependence of immersed object

Choosing definite functions for the MO potentials V_{CP} and Γ, to model the immersion process, one can go arbitrarily deep into detail. For instance, the object is brought to overlap with the condensate, following a certain immersion trajectory $\mathbf{r}(t)$. Attraction and loss would then be of the form $V_{\text{CP}}(\mathbf{x}-\mathbf{r}(t))$ and $\Gamma(\mathbf{x}-\mathbf{r}(t))$, respectively. If this process is too rapid, complicated excitations may be triggered in both subsystems, BEC and MO. Rather than incorporating every minor effect, we opt for a quite basic model. After all, being interested in global features, like loss of total particle number, microscopic details are less relevant. Also, local effects like sound waves can be studied on an elementary level.

In our model, instead of a smooth immersion process, we let the MO appear instantaneously at certain position inside the atom cloud. Once popped up, it rests motionless for the interaction time until it instantaneously disappears again. Moreover, we assume the MO's spatial extend to be far smaller than the cloud size. It is thus effectively described by a delta function. Based on that, the influence of elongated objects like CNTs may be modeled by adding up the effects of many point-like disturbances.6

5.2 Perturbation theory

Assuming the influence of the MO on the BEC to be sufficiently small, we derive approximate expressions for the hydrodynamic equations (5.2) and (5.3). As noted above, prior to any interaction with the MO, we assume the atom cloud to be completely condensed to the interaction dominated ground state, described by the THOMAS-FERMI density (3.81). The response of the condensate is expanded into a perturbation series. To keep track of the order of perturbation, we introduce the smallness parameter λ which formally quantizes the strength of interaction between BEC and MO. This means we write $V_{\text{CP}} \to \lambda V_{\text{CP}}$ and $\Gamma \to \lambda\Gamma$ and, eventually, set $\lambda \to 1$ when expressing final results. Thus, the response of the atom cloud to MO immersion can be expanded as

$$n = \sum_{j=0}^{\infty} \lambda^j n_j \quad , \qquad\qquad S = \sum_{j=0}^{\infty} \lambda^j S_j. \tag{5.4}$$

The zeroth order describes the unperturbed ground state values. According to section 3.3.2, these are a time-independent density and a position-independent phase,

$$n_0(\mathbf{x}) = \tfrac{1}{g}\big(\mu - V_{\text{ext}}(\mathbf{x})\big), \tag{5.5}$$

$$S_0(t) = -\mu t. \tag{5.6}$$

Plugging ansatz (5.4) into the modified hydrodynamic equations (5.2) and (5.3), with the quantum pressure U_q neglected, yields a hierarchy of differential equations. Isolating first-order terms carrying λ^1, we obtain an equation of motion for linearized deviations from the ground state,

$$\begin{pmatrix} \partial_t & g \\ \frac{1}{M}\nabla n_0 \nabla & \partial_t \end{pmatrix} \begin{pmatrix} S_1 \\ n_1 \end{pmatrix} = -\begin{pmatrix} V_{\text{CP}} \\ n_0 \Gamma \end{pmatrix}. \tag{5.7}$$

We arranged the homogeneous part of the partial differential equation on the left-hand side and the inhomogeneity on the right-hand side. Moreover, gathering terms with λ^2, one finds the second order to be

$$\begin{pmatrix} \partial_t & g \\ \frac{1}{M}\nabla n_0 \nabla & \partial_t \end{pmatrix} \begin{pmatrix} S_2 \\ n_2 \end{pmatrix} = -\begin{pmatrix} \frac{1}{2M}(\nabla S_1)^2 \\ \frac{1}{M}\nabla \cdot (n_1 \nabla S_1) + \Gamma n_1 \end{pmatrix}. \tag{5.8}$$

Equations (5.7) and (5.8) as well as any higher-order equation can be written in the form

$$\hat{\mathrm{D}}\underline{\Psi}_j = \underline{h}_j, \tag{5.9}$$

combining the j-th order phase and density into a vector $\underline{\Psi}_j = (S_j, n_j)^{\mathsf{T}}$. All members of the hierarchy (5.9) have the same differential operator

$$\hat{\mathrm{D}} \equiv \begin{pmatrix} \partial_t & g \\ \frac{1}{M}\nabla n_0 \nabla & \partial_t \end{pmatrix}. \tag{5.10}$$

The perturbation terms in the various orders have also been written in a vector notation $\underline{h}_j = (h_{S_j}, h_{n_j})^{\mathsf{T}}$. We can formally solve these equations,

$$\underline{\Psi}_j(\mathbf{x}, t) = \int_{-\infty}^{\infty} \mathrm{d}t' \int_{\mathbb{R}^3} \mathrm{d}^D x' \; \mathrm{G}(\mathbf{x}, t|\mathbf{x}', t')\, \underline{h}_j(\mathbf{x}', t'), \tag{5.11}$$

introducing the Green’s function G to the differential operator $\hat{\mathrm{D}}$. It is defined by satisfying the relation

$$\hat{\mathrm{D}}\, \mathrm{G}(\mathbf{x}, t|\mathbf{x}', t') = \delta(\mathbf{x}-\mathbf{x}')\delta(t-t')\mathbb{1}. \tag{5.12}$$

Note that we took the liberty to leave the dimension of the problem unspecified in order to cover the real three-dimensional system as well as simple one-dimensional models.

5.2.1 Local density approximation

Finding a differential operator $\hat{\mathrm{D}}$ that satisfies relation (5.12) is greatly simplified, by neglecting the spatial variation of the ground state density n_0. This is justified if the perturbation introduced by the MO is limited to areas which are tiny compared to the spatial extend of the cloud. This way, the ground state density is approximately constant in the vicinity of the perturbation, and hence we may assume $\nabla n_0 \approx 0$. Consequently, the differential operator $\hat{\mathrm{D}}$ is independent of position and time, giving rise to a Green’s function that is just a function of position and time differences, $\Delta\mathbf{x}$ and Δt, respectively. A solution can now be easily calculated by Fourier-transforming equation (5.12). The resulting equation in the transformed Green’s function $\tilde{\mathrm{G}}(\mathbf{k}, \omega)$ can be solved algebraically, obtaining

$$\tilde{\mathrm{G}}(\mathbf{k}, \omega) = \frac{1}{c^2\mathbf{k}^2 - \omega^2} \begin{pmatrix} i\omega & -g \\ \frac{c^2}{g}\mathbf{k}^2 & i\omega \end{pmatrix}. \tag{5.13}$$

We have used again the speed of sound of the condensate $c = (g n_0/M)^{1/2}$, introduced in section 3.3.2. Finally, inverse Fourier transformation from the $\mathbf{k}$-ω-space into the $\mathbf{x}$-t-space yields the retarded Green’s function

$$\mathrm{G}(\Delta\mathbf{x}, \Delta t) = \Theta(\Delta t) \begin{pmatrix} \partial_t & -g \\ -\frac{1}{g}\partial_t^2 & \partial_t \end{pmatrix} \frac{1}{(2\pi)^D} \int \mathrm{d}^D k \; e^{i\mathbf{k}\Delta\mathbf{x}} \frac{\sin(c|\mathbf{k}|\Delta t)}{c|\mathbf{k}|}. \tag{5.14}$$

Clearly, the advanced GREEN's function $\mathrm{G}(\Delta\mathbf{x},-\Delta t)$ is also a solution of equation (5.12). However, we are only interested in the retarded solution describing the response of the BEC as causal consequence of the MO immersion. The definite form of the GREEN's function given in (5.14) depends on the dimension of the problem. Relevant in most situations are the three-dimensional and the one-dimensional case. The former for realistic descriptions of most experimental setups, the latter for simple models that provide valuable insight. For these cases, we find the following.

1D: In the one-dimensional case, the retarded GREEN's function is found to be

$$\mathrm{G}(\Delta x,\Delta t)=\frac{1}{c}\Theta(\Delta t)\begin{pmatrix}\partial_t & -g\\ -\frac{1}{g}\partial_t^2 & \partial_t\end{pmatrix}\Big[\Theta(\Delta x+c\Delta t)-\Theta(\Delta x-c\Delta t)\Big]. \tag{5.15}$$

Obviously, Any local perturbation of the BEC propagates with sound velocity c in both directions.

3D: In the three-dimensional case, on the other hand, one has

$$\mathrm{G}(\Delta\mathbf{x},\Delta t)=\frac{1}{4\pi c}\Theta(\Delta t)\begin{pmatrix}\partial_t & -g\\ -\frac{1}{g}\partial_t^2 & \partial_t\end{pmatrix}\frac{\delta(|\mathbf{x}|-c\Delta t)}{|\mathbf{x}|}. \tag{5.16}$$

The expression $\delta(|\mathbf{x}|-ct)/|\mathbf{x}|$ may be familiar from the solutions of the HELMHOLZ equation for the propagation of electro magnetic waves [80]. The response to a perturbation can be constructed by spherical waves that expand radially with c.

For the sake of brevity and ease of demonstration, we will only use the one-dimensional GREEN's function in the subsequent discussion. All calculations can however be easily repeated for the three-dimensional case.

5.3 First-order effects on BEC

We now examine the linear response of the BEC to the immersion of a MO. We thus assume the BEC-MO interaction quantified by V_{CP} and Γ to be sufficiently small so that higher orders can be neglected.

5.3.1 Perturbation functions

Having available the GREEN's function, the evolution of phase and density of the BEC can be calculated straightforwardly by appointing the first-order inhomogeneity

$$\begin{pmatrix}h_{S_1}(\mathbf{x}',t')\\ h_{n_1}(\mathbf{x}',t')\end{pmatrix}=-\begin{pmatrix}V_{\mathrm{CP}}(\mathbf{x}')\\ n_0\,\Gamma(\mathbf{x}')\end{pmatrix}\Theta(t'). \tag{5.17}$$

Concerning the time dependence, as elaborated above, our model assumes the MO to instantaneously appear inside the condensate. This discontinuous behavior is described by the function $\Theta(t')$ in expression (5.17). For the BEC-MO interaction potential V_{CP} we use

$$V_{\mathrm{CP}}(\mathbf{x}) = \sum_{m\geq 2}^{m_{\max}} \frac{C_m}{\left(\frac{|\mathbf{x}|}{b}\right)^m + 1}, \tag{5.18}$$

decaying for larger distances at least as fast as $|\mathbf{x}|^{-2}$, i.e. faster than the COULOMB potential. Simultaneously, it assumes finite values for smaller distances. Furthermore, we describe the position dependent loss of particles by a Gaussian

$$\Gamma(r) = \gamma e^{-|\mathbf{x}|^2/b^2}, \tag{5.19}$$

with γ being a constant rate. In both expressions, the parameter b is connected to the spatial extent of the MO.

5.3.2 Sound waves in one dimension

In order to gain some insight into the behavior of the BEC after the immersion of an MO, we consider a one-dimensional system in local density approximation. Gathering ingredients from previous sections, the linear response of the condensate is expressed as

$$\begin{pmatrix} S_1 \\ n_1 \end{pmatrix} = -\frac{1}{c}\int_{-\infty}^{\infty} \mathrm{d}x' \int_0^t \mathrm{d}t' \begin{pmatrix} \partial_t & -g \\ -\frac{1}{g}\partial_t^2 & \partial_t \end{pmatrix} \Big[\Theta(\Delta x + c\Delta t) - \Theta(\Delta x - c\Delta t)\Big] \begin{pmatrix} V_{\mathrm{CP}}(x') \\ n_0\Gamma(x') \end{pmatrix}. \tag{5.20}$$

From expression (5.20) we can extract the linearized deviation of the ground state density,

$$n_1(x,t) = -\frac{1}{g}\Big(2V_{\mathrm{CP}}(x) - V_{\mathrm{CP}}(x+ct) - V_{\mathrm{CP}}(x-ct)\Big) - \frac{n_0}{c}\int_{x-ct}^{x+ct} \mathrm{d}x'\, \Gamma(x'). \tag{5.21}$$

One recognizes the propagation of the perturbation to both directions, traveling with velocity c. Remember that we are in local density approximation. Hence, the ground state density n_0 as well as speed of sound $\pm c$ are constants. Solution (5.21) is visualized in figure 5.1**b** assuming an attractive potential V_{CP} and a tightly localized loss area Γ. The attraction towards the MO leads to an increased density in the vicinity of the object at $x = 0$. The shock wave that is triggered by instantaneous onset of BEC-MO interaction erodes through the density profile. The shape of the wave front is determined by the potential V_{CP} as well as the antiderivatives of the loss function $\int^x \mathrm{d}x'\, \Gamma(x')$.

In addition, the solution for the action response is found to be

$$S_1(x,t) = -\frac{1}{c}\int_{x-ct}^{x+ct} \mathrm{d}x'\, V_{\mathrm{CP}}(x') + \frac{M}{2}\int_x^{x+ct} \mathrm{d}x' \int_{x'}^{x'-ct} \mathrm{d}x''\, \Gamma(x''). \tag{5.22}$$

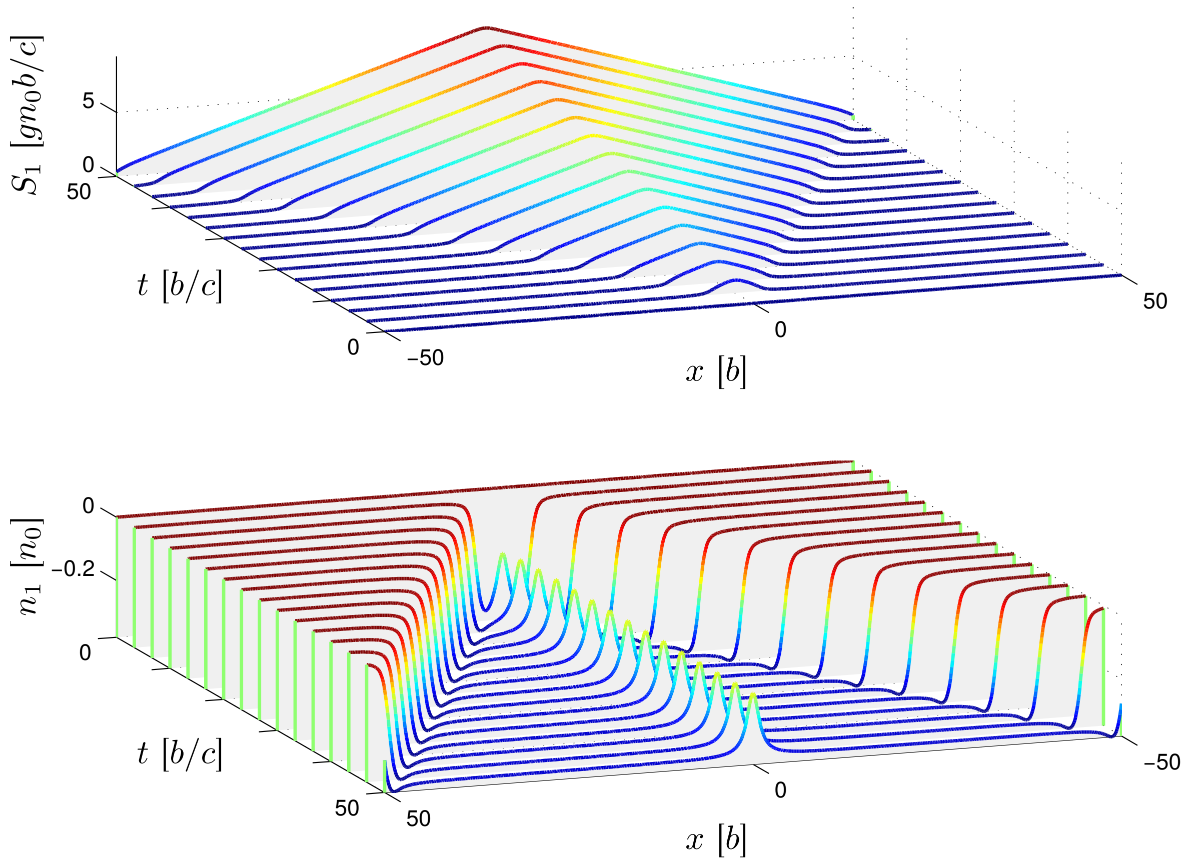

Figure 5.1.: Numerical solution of GP equation with MO perturbation. Part **a**: Action over position and time since immersion. Part **b**: Density response over position and time since immersion. Note: The time axis in part **a** is reversed compared to that of part **b** for enhanced visibility of plots. Parameters of MO potentials as defined in (5.18) and (5.19) are $\gamma = 0.2\, c/b$, $C_2 = -0.2\, g n_0$.

Like the first-order density (5.21), the perturbation in S spreads in the form of a shock wave. It is plotted in figure 5.1**a**. Inside the wave fronts, the action grows linearly towards the location of the MO at $x = 0$. Recalling the velocity field to be proportional to the action gradient, $v = \partial_x S/M$, this means that in the wake of the shock wave, particles are flowing uniformly towards the MO, where they are scattered to unobserved channels and thus lost. The linear slope of the action solely depends on the loss function Γ or, more precisely, on its double antiderivative in the second term of the right-hand side in equation (5.22). This can be best realized by considering the ideal case of Γ being a delta function, $\Gamma(x) = \gamma b\,\delta(x)$. In this case, the simple antiderivative is a square function. Consequently, the double antiderivative is a piecewise linear function. Its slopes are given by $\pm M b\gamma$, corresponding to a velocity $b\gamma$ with which the particles flow towards the origin.

5.3.3 Beyond local density approximation

Extending the local solutions beyond the spatial vicinity of the perturbation, we consider the full ground state density profile $n_0(x)$. Typically, going away from the center, it decreases monotonically towards the cloud edges. Thus, sound wave excitations that are born in the MO, start to propagate with velocity $\propto n_0^{1/2}(\mathbf{0})$, are decelerated when moving towards regions of lower densities and, eventually, reflected at the cloud edge. Being interested, for instance, in the evolution of the density only, we differentiate the lower component of equation (5.7) with respect to time and plug in $\partial_t S_1$ given by the upper component. This way, we have rewritten a system of first order differential equations as a single second-order differential equation in the first-order density response,

$$\left[\partial_t^2 - \left(\tfrac{g}{M}\,\partial_x n_0\right)\partial_x - \tfrac{g}{M} n_0\,\partial_x^2\right] n_1 = \tfrac{1}{M}\,\partial_x\!\left(n_0\,\partial_x V_{\mathrm{CP}}\right)\Theta(t) - n_0\,\Gamma\,\delta(t). \tag{5.23}$$

The coefficients of the terms with second derivatives have opposite signs, making (5.23) a *hyperbolic* equation [81, 82]. In this case, the propagation of its solutions can be described by its characteristics, defined by the ordinary differential equation

$$\frac{\mathrm{d}x^{(c)}}{\mathrm{d}t} = \pm\sqrt{\frac{g n_0}{M}}. \tag{5.24}$$

One easily recognizes the definition of the speed of sound on the right-hand side. In deed, if the ground state density n_0 is assumed to be constant as in last subsection, the characteristics are trivially given by $x^{(c)}(t) = \pm ct$, describing the wave front propagation with constant speed of sound. Abandoning the local density approximation in favor of the THOMAS-FERMI approximation, the spatially varying ground state density is given equation (3.82). In this case, from relation (5.24) one obtains the characteristics

$$x^{(c)}(t) = \pm R\,\sin\!\left(\frac{\omega t}{\sqrt{2}}\right). \tag{5.25}$$

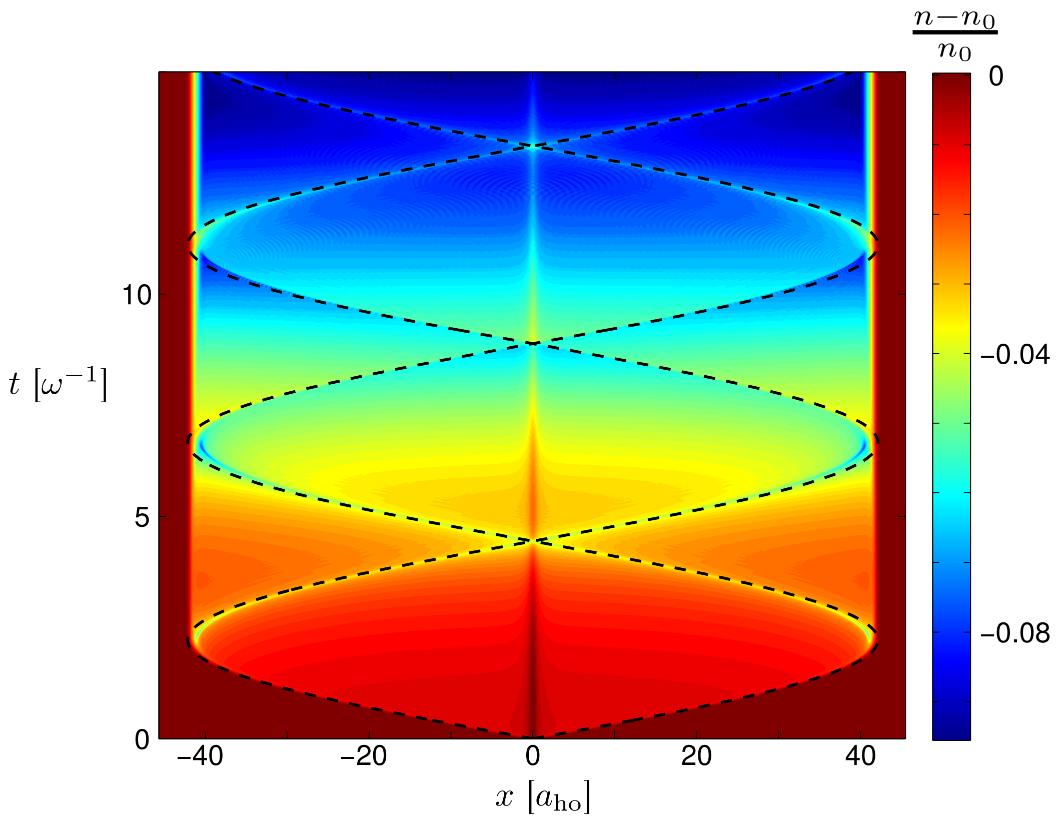

Figure 5.2.: Density response from numerical GP solution. Dashed lines are characteristics of PDE (5.23), explicitly given in (5.25) for TF ground state. Parameters of system are $M = 87\text{amu}$, $\omega = 2\pi \cdot 3\text{s}^{-1}$, $g = 0.499\hbar\omega a_{\text{ho}}$.

Thus, sound wave excitations oscillate back and forth across the density profile being reflected at the cloud edge at $x = \pm R$.

The density response upon a realistic condensate in a harmonic potential is shown in figure 5.2. To this end, we have solved the time-dependent modified Gross-Pitaevskii equation (5.1) numerically. One can see that the characteristics (5.25), that are indicated as dashed lines, trace the wave front propagation quite well. In addition to the sound waves, the condensate is constantly loosing atoms. Consequently, equation (5.23), describing the linear response n_1 on top of a time-independent ground state $n_0(x)$, becomes inadequate in the long term. Rather than circulating incessantly across a static medium, the sound waves erode the bulk density; inevitably shrinking it. Nevertheless, if we can assume the total number of particles that are lost during a single sound wave circulation to be small, i.e. $\dot{N} \ll \omega/\sqrt{2}$, we can adequately describe wave front propagation with expression (5.25) in the limit of a few cycles. Looking closely at figure (5.2), one can already recognize that wave fronts do not reach as far from the center after a few cycles as they do in the very beginning. The shrinking of the bulk density on longer time scales and its implications for the dynamics of the total particle number is discussed in the following section.

5.3.4 Particle loss

So far, we have priorly considered local effects of a BEC. In contrast to local phenomena like sound wave excitations, we now discuss the decay of the global particle number that is triggered by interactions with the MO. For this purpose, we assume the linear density response to be sufficiently small compared to the ground state density. Thus, we can write the evolution equation for the complete density as

$$\partial_t n = -\tfrac{1}{M}\,\nabla(n\,\nabla S_1) - \Gamma\, n, \tag{5.26}$$

exploiting relations $n = n_0 + n_1 \approx n_0$ and $\partial_t n = \partial_t n_1$. While the one-dimensional model was useful to obtain simple results and illustrative visualizations in the last subsection, we consider the more realistic three-dimensional case in the following. A differential equation for the particle number is obtained by integrating equation (5.26) over the complete system and neglecting boundary terms. This yields

$$\frac{\mathrm{d}N}{\mathrm{d}t} = -\int \mathrm{d}^3x\; n(N,\mathbf{x})\,\Gamma(\mathbf{x}). \tag{5.27}$$

Hence, the total loss rate is the overlap of position dependent loss function Γ and density n. As mentioned above, we now ignore local excitations. In deed, one can check that all sound waves that are caused by the sudden switch-on of the MO attraction, $V_{\mathrm{CP}}(\mathbf{x})\,\Theta(t)$, vanish exactly during integration. For example, spatially integrating expression (5.21), the density bump at the origin described by $2V_{\mathrm{CP}}(x)$ is compensated by two traveling dimples given by $-V_{\mathrm{CP}}(x \pm ct)$.

In addition to sound wave excitations, particles are constantly flowing towards the MO where they are lost from the condensate. As discussed in the last subsection, this particle loss entails a steadily shrinking condensate. Thus, one has to consider the density as a function of N as we have indicated in expression (5.27). We again assume the condensate to be initially prepared in a trap and dominated by mean field interactions such that THOMAS-FERMI limit applies. The particle-number-dependent density is then written as

$$n(N,\mathbf{x}) = \tfrac{1}{g}\Big(\mu_{\mathrm{TF}}(N) - V_{\mathrm{ext}}(\mathbf{x})\Big), \tag{5.28}$$

where $\mu_{\mathrm{TF}} > V_{\mathrm{ext}}$ and $n = 0$ otherwise. As an example we consider an anisotropic harmonic trapping potential $V_{\mathrm{ext}}(\mathbf{x}) = M\omega^2\mathbf{x}^2/2$ and a point-like MO, so that the loss function can be written as $\Gamma(\mathbf{x}) = \gamma\mathcal{V}\,\delta(\mathbf{x})$. Here, the factor γ is a constant loss rate in inverse time units and $\mathcal{V}$ describes an effective volume quantifying the spatial extent of the loss area. Approximating Γ with a delta function, of course, we have presumed the effective volume $\mathcal{V}$ to be small on the length scale of the cloud. In this case, the right-hand side of the differential equation for the

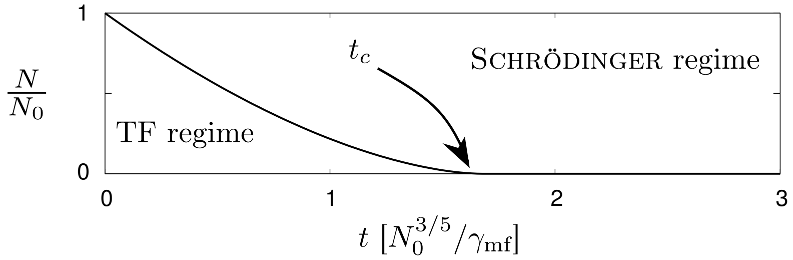

Figure 5.3.: Decay of particle number of a BEC in harmonic trap with point-like MO

particle number (5.27) becomes $-\gamma\mathscr{V}\mu(N)/g$. Consequently, using relation (4.25) with $D=3$ to write out the chemical potential in THOMAS-FERMI limit for a harmonic oscillator, we obtain

$$\frac{\mathrm{d}N}{\mathrm{d}t} = -\gamma_{\mathrm{mf}} N^{2/5}. \tag{5.29}$$

In order to arrive at this compact form, we have defined the effective loss rate in the mean field regime as

$$\gamma_{\mathrm{mf}} = \left(\tfrac{15}{8\pi}\right)^{2/5} \left(\tfrac{M\omega^2}{2g}\right)^{3/5} \mathscr{V}\gamma. \tag{5.30}$$

In the regime of large particle numbers, $N \gg 1$, equation (5.29) is readily solved by

$$N(t) = \left(N_0^{3/5} - \tfrac{3}{5}\gamma_{\mathrm{mf}} t\right)^{5/3}, \tag{5.31}$$

describing an algebraic decay of the particle number. This solution is valid as long as N is large enough to make mean field interaction dominant so that TF limit applies.

After a critical time $t_c = 5/(3\gamma_{\mathrm{mf}})$, only few particles are left, i.e. $N \gtrsim 1$. In this regime, particle interactions can be neglected and the behavior of the remaining atoms is rather described by the single-particle SCHRÖDINGER equation. If we assume the condensate density after t_c to be described by the ground state of the noninteracting quantum-mechanical harmonic oscillator,

$$n(N,\mathbf{x}) = N\left(\tfrac{M\omega}{\pi\hbar}\right)^{3/2} \exp\left(-\tfrac{M\omega}{\hbar}\mathbf{x}^2\right), \tag{5.32}$$

the differential equation in the particle number (5.27) becomes

$$\frac{\mathrm{d}N}{\mathrm{d}t} = -\gamma_{\mathrm{ni}} N, \tag{5.33}$$

implying an exponential decay of the particle number. Here, we have identified the effective loss rate in the noninteracting regime,

$$\gamma_{\mathrm{ni}} = \left(\frac{M\omega}{\pi\hbar}\right)^{3/2} \mathscr{V}\gamma. \tag{5.34}$$

The evolution of $N(t)$ is shown in figure 5.3.

6 Phase space description of atom interferometers

Interferometry with neutral atoms is an active research field that is thematically situated between atomic physics and quantum optics. Nevertheless, the beginnings of matter wave interferometry date back to the early days of quantum mechanics. A comprehensive review on optics and interferometry with atoms and molecules was given by A. Cronin, J. Schmiedmayer, and D. Pritchard [29].

Roughly speaking, matter wave interferometry is about coherently splitting the motion of atoms and molecules into two or more paths. These paths separate spatially so that atoms following different paths will be subject to different external influences. Eventually, they are – completely or partially – recombined to produce a detectable density profile that contains information about the difference of phases that are accumulated along different evolution paths. This way, matter wave interferometry is, of course, completely analog to traditional interferometry utilizing light beams. This discipline was developed more that 100 years ago [83–86] and is an essential part of textbooks which are considered standard (see e.g. [87]). There are many advantages that come with extending these quasi-ancient ideas of optical interferometry to massive particles. Clearly, the earliest motivation was the experimental confirmation of de Broglie's matter wave picture formulated in 1923 [88]. This wave picture for massive particles was first demonstrated for electrons by Davisson and Germer in 1927 [89]. The first experiment on atom diffraction was already done in 1930 by Esterman and Stern [90]. Later, interference phenomena were also observed for neutrons [91]. Nowadays, the high controllability of atoms in laser fields enables the design of sensor devices with unprecedented precision.

In most cases, coherent manipulation of the atom's transverse motion is achieved by imposing periodical potentials on them. These can be realized by laser fields [92] as well as massive structures forming transmission gratings [93]. In this work, we consider only interferometer elements that are based on atom-light interactions. Moreover, the interferometer scheme shall be a Mach-Zehnder interferometer (MZI), sketched in figure 6.1.

In the following, we first recapitulate on how atomic beam splitters are realized with atom-laser interactions. These aspects are standard elements of many textbooks on quantum optics [30, 94, 95]. After that, we formulate a simple model of beam splitters in phase space and consider the propagation of wave functions through a MZI-setup. Finally, we translate the wave function formulation into a phase space language utilizing Wigner functions. This enables us to describe these elements in our ray tracing formalism that will be subject of chapter 7.

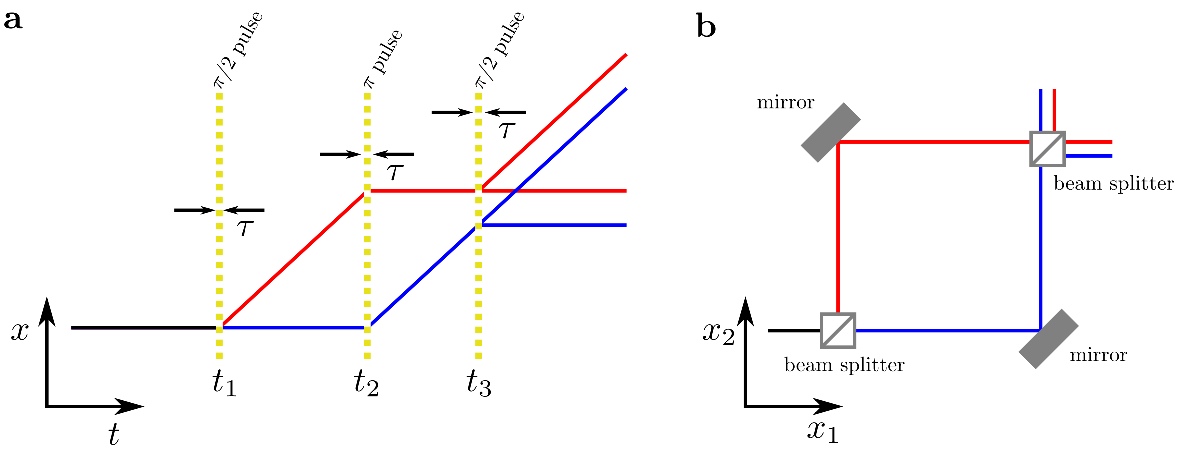

Figure 6.1.: Sketch of atomic and optical Mach-Zehnder interferometer (MZI). **a**: MZI for atoms realized by three laser pulses. We will elaborate on this configuration in section 6.3. **b**: Optical MZI with two beam splitter and two mirrors

6.1 Optical beam splitters for two-level atoms

The splitting of an incident atomic wave function into two or more paths by a light field shall be realized by a two or $2N_{\mathrm{ph}}$-photon transition. Therefore, consider two counter-propagating laser beams with wave vectors $\mathbf{k}_1 = \mathbf{k}_l$ and $\mathbf{k}_2 = -\mathbf{k}_l$, forming a standing wave. The electrical field is given by

$$\mathbf{E}(\mathbf{x}, t) = \tfrac{1}{2}\mathbf{E}_0\, e^{-i\omega_l t} \cos\left(\mathbf{k}_l \mathbf{x} + \tfrac{\zeta}{2}\right) + \text{h.c.}, \tag{6.1}$$

including the laser frequency $\omega_l = c|\mathbf{k}_l|$ and an arbitrary offset $\zeta/2$. The atoms that are exposed to the laser field shall be described by two-level systems with internal states $|g\rangle$ and $|e\rangle$. The Hamiltonian for the complete system comprises two parts,

$$\hat{H} = \hat{H}_{\mathrm{at}} + \hat{H}_{\mathrm{int}}. \tag{6.2}$$

If the atomic energies are given by $\hbar\omega_g$ and $\hbar\omega_e$, respectively, the atomic Hamiltonian reads

$$\hat{H}_{\mathrm{at}} = \hbar\omega_g\,|g\rangle\langle g| + \hbar\omega_e\,|e\rangle\langle e| + \frac{\hat{\mathbf{p}}^2}{2M}. \tag{6.3}$$

We have explicitly taken into account the external degrees of freedom, appearing in the kinetic contribution $\hat{\mathbf{p}}^2/(2M)$. In the following, we will refer to $|g\rangle$ as the ground state and to $|e\rangle$ as excited state. Their energy difference is denoted by $\hbar\omega_{eg}$. The interaction between the neutral atoms and the light field through the electric dipole moment $\hat{\boldsymbol{\mu}}$ gives rise to a lattice potential

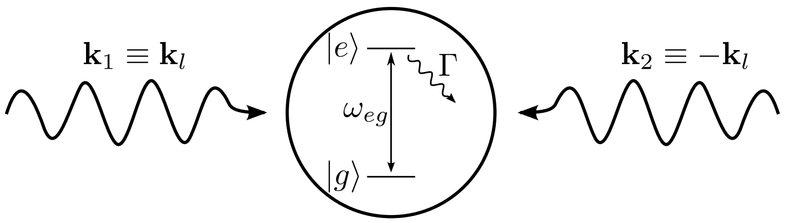
$\mathbf{k}_1 \equiv \mathbf{k}_l$
$|e\rangle$
Γ
ω_{eg}
$|g\rangle$
$\mathbf{k}_2 \equiv -\mathbf{k}_l$

Figure 6.2.: Sketch of laser field interacting with two-level atom

that can be described by the reciprocal lattice vector $\mathbf{G} = \mathbf{k}_1 - \mathbf{k}_2 = 2\mathbf{k}_l$. Using electrical dipole approximation, the interaction Hamiltonian is written as

$$\begin{aligned}\hat{H}_{\text{int}} &= -\hat{\boldsymbol{\mu}} \cdot \mathbf{E}(\hat{\mathbf{x}}) \\ &= \frac{\hbar\omega_{\text{R}}}{2}\left(e^{i\mathbf{k}_l\hat{\mathbf{x}}+\zeta/2} + e^{-i\mathbf{k}_l\hat{\mathbf{x}}-\zeta/2}\right)\left(e^{-i\omega_l t}\,|e\rangle\langle g| + \text{h.c.}\right),\end{aligned} \tag{6.4}$$

introducing the Rabi-frequency $\omega_{\text{R}} = -\mathbf{E}_0 \cdot \langle e|\hat{\boldsymbol{\mu}}|g\rangle / \hbar$ [30, 94, 96]. The atom-field system is sketched in figure 6.2. Expanding the position dependent factor in H_{int} as

$$e^{\pm i\mathbf{k}_l\hat{\mathbf{x}}} = \int \mathrm{d}^3p \; |\mathbf{p} \pm \hbar\mathbf{k}_k\rangle\langle\mathbf{p}|, \tag{6.5}$$

one can see that the interaction of atoms with the laser field couples the states $|g,\mathbf{p}\rangle$ with $|e,\mathbf{p}\pm\hbar\mathbf{k}_k\rangle$. Physically, this transition is achieved by absorption of a single photon with energy $\hbar k_l$ by the atom. Subsequent emission of a photon then couples $|e,\mathbf{p}\pm\hbar\mathbf{k}_k\rangle$ to $|g,\mathbf{p}\pm 2\hbar\mathbf{k}_l\rangle$. Consequently, chaining these absorption/emission processes together, a $2N_{\text{ph}}$-photon transfer results in $\left|g,\mathbf{p}\pm 2N_{\text{ph}}\hbar\mathbf{k}_l\right\rangle$. Here, we utilize a wave function in $3+1$ degrees of freedom. On one hand, there is the external translational motion of the atoms in three dimensions, quantified by the momentum $\mathbf{p}$. On the other, the internal degree of freedom is spanned by atomic states $|g\rangle$ and $|e\rangle$. In a more rigorous notation, one would write e.g. $|g,\mathbf{p}\rangle = |g\rangle \otimes |\mathbf{p}\rangle$.

Of course, the two-level model does not describe the coupling of the excited state to unobserved states other than $|e\rangle$. This effectively leads to a loss of population from $|g\rangle$ quantified by a loss rate Γ. The influence of such a dissipative mechanism can however be minimized by chosing the laser frequency to be sufficiently far detuned from resonance,

$$\omega_{eg} - \omega_l = \delta \gg \Gamma. \tag{6.6}$$

Starting with an atom in its ground state $|g\rangle$, the excited state can then be adiabatically eliminated. Hence, the resulting wave function is produced by $2N_{\text{ph}}$-photon transitions between two ground states $|g,\mathbf{p}\rangle$ and $|g,\mathbf{p}\pm 2n\hbar\mathbf{k}_l\rangle$ with the excited state $|e,\mathbf{0}\rangle$ being a virtual intermediate state. In the following, we assume condition (6.6) to be always fulfilled.

Concerning the course of events, we let the atoms enter the laser field at time instance $t_1 - \tau/2$ where they are subject to atom-light interactions until $t_1 + \tau/2$. Depending on the interaction time τ and depth $\hbar\omega_\mathrm{R}$ of the optical potential, the passage of the wave packet through the beam splitter is ruled by different regimes [96–98]. Two cases that are particularly useful in the context of matter wave interferometry are the Kapitza-Dirac and the Bragg regime which will be briefly discussed in the following.

6.1.1 Kapitza-Dirac diffraction

In the limit of short interaction time τ, the atomic state that results from interaction with the laser field is described by Kapitza-Dirac diffraction [92, 96, 99–101]. Assuming $\tau \ll 1/\omega_\mathrm{rec}$, with $\omega_\mathrm{rec} = \hbar\mathbf{k}_l^2/(2M)$ being the recoil frequency, the kinetic contribution to the total Hamiltonian can be neglected. This approximation is referred to as Raman-Nath regime [30, 102]. Eliminating the excited state $|e\rangle$, the atom-light interaction is effectively given by an AC-Stark shift potential

$$\hat{H}(t) = \tfrac{1}{2}\,\hbar\omega_\mathrm{R}^{(2)}(t)\,\cos^2(\mathbf{k}_l\hat{\mathbf{x}} + \zeta/2), \tag{6.7}$$

using the effective two-photon Rabi frequency $\omega_\mathrm{R}^{(2)}(t) = \omega_\mathrm{R}^2(t)/(2\delta)$. Hence, the periodical light field acts as phase grating for the incident wave function $\left|\psi(t_1 - \frac{\tau}{2})\right\rangle$. Respecting the on- and off-switching process of the laser pulse, the temporally varying intensity gives rise to a time-dependent effective Rabi frequency $\omega_\mathrm{R}^{(2)}(t)$. The output wave function is then written as

$$\left|\psi(t_1 + \tfrac{\tau}{2})\right\rangle = \exp\left[-\frac{i}{\hbar}\int_{t_1-\tau/2}^{t_1+\tau/2} \mathrm{d}t'\,\hat{H}(t')\right]\left|\psi(t_1 - \tfrac{\tau}{2})\right\rangle. \tag{6.8}$$

Plugging in expression (6.7) for the Hamiltonian, we obtain the resulting wave function as a superposition of many copies of the incident wave function being affected by different operators $\exp\left(i\ell\mathbf{G}\hat{\mathbf{x}}\right)$,

$$\left|\psi(t_1 + \tfrac{\tau}{2})\right\rangle = e^{-i\vartheta(\tau)} \sum_{\ell=-\infty}^{\infty} \alpha_\ell(\tau)\, e^{i\ell(\mathbf{G}\hat{\mathbf{x}}+\zeta)} \left|\psi(t_1 - \tfrac{\tau}{2})\right\rangle. \tag{6.9}$$

The coefficients α_ℓ of this superposition depend on the interaction time τ and are given in terms of Bessel functions of the first kind [75] as

$$\alpha_\ell(\tau) = i^\ell\, J_\ell(\vartheta(\tau))\, e^{i\ell\zeta}, \qquad \text{with} \quad \vartheta(\tau) = \int_{t_1-\tau/2}^{t_1+\tau/2} \mathrm{d}t'\,\omega_\mathrm{R}^{(2)}(t'). \tag{6.10}$$

We have abbreviated the argument of the Bessel functions as a parameter $\vartheta(\tau)$ that grows linearly with interaction time τ, assuming the laser intensity and thus the Rabi frequency $\omega_\mathrm{R}^{(2)}(t)$ to

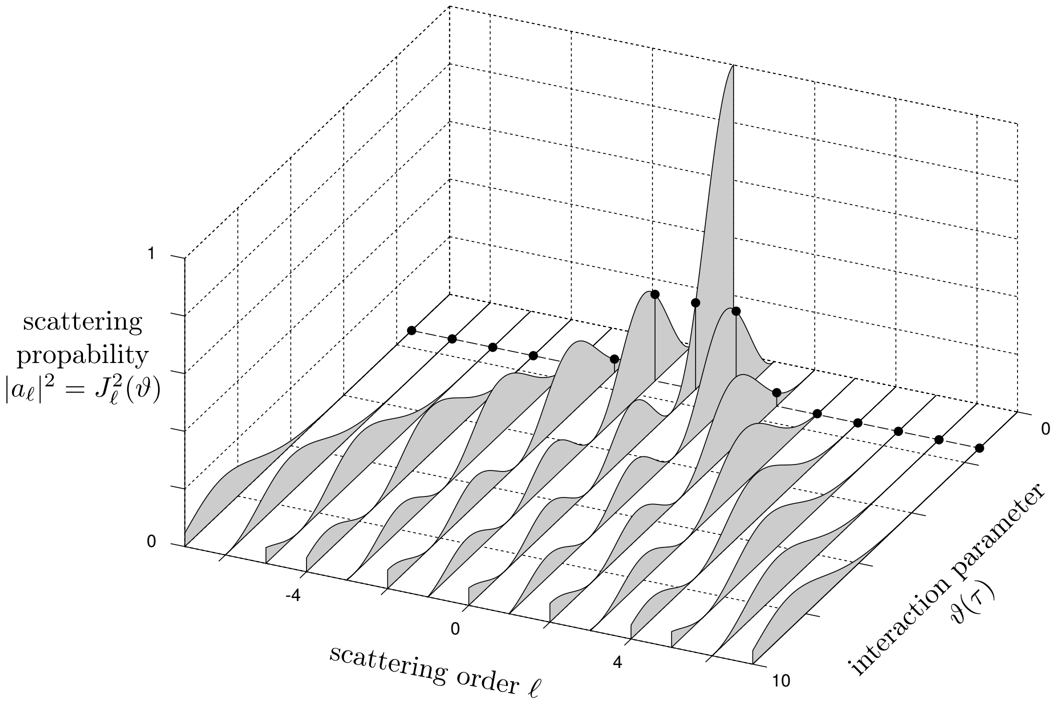

Figure 6.3.: Probabilities $|\alpha_\ell|^2$ of Kapitza-Dirac scattering orders ℓ over interaction parameter ϑ according to (6.10). Integrated stem plot indicates probabilities for a fixed choice of $\tau \approx 1.4347$.

be zero outside the interval $(t_1 - \tau/2, t_1 + \tau/2)$. From equation (6.9) we can easily extract an operator

$$\hat{U}_{\mathrm{KD}}(\vartheta) = e^{-i\vartheta} \sum_{\ell=-\infty}^{\infty} i^\ell J_\ell(\vartheta)\, e^{i\ell \mathbf{G}\hat{\mathbf{x}}}, \tag{6.11}$$

that acts on incident states and produces the resulting state of a Kapitza-Dirac pulse, $\left|\psi(t_1 + \frac{\tau}{2})\right\rangle = \hat{U}_{\mathrm{KD}} \left|\psi(t_1 - \frac{\tau}{2})\right\rangle$.

At first glimpse, the output state (6.9) is a superposition of infinitely many scattering orders ℓ. The number of contributing orders is then successively increased by extending the interaction time τ. Only for longer interaction times τ, more diffraction orders come into play. A comparison of several coefficients for variable interaction time is shown in figure 6.3. Note that the sum of all scattering probabilities must be unity,

$$\sum_{\ell=-\infty}^{\infty} |\alpha_\ell|^2 = \sum_{\ell=-\infty}^{\infty} J_\ell^2(\vartheta) = 1, \tag{6.12}$$

where the second equal sign is justified by Neumann's addition theorem for Bessel functions [75].

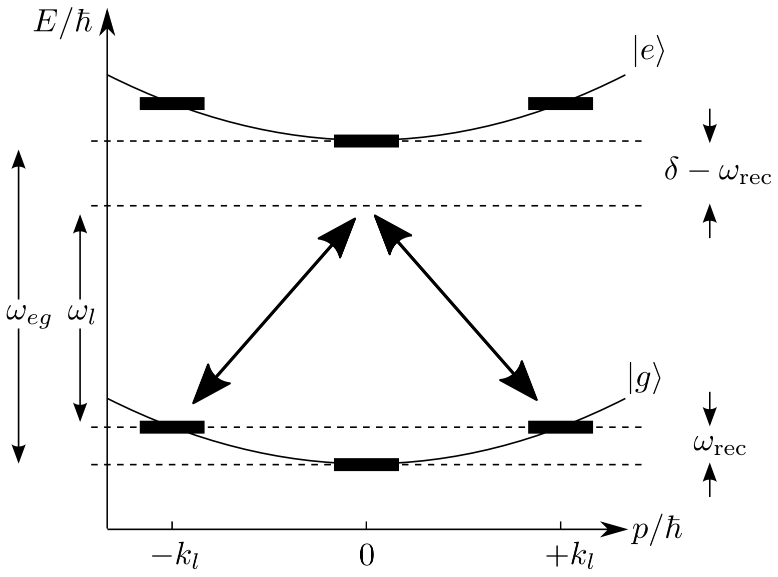

Figure 6.4.: Sketch of first-order Bragg diffraction by means of two-level dispersion relation [96, 106]. The laser field resonantly couples to external states of atomic motion with a two photon transition.

6.1.2 Bragg diffraction

Bragg diffraction [96, 98, 103–105] occurs in the limit of long interaction times and shallow optical potentials. Taking into account the kinetic contribution to the Hamiltonian which cannot be neglected anymore, only few transitions are permitted by energy conservation. For the sake of brevity, we limit our discussion to first order Bragg scattering. This means that single-photon transitions only couple the ground states $|g,\pm\mathbf{k}_l\rangle$ to the excited state $|e,\mathbf{0}\rangle$ and vice versa as indicated in figure 6.4. Respecting the kinetic energy, emission and absorption of laser photons leads to an increase or decrease of the translational energy of $\hbar\omega_\mathrm{rec}$, respectively, where the recoil frequency is given in terms of the laser wave length as $\omega_\mathrm{rec}=\hbar\mathbf{k}_l^2/(2M)$. Recalling the interpretation of $\exp(\pm i\mathbf{k}_l\hat{\mathbf{x}})$ as kick operators as indicated in expression (6.5), the complete Hamiltonian is written

$$\begin{aligned}\hat{H}=\ &\hbar\omega_{eg}\,|e,\mathbf{0}\rangle\langle e,\mathbf{0}|\ +\ \hbar\omega_\mathrm{rec}\big(|g,-\mathbf{k}_l\rangle\langle g,-\mathbf{k}_l|\ +\ |g,+\mathbf{k}_l\rangle\langle g,+\mathbf{k}_l|\big)\\&-\frac{\hbar\omega_\mathrm{R}}{2}\left[e^{-i\omega_l t}\left(e^{i\zeta/2}\,|e,\mathbf{0}\rangle\langle g,-\mathbf{k}_l|\ +\ e^{-i\zeta/2}\,|e,\mathbf{0}\rangle\langle g,+\mathbf{k}_l|\right)+\mathrm{h.c.}\right].\end{aligned}\tag{6.13}$$

In contrast to Kapitza-Dirac pulses, dealing now with longer atom-laser interaction times τ, we ignore the details of switching on and off, assuming the Rabi frequency ω_R to be constant inside the interval $(t_1-\tau/2,\ t_1+\tau/2)$, and zero outside. The Schrödinger equation $i\hbar\,\partial_t\,|\psi\rangle=\hat{H}\,|\psi\rangle$ with the Hamiltonian (6.13) can be solved using the ansatz

$$|\psi(t)\rangle=\alpha_-(t)e^{-i\omega_\mathrm{rec}t}\,|g,-\mathbf{k}_l\rangle+\alpha_0(t)e^{-i\omega_{eg}t}\,|e,\mathbf{0}\rangle+\alpha_+(t)e^{-i\omega_\mathrm{rec}t}\,|g,+\mathbf{k}_l\rangle\,.\tag{6.14}$$

This leads to differential equations in the time-dependent coefficients,

$$\dot{\alpha}_0 = -\frac{\omega_{\mathrm{R}}}{2} e^{i\Delta\, t}\left(e^{-i\zeta/2}\alpha_- + e^{+i\zeta/2}\alpha_+\right), \qquad e^{\pm i\zeta/2}\dot{\alpha}_\mp = -\frac{\omega_{\mathrm{R}}}{2} e^{-i\Delta\, t}\alpha_0, \tag{6.15}$$

where we have abbreviated the effective detuning $\Delta = \omega_{\mathrm{rec}} + \delta$ (including photon recoil). In the limit of large detuning $\Delta^2 \gg \omega_{\mathrm{R}}^2$, the coefficients, after having passed the optical field, become

$$\alpha_{-}(t_1+\tfrac{\tau}{2}) = e^{\frac{i}{2}\omega_{\mathrm{R}}^{(2)}\tau}\left[\cos\frac{\omega_{\mathrm{R}}^{(2)}\tau}{2}\,\alpha_{-}(t_1-\tfrac{\tau}{2}) + ie^{-i\zeta}\sin\frac{\omega_{\mathrm{R}}^{(2)}\tau}{2}\,\alpha_{+}(t_1-\tfrac{\tau}{2})\right], \tag{6.16a}$$

$$\alpha_{+}(t_1+\tfrac{\tau}{2}) = e^{\frac{i}{2}\omega_{\mathrm{R}}^{(2)}\tau}\left[ie^{i\zeta}\sin\frac{\omega_{\mathrm{R}}^{(2)}\tau}{2}\,\alpha_{-}(t_1-\tfrac{\tau}{2}) + \cos\frac{\omega_{\mathrm{R}}^{(2)}\tau}{2}\,\alpha_{+}(t_1-\tfrac{\tau}{2})\right]. \tag{6.16b}$$

where we encounter again the effective two photon Rabi frequency, $\omega_{\mathrm{R}}^{(2)} = \omega_{\mathrm{R}}^2/(2\delta)$. Having now available a mapping between amplitudes, it is easy to write a mapping between the wave function before and after the Bragg pulse. Therefore, assuming the incident state to be a superposition

$$|\psi(t_1-\tfrac{\tau}{2})\rangle = \alpha_{-}(t_1-\tfrac{\tau}{2})\,|g,-\mathbf{k}_l\rangle + \alpha_{+}(t_1-\tfrac{\tau}{2})\,|g,+\mathbf{k}_l\rangle \tag{6.17}$$

of the two ground states $|g,\pm\mathbf{k}_l\rangle$ with no population in the excited state $|e,\mathbf{0}\rangle$, $\alpha_0(t_1-\tau/2) = 0$, the output wave function becomes

$$\begin{aligned} |\psi(t_1+\tfrac{\tau}{2})\rangle = e^{i\vartheta/2}\Big[&\left(\cos\tfrac{\vartheta}{2}\;|g,-\mathbf{k}_l\rangle + i\sin\tfrac{\vartheta}{2}\,e^{i\zeta}\;|g,+\mathbf{k}_l\rangle\right)\,\langle g,-\mathbf{k}_l|\psi(t_1-\tfrac{\tau}{2})\rangle \\ &+\left(i\sin\tfrac{\vartheta}{2}\,e^{-i\zeta}\;|g,-\mathbf{k}_l\rangle + \cos\tfrac{\vartheta}{2}\;|g,+\mathbf{k}_l\rangle\right)\,\langle g,+\mathbf{k}_l|\psi(t_1-\tfrac{\tau}{2})\rangle\Big] \end{aligned} \tag{6.18}$$

identifying again an interaction parameter $\vartheta = \omega_{\mathrm{R}}^{(2)}\tau$. This solution describes an oscillation of population between two momentum states at $\mp\mathbf{k}_l$ as we tune the interaction time τ. It is known as *Pendellösung* in diverse physical contexts [107–109]. Like before, we can easily extract an operator from expression (6.18),

$$\begin{aligned} \hat{U}_{\mathrm{B}}(\vartheta) = \Big[&\left(\cos\tfrac{\vartheta}{2} + i\sin\tfrac{\vartheta}{2}\,e^{i(\mathbf{G}\hat{\mathbf{x}}+\zeta)}\right)\,|g,-\mathbf{k}_l\rangle\,\langle g,-\mathbf{k}_l| \\ &+\left(i\sin\tfrac{\vartheta}{2}\,e^{-i(\mathbf{G}\hat{\mathbf{x}}+\zeta)} + \cos\tfrac{\vartheta}{2}\right)\,|g,+\mathbf{k}_l\rangle\,\langle g,+\mathbf{k}_l|\Big], \end{aligned} \tag{6.19}$$

acting on incident states to produce the outcome of the Bragg pulse, $|\psi(t_1+\tfrac{\tau}{2})\rangle = \hat{U}_{\mathrm{B}}(\vartheta)\,|\psi(t_1-\tfrac{\tau}{2})\rangle$. It contains the projectors $|\pm\mathbf{k}_l\rangle\,\langle\pm\mathbf{k}_l|$ on the two external momentum states that are coupled by the two-photon transition.

Influence of momentum width

The above discussion only treats states $|\pm\mathbf{k}_l\rangle$ that are infinitely sharply localized in k-space. In this model, momentum states that deviate from the Bragg condition – even by an arbitrarily small amount – are not affected by the laser pulse. In fact, the Bragg condition is not infinitely sharp. The coupling efficiency rather decreases continuously when diverging about $\delta\mathbf{k}$ from the resonant cases $\mathbf{k} = \pm\mathbf{k}_k$. Szigeti et al have considered the coupling of states $|\pm\mathbf{k}_l + \delta\mathbf{k}\rangle$ being described by modified coefficients $\alpha_\pm(\delta\mathbf{k}, t)$ [110]. For initial conditions $\alpha_-(\delta\mathbf{k}, t) = 1$ and $\alpha_+(\delta\mathbf{k}, t) = 0$ they have calculated the absolute square of the resulting coefficient α_+ to be

$$|\alpha_+(\delta\mathbf{k}, t_1 + \tfrac{\tau}{2})|^2 = \frac{1}{1 + \left(\frac{4\omega_\text{rec}}{\omega_\text{R}^{(2)} k_l}\delta k\right)^2} \sin\left(\sqrt{1 + \left(\frac{4\omega_\text{rec}}{\omega_\text{R}^{(2)} k_l}\delta k\right)^2}\, \frac{\omega_\text{R}^{(2)}\tau}{2}\right). \tag{6.20}$$

Thus, the coupling efficiency from $|-\mathbf{k}_l\rangle$ to the kicked state $|+\mathbf{k}_l\rangle$ as a function of the deviance $\delta k = |\delta\mathbf{K}|$ is oscillating with a Lorentz-shaped envelope. It can nevertheless be considered approximately constant for small deviations $\delta k \ll k_l\omega_\text{R}^{(2)}/(4\omega_\text{rec})$. The “softening” of the Bragg condition means that not only the momentum states $|\pm\mathbf{k}_l\rangle$ are coupled. Also complete wave packets with finite but sufficiently small width in k-space are affected. Consequently, the most general incident state that is completely affected by a Bragg pulse is a superposition of two wave packets that are centered at $\mathbf{k} = \pm\mathbf{k}_l$,

$$|\psi(t_1 - \tfrac{\tau}{2})\rangle = \int \mathrm{d}^3k \left(|-\mathbf{k}_l + \mathbf{k}\rangle \langle\mathbf{k}|\phi_-\rangle + |+\mathbf{k}_l + \mathbf{k}\rangle \langle\mathbf{k}|\phi_+\rangle\right). \tag{6.21}$$

The functions $|\phi_\pm\rangle$ shall satisfy $\langle\phi_\pm|\hat{\mathbf{k}}|\phi_\pm\rangle = \mathbf{0}$ and $\langle\phi_\pm|\hat{\mathbf{k}}^2|\phi_\pm\rangle \ll (4k_l\omega_\text{rec}/\omega_\text{R}^{(2)})^2$. After passing the beam splitter, the resulting state is

$$\begin{aligned} |\psi(t_1 + \tfrac{\tau}{2})\rangle = e^{i\vartheta/2} \int \mathrm{d}^3k \Big[&\left(\cos\tfrac{\vartheta}{2} + i\sin\tfrac{\vartheta}{2}\, e^{i(\mathbf{G}\hat{\mathbf{x}}+\zeta)}\right) |-\mathbf{k}_l + \mathbf{k}\rangle \langle\mathbf{k}|\phi_-\rangle \\ &+ \left(i\sin\tfrac{\vartheta}{2}\, e^{-i(\mathbf{G}\hat{\mathbf{x}}+\zeta)} + \cos\tfrac{\vartheta}{2}\right) |+\mathbf{k}_l + \mathbf{k}\rangle \langle\mathbf{k}|\phi_+\rangle \Big]. \end{aligned} \tag{6.22}$$

Extracting a beam splitter operator that unifies the mapping between the wave functions (6.21) and (6.22) is not as straightforward as in the case of momentum eigenstates. There, we have expressed $\hat{U}_\text{B}$ in (6.19) in terms of projectors $|\pm\mathbf{k}_l\rangle\langle\pm\mathbf{k}_l|$. Assuming now the coupling efficiency to be approximately constant in the near vicinity of the Bragg condition, i.e.

$$|\mathbf{k} - \mathbf{k}_l| < \delta k \ll k_l\omega_\text{R}^{(2)}/(4\omega_\text{rec}),$$

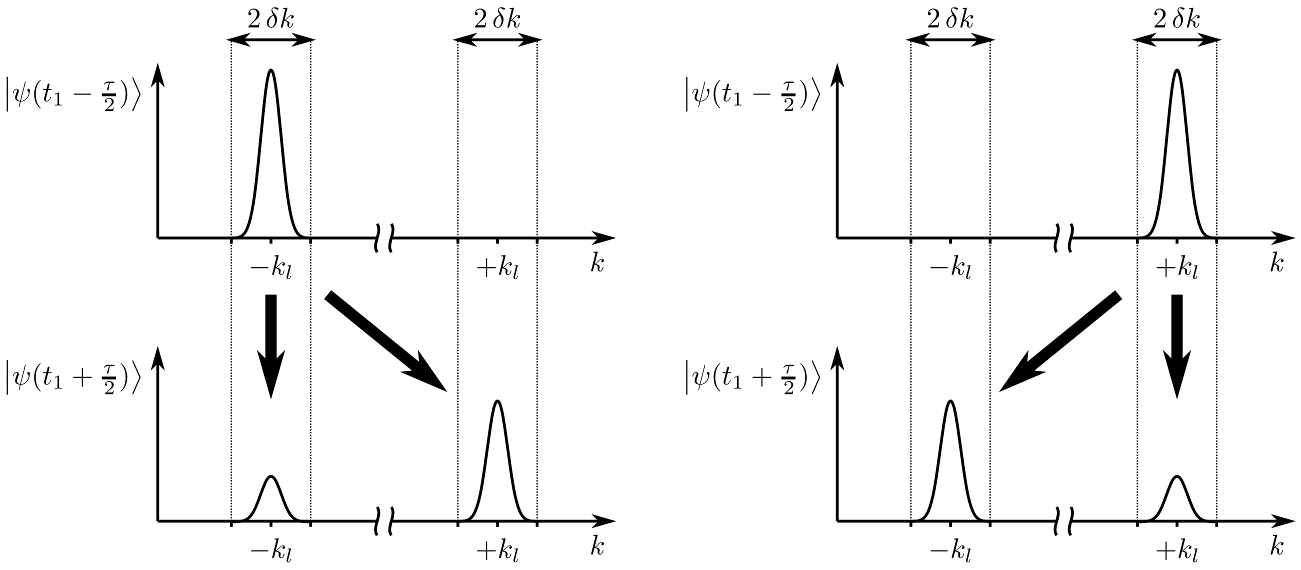

$2\,\delta k$
$2\,\delta k$
$2\,\delta k$
$2\,\delta k$
$|\psi(t_1 - \frac{\tau}{2})\rangle$
$|\psi(t_1 - \frac{\tau}{2})\rangle$
$-k_l$
$+k_l$
k
$-k_l$
$+k_l$
k
$|\psi(t_1 + \frac{\tau}{2})\rangle$
$|\psi(t_1 + \frac{\tau}{2})\rangle$
$-k_l$
$+k_l$
k
$-k_l$
$+k_l$
k

Figure 6.5.: Illustration of how Bragg pulses affect incident wave packets that are within a small domain of extent $2\,\delta k$ around the resonant wave numbers $\pm k_l$.

these infinitely sharp projectors may be extended as

$$\hat{P}_{\pm k_l} = \int \mathrm{d}^3 k\, \Theta(\delta k - |\mathbf{k}|)\; |\pm\mathbf{k}_l + \mathbf{k}\rangle\, \langle \pm\mathbf{k}_l + \mathbf{k}|\,. \tag{6.23}$$

With this definition, the operator that maps the input wave function on the output wave function, $|\psi(t_1+\tau/2)\rangle = \hat{U}_{\mathrm{B}}\,|\psi(t_1-\tau/2)\rangle$, is written as

$$\hat{U}_{\mathrm{B}}(\vartheta) = \left[\left(\cos\tfrac{\vartheta}{2} + i\sin\tfrac{\vartheta}{2}\, e^{i(\mathbf{G}\hat{\mathbf{x}}+\zeta)}\right)\hat{P}_{-k_l} + \left(i\sin\tfrac{\vartheta}{2}\, e^{-i(\mathbf{G}\hat{\mathbf{x}}+\zeta)} + \cos\tfrac{\vartheta}{2}\right)\hat{P}_{+k_l}\right]. \tag{6.24}$$

The softened Bragg condition is illustrated in figure 6.5.

The restriction to incident states with small widths in k-space is not only useful for theoreticians that want to avoid overly complicated models. In deed, a large incident momentum width would result in only a fraction of the wave packet being affected by the Bragg pulse. This, in turn, has negative consequences for interferometry applications, e.g. signal-to-noise ration of interference fringes [110]. Decreasing the momentum width may be achieved practically by applying a confining potential for a short time span, also known as *delta-kick cooling* [111, 112]. Alternatively, one can velocity-select incident atoms by yet another Bragg pulse [113–115]. Clearly, one disadvantage of the latter method is a loss of atoms and thus an decreased signal in the output of an interferometer.

In the following, we assume the momentum width of the incident state to be small enough, so that Bragg pulses affect the entire wave packet (given it is centered at the right spots in momentum space). This will allow for a simple model of interferometer elements.

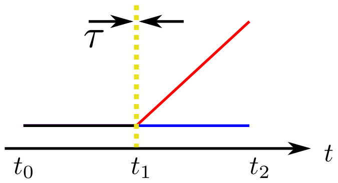

Figure 6.6.: Sketch of time spans for applying a beam splitter at t_1 between two periods with time spans t_{01} and t_{12} of classical transport.

6.2 Beam splitter in phase space

As we saw in section 3.2.2, the WIGNER function is well suited for examining the dynamics of quantum states in quadratic or relatively smooth potential. In that case, one can safely ignore all quantum corrections $\propto \hbar$ to the classical equation of motion (3.40). However, this smoothness condition is heavily violated when the atoms enter rapidly oscillating laser fields that utilized as interferometer elements (e.g. beam splitters). Being subject to periodic potentials that vary on very short length scales, the evolution of the WIGNER function is dominated by the terms on the rhs of (3.40), entailing phase space dynamics that differ significantly from classical transport. Nevertheless, these building elements of matter-wave interferometers can be expressed rather simply in terms of wave functions (see last section). These wave function expressions may then be translated onto phase space distributions. Evolution before and after the beam splitter shall be ruled by classical transport. Comparing these two regimes of propagation, i.e. classical transport and laser pulse application, we assume the atom-laser interaction time to be negligible on the time scale of classical transport, $\tau \to 0$. This means, we describe the laser pulses to act instantaneously: An incident state right before the laser pulse at, say, $t_1^- = t_1 - \tau/2$ is mapped onto the output state right after it at $t_1^+ = t_1 + \tau/2$. In contrast, classical transport leads to a continuous transformation of states.

6.2.1 Beam splitter model

After having presented two widespread methods for splitting atomic states in the last section, we want to stipulate a generic beam splitter operator. An essential ingredient to all discussed beam splitting processes was the application of a kick operators to different orders ℓ. Thus, we assume a generic beam splitter operator that is simply an arbitrary linear combination of these kicks, writing

$$\hat{U}_{\text{bs}} = \sum_{\ell=-\infty}^{\infty} \alpha_\ell \, e^{i\ell \mathbf{G}\hat{\mathbf{x}}}. \tag{6.25}$$

Comparing this definition with last section's results, it is clearly trivial to see the connection to KAPITZA-DIRAC diffraction. Inserting the coefficients (6.10) into expression (6.25) exactly

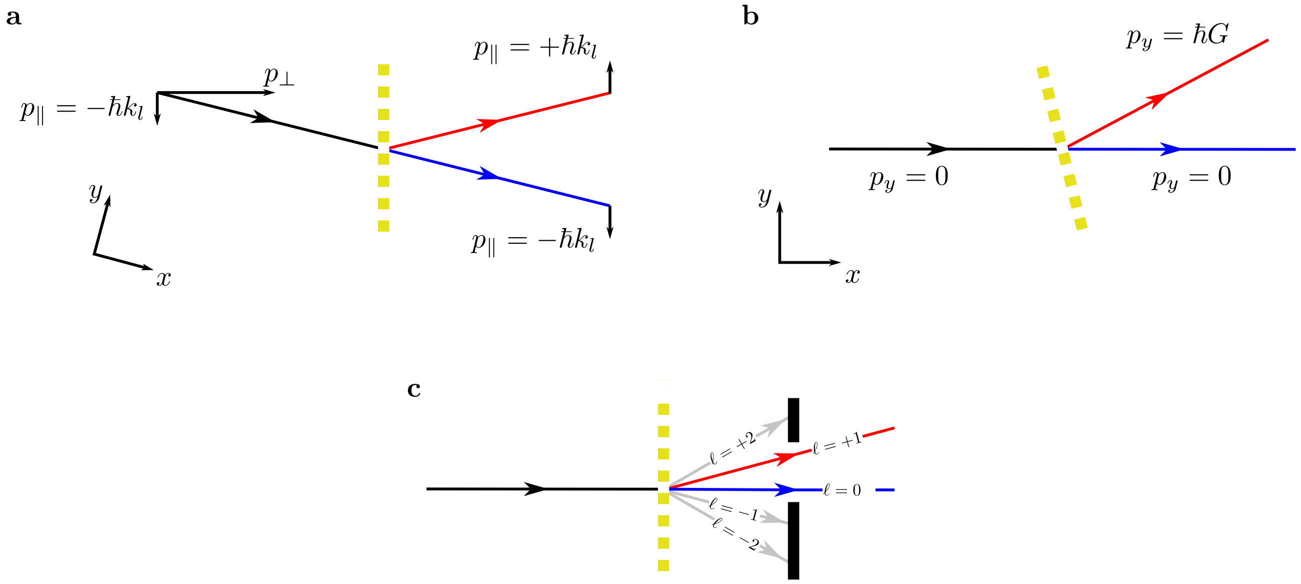

Figure 6.7.: Illustration of atomic beam splitters. Part **a**: Bragg pulse. Part **b**: Bragg pulse with tilted laser beam. Part **c**: Kapitza-Dirac pulse.

yields the operator $\hat{U}_{\text{KD}}$ as given in (6.11) (apart a phase that is common to all orders). Here, one disadvantage is the presence of many scattering orders, far more than one usually needs to build an interferometer. For example, given we require a beam splitter that equally populates the unkicked and the kicked state, $\ell = 0, 1$, and we need only those two for subsequent applications. An interaction parameter of $\vartheta \approx 1.43$ does the trick to yield equal output probabilities $|\alpha_0|^2 = |\alpha_1|^2 \approx 0.30$. However, about 40% of the incident population are lost to unobserved scattering orders $\ell \neq 0, 1$ in this case. If we filter out the few scattering orders that are needed, every application of such a beam splitter therefore involves a loss of the total (observed) population.

In case of Bragg pulses, on the other hand, we are dealing with two scattering orders right from the start. The associated coefficients α_0 and α_1 are fixed by relation (6.16), renaming indices from ± to 0, 1. One apparent inconsistency is that in 6.1.2 the involved states were centered at $\mathbf{k} = \pm\mathbf{k}_l = \pm\mathbf{G}/2$ rather than, as we suggest now, at $\mathbf{k} = \mathbf{0}$ and $\mathbf{k} = \mathbf{G}$. In many practical realizations, the incident wave packet is not at rest but rather traveling with momentum $\mathbf{p} = \mathbf{p}_{\perp} - \hbar\mathbf{k}_l$. Here, $\mathbf{p}_{\perp}$ is perpendicular to the laser while $-\hbar\mathbf{k}_l$ is obviously parallel to it. The resulting states after the pulse comprises two parts. Both still travel with $\mathbf{p}_{\perp}$ in the perpendicular direction but with $\pm\hbar\mathbf{k}_l$ parallel to the laser. Thus, taking the trajectory of the incident state as a reference axis, say x-axis, rather than the laser beam, the latter is slightly tilted in the, say, x-y-plane. Keeping the momentum component p_x constant, the Bragg pulse couples now the momentum components $p_y = 0$ and $p_y = G$. In this setup, the atoms enter a laser beam which is slightly tilted to the normal plane of the incident motion (see figure 6.7).

As an additional remark, note that laser phases ζ which we have written explicitly in the last section are now included in the amplitudes of the superposition (6.25).

6.2.2 Formulation in terms of density matrices and Wigner functions

Right before the application of the beam splitter at $t_1^- = t_1 - \tau/2$, we assume a state that has only been subject to classical transport since its release from the trap at $t = t_0$. The corresponding density matrix thus reads

$$\hat{\rho}(t_1^-) = \hat{U}(t_{01})\, \hat{\rho}_0\, \hat{U}^\dagger(t_{01}). \tag{6.26}$$

The Hilbert space operator that corresponds to classical transport is simply $\hat{U}(t) = \exp(-i\hat{H}_{\mathrm{ct}} t/\hbar)$ where the Hamiltonian $\hat{H}_{\mathrm{ct}}$ is either quadratic or possesses small higher-than-quadratic contributions. With this incident state, applying the operator (6.25), the output state right after the beam splitter becomes

$$\begin{aligned}\hat{\rho}(t_1^+) &= \hat{U}\, \hat{\rho}(t_1^-)\, \hat{U}^\dagger \\ &= \sum_{\ell,\ell'=-\infty}^{\infty} \alpha_\ell \alpha_{\ell'}^*\, \hat{K}_\ell\, \hat{U}(t_{01})\, \hat{\rho}_0\, \hat{U}^\dagger(t_{01}) \hat{K}_{\ell'}^\dagger.\end{aligned} \tag{6.27}$$

Obviously, the input state $\hat{\rho}(t_1^-)$ is mapped onto a sum of copies of itself which are “sandwiched” by kick operators

$$\hat{K}_\ell = e^{i\ell \mathbf{G}\hat{\mathbf{x}}} \tag{6.28}$$

and weighted with an amplitude product $\alpha_\ell \alpha_{\ell'}^*$.

The physical content of these expressions is revealed nicely by translating it into phase space distributions. Therefore, in contrast to the foundations chapters 2 and 3, we use Wigner functions in terms of position and velocity rather than position and momentum. This saves us from explicitly writing factors $1/M$ in many places. The Wigner function in terms of position and velocity is calculated from the density matrix as

$$f(\mathbf{x}, \mathbf{v}, t) = \left(\frac{M}{2\pi\hbar}\right)^3 \int \mathrm{d}^3\xi\, e^{-i\frac{M}{\hbar}\xi\mathbf{v}} \left\langle \mathbf{x} + \tfrac{\xi}{2} \middle| \hat{\rho}(t) \middle| \mathbf{x} + \tfrac{\xi}{2} \right\rangle. \tag{6.29}$$

The great advantage of using Wigner functions instead of wave functions and density matrices is the greatly simplified formulation of classical transport that comes along. As we have seen above in section 3.2.2, it is expressed by a coordinate transformation in phase space. For instance, this allows us to write the Wigner function right before the application of the beam splitter as

$$f\left(\mathbf{z}, t_1^-\right) = f_0\left(\hat{\mathscr{U}}^{-1}(t_{01})\, \mathbf{z}\right) \tag{6.30}$$

combining position and velocity into a phase space coordinate $\mathbf{z} = (\mathbf{x}, \mathbf{v})^\mathsf{T}$. Now, for finding the phase space distribution that corresponds to the density matrix after the beam splitter $\hat{\rho}(t_1^+)$, we can translate the rhs of equation (6.27) according to expression (6.29) term by term. From the auxiliary relation

$$\left(\frac{M}{2\pi\hbar}\right)^3 \int \mathrm{d}^3\xi\; e^{-i\frac{M}{\hbar}\xi\mathbf{v}} \left\langle \mathbf{x}+\tfrac{\xi}{2} \middle| e^{i\ell\mathbf{G}\hat{\mathbf{x}}}\,\hat{\rho}(t_1^-)\,e^{-i\ell'\mathbf{G}\hat{\mathbf{x}}} \middle| \mathbf{x}+\tfrac{\xi}{2} \right\rangle \\ = e^{i(\ell-\ell')\mathbf{G}\mathbf{x}}\, f\left(\mathbf{x},\, \mathbf{v}-\tfrac{\ell+\ell'}{2}\mathbf{v}_G,\, t_1^-\right), \quad (6.31)$$

one can already see that the resulting Wigner function after the beam splitter is a sum of several contributions,

$$f(\mathbf{z},t_1^+) = \sum_\ell f_{\ell\ell}(\mathbf{z},t_1^+) + \sum_{\ell<\ell'} f_{\ell\ell'}(\mathbf{z},t_1^+), \qquad (6.32)$$

divided into diagonal ($\ell=\ell'$) and non-diagonal terms ($\ell\neq\ell'$). The *kick velocity* $\mathbf{v}_G=\hbar\mathbf{G}/M$ which results from atom-laser interaction is also called *two-photon recoil velocity* in the literature. The first term on the right-hand side of equation (6.32) contains contributions of the form

$$f_{\ell\ell}(\mathbf{x},\mathbf{v},t_1^+) = |\alpha_\ell|^2 f\left(\mathbf{x},\, \mathbf{v}-\ell\mathbf{v}_G,\, t_1^-\right). \qquad (6.33)$$

They are copies of the original distribution displaced by integer multiples of the kick velocity $\mathbf{v}_G$. Terms of the form (6.33) will be also called 'classical' because they carry no information about phase coherence between different scattering orders. In contrast, the off-diagonal terms with $\ell\neq\ell'$ are given by

$$f_{\ell\ell'}(\mathbf{x},\mathbf{v},t_1^+) = 2\mathfrak{Re}\left[\alpha_\ell\alpha_{\ell'}^*\, e^{i(\ell-\ell')\mathbf{G}\mathbf{x}}\right] f_0\left(\mathbf{x},\, \mathbf{v}-\tfrac{\ell+\ell'}{2}\mathbf{v}_G,\, t_1^-\right). \qquad (6.34)$$

These contributions are also copies of the input distribution which sit half-way between the classical terms. However, they are modulated by a factor which oscillates parallel to the lattice vector **G** in position space. Its frequency is proportional to the separation of the corresponding classical parts $f_{\ell\ell}$ and $f_{\ell'\ell'}$ in velocity space. Extracting the phases of the amplitudes as

$$\alpha_\ell\alpha_{\ell'}^* = |\alpha_\ell|\,|\alpha_{\ell'}|\,e^{i\zeta_{\ell\ell'}}, \qquad (6.35)$$

we can rewrite the interference term as

$$f_{\ell\ell'}(\mathbf{x},\mathbf{v},t_1^+) = 2|\alpha_\ell|\,|\alpha_{\ell'}|\,\cos\left[\varphi_{\ell\ell'}(\mathbf{x},t_1^+)\right] f_0\left(\mathbf{x},\, \mathbf{v}-\tfrac{\ell+\ell'}{2}\mathbf{v}_G,\, t_1^-\right), \qquad (6.34')$$

identifying the oscillation phase

$$\varphi_{\ell\ell'}(\mathbf{x},t_1^+) = (\ell-\ell')\mathbf{G}\mathbf{x} + \zeta_{\ell\ell'}. \qquad (6.36)$$

The time argument to $\varphi_{\ell\ell'}$ already indicates that the oscillatory pattern will not remain fixed during subsequent classical transport. We discuss its evolution below. An example of a beam splitter producing two direct contributions and their interference term is drawn in figure 6.8.

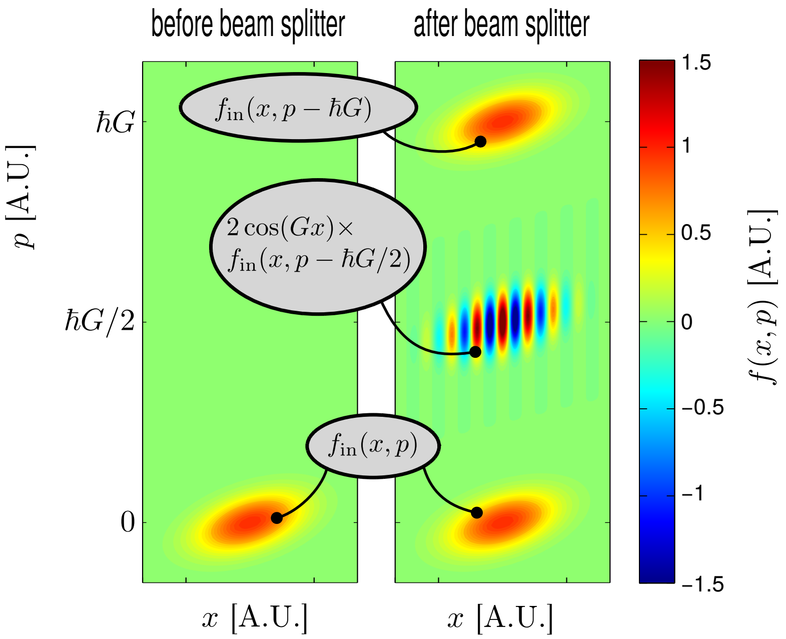

Figure 6.8.: Example of a Wigner function after a beam splitter with two orders $\ell = 0, 1$ an equal amplitudes $\alpha_\ell = \alpha_{\ell'}$.

The interference vector

Aiming for a formulation exclusively in terms of phase space coordinates $\mathbf{z}$, we express the scalar product $\mathbf{Gx}$ in three-dimensional position space as a scalar product $\mathbf{Q}_0\mathbf{z}$ in six-dimensional phase space, defining

$$\mathbf{Q}_0 = \begin{pmatrix} \mathbf{G} \\ \mathbf{0} \end{pmatrix}. \tag{6.37}$$

This way, the vector $\mathbf{Q}_0$ characterizes the oscillatory pattern in phase space that describes the interference between the classical parts. We therefore call it the initial *interference vector*. Thus, the oscillation phase can be written as

$$\varphi_{\ell\ell'}(\mathbf{z}, t_1^+) = (\ell - \ell')\,\mathbf{Q}_0\mathbf{z} + \zeta_{\ell\ell'}. \tag{6.36'}$$

Classical transport after the beam splitter

Exiting the beam splitter, we let the complete state follow classical transport. Thus, for a time interval $t_{12} = t_2 - t_1$ after the beam splitter, the density matrix becomes

$$\begin{aligned}\hat\rho(t_2) &= \hat U(t_{01})\,\hat\rho(t_1^+)\,\hat U^\dagger(t_{01}) \\ &= \sum_{\ell\ell'} \alpha_\ell\alpha_{\ell'}^*\,\hat U(t_{12})\,e^{i\mathbf{G}\hat{\mathbf{x}}}\,\hat U(t_{01})\,\hat\rho_0\,\hat U^\dagger(t_{01})\,e^{-i\mathbf{G}\hat{\mathbf{x}}}\,\hat U^\dagger(t_{12}).\end{aligned} \tag{6.38}$$

Each part that is produced by the beam splitter evolves differently after its application at t_1. Once again, this becomes quite obvious by switching to the corresponding phase space formulation. The Wigner function that had emanated from the output of the beam splitter at t_1^+ and has followed classical transport thereafter until t_2 reads

$$f(\mathbf{z}, t_2) = \sum_{\ell} f_{\ell\ell}(\mathbf{z}, t_2) + \sum_{\ell<\ell'} f_{\ell\ell'}(\mathbf{z}, t_2). \tag{6.39}$$

We can express the evolved distribution $f(\mathbf{z}, t_2)$ in terms of the initial one $f_0(\mathbf{z})$ simply by applying phase space coordinate transformations. On one hand, as elaborated, the transformations corresponding to classical transport are given by the phase space propagators $\hat{\mathscr{U}}(t)$. On the other, the laser pulses instantaneously add multiples of the kick velocity $\mathbf{v}_G$ to the distributions' coordinates. We denote these by a discrete map $\hat{\mathscr{K}}_G$, such that

$$\hat{\mathscr{K}}_\ell\, \mathbf{z} = \begin{pmatrix} \mathbf{x} \\ \mathbf{v} + \ell \mathbf{v}_G \end{pmatrix}, \qquad\qquad \hat{\mathscr{K}}_\ell^{-1}\, \mathbf{z} = \begin{pmatrix} \mathbf{x} \\ \ell\mathbf{v} - \mathbf{v}_G \end{pmatrix}. \tag{6.40}$$

Consequently, the classical terms of expression (6.39) can be written explicitly as

$$\begin{aligned} f_{\ell\ell}(\mathbf{z}, t_2) &= f_{\ell\ell}\left(\hat{\mathscr{U}}^{-1}(t_{12})\,\mathbf{z},\ t_1^+\right) \\ &= |\alpha_\ell|^2\, f_0\Big(\hat{\mathscr{U}}^{-1}(t_{01})\,\hat{\mathscr{K}}_\ell^{-1}\,\hat{\mathscr{U}}^{-1}(t_{12})\,\mathbf{z}\Big), \end{aligned} \tag{6.41a}$$

while the interference terms are

$$\begin{aligned} f_{\ell\ell'}(\mathbf{z}, t_2) &= f_{\ell\ell'}\left(\hat{\mathscr{U}}^{-1}(t_{12})\,\mathbf{z},\ t_1^+\right) \\ &= 2|\alpha_\ell|\,|\alpha_{\ell'}|\ \cos\Big[\varphi_{\ell\ell'}\Big(\hat{\mathscr{U}}^{-1}(t_{12})\,\mathbf{z},\ t_1^+\Big)\Big]\, f_0\left(\hat{\mathscr{U}}^{-1}(t_{01})\,\hat{\mathscr{K}}_{\frac{\ell+\ell'}{2}}^{-1}\,\hat{\mathscr{U}}^{-1}(t_{12})\,\mathbf{z}\right). \end{aligned} \tag{6.41b}$$

The notational and conceptual convenience of the Wigner function formulation in this context is obvious. We can express all contributions to the final distribution in terms of the same function, i.e. the initial distribution f_0. Each of these contributions is thus uniquely described by a phase space coordinate transformation that is composed of classical transport $\hat{\mathscr{U}}$ and discrete kicks $\hat{\mathscr{K}}$. In addition, the phases of the interference term oscillations evolve according to

$$\varphi_{\ell\ell'}(\mathbf{z}, t_2) = \varphi_{\ell\ell'}\Big(\hat{\mathscr{U}}^{-1}(t_{12})\,\mathbf{z},\ t_1^+\Big) = (\ell - \ell')\mathbf{Q}_0\,\hat{\mathscr{U}}^{-1}(t_{12})\,\mathbf{z} + \zeta_{\ell\ell'}. \tag{6.42}$$

This way, classical transport does not only change position and shape of the distributions' envelope but it also modifies the oscillatory patterns in phase space. Here and in the following, we call all functions, that emanate from the initial distribution f_0 via coordinate transformation, *envelopes*. They are assumed to vary on a much shorter length scale the oscillations of the interference terms.

Special case: quadratic Hamiltonians

Assuming classical transport to be ruled by quadratic Hamiltonians allows for a more concrete and illustrative formulation of the above results. As shown in section 2.3, phase space evolution that is produced by these potentials can be described by affine transformations. Consequently, during classical transport the WIGNER function evolves as

$$f(\mathbf{z}, t_j) = f\Big(\mathsf{U}^{-1}(t_{ij})\,(\mathbf{z} - \overline{\mathbf{z}}(t_{ij})),\ t_i\Big), \tag{2.68}$$

where we have denoted the propagation matrix as U and the time-dependent offset as $\overline{\mathbf{z}}$. This way, according to expressions (6.41a) and (6.41b), the contributions to the final distribution function $f(\mathbf{z}, t_2)$ are written

$$f_{\ell\ell}(\mathbf{z}, t_2) = |\alpha_\ell|^2\, f_0\left(\hat{\mathscr{U}}^{-1}(t_{02})\,\mathbf{z} - \ell\,\mathsf{U}^{-1}(t_{12})\,\mathbf{z}_G\right), \tag{6.43a}$$

$$f_{\ell\ell'}(\mathbf{z}, t_2) = 2|\alpha_\ell|\,|\alpha_{\ell'}|\,\cos\Big[\varphi_{\ell\ell'}(\mathbf{z}, t_2)\Big]\, f_0\left(\hat{\mathscr{U}}^{-1}(t_{02})\,\mathbf{z} - \tfrac{\ell+\ell'}{2}\mathsf{U}^{-1}(t_{12})\,\mathbf{z}_G\right). \tag{6.43b}$$

Obviously, since $\hat{\mathscr{U}}^{-1}(t_{02})\,\mathbf{z}$ describes the evolution without the presence of the laser pulse, the restriction to quadratic potentials enables us explicitly isolate the influence of the beam splitter on the motion of the distribution functions in phase space. These are given by the terms proportional to $\mathbf{v}_G$ in the arguments of f_0 in equations (6.43a) and (6.43b).

Concerning the oscillation phase $\varphi_{\ell\ell'}$, in quadratic potentials we can write

$$\varphi_{\ell\ell'}(\mathbf{z}, t_2) = (\ell - \ell')\mathbf{Q}_0^{\mathsf{T}}\left(\mathsf{U}^{-1}(t_{12})\,\mathbf{z} - \overline{\mathbf{z}}(t_{12})\right) + \zeta_{\ell\ell'}. \tag{6.44}$$

In this picture, we have a constant interference vector $\mathbf{Q}_0$ and transformed phase space coordinates $\mathbf{z}$. Equivalently, the evolution of $\varphi_{\ell\ell'}$ can be described by a time-dependent interference vector and constant coordinates, writing

$$\varphi_{\ell\ell'}(\mathbf{z}, t_2) = (\ell - \ell')\mathbf{Q}(t_{12})\,\mathbf{z} - \overline{\varphi}_{\ell\ell'}(t), \tag{6.45}$$

This way, the frequency and orientation of the oscillatory pattern are described by the time-dependent interference vector

$$\mathbf{Q}(t_{12}) = \begin{pmatrix} \mathbf{q}_x(t) \\ \mathbf{q}_v(t) \end{pmatrix} = \mathsf{U}^{-1\mathsf{T}}(t_{12})\,\mathbf{Q}_0, \tag{6.46}$$

and a time-dependent phase offset

$$\overline{\varphi}_{\ell\ell'}(t) = -(\ell - \ell')\,\mathbf{Q}_0\,\overline{\mathbf{z}}(t) + \zeta_{\ell\ell'}. \tag{6.47}$$

Since all coordinate transformations are affine transformations, the oscillation phases $\varphi_{\ell\ell'}$ remain linear function of the phase space coordinate. Directly after the beam splitter, it lies completely in the position subspace, i.e its projection along all velocity axes is zero, $\mathbf{Q}_0 = (\mathbf{q}_{x0}, \mathbf{0})^\mathsf{T} = (\mathbf{G}, \mathbf{0})^\mathsf{T}$. This means the oscillation of the laser field with wave vector $\mathbf{G}$ is directly imprinted on the position density profile. As time progresses, however, the interference vector evolves in phase space such that its velocity components become non-zero, $\mathbf{Q}_0 \to \mathbf{Q}(t) = (\mathbf{q}_x(t), \mathbf{q}_v(t))^\mathsf{T}$. Writing the propagation matrix U as abcd-matrix as in (2.65),

$$\mathsf{U}(t) = \begin{pmatrix} \mathsf{a}(t) & \mathsf{b}(t) \\ \mathsf{c}(t) & \mathsf{d}(t) \end{pmatrix},$$

the evolved interference vector can be expressed as $\mathbf{Q}(t) = (\mathsf{d}(t)\,\mathbf{G},\ -\mathsf{b}(t)\,\mathbf{G})^\mathsf{T}$. In case of free propagation, for example, one has $\mathsf{d} = \mathbb{1}$ and $\mathsf{b}(t) = \mathbb{1}\,t$. This special case of quadratic Hamiltonians is discussed in detail below.

6.2.3 Obtaining the position density

Being interested in the position density $n(\mathbf{x})$, one has to integrate the phase space distribution $f(\mathbf{z})$ over the velocity axes. Since this is a linear operation, expression (6.39) can be integrated term by term so that the resulting density profile may be written as

$$\begin{aligned} n(\mathbf{x}) &= \int \mathrm{d}^3 v\, f(\mathbf{z}) \\ &= \sum_{\ell} n_{\ell\ell}(\mathbf{x}) + \sum_{\ell<\ell'} n_{\ell\ell'}(\mathbf{x}). \end{aligned} \tag{6.48}$$

The contributions from the direct terms, $n_{\ell\ell}(\mathbf{x}) = \int \mathrm{d}^3 v\, f_{\ell\ell}(\mathbf{z})$, are positive everywhere and add up to a classical density profile, i.e. without any signature of interference. The contribution from the interference terms, $n_{\ell\ell'} = \int \mathrm{d}^3 v\, f_{\ell\ell'}$, in contrast, are oscillating between positive and negative values. Of course, the total position density (6.48), which is the sum of all contributions – classical and interference – is positive everywhere and may exhibit signature of interference between individual parts.

Right after the beam splitter, all contributions to the phase space distribution are fragmented along the velocity axes but are located at the same position. In particular, all classical contributions to the density $n_{\ell\ell}$ are identical, being exact copies of the input density. In addition to that, the interference contributions $n_{\ell\ell'}$ bring forth an oscillatory modulation of the envelope, where each term adds an oscillation with frequency $(\ell - \ell')|\mathbf{G}|$. After some evolution time, the several contributions follow different trajectories and separate in position subspace. Consequently, the associated density contributions, at first sitting on top of each other, travel apart as time progresses. Particularly interesting is the behavior of the interference terms in the limit of long evolution time after the beam splitter. Integrating $\tilde{f}_{\ell\ell'}$ over velocity axes, the higher the interference vector component $|\mathbf{q}_v|$, the smaller will be their contribution to the total position density since many oscillations cancel in the integral.

Special case: Gaussians in quadratic potentials

In order to obtain more concrete results, it is quite convenient to consider again Gaussian phase space distributions and assume classical transport to be determined by quadratic Hamiltonians (see 2.3). In this case, the initial distribution is written as

$$f_0(\mathbf{z}) = N \, \frac{e^{-\mathbf{z}^\mathsf{T}\, \mathsf{C}_{z0}^{-1}\, \mathbf{x}}}{\sqrt{\pi^6 \det \mathsf{C}_{z0}}}. \tag{6.49}$$

After propagating in quadratic Hamiltonians, the correlation matrix becomes,

$$\mathsf{C}_{z(t_2)} = \mathsf{U}(t_{02})\, \mathsf{C}_{z0}\, \mathsf{U}^\mathsf{T}(t_{02}).$$

The velocity kicks that are given by the laser pulses do not affect C_z. In addition to the evolving shape, the distribution centers are shifted. These offsets, in contrast to the correlation matrix, invlove influences of the laser kicks and are thus denoted by $\langle \mathbf{z} \rangle_{\ell\ell'}$. Since the initial distribution f_0 is centered at the phase space point $\mathbf{z} = \mathbf{0}$, the time-evolved centers are given by

$$\langle \mathbf{z} \rangle_{\ell\ell'} = \overline{\mathbf{z}}(t_{02}) + \tfrac{\ell+\ell'}{2} \mathbf{z}_G, \tag{6.50}$$

where $\overline{\mathbf{z}}(t_{02})$ is the offset of propagation without the beam splitter. Altogether, the classical contributions to the phase space distribution thus read

$$f_{\ell\ell}(\mathbf{z}) = N \, |\alpha_\ell|^2 \, \frac{e^{-(\mathbf{z}-\langle \mathbf{z} \rangle_{\ell\ell})^\mathsf{T}\, \mathsf{C}_z^{-1}\, (\mathbf{z}-\langle \mathbf{z} \rangle_{\ell\ell})}}{\sqrt{\pi^6 \det \mathsf{C}_z}} \tag{6.51a}$$

and

$$f_{\ell\ell'}(\mathbf{z}) = 2N \, |\alpha_\ell|\, |\alpha_{\ell'}| \, \cos(\varphi_{\ell\ell'}) \, \frac{e^{-(\mathbf{z}-\langle \mathbf{z} \rangle_{\ell\ell'})^\mathsf{T}\, \mathsf{C}_z^{-1}\, (\mathbf{z}-\langle \mathbf{z} \rangle_{\ell\ell'})}}{\sqrt{\pi^6 \det \mathsf{C}_z}}, \tag{6.51b}$$

respectively. Based on these entities that live in six-dimensional phase space, one can deduce the three-dimensional correlation matrix and offset that determine the position density profile. For the sake of notational compactness, we absorb the COM into the position coordinate by defining $\mathbf{X}_{\ell\ell'} = \mathbf{x} - \langle \mathbf{x} \rangle_{\ell\ell'}$. According to equations (2.73) and (2.74), all classical contributions to the density profile after the beam splitter, can then be written as

$$n_{\ell\ell}(\mathbf{x}) = N \, |\alpha_\ell|^2 \, \frac{e^{-\mathbf{X}_{\ell\ell}^\mathsf{T}\, \mathsf{C}_x^{-1}\, \mathbf{X}_{\ell\ell}}}{\sqrt{\pi^D \det \mathsf{C}_x}}. \tag{6.52}$$

The correlation matrix of the position density C_x can be easily derived from the full correlation matrix C_z as shown in section A.2. To this end, we subdivide the inverse phase space correlation matrix as

$$\mathsf{C}_z^{-1} = \begin{pmatrix} \mathsf{A}_{xx} & \mathsf{A}_{xv} \\ \mathsf{A}_{vx} & \mathsf{A}_{vv} \end{pmatrix} \tag{6.53}$$

to arrive at

$$\mathsf{C}_x^{-1} = \mathsf{A}_{xx} - \mathsf{A}_{xv}\,\mathsf{A}_{vv}^{-1}\,\mathsf{A}_{vx}. \tag{6.54}$$

In expression (6.52), the drifting-apart of the several contributions is hidden in the dynamical offsets $\langle \mathbf{x} \rangle_{\ell\ell'}$. Moreover, the oscillating interference contribution to the density can be obtained using relation (A.16). We find

$$n_{\ell\ell'}(\mathbf{x}) = 2N\;|\alpha_\ell|\,|\alpha_{\ell'}|\;\mathscr{C}_{\mathrm{if}}\;\cos\left[\mathbf{k}_{\mathrm{if}}\mathbf{X}_{\ell\ell'} + \zeta_{\ell\ell'}\right]\frac{e^{-\mathbf{x}_{\ell\ell'}^{\mathsf{T}}\,\mathsf{C}_x^{-1}\,\mathbf{x}_{\ell\ell'}}}{\sqrt{\pi^3 \det \mathsf{C}_x}}. \tag{6.55}$$

The last factor on the rhs is the Gaussian envelope of the oscillating interference term. It is similar to the profile of the classical contributions. The first two factors relate to the oscillatory pattern of the interference terms, i.e. the contrast

$$\mathscr{C}_{\mathrm{if}} = \exp\left(-\tfrac{1}{4}\mathbf{q}_v^{\mathsf{T}}\,\mathsf{A}_{vv}\,\mathbf{q}_v\right) \tag{6.56}$$

and the spatial frequency of the interference pattern

$$\mathbf{k}_{\mathrm{if}} = \mathbf{q}_x - \mathsf{A}_{xv}\mathsf{A}_{vv}^{-1}\mathbf{q}_v. \tag{6.57}$$

The former leads to a damping of the amplitude, the latter to decreasing frequency of spatial oscillations, as the velocity component of the interference vector $\mathbf{q}_v$ increases. Both depend on the widths and orientation of the distribution envelope.

Example: Freely propagating Gaussians

The above results can be made more comprehensible by considering free propagation as a special case of classical transport. This assumption is convenient as well as adequate for modeling many simple systems. In particular, for describing the beam splitter, one only needs to consider dynamics along the direction of the laser pulse which is independent of the other directions. We are thus effectively dealing with a one-dimensional problem and thus a two-dimensional phase space. The initial distribution f_0 is a Gaussian with widths σ_x and σ_v along the position axis and the velocity axis, respectively. Both are related to each other by $\sigma_v = \omega\sigma_x$, where ω is the trap frequency defining the initial distribution. Thus, we write

$$f_0(x,v) = \frac{N}{\pi\sigma_{x0}^2\omega}\exp\left(-\frac{x^2+v^2/\omega^2}{\sigma_{x0}^2}\right), \tag{6.58}$$

which implies the initial density to be

$$n_0(x) = \frac{N}{\sqrt{\pi\sigma_{x0}^2}}\exp\left(-\frac{x^2}{\sigma_{x0}^2}\right). \tag{6.59}$$

Before and after the beam splitter, the atom cloud shall be subject to free propagation. Traveling for a total time interval t_{02}, we can, according to prescription (2.83), replace the blocks of the inverse phase space correlation matrix (6.53) as $\mathsf{A}_{xx} \to \sigma_x^{-2}$, $\mathsf{A}_{xv} \to -\sigma_x^{-2}t_{02}$, and $\mathsf{A}_{vv} \to \sigma_v^{-2}+\sigma_x^{-2}t_{02}^2$. In the output of the beam splitter at t_1^+, each classical contribution to the density $n_{\ell\ell}$ moves uniformly with velocity ℓv_G. Consequently, after another interval $t_{12} = t_1 - t_2$ it has traveled a distance $\ell v_G t_{12}$ off the origin. Altogether, we write

$$n_\ell(x,t_2) = \frac{N}{\sqrt{\pi\sigma_x^2(t)}}\exp\left[-\frac{(x-\ell v_G t_{12})^2}{\sigma_x^2(t)}\right]. \tag{6.60}$$

Here, the function $\sigma_x(t) = (1+\omega^2t^2)^{1/2}\,\sigma_{x0}$, known from section 2.3.1, describes the spreading of the cloud after release from the trap. The interference contributions $f_{\ell\ell'}$, on the other hand, move with velocity $\frac{\ell+\ell'}{2}v_G$. This means they remain located exactly halfway between their corresponding classical parts, $f_{\ell\ell}$ and $f_{\ell'\ell'}$. Concerning their oscillatory patterns, the components of the interference vector become $\mathbf{q}_x \to G$ and $\mathbf{q}_v \to -Gt_{12}$, and hence

$$n_{\ell\ell'}(x,t_2) = \mathscr{C}_{\mathrm{if}}\cos\Big[(\ell-\ell')k_{\mathrm{if}}\,x\Big]\frac{N}{\sqrt{\pi\sigma_x^2(t)}}\exp\left[-\frac{\left(x-\frac{\ell+\ell'}{2}v_G t_{12}\right)^2}{\sigma_x^2(t)}\right]. \tag{6.61}$$

The contrast is now explicitly given as

$$\mathscr{C}_{\mathrm{if}}(t_{02}) = \exp\left(-\frac{1}{4}\frac{(\sigma_x(\ell-\ell')G)^2(\omega\,t_{12})^2}{1+(\omega t_{02})^2}\right), \tag{6.62}$$

while the spatial frequency of interference fringes reads

$$k_{\mathrm{if}}(t_{02}) = G\,\frac{1+\omega^2t_{01}t_{02}}{1+\omega^2t_{02}^2}. \tag{6.63}$$

In these expressions, the factor ωt_{12} can be seen as a dimensionless measure for the spatial separation of the classical contributions, while $\omega t_{02}/(1+\omega^2t_{02}^2)$ corresponds to the spreading

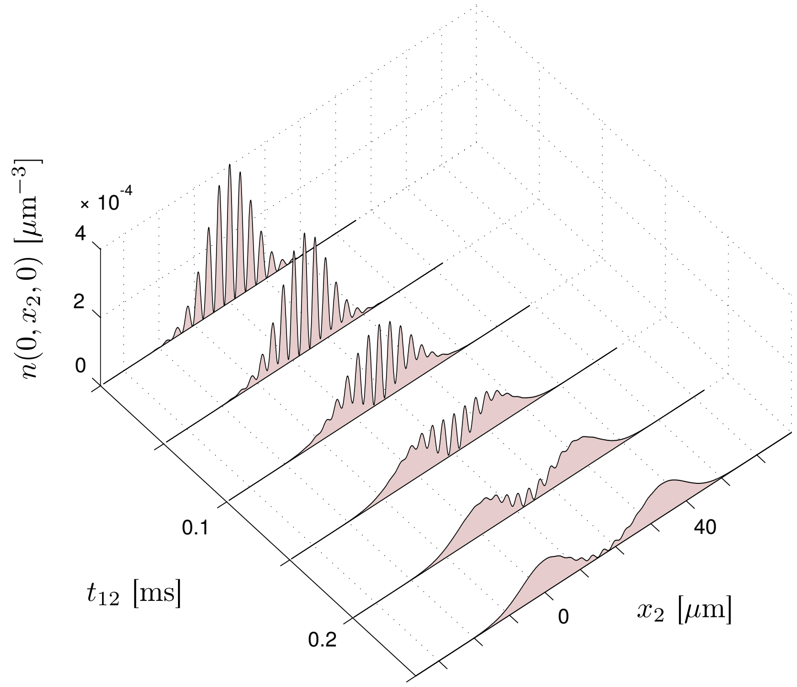

Figure 6.9.: Freely expanding density after beam splitter with scattering orders $\ell, \ell' = 0, 1$. The 3D density is plotted only along the direction of the laser beam, which was chosen to align with the x_2 direction in this case. Relevant parameters are $\omega_2 = 800$ Hz, $M = 1.67 \cdot 10^{-27}$ kg (H-atom), $T = 1$ nK, N=1, $G = 2.094\ \mu\mathrm{m}^{-1}$, $t_{01} = 0.05\ \mu$s.

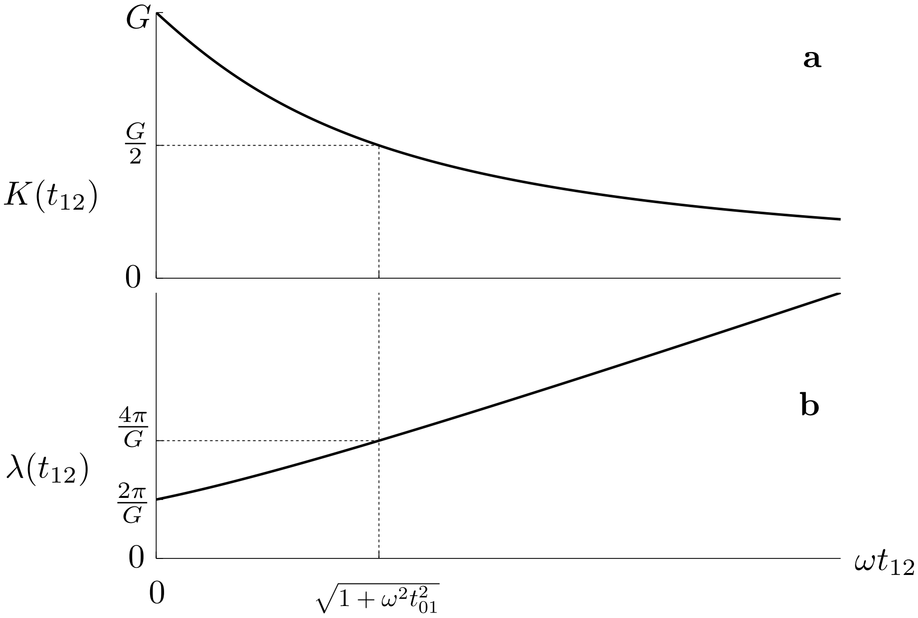

Figure 6.10.: Wave number (**a**) and wave length (**b**) of interference pattern depending on time after the beam splitter, t_{12}, according to equations (6.63) and (6.64), respectively. The first one is doubled (the latter on is halved) at $t_{12} = \omega^{-1}\sqrt{1 + \omega^2 t_{12}^2}$. In this example the time before the beam splitter is given by $\omega t_{01} = 1.2$.

of the Gaussian envelopes. The wave length that is associated with k_{if} is known as *interference fringe spacing* λ_{if}. It is given by the inverse of expression (6.63) multiplied with 2π. In the current case, we obtain

$$\lambda_{\mathrm{if}} = \frac{2\pi}{G}\,\frac{1+\omega^2 t_{01}^2}{1+\omega^2 t_{01} t_{02}}. \tag{6.64}$$

In the asymptotic limit $t_{02} \to \infty$, the fringe spacing grows linearly,

$$\lambda_{\mathrm{if}} \overset{t_{02}\to\infty}{\approx} \frac{2\pi}{G}\,\frac{t_{02}}{t_{01}} = \frac{2\pi\hbar}{M v_G t_{01}} t_{02}. \tag{6.65}$$

An example of a density profile after the beam splitter is displayed in figure 6.9. One can observe that the contrast of the interference fringes decreases with vanishing overlap of the two classical contributions, n_1 and n_2. In addition to the contrast, the wave number of the interference pattern is decreasing as time progresses. Both, wave number and wave length are plotted in figure 6.10.

6.3 Mach-Zehnder interferometer

Having discussed the beam splitter in the last section, we assemble now a complete MACH-ZEHNDER interferometer and describe it in phase space. The sequence of this setup is as follows.

- $t = t_0$: Release from trap. Initial state is centered at $\mathbf{k} = \mathbf{0}$.
- $t_0 < t < t_1$: Classical transport.
- $t = t_1$: First beam splitter, producing two paths. These are an un-kicked path at $\mathbf{k} = \mathbf{0}$ (path 'a') and a kicked path at $\mathbf{k} = \mathbf{G}$ (path 'b').
- $t_1 < t < t_2$: Classical transport. The two paths separate in position space.
- $t = t_2$: π-pulse. Now, path 'a' is kicked to $\mathbf{k} = \mathbf{G}$ while path $'b$' is kicked back to $\mathbf{k} = \mathbf{0}$ again. Loosely speaking, the two paths are swapped in k-space.
- $t_2 < t < t_3$: Classical transport. The two paths are closing in again in position space.
- $t = t_3$: Second beam splitter. The two paths are split another time, producing two output ports which are centered at $\mathbf{k} = \mathbf{0}$ and $\mathbf{k} = \mathbf{G}$ in phase space. Each of the ports is a recombination of the paths 'a' and 'b', potentially exhibiting interference effects.
- $t_2 < t < t_3$: Classical transport. The two output ports separate in position space.
- $t = t_4$: Detection.

The sequence is visualized in figure 6.11.

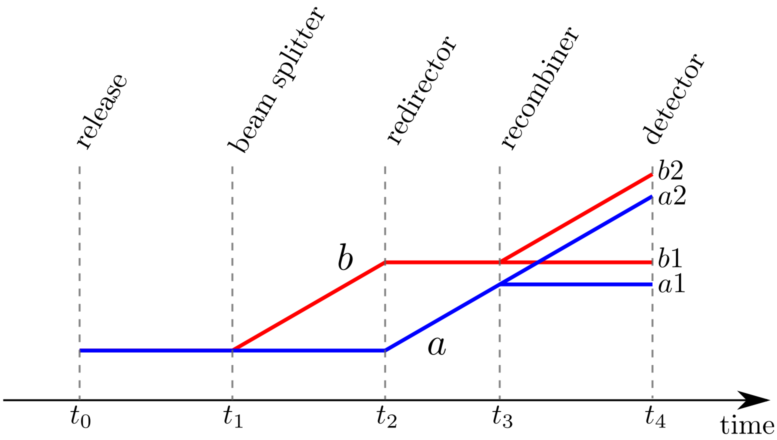

Figure 6.11.: Sketch of MACH-ZEHNDER interferometer indicating time instances of laser pulse application and path labeling.

6.3.1 Model for interferometer elements

For conveniently expressing the MZI elements as a propagation of states, we formulate two model operators. First, for the two beam splitter pulses, we write

$$\hat{U}_{\text{bs}} = \left(\alpha + \beta\, e^{i\mathbf{Gx}}\right)\hat{P}_0 + \left(\alpha - \beta^*\, e^{-i\mathbf{Gx}}\right)\hat{P}_G. \tag{6.66}$$

In comparison to the more general beam splitter model of the last section (6.25), the operator (6.66) is defined explicitly for un-kicked and singly kicked input states, i.e. centered at $\mathbf{k} = \mathbf{0}$ and $\mathbf{k} = \mathbf{G}$, respectively. It produces a superposition of an un-kicked and a “positively kicked” copy of the former, and an un-kicked and “negatively kicked” copy of the latter. Since we consider only two scattering orders, we distinguish their amplitudes by different letters α, β, rather than by indices. Moreover, we use now amplitude indices to denote to which of the three laser pulses a particular amplitudes relates. In addition to beam splitters, the MZI scheme comprises a laser pulse that leaves the total number of paths constant swaps the two paths in k-space. Referring to the nomenclature of the BRAGG regime, we call

$$\hat{U}_{\pi} = i\hat{K}_1\hat{P}_0 + i\hat{K}_1^{-1}\hat{P}_G \tag{6.67}$$

the operator of a π-pulse. It can be realized, for example, by using a BRAGG-pulse with interaction parameter $\vartheta = \pi$.

One might object that the operator (6.67) is merely a special case of (6.66). So for $\hat{U}_{\text{bs}}$ to be a genuine beam splitter, we may demand $\alpha, \beta \neq 0$. On the other hand, we do not necessarily require the condition $|\alpha + \beta|^2 = 1$ to be satisfied. Consider for example a beam splitter pulse in the KAPITZA-DIRAC regime, where only two scattering orders are used and the others are masked, as already discussed in section 6.2.1. Losing population to unobserved orders clearly implies $|\alpha + \beta|^2 < 1$.

6.3.2 Wave function formulation

Before coming to the phase space description of the atom cloud, we give an expression for a wave function passing the MZI. We denote the initial state that is released from the preparing trap at t_0 as $|\psi_0\rangle$. Retracing the several steps of the MZI that were outlined in the beginning of this section, we use propagators of classical transport $\hat{\mathscr{U}}(t)$, as well as the laser pulse operators, $\hat{U}_{\text{bs}}$ and $\hat{U}_\pi$, defined above. With these, the final wave function becomes

$$\begin{aligned} |\psi(t_4)\rangle &= \hat{U}(t_{34})\,\hat{U}_{\text{bs}}\,\hat{U}(t_{23})\,\hat{U}_\pi\,\hat{U}(t_{12})\,\hat{U}_{\text{bs}}\,\hat{U}(t_{01})\;|\psi_0\rangle \\ &= |\psi_{a1}\rangle + |\psi_{b1}\rangle + |\psi_{a2}\rangle + |\psi_{b2}\rangle\,. \end{aligned} \tag{6.68}$$

It can be written as the sum of four parts. They relate to the different paths of the scheme as indicated in figure 6.11. Each of which can be expressed in terms of an associated composite propagator and amplitude

$$|\psi_\ell\rangle = \gamma_\ell\,\hat{U}_\ell\,|\psi_0\rangle\,, \qquad \ell \in \{a1, b1, a2, b2\}, \tag{6.69}$$

where the complex coefficients γ_ℓ are products of three amplitudes, relating to the laser pulses in the MZI scheme:

$$\gamma_{a1} = -\alpha_1\beta_2\beta_3^*, \qquad \gamma_{b1} = -\beta_1\beta_2^*\alpha_3, \qquad \gamma_{a1} = +\alpha_1\beta_2\alpha_3, \qquad \gamma_{b1} = -\beta_1\beta_2^*\beta_3. \tag{6.70}$$

Furthermore, the propagators, that connect the individual parts to the initial state, are

$$\begin{aligned} \hat{U}_{a1} &= \hat{U}(t_{34})\,e^{-i\mathbf{G}\hat{\mathbf{x}}}\,\hat{U}(t_{23})\,e^{+i\mathbf{G}\hat{\mathbf{x}}}\,\hat{U}(t_{02}), \\ \hat{U}_{b1} &= \hat{U}(t_{24})\,e^{-i\mathbf{G}\hat{\mathbf{x}}}\,\hat{U}(t_{12})\,e^{+i\mathbf{G}\hat{\mathbf{x}}}\,\hat{U}(t_{01}), \\ \hat{U}_{a2} &= \hat{U}(t_{24})\,e^{+i\mathbf{G}\hat{\mathbf{x}}}\,\hat{U}(t_{02}), \\ \hat{U}_{b2} &= \hat{U}(t_{34})\,e^{i\mathbf{G}\hat{\mathbf{x}}}\,\hat{U}(t_{23})\,e^{-i\mathbf{G}\hat{\mathbf{x}}}\,\hat{U}(t_{12})\,e^{+i\mathbf{G}\hat{\mathbf{x}}}\,\hat{U}(t_{01}). \end{aligned} \tag{6.71a}$$

The composition of these can be easily understood by retracing the individual paths in figure 6.11. One can read from these expressions that all contributions to the first output port end up in momentum states centered at $\mathbf{k} = \mathbf{0}$, while those in the second output port end up in a kicked momentum state at $\mathbf{k} = \mathbf{G}$.

A popular special case of the above description involves symmetric beam splitters. Since they are, in case of BRAGG-pulses, realized by an interaction parameter of $\vartheta = \pi/2$ (see e.g. expression (6.24)), symmetric beam splitter pulses are generally termed $\pi/2$-pulses. Consequently, the coefficients of the laser-induced kicks are

$$\alpha_1 = \tfrac{1}{\sqrt{2}}, \quad \beta_1 = \tfrac{1}{\sqrt{2}}e^{i\zeta_1}, \quad \beta_2 = e^{i\zeta_2}, \quad \alpha_3 = \tfrac{1}{\sqrt{2}}, \quad \beta_3 = \tfrac{1}{\sqrt{2}}e^{i\zeta_3}. \tag{6.72}$$

Note that we have allowed each laser pulse to have a different phase offset ζ_i which reoccurs in the phase of the amplitudes. The composite coefficients of the final wave function are easily found to be

$$\gamma_{a1} = -\tfrac{1}{2}e^{i(\zeta_2-\zeta_3)}, \quad \gamma_{b1} = -\tfrac{1}{2}e^{i(\zeta_1-\zeta_2)}, \quad \gamma_{a2} = +\tfrac{1}{2}e^{i\zeta_2}, \quad \gamma_{b2} = -\tfrac{1}{2}e^{i(\zeta_1-\zeta_2+\zeta_3)}, \tag{6.73}$$

6.3.3 Phase space formulation

We now translate the wave function expressions into a phase space formulation in terms of WIGNER functions. For calculating $f(\mathbf{z}, t_4)$ we have to first find the final density matrix. Assuming the initial state to be described by $\hat{\rho}_0$, the evolved state that arrives at the detector is written

$$\hat{\rho}(t_4) = \sum_{\ell,\ell' \in \{a1,b1,a2,b2\}} \gamma_\ell \gamma_{\ell'}^* \, \hat{U}_\ell \, \hat{\rho}_0 \, \hat{U}_{\ell'}^\dagger, \tag{6.74}$$

utilizing the four composite propagators $\hat{U}_{a1}$, $\hat{U}_{b1}$, $\hat{U}_{a2}$, and $\hat{U}_{b2}$, we have defined in (6.71). The double-summation in equation (6.74) comprises 16 terms in total. The final WIGNER function can again be divided into a sum of several contributions,

$$f(\mathbf{z}, t_4) = \sum_\ell f_\ell(\mathbf{z}, t_4) + \sum_{\ell<\ell'} f_{\ell\ell'}(\mathbf{z}, t_4), \tag{6.75}$$

akin to expression (6.32) in section 6.2.1. Like before, the first term on the rhs is a sum over the classical contributions. They are given by

$$\begin{aligned} f_{\ell\ell}(\mathbf{z}, t_4) &= |\gamma_\ell|^2 \left(\tfrac{M}{2\pi\hbar}\right)^3 \int \mathrm{d}^3\xi \; e^{-i\frac{M}{\hbar}\xi\mathbf{x}} \left\langle \mathbf{x} + \tfrac{\xi}{2} \middle| \hat{U}_\ell \, \hat{\rho}_0 \, \hat{U}_\ell^\dagger \middle| \mathbf{x} - \tfrac{\xi}{2} \right\rangle \\ &= |\gamma_\ell|^2 \, f_0\left(\hat{\mathscr{U}}_\ell^{-1} \mathbf{z}\right). \end{aligned} \tag{6.76}$$

Similar to the final wave function that is connected to $|\psi_0\rangle$ via a HILBERT-space operator $\hat{U}_\ell$, the final WIGNER function is given as the initial contribution that has been coordinate-transformed. The transformations describing the classical parts are

$$\hat{\mathscr{U}}_{a1} = \hat{\mathscr{U}}(t_{34}) \, \hat{\mathscr{K}}_{-G} \, \hat{\mathscr{U}}(t_{23}) \, \hat{\mathscr{K}}_G \, \hat{\mathscr{U}}(t_{02}), \tag{6.77a}$$

$$\hat{\mathscr{U}}_{b1} = \hat{\mathscr{U}}(t_{24}) \, \hat{\mathscr{K}}_{-G} \, \hat{\mathscr{U}}(t_{12}) \, \hat{\mathscr{K}}_G \, \hat{\mathscr{U}}(t_{01}), \tag{6.77b}$$

$$\hat{\mathscr{U}}_{a2} = \hat{\mathscr{U}}(t_{24}) \, \hat{\mathscr{K}}_G \, \hat{\mathscr{U}}(t_{02}), \tag{6.77c}$$

$$\hat{\mathscr{U}}_{b2} = \hat{\mathscr{U}}(t_{34}) \, \hat{\mathscr{K}}_G \, \hat{\mathscr{U}}(t_{23}) \, \hat{\mathscr{K}}_{-G} \, \hat{\mathscr{U}}(t_{12}) \, \hat{\mathscr{K}}_G \, \hat{\mathscr{U}}(t_{01}). \tag{6.77d}$$

They show formal resemblance the operators defined in (6.71). The transformations that describe the velocity kicks $\hat{\mathscr{K}}_{\pm G}$ were defined in (6.40). Concerning the second term of the rhs of (6.75), the summation prescription $\ell < \ell'$ may seem absurd for indices ℓ, ℓ' running over path labels, '$a1$', '$b1$', '$a2$', '$b2$', rather than numbers. We use it, nevertheless, as shorthand indication that each combination of different paths appears only once, regardless of index ordering. This means, the interference contributions to the total WIGNER function are defined as

$$f_{\ell\ell'}(\mathbf{z}, t_4) = (\mathfrak{Re}\, \gamma_\ell \gamma_{\ell'}^*) \left(\tfrac{M}{2\pi\hbar}\right)^3 \int \mathrm{d}^3\xi \; e^{-i\frac{M}{\hbar}\xi\mathbf{x}} \left\langle \mathbf{x} + \tfrac{\xi}{2} \middle| \left(\hat{U}_\ell \, \hat{\rho}_0 \, \hat{U}_{\ell'}^\dagger + \text{h.c.}\right) \middle| \mathbf{x} - \tfrac{\xi}{2} \right\rangle. \tag{6.78}$$

Directly combining the Wigner function parts that relate to $\hat{U}_\ell\,\hat{\rho}\,\hat{U}^\dagger_{\ell'}$ and $\hat{U}_{\ell'}\,\hat{\rho}\,\hat{U}^\dagger_{\ell}$ into a one term, yields a single real-valued distribution that describes the interference between the paths ℓ and ℓ'. The fact that $f_{\ell\ell'}$ is a real function is made more obvious by separating the phase from the amplitudes as

$$\gamma_j = |\gamma_j| e^{i\zeta_j}.$$

With this, the interference contributions in terms of the initial distribution read

$$f_{\ell\ell'}(\mathbf{z}, t_4) = 2|\gamma_\ell|\,|\gamma_{\ell'}|\,\cos(\varphi_{\ell\ell'})\, f_0\left(\hat{\mathscr{U}}^{-1}_{\ell\ell'}\,\mathbf{z}\right). \tag{6.79}$$

The involved phase space coordinate transformations are

$$\hat{\mathscr{U}}_{a1b1} = \hat{\mathscr{U}}(t_{34})\,\hat{\mathscr{K}}_{-G/2}\,\hat{\mathscr{U}}(t_{13})\,\hat{\mathscr{K}}_{G/2}\,\hat{\mathscr{U}}(t_{01}), \tag{6.80a}$$
$$\hat{\mathscr{U}}_{a2b2} = \hat{\mathscr{U}}(t_{34})\,\hat{\mathscr{K}}_{G/2}\,\hat{\mathscr{U}}(t_{13})\,\hat{\mathscr{K}}_{G/2}\,\hat{\mathscr{U}}(t_{01}), \tag{6.80b}$$
$$\hat{\mathscr{U}}_{a1a2} = \hat{\mathscr{U}}(t_{34})\,\hat{\mathscr{K}}_{-G/2}\,\hat{\mathscr{U}}(t_{23})\,\hat{\mathscr{K}}_{G}\,\hat{\mathscr{U}}(t_{02}), \tag{6.80c}$$
$$\hat{\mathscr{U}}_{b1b2} = \hat{\mathscr{U}}(t_{34})\,\hat{\mathscr{K}}_{G/2}\,\hat{\mathscr{U}}(t_{23})\,\hat{\mathscr{K}}_{-G}\,\hat{\mathscr{U}}(t_{12})\,\hat{\mathscr{K}}_{G}\,\hat{\mathscr{U}}(t_{01}), \tag{6.80d}$$
$$\hat{\mathscr{U}}_{a1b2} = \hat{\mathscr{U}}(t_{14})\,\hat{\mathscr{K}}_{G/2}\,\hat{\mathscr{U}}(t_{01}), \tag{6.80e}$$
$$\hat{\mathscr{U}}_{a2b1} = \hat{\mathscr{U}}(t_{14})\,\hat{\mathscr{K}}_{G/2}\,\hat{\mathscr{U}}(t_{01}), \tag{6.80f}$$

These give rise to trajectories that run in between the trajectories that are connected to the classical contributions. Moreover, the oscillation of $f_{\ell\ell'}$, a signature of interference between the associated paths, is described by the phases

$$\varphi_{a1b1} = \mathbf{Q}_0\left(\hat{\mathscr{U}}^{-1}(t_{13})\,\hat{\mathscr{K}}^{-1}_{-G/2}\,\hat{\mathscr{U}}^{-1}(t_{34}) - 2\,\hat{\mathscr{U}}^{-1}(t_{23})\,\hat{\mathscr{K}}^{-1}_{-G/2}\,\hat{\mathscr{U}}^{-1}(t_{34}) + \hat{\mathscr{U}}^{-1}(t_{34})\right)\mathbf{z} + \delta\zeta, \tag{6.81a}$$
$$\varphi_{a2b2} = \mathbf{Q}_0\left(\hat{\mathscr{U}}^{-1}(t_{13})\,\hat{\mathscr{K}}^{-1}_{G/2}\,\hat{\mathscr{U}}^{-1}(t_{34}) - 2\,\hat{\mathscr{U}}^{-1}(t_{23})\,\hat{\mathscr{K}}^{-1}_{G/2}\,\hat{\mathscr{U}}^{-1}(t_{34}) + \hat{\mathscr{U}}^{-1}(t_{34})\right)\mathbf{z} + \delta\zeta + \pi, \tag{6.81b}$$
$$\varphi_{a1b2} = \mathbf{Q}_0\left(\hat{\mathscr{U}}^{-1}(t_{14}) - 2\,\hat{\mathscr{U}}^{-1}(t_{24}) + 2\hat{\mathscr{U}}^{-1}(t_{34})\right)\mathbf{z} + \zeta_1 - 2\zeta_2 + 2\zeta_3, \tag{6.81c}$$
$$\varphi_{a2b1} = \mathbf{Q}_0\left(\hat{\mathscr{U}}^{-1}(t_{14}) - 2\,\hat{\mathscr{U}}^{-1}(t_{24})\right)\mathbf{z} + \zeta_1 - 2\zeta_2 + \pi, \tag{6.81d}$$
$$\varphi_{a1a2} = \mathbf{Q}_0\,\hat{\mathscr{U}}^{-1}(t_{34})\,\mathbf{z} + \zeta_3 + \pi, \tag{6.81e}$$
$$\varphi_{a1a2} = \mathbf{Q}_0\,\hat{\mathscr{U}}^{-1}(t_{34})\,\mathbf{z} + \zeta_3, \tag{6.81f}$$

where we have abbreviated $\delta\zeta = \zeta_1 - 2\zeta_2 + \zeta_3$ and the initial interference vector has been defined as $\mathbf{Q}_0 = (\mathbf{G}, \mathbf{0})^\mathsf{T}$. We exemplify the emergence of the phase expressions for the case of $\ell\ell' = a1b1$. The first beam splitter at t_1 kicks path 'b' and leaves path 'a' unaltered, implying a leap of the interference phase about $\mathbf{Q}_0\mathbf{z} + \zeta_1$. Until detection, this $\mathbf{z}$-dependent phase evolves along the trajectories of its associated envelope, described by $\hat{\mathscr{U}}_{a1b1}$. Taking now the propagator (6.80a) between the laser-induced phase leap at t_1 and detection at t_4, leads to the occurrence of the inverse of the composite propagator $\hat{\mathscr{U}}(t_{34})\,\hat{\mathscr{K}}_{-G/2}\,\hat{\mathscr{U}}(t_{13})$ in the first term of the phase

(6.81a). Next, the π-pulse at t_2 kicks both paths with opposite velocities, resulting in a phase leap of $-2(\mathbf{Q}_0\,\mathbf{z}+\zeta_2)$. Subsequent evolution is expressed by the propagator $\hat{\mathscr{U}}(t_{34})\,\hat{\mathscr{K}}_{-G/2}\,\hat{\mathscr{U}}(t_{23})$. Finally, the second beam splitter kicks path 'a' and leaves path 'b' unaltered , giving again a phase leap about $\mathbf{Q}_0\,\mathbf{z}+\zeta_3$. Evolution until detection is described by $\hat{\mathscr{U}}(t_{34})$. Obviously, the final oscillation phase φ_{a1b1} is a sum of all these evolved phase leaps. All other expressions in (6.81) can be made plausible in a similar way.

Distributions of the output ports

The composition of propagators and the interference phase evolution is illustrated for the contributions of output port 1 in figure 6.12. When discussing the final Wigner function in the remainder of this work, most of the time we will not consider the complete final distribution $f(\mathbf{z},t_4)$ but only parts of it that are associated with the two output ports. From all contributions $f_{\ell\ell'}$ that were introduced above, we can assemble the Wigner function of the first output port as

$$f_{11}(\mathbf{z})=|\gamma_{a1}|^2 f_0\left(\hat{\mathscr{U}}_{a1}^{-1}\mathbf{z}\right)+|\gamma_{b1}|^2 f_0\left(\hat{\mathscr{U}}_{b1}^{-1}\mathbf{z}\right)+2|\gamma_{a1}|\,|\gamma_{b1}|\,\cos(\varphi_{a1b1})\,f_0\left(\hat{\mathscr{U}}_{a1b1}^{-1}\mathbf{z}\right). \tag{6.82a}$$

On the other hand, the distribution of the second output port is

$$f_{22}(\mathbf{z})=|\gamma_{a2}|^2 f_0\left(\hat{\mathscr{U}}_{a2}^{-1}\mathbf{z}\right)+|\gamma_{b2}|^2 f_0\left(\hat{\mathscr{U}}_{b2}^{-1}\mathbf{z}\right)+2|\gamma_{a2}|\,|\gamma_{b2}|\,\cos(\varphi_{a2b2})\,f_0\left(\hat{\mathscr{U}}_{a2b2}^{-1}\mathbf{z}\right). \tag{6.82b}$$

The individual shapes of these parts as their relative population exhibit interference effects due to different phase accumulation along the paths 'a' and 'b' between the time instances t_1 and t_3. This will become more apparent below when considering some examples.

The Wigner functions f_1 and f_2 do not comprise all parts of the final distribution. The missing parts relate to the interference between the two ports. They are given by

$$\begin{aligned}f_{12}(\mathbf{z})=2|\gamma_{a1}|\,|\gamma_{a2}|\,\cos(\varphi_{a1a2})\,f_0\left(\hat{\mathscr{U}}_{a1a2}^{-1}\mathbf{z}\right)+2|\gamma_{b1}|\,|\gamma_{b2}|\,\cos(\varphi_{b1b2})\,f_0\left(\hat{\mathscr{U}}_{b1b2}^{-1}\mathbf{z}\right)\\+2|\gamma_{a1}|\,|\gamma_{b2}|\,\cos(\varphi_{a1b2})\,f_0\left(\hat{\mathscr{U}}_{a1b2}^{-1}\mathbf{z}\right)+2|\gamma_{b1}|\,|\gamma_{a2}|\,\cos(\varphi_{b1a2})\,f_0\left(\hat{\mathscr{U}}_{b1a2}^{-1}\mathbf{z}\right).\end{aligned} \tag{6.83}$$

If we assume f_1 and f_2 to be well separated in position space, the interference terms in f_{12} are oscillating in velocity space, approximately with a frequency $\lesssim G t_{34}$. Computing the density profile, for example, these rapidly oscillating contributions cancel during integration over the phase space density. Therefore, we will often neglect f_{12} in the following.

6.3.4 Quadratic Hamiltonians

As was the case in our discussion of a single beam splitter, we gain valuable insight in the above solutions by considering quadratic Hamiltonians. Consequently, we write again

$$\hat{\mathscr{U}}(t)\,\mathbf{z}=\mathsf{U}(t)\,\mathbf{z}+\bar{\mathbf{z}}(t), \tag{6.84}$$

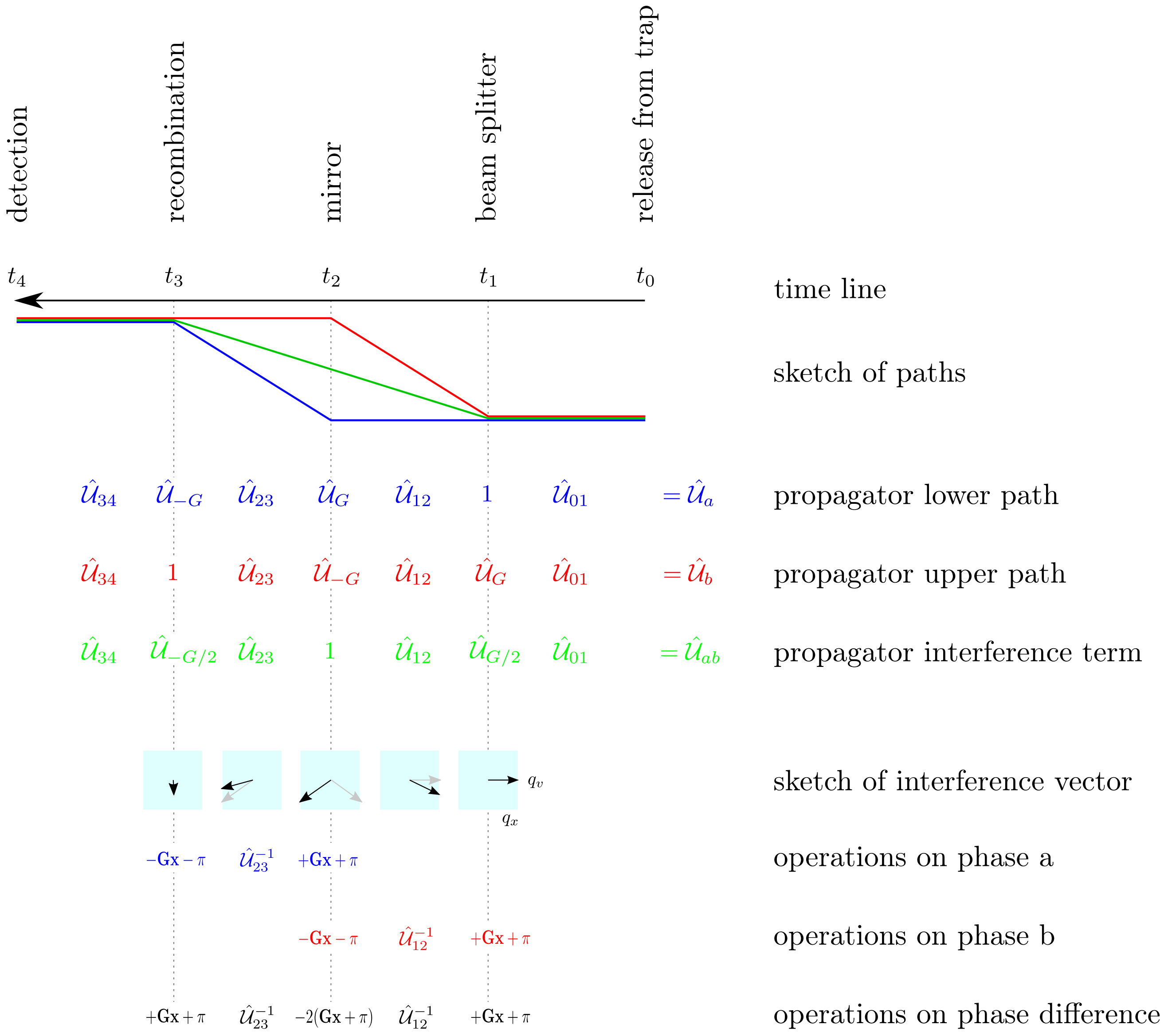
detection
recombination
mirror
beam splitter
release from trap
t_4
t_3
t_2
t_1
t_0
time line
sketch of paths
$\hat{\mathcal{U}}_{34}$ $\hat{\mathcal{U}}_{-G}$ $\hat{\mathcal{U}}_{23}$ $\hat{\mathcal{U}}_{G}$ $\hat{\mathcal{U}}_{12}$ 1 $\hat{\mathcal{U}}_{01}$ $=\hat{\mathcal{U}}_{a}$
propagator lower path
$\hat{\mathcal{U}}_{34}$ 1 $\hat{\mathcal{U}}_{23}$ $\hat{\mathcal{U}}_{-G}$ $\hat{\mathcal{U}}_{12}$ $\hat{\mathcal{U}}_{G}$ $\hat{\mathcal{U}}_{01}$ $=\hat{\mathcal{U}}_{b}$
propagator upper path
$\hat{\mathcal{U}}_{34}$ $\hat{\mathcal{U}}_{-G/2}$ $\hat{\mathcal{U}}_{23}$ 1 $\hat{\mathcal{U}}_{12}$ $\hat{\mathcal{U}}_{G/2}$ $\hat{\mathcal{U}}_{01}$ $=\hat{\mathcal{U}}_{ab}$
propagator interference term
q_v
q_x
sketch of interference vector
$-\mathrm{Gx}-\pi$ $\hat{\mathcal{U}}_{23}^{-1}$ $+\mathrm{Gx}+\pi$
operations on phase a
$-\mathrm{Gx}-\pi$ $\hat{\mathcal{U}}_{12}^{-1}$ $+\mathrm{Gx}+\pi$
operations on phase b
$+\mathrm{Gx}+\pi$ $\hat{\mathcal{U}}_{23}^{-1}$ $-2(\mathrm{Gx}+\pi)$ $\hat{\mathcal{U}}_{12}^{-1}$ $+\mathrm{Gx}+\pi$
operations on phase difference

Figure 6.12.: Illustration of phase space propagators in a MZI. Only paths of the first output port are shown.

where $\mathsf{U}(t)$ is a matrix and $\bar{\mathbf{z}}(t)$ a vector. We first discuss the classical parts, before considering the interference terms in the output ports. This enables us to specify expressions (6.82) for f_1 and f_2 in case of quadratic Hamiltonians. The four interference terms between the two output ports ('$a1a2$', '$b1b2$', '$a1b2$', and '$a2b1$'), subsumed in expression (6.83), are ignored altogether.

General distribution functions

With classical transport being an affine transformation, the propagators $\hat{\mathscr{U}}_\ell$ that determine the classical contributions to the final Wigner function have the form

$$\begin{aligned} \hat{\mathscr{U}}_\ell\, \mathbf{z} &= \mathsf{U}(t_{04})\, \mathbf{z} + \bar{\mathbf{z}}(t_{04}) + \delta \mathbf{z}_\ell \\ &= \hat{\mathscr{U}}_\ell(t_{04})\, \mathbf{z} + \delta \mathbf{z}_\ell . \end{aligned} \tag{6.85}$$

This way, we have isolated the influence of the MZI elements on the evolution ($\delta \mathbf{z}_\ell$) from the classical transport which is independent of MZI elements ($\hat{\mathscr{U}}(t_{04})$). The offsets that emanate from the laser-induced kicks are

$$\delta \mathbf{z}_{a1} = [\mathsf{U}(t_{24}) - \mathsf{U}(t_{34})]\, \mathbf{z}_G, \tag{6.86a}$$

$$\delta \mathbf{z}_{b1} = [\mathsf{U}(t_{14}) - \mathsf{U}(t_{24})]\, \mathbf{z}_G, \tag{6.86b}$$

$$\delta \mathbf{z}_{a2} = \mathsf{U}(t_{24})\, \mathbf{z}_G, \tag{6.86c}$$

$$\delta \mathbf{z}_{b2} = [\mathsf{U}(t_{14}) - \mathsf{U}(t_{24}) + \mathsf{U}(t_{34})]\, \mathbf{z}_G, \tag{6.86d}$$

Consequently, the classical terms can be expressed as

$$f_{\ell\ell}(\mathbf{z}, t_4) = |\gamma_\ell|^2\, f_0\big(\hat{\mathscr{U}}^{-1}(t_{04})\, (\mathbf{z} - \delta \mathbf{z}_\ell)\big). \tag{6.87}$$

This expression reveals nicely, that the laser-induced kicks do not influence the distributions' shapes but only their offsets. Similarly, the envelopes of the interference terms are connected to the initial distribution f_0 via transformations of the form

$$\hat{\mathscr{U}}_{\ell\ell'}\, \mathbf{z} = \hat{\mathscr{U}}(t_{04}) + \delta \mathbf{z}_{\ell\ell'}. \tag{6.88}$$

Here, the MZI-induced offsets $\delta \mathbf{z}_{\ell\ell'}$ are located exactly halfway between the offsets of their corresponding classical, i.e.

$$\delta \mathbf{z}_{a1b1} = \tfrac{1}{2}\,(\delta \mathbf{z}_{a1} + \delta \mathbf{z}_{b1}), \tag{6.89a}$$

$$\delta \mathbf{z}_{a2b2} = \tfrac{1}{2}\,(\delta \mathbf{z}_{a2} + \delta \mathbf{z}_{b2}). \tag{6.89b}$$

Moreover, by virtue of all propagators being affine transformations, the oscillation phases of the interference terms remain linear functions of phase space coordinate,

$$\varphi_{\ell\ell'} = \mathbf{Q}\,\mathbf{z} + \overline{\varphi}_{\ell\ell'}. \tag{6.90}$$

The final interference vector $\mathbf{Q}_{(t_4)}$ and phase space offset $\overline{\varphi}_{\ell\ell'(t_4)}$ have already been introduced in the context of a single beam splitter at the end of section 6.2.2. We postpone explicit expressions for $\mathbf{Q}$ and $\overline{\varphi}_{\ell\ell'}$ until we consider special cases of quadratic Hamiltonians (free propagation, linear gravity) at the end of this chapter. With the above specifications, the interference terms in the two output ports are written as

$$f_{a1b1}(\mathbf{z},t_4) = 2|\gamma_{a1}|\,|\gamma_{b1}|\,\cos\Big(\mathbf{Q}_{(t_4)}\,\mathbf{z} + \overline{\varphi}_{a1b1(t_4)}\Big)\, f_0\left(\hat{\mathscr{U}}^{-1}_{a1b1}(\mathbf{z}-\delta\mathbf{z}_{a1b1})\right), \tag{6.91a}$$

$$f_{a2b2}(\mathbf{z},t_4) = -2|\gamma_{a2}|\,|\gamma_{b2}|\,\cos\Big(\mathbf{Q}_{(t_4)}\,\mathbf{z} + \overline{\varphi}_{a2b2(t_4)}\Big)\, f_0\left(\hat{\mathscr{U}}^{-1}_{a2b2}(\mathbf{z}-\delta\mathbf{z}_{a2b2})\right). \tag{6.91b}$$

All envelopes of the final WIGNER function contributions have equal shapes: they are all expressed by a common transformation $\hat{\mathscr{U}}_{(t_{04})}$. The only difference between the envelopes are the differently shifted centers, expressed in $\delta\mathbf{z}_\ell$ and $\delta\mathbf{z}_{\ell\ell'}$. These differences are caused by the laser-induced kicks and subsequent evolution. A particular benefit of quadratic Hamiltonians is that oscillation phases of the interferecne terms are merely linear functions in coordinates $\mathbf{z}$. This implies straight-lined oscillatory patterns in phase space.

Gaussian distributions

Let the initial WIGNER function be a Gaussian,

$$f_0(\mathbf{z}) = N\,\frac{\exp\left(-\mathbf{z}^{\mathsf{T}}\,\mathsf{C}_z^{-1}{}_{(t_0)}\,\mathbf{z}\right)}{\sqrt{\pi \det \mathsf{C}_{z(0)}}}. \tag{6.92}$$

Then, in case of quadratic Hamiltonians we can specify the above results to write the classical parts of the final distribution function as

$$f_{\ell\ell}(\mathbf{z},t_4) = N\,|\gamma_\ell|^2\,\frac{\exp\left[-(\mathbf{z}-\overline{\mathbf{z}}_{(t_{04})}-\delta\mathbf{z}_\ell)^{\mathsf{T}}\,\mathsf{C}_z^{-1}{}_{(t_{04})}\,(\mathbf{z}-\overline{\mathbf{z}}_{(t_{04})}-\delta\mathbf{z}_\ell)\right]}{\sqrt{\pi^6 \det \mathsf{C}_{z(t_{04})}}}. \tag{6.93}$$

Remember, that $\overline{\mathbf{z}}$ denotes the offset from classical transport while $\delta\mathbf{z}_\ell$ arises due to the laser pulses. Furthermore, the interference terms read

$$\begin{aligned} f_{\ell\ell}(\mathbf{z},t_4) = 2N\,|\gamma_\ell|\,|\gamma_{\ell'}|\,\cos\left(\mathbf{Q}^{(t_{04})}\,\mathbf{z} + \overline{\varphi}_{\ell\ell'(t_{04})}\right)& \\ \times\,\frac{\exp\left[-(\mathbf{z}-\overline{\mathbf{z}}_{(t_{04})}-\delta\mathbf{z}_{\ell\ell'})^{\mathsf{T}}\,\mathsf{C}_z^{-1}{}_{(t_{04})}\,(\mathbf{z}-\overline{\mathbf{z}}_{(t_{04})}-\delta\mathbf{z}_{\ell\ell'})\right]}{\sqrt{\pi^6 \det \mathsf{C}_{z(t_{04})}}}&. \end{aligned} \tag{6.94}$$

Thus, all contributions have the same correlation matrix, given in terms of the initial correaltion matrix as

$$\mathsf{C}_z(t_{04}) = \mathsf{U}(t_{04})\,\mathsf{C}_{z0}\,\mathsf{U}^{\mathsf{T}}(t_{04}).$$

Like the WIGNER function $f(\mathbf{z}, t_4)$, the corresponding position density $n(\mathbf{x}, t_4)$ is again a sum of classical and interference terms. Considering only the two output ports, we write

$$\begin{aligned} n(\mathbf{x}, t_4) &= \int \mathrm{d}^3 v\, f(\mathbf{z}, t_4) \\ &= \sum_{\ell \in \{a1, b1, a2, b2\}} n_{\ell\ell}(\mathbf{x}, t_4) \quad + \sum_{(\ell,\ell') \in \{a1b1, a2b2\}} n_{\ell\ell'}(\mathbf{x}, t_4). \end{aligned} \tag{6.95}$$

All density contributions are Gaussians in position space. Finding expressions for all these terms is quite similar to corresponding procedures in case of a single beam splitter, discussed in section 6.2.3. For instance, the correlation matrix C_x, common to all density contributions, is calculated from C_z by writing C_z^{-1} as block matrix, as instructed in equation (6.53), to arrive at the inverse of the effective correlation matrix in position space,

$$\mathsf{C}_x^{-1}(t_{04}) = \mathsf{A}_{xx} - \mathsf{A}_{xv}\mathsf{A}_{vv}^{-1}\mathsf{A}_{vx}.$$

Hence, the classical contributions to the final position density are given by

$$n_{\ell\ell}(\mathbf{x}, t_4) = N\, |\gamma_\ell|^2\, \frac{\exp\left[-(\mathbf{x} - \overline{\mathbf{x}}(t_{04}) - \delta\mathbf{x}_\ell)^{\mathsf{T}}\, \mathsf{C}_x^{-1}(t_{04})\, (\mathbf{x} - \overline{\mathbf{x}}(t_{04}) - \delta\mathbf{x}_\ell)\right]}{\sqrt{\pi^3 \det \mathsf{C}_x(t_{04})}}. \tag{6.96}$$

The main difference to section 6.2.3 are the offsets $\delta\mathbf{x}_\ell$. They involve several laser-induced kicks with subsequent classical transport. Furthermore, for conveniently expressing the interference terms,

$$\begin{aligned} n_{\ell\ell'}(\mathbf{x}, t_4) = 2N\, |\gamma_\ell|\,|\gamma_{\ell'}|\, \mathscr{C}_{\mathrm{if}}\, \cos\left[\mathbf{k}_{\mathrm{if}}\mathbf{x} + \overline{\varphi}_{\ell\ell'}\right] \\ \times \frac{\exp\left[-(\mathbf{x} - \overline{\mathbf{x}}(t_{04}) - \delta\mathbf{x}_{\ell\ell'})^{\mathsf{T}}\, \mathsf{C}_x^{-1}(t_{04})\, (\mathbf{x} - \overline{\mathbf{x}}(t_{04}) - \delta\mathbf{x}_{\ell\ell'})\right]}{\sqrt{\pi^3 \det \mathsf{C}_x(t_{04})}}. \end{aligned} \tag{6.97}$$

we have divided the interference vector into a position and a velocity component, $\mathbf{Q} = (\mathbf{q}_x, \mathbf{q}_v)^{\mathsf{T}}$. The abbreviations for contrast and wave number of the oscillatory pattern,

$$\begin{aligned} \mathscr{C}_{\mathrm{if}} &= e^{-\frac{1}{4}\mathbf{q}_v^{\mathsf{T}}\,\mathsf{A}_{vv}^{-1}\,\mathbf{q}_v}, \\ \mathbf{k}_{\mathrm{if}} &= \mathbf{q}_x - \mathsf{A}_{xv}\mathsf{A}_{vv}^{-1}\mathbf{q}_v, \end{aligned}$$

respectively, is formally identical to section 6.2.3. The difference is hidden in the details. Passing a complete MZI instead of a single beam splitter, the explicit form of the interference vector $\mathbf{Q}$ in the current case is slightly more complicated. This is demonstrated in the context of the following examples.

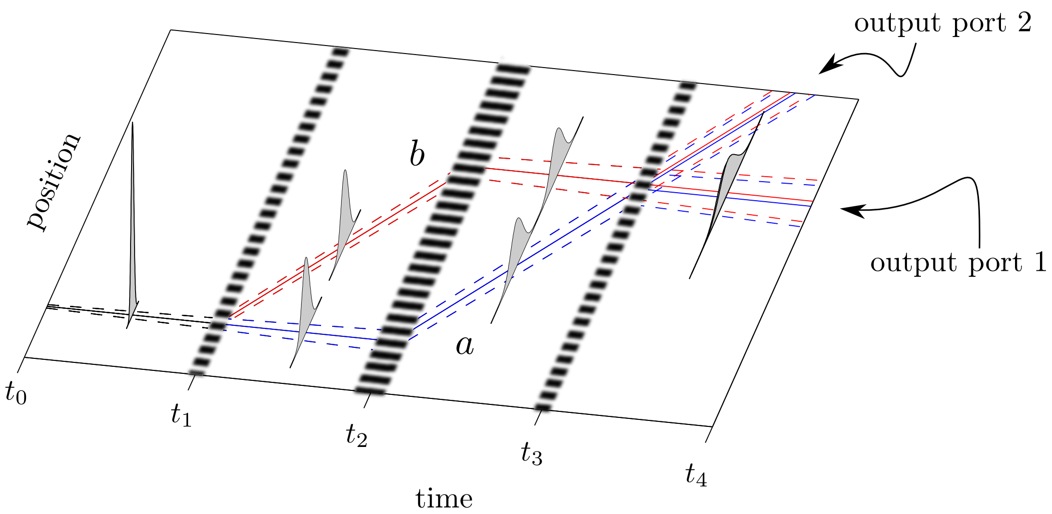

Figure 6.13.: Scheme of a Mach-Zehnder interferometer for freely expanding matter waves.

6.3.5 Example 1: Free evolution

The most simple but also most important example, is propagation in the absence of external forces. For a detailed discussion of free propagation see section 2.3.1. According to expression (2.80), evolution of positions and velocities over a time interval t is described by the transformation

$$\hat{\mathscr{U}}(t)\begin{pmatrix}\mathbf{x}\\ \mathbf{v}\end{pmatrix}=\begin{pmatrix}\mathbf{x}+\mathbf{v}t\\ \mathbf{v}\end{pmatrix}=\begin{pmatrix}\mathbb{1} & \mathbb{1}t\\ \mathbb{0} & \mathbb{1}\end{pmatrix}\begin{pmatrix}\mathbf{x}\\ \mathbf{v}\end{pmatrix}, \tag{6.98}$$

being a simple matrix multiplication. The only effects that determine the distribution are the velocity kicks imparted by the interferometer elements and the free expansion of the cloud. The former shifts the distribution centers while the latter leads to a spreading of the position density profile. The behavior of $n(\mathbf{x})$ passing the MZI is sketched in figure 6.13.

Before dealing with the distribution functions, we take a look at the propagation of their central points in phase space, $\langle\mathbf{z}\rangle_\ell(t)$. Starting at the minimum of the trap at $\langle\mathbf{z}\rangle_\ell(t_0)=(\mathbf{0},\mathbf{0})$, the center of each part rests until it is kicked by a laser pulse. Thereafter, it moves uniformly with the kick velocity until it receives a kick in the opposite direction. In output port 1, all central velocities are zero after leaving the interferometer,

$$\langle\mathbf{v}\rangle_{a1}(t_4)=\langle\mathbf{v}\rangle_{b1}(t_4)=\langle\mathbf{v}\rangle_{a1b1}(t_4)=\mathbf{0}, \tag{6.99a}$$

while the mean positions become

$$\langle\mathbf{x}\rangle_{a1}(t_4)=\delta\mathbf{x}_{a1}=\mathbf{v}_G t_{23}, \tag{6.99b}$$

$$\langle\mathbf{x}\rangle_{b1}(t_4)=\delta\mathbf{x}_{b1}=\mathbf{v}_G t_{12}, \tag{6.99c}$$

$$\langle\mathbf{x}\rangle_{a1b1}(t_4)=\delta\mathbf{x}_{a1b1}=\tfrac{1}{2}\mathbf{v}_G t_{13}. \tag{6.99d}$$

The spatial separation of the parts is directly proportional to the pulse distances of the laser, t_{12}, t_{23}. In case of symmetric interferometers, $t_{12} = t_{23}$, they coincide. The contributions to the second output port, on the other hand, exit the recombiner with their velocities being centered around the kick velocity,

$$\langle \mathbf{v} \rangle_{a2\,(t_4)} = \langle \mathbf{v} \rangle_{b2\,(t_4)} = \langle \mathbf{v} \rangle_{a2b2\,(t_4)} = \mathbf{v}_G. \tag{6.99e}$$

The associated mean positions at the detector are

$$\langle \mathbf{x} \rangle_{a2\,(t_4)} = \delta \mathbf{x}_{a2} = \mathbf{v}_G t_{24}, \tag{6.99f}$$

$$\langle \mathbf{x} \rangle_{b2\,(t_4)} = \delta \mathbf{x}_{b2} = \mathbf{v}_G (t_{12} + t_{34}), \tag{6.99g}$$

$$\langle \mathbf{x} \rangle_{a2b2\,(t_4)} = \delta \mathbf{x}_{a2b2} = \tfrac{1}{2} \mathbf{v}_G (t_{13} + 2t_{34}). \tag{6.99h}$$

These are the mean positions from the first port (6.99b)-(6.99d) plus a common offset $\mathbf{v}_G t_{34}$ that separates both ports in position space.

Wigner function

Applying formulas for distribution parts evolving in a MZI with quadratic Hamiltonians (see 6.3.4) to the current case of free propagation, the classical contributions are written

$$f_{a1}(\mathbf{z}, t_4) = |\gamma_{a1}|^2 \, f_0 \left(\mathbf{x} - \mathbf{v} t_{04} - \mathbf{v}_G t_{23},\ \mathbf{v} \right), \tag{6.100a}$$

$$f_{b1}(\mathbf{z}, t_4) = |\gamma_{b1}|^2 \, f_0 \left(\mathbf{x} - \mathbf{v} t_{04} - \mathbf{v}_G t_{12},\ \mathbf{v} \right), \tag{6.100b}$$

$$f_{a2}(\mathbf{z}, t_4) = |\gamma_{a2}|^2 \, f_0 \left(\mathbf{x} - (\mathbf{v} - \mathbf{v}_G) t_{04} - \mathbf{v}_G t_{24},\ \mathbf{v} - \mathbf{v}_G \right), \tag{6.100c}$$

$$f_{b2}(\mathbf{z}, t_4) = |\gamma_{b2}|^2 \, f_0 \left(\mathbf{x} - (\mathbf{v} - \mathbf{v}_G) t_{04} - \mathbf{v}_G (t_{12} + t_{34}),\ \mathbf{v} - \mathbf{v}_G \right). \tag{6.100d}$$

These expressions explicitly contain the shifted centers given in equations (6.99b-6.99h). One can also recognize the shearing of the phase space distribution by subtraction of $(\mathbf{v} - \langle \mathbf{v} \rangle_\ell) t_{04}$ in the position argument describing a spreading position density. Moreover, the final interference vector that characterizes frequency and orientation of the oscillatory pattern is

$$\mathbf{Q}(t_4) = \begin{pmatrix} 0 \\ \mathbf{G}(t_{23} - t_{12}) \end{pmatrix}. \tag{6.101}$$

Obviously, the interference terms oscillate only along the velocity axis with a frequency proportional to the asymmetry of the interferometer, i.e. $t_{23} - t_{12}$. The complete interference term of the first output port is

$$f_{11}(\mathbf{z}, t_4) = 2 |\gamma_{a1}| \, |\gamma_{b1}| \, \cos \left[\mathbf{G} \left(\mathbf{v} + \frac{\mathbf{v}_G}{2} \right) (t_{23} - t_{12}) + \delta\zeta \right] \times f_0 \left(x - \mathbf{v} t_{04} - \frac{\mathbf{v}_G}{2} t_{13},\ \mathbf{v} \right), \tag{6.102a}$$

while the one of the second output port reads

$$f_{22}(\mathbf{z}, t_4) = -2|\gamma_{a2}|\,|\gamma_{b2}|\,\cos\left[\mathbf{G}\left(\mathbf{v} - \frac{\mathbf{v}_G}{2}\right)(t_{23} - t_{12}) + \delta\zeta\right] \\ \times f_0\left(x - (\mathbf{v} - \mathbf{v}_G)t_{04} - \frac{\mathbf{v}_G}{2}(t_{13} + 2t_{34}),\ \mathbf{v} - \mathbf{v}_G\right) \quad (6.102b)$$

The total Wigner function $f(\mathbf{z}, t_4)$ is the sum of all terms found in equations (6.100) and (6.102). Remember that we have neglected interference terms between the two output ports, which were collected under the label f_{12} and written in equation (6.83). This was justified by assuming f_1 and f_2 to be sufficiently far separated in position space. Figure 6.14 shows an example for the propagation of the Wigner function through the MZI.

Action along paths

It is interesting to note that the offsets to the oscillation phases in expressions (6.102) can be related to the difference of actions that are accumulated along different paths. The action, being the integral of the Lagrangian along a certain trajectory (see (2.5)), is very easy to calculate for free propagation. One finds

$$\begin{aligned} S(t_j) &= \int_0^{t_{ij}} \mathrm{d}t\ L(\mathbf{x}(t), \mathbf{v}(t)) \\ &= S(t_i) + \tfrac{M}{2}\mathbf{v}^2(t_i)\, t_{ij}, \end{aligned} \quad (6.103)$$

As mentioned in section 3.3.2, the action can be identified with the wave function's phase in units of $\hbar$. Hence, in addition to the dynamical phase that is acquired during the periods of free propagation (given in (6.103)), the laser pulses give rise sudden phase leaps. These are a byproduct of the application of kick operators $\exp[\pm i(\mathbf{G}\hat{\mathbf{x}} + \zeta_i)]$. Consequently, applying a laser pulse at a certain time instance t_i such that the wave function of path ℓ is kicked,

$$\left|\psi(t_i^+)\right\rangle = |\alpha_\ell|\ \exp[\pm i(\mathbf{G}\hat{\mathbf{x}} + \zeta_i)]\ \left|\psi(t_i^-)\right\rangle, \quad (6.104)$$

the associated action leap is

$$S_\ell(t_i^+) = S_\ell(t_i^-) \pm \hbar(\mathbf{G}\mathbf{x} + \zeta_i). \quad (6.105)$$

With these relations, the final actions along all paths are found to be

$$S_{a1}(t_4) = -M\frac{v_G^2}{2}t_{23} + \hbar(\zeta_2 - \zeta_3), \quad (6.106a)$$

$$S_{b1}(t_4) = -M\frac{v_G^2}{2}t_{12} + \hbar(\zeta_1 - \zeta_2), \quad (6.106b)$$

$$S_{a2}(t_4) = M\frac{v_G^2}{2}t_{24} + \hbar\zeta_2, \quad (6.106c)$$

$$S_{b2}(t_4) = M\frac{v_G^2}{2}(t_{12} - t_{23} + t_{34}) + \hbar(\zeta_1 - \zeta_2 + \zeta_3). \quad (6.106d)$$

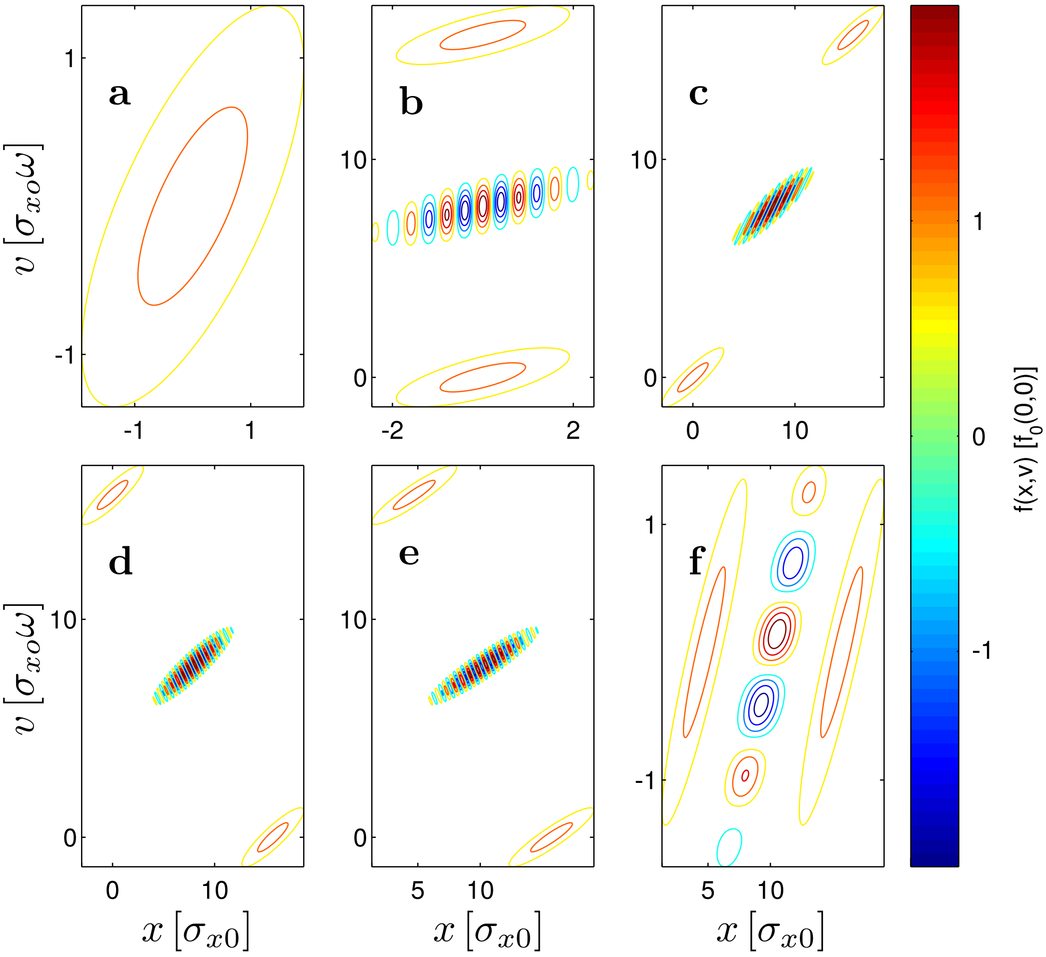

Figure 6.14.: Contour plots of WIGNER function before and after the laser pulses of an asymmetric MZI assuming free propagation. Time instances of laser pulse application are $(t_1, t_2, t_3) = (1,\, 2,\, 2.3)\omega^{-1}$, lattice vector of optical potential is $G = 2\pi/(0.8\,\sigma_{x0})$. **a**: $t = t_1^-$, before the first beam splitter. **b**: $t = t_1^+$, after the first beam splitter. **c**: $t = t_2^-$, before the $\pi/2$-pulse. **d**: $t = t_2^+$, after the $\pi/2$-pulse. **e**: $t = t_3^-$, before the second beam splitter. **f**: $t = t_3^+$, after the second beam splitter, output port 1. Mind the different scalings of the axes.

Their differences in units of $\hbar$ are just the offsets of the oscillation frequencies of the interference terms,

$$\overline{\varphi}_{a1b1}(t_4) = \frac{1}{\hbar}\Big(S_{b1}(t_4) - S_{a1}(t_4)\Big), \tag{6.107a}$$

$$\overline{\varphi}_{a2b2}(t_4) = \frac{1}{\hbar}\Big(S_{b2}(t_4) - S_{a2}(t_4)\Big). \tag{6.107b}$$

Position density

Being interested in the position density associated with a Gaussian phase space distribution, we can apply the recipes from section 6.3.4 for the current special case of free propagation. The shape of all contributions is determined by the correlation matrix. Starting initially with a Gaussian phase space distribution

$$f_0(\mathbf{z}) = \frac{\exp(-\mathbf{z}^{\mathsf{T}}\,\mathsf{C}_{z0}^{-1}\,\mathbf{z})}{\sqrt{\pi^6 \det \mathsf{C}_{z0}}},$$

including

$$\mathsf{C}_{z0} = \begin{pmatrix} \mathsf{C}_{x0} & \mathbb{O} \\ \mathbb{O} & \Omega^{-2}\mathsf{C}_{x0} \end{pmatrix}, \tag{6.108}$$

the inverse time-evolved correlation matrix in phase space becomes

$$\mathsf{C}_z^{-1}(t_4) = \begin{pmatrix} \mathsf{C}_{x0}^{-1} & -t_{04}\mathsf{C}_{x0}^{-1} \\ -t_{04}\mathsf{C}_{x0}^{-1} & (\Omega^{-2}+t_{04}^2)\mathsf{C}_{x0}^{-1} \end{pmatrix} = \begin{pmatrix} \mathsf{A}_{xx} & \mathsf{A}_{xv} \\ \mathsf{A}_{vx} & \mathsf{A}_{vv} \end{pmatrix}. \tag{6.109}$$

This is equivalent to expression (2.83). Having identified the block matrices of C_z, the correlation matrix of the position density is found to be

$$\mathsf{C}_x(t_4) = (\mathbb{1} + \Omega^2 t_{04}^2)\,\mathsf{C}_{x0}., \tag{2.84}$$

using the prescription from the appendix A.2. The classical contributions to the final density profile are thus written as

$$n_{\ell\ell}(\mathbf{x}, t_4) = |\gamma_\ell|^2 \frac{\exp\left[-(\mathbf{x}-\delta\mathbf{x}_\ell)^{\mathsf{T}}\,\mathsf{C}_{x0}^{-1}\,(\mathbf{x}-\delta\mathbf{x}_\ell)\right]}{\sqrt{\pi^3 \det \mathsf{C}_{x0}(\mathbb{1}+\Omega^2 t_{04}^2)}} \tag{6.110}$$

while the interference terms read

$$n_{\ell\ell'}(\mathbf{x}, t_4) \;=\; 2N \;\; |\gamma_\ell|\,|\gamma_{\ell'}| \;\; \mathscr{C}_{\text{if}} \;\; \cos(\mathbf{k}_{\text{if}}\mathbf{x} + \overline{\varphi}_{\ell\ell'}) \;\; \frac{\exp\left[-(\mathbf{x}-\delta\mathbf{x}_{\ell\ell'})^{\mathsf{T}}\,\mathsf{C}_{x0}^{-1}\,(\mathbf{x}-\delta\mathbf{x}_{\ell\ell'})\right]}{\sqrt{\pi^3 \det \mathsf{C}_{x0}(\mathbb{1}+\Omega^2 t_{04}^2)}}. \tag{6.111}$$

All laser-induced offsets $\delta\mathbf{x}_\ell$ and $\delta\mathbf{x}_{\ell\ell'}$ were given in equations (6.99). The phase offsets $\overline{\varphi}_{\ell\ell'}$ were expressed in terms of the classical action. Additionally, the contrast and wave number of the oscillatory pattern is given by

$$\mathscr{C}_{\text{if}} = \exp\left[-\tfrac{1}{4}(t_{23}-t_{12})^2\,\mathbf{G}^{\mathsf{T}}\,\mathsf{C}_{x0}\Omega^2(\mathbb{1}+\Omega^2 t_{04}^2)^{-1}\,\mathbf{G}\right], \tag{6.112}$$

$$\mathbf{k}_{\text{if}} = t_{04}(t_{23}-t_{12})\,\Omega^2\left(\mathbb{1}+\Omega^2 t_{04}^2\right)^{-1}\mathbf{G},, \tag{6.113}$$

respectively. Both of these essentially depend on two quantities. On one hand, the fringe frequency increases for bigger asymmetries of the pulse timings, $t_{23}-t_{12}$. This asymmetry is proportional to the separation of the paths inside one output port. The farther these are seperated, however, the lower will be the contrast $\mathscr{C}_{\text{if}}$ of the interference fringes. On the other hand, free expansion of the cloud leads to a spreading of the interference fringes. Their wave length in direction of the laser pulse is given by

$$\lambda_{\text{if}} = \frac{2\pi}{G}\,\frac{1+\omega^2 t_{04}^2}{\omega^2 t_{04}|t_{23}-t_{12}|}, \tag{6.114}$$

including $\omega^2 = \mathbf{G}^{\mathsf{T}}\Omega^2\mathbf{G}/G^2$. Keeping all laser pulse timings fixed and increasing only the time span between the second beam splitter and the detector, t_{34}, the fringe spacing grows linearly in the asymptotic limit,

$$\lambda_{\text{if}} \overset{t_{34}\to\infty}{\approx} \frac{2\pi}{G}\,\frac{t_{34}}{|t_{23}-t_{12}|}. \tag{6.115}$$

This relation can be rewritten in terms of the distance between the two paths $d = \hbar G|t_{23}-t_{12}|/M$ as

$$\lambda_{\text{if}} \overset{t_{34}\to\infty}{\approx} \frac{h}{M\,d}\,t_{34} \tag{6.116}$$

where $h = 2\pi\hbar$ is PLANCK's quantum of action. Figure 6.15 shows an example of a 1D density profile after a MZI. Furthermore, for the case of a 1D density profile, figure 6.16 displays the wave number of the interference pattern over time after the last laser pulse for various path separations.

Symmetric interferometer

When we discussed the influence of interference on the final density so far, we always considered the oscillatory patterns in the position density profile. In addition to this phenomenon, the relative distribution of density between both output ports changes depending on laser pulse timings. This is most conveniently studied in case of symmetric interferometers. Here, the meaning of symmetric is twofold. First, the time spans between the laser pulses are equal,

$$t_{12} = t_{23} = T.$$

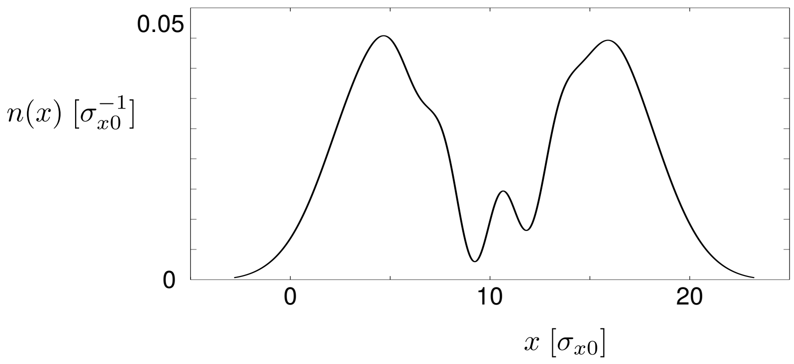

Figure 6.15.: Position density in output port 1, associated to the Wigner function drawn in part **f** of 6.14.

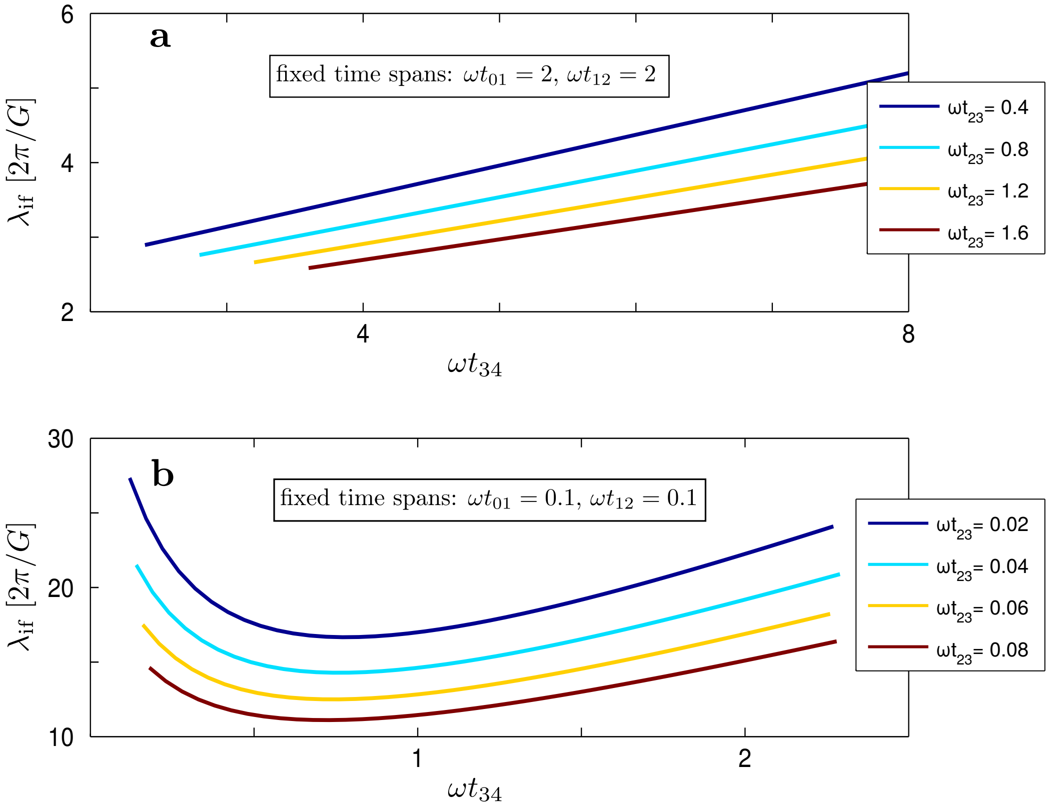

Figure 6.16.: Interference fringe spacing λ_{if} against time after recombination t_{34} for various pulse timings in an one-dimensional model. The initial state is assumed to be prepared in a harmonic trap with frequency ω. Various colors represent different time spans ωt_{23} and thus different amounts of asymmetry $t_{23} - t_{12}$. Part **a**: Fixed time spans are $\omega t_{01} = \omega t_{12} = 2$. Part **b**: Fixed time spans are $\omega t_{01} = \omega t_{12} = 0.1$.

Second, we assume symmetric beam splitters, creating 50-50 superpositions of incident states so that we finally obtain the coefficients

$$|\gamma_{a1}| = |\gamma_{b1}| = |\gamma_{a2}| = |\gamma_{b2}| = \frac{1}{2}.$$

In this setup, the total WIGNER function reads

$$\begin{aligned} f(\mathbf{z}, t_4) &= f_{11}(\mathbf{z}, t_4) + f_{22}(\mathbf{z}, t_4) \\ &= \cos^2\left(\frac{\delta\zeta}{2}\right) f_0\Big(\mathbf{x} - \mathbf{v}t_{04} - \mathbf{v}_G T,\ \mathbf{v}\Big) \\ &\quad + \sin^2\left(\frac{\delta\zeta}{2}\right) f_0\Big(\mathbf{x} - (\mathbf{v} - \mathbf{v}_G)t_{04} - \mathbf{v}_G T - \mathbf{v}_G t_{34},\ (\mathbf{v} - \mathbf{v}_G)\Big), \end{aligned} \tag{6.117}$$

being a sum of two contributions. The corresponding densities , $n_{11} = \int \mathrm{d}^3 v\ f_1$ and $n_{22} = \int \mathrm{d}^3 v\ f_2$, are separated by a distance $\mathbf{v}_G t_{34}$. They add up to the complete density profile,

$$n(\mathbf{x}, t_{34}) = n_{11}(\mathbf{x}, t_{34}) + n_{22}(\mathbf{x}, t_{34}). \tag{6.118}$$

If the spatial separation between the two output ports is sufficiently large, one can distinguish the individual contributions simply by looking at the complete density profile. According to the distribution (6.117), the relative population of both output ports is

$$\frac{n(\mathbf{x}, t_4)}{n(\mathbf{x}, t_4) + n(\mathbf{x} + \mathbf{v}_G t_{34}, t_4)} = \cos^2\left(\frac{\delta\zeta}{2}\right), \tag{6.119a}$$

$$\frac{n(\mathbf{x} + \mathbf{v}_G t_{34}, t_4)}{n(\mathbf{x}, t_4) + n(\mathbf{x} + \mathbf{v}_G t_{34}, t_4)} = \sin^2\left(\frac{\delta\zeta}{2}\right). \tag{6.119b}$$

Obviously, we can redistribute density among the output ports by tuning the phase differences of the lasers, $\delta\zeta = \zeta_1 - 2\zeta_2 + \zeta_3$.

6.3.6 Example 2: Linear gravity

Having just discussed system without any forces on the particles during classical transport, the next more complicated model involves a constant force. In the absence of trapping potentials, the atoms are usually subject to gravity. Typically, for experiments on the earth's surface, the true $1/r$ potential of Newtonian gravity is very well approximated by a linear-slope potential, entailing constant acceleration. Choosing the third component x_3 to be orthogonal to the isosurface of the gravity potential, we have $\dot{\mathbf{v}} = (0, 0, -g)^\mathsf{T}$. The value for linear gravity acceleration is around $g = 9.81 m/s^2$ on the earth's surface.

Classical phase space trajectories for linear gravity has been discussed in section 2.3.2. For the sake of notational convenience, we consider only dynamics the direction of the acceleration.

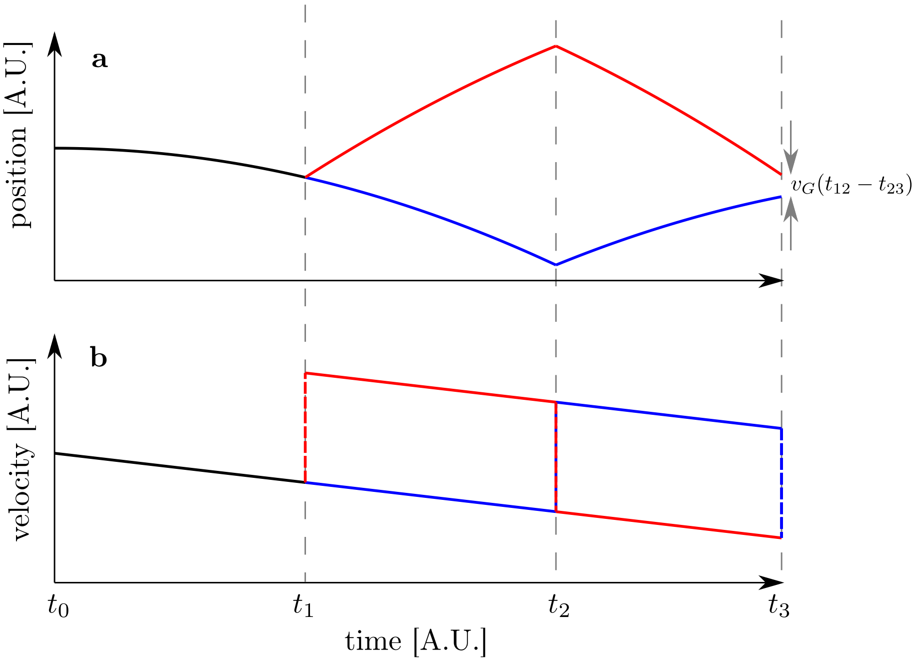

Figure 6.17.: Sketch of position (a) and velocity (b) in a MZI with linear gravity potential. Colors and dashed lines have the same meaning as in figure 6.18.

This allows us to utilize a one-dimensional formalism. Then, according to expression (2.88), the phase space propagator reads

$$\hat{\mathscr{U}}(t)\begin{pmatrix} x \\ v \end{pmatrix} = \begin{pmatrix} x + vt - \frac{g}{2}t^2 \\ v - gt \end{pmatrix} = \begin{pmatrix} 1 & t \\ 0 & 1 \end{pmatrix}\begin{pmatrix} x \\ v \end{pmatrix} + \begin{pmatrix} -\frac{g}{2}t^2 \\ -gt \end{pmatrix}. \tag{6.120}$$

It comprises matrix multiplication as well as vector addition. Without the laser pulses of the MZI, a trajectory that starts at time t_0 in the origin of phase space, $\langle \mathbf{z} \rangle(t_0) = (0,0)^{\mathsf{T}}$, ends up in the point $\overline{\mathbf{z}}(t_{04}) = (-\frac{g}{2}t_{04}^2, -gt_{04})$ after freely falling towards the gravity center. As we have shown with equations (6.86) and (6.89b), the MZI-induced offsets depend only on the kick velocity $\mathbf{v}_G$ and the matrix part $\mathsf{U}(t)$ of the affine transformation (6.120). This matrix part, however, is the same for constant acceleration and free propagation. Hence, the influence of the laser pulses on the phase space trajectories, denoted by δz, is the same as in the case of free evolution. In output port 1, on one hand, the contribution of the MZI offsets to the mean velocities is zero, $\delta v_{a1} = \delta v_{b1} = \delta v_{a1b1} = 0$, while the position offsets are $\delta x_{a1} = v_G t_{23}$, $\delta x_{b1} = v_G t_{12}$, and $\delta x_{a1b1} = \frac{1}{2} v_G t_{13}$. In the second output port, on the other, the laser pulses lead to an offset in the mean velocities of $\delta v_{a2} = \delta v_{b2} = \delta v_{a2b2} = v_G$, and in mean positions $\delta x_{a2} = v_G t_{24}$, $\delta x_{b2} = v_G(t_{12} + t_{34})$, and $\delta x_{a2b2} = \frac{1}{2}(t_{13} + 2t_{34})$. The only difference of linear gravity to free propagation is the offset due to constant acceleration. It is expressed by the addition of $(-gt^2/2, -gt)$ in equation (6.120). Altogether, the center coordinates in phase space for all

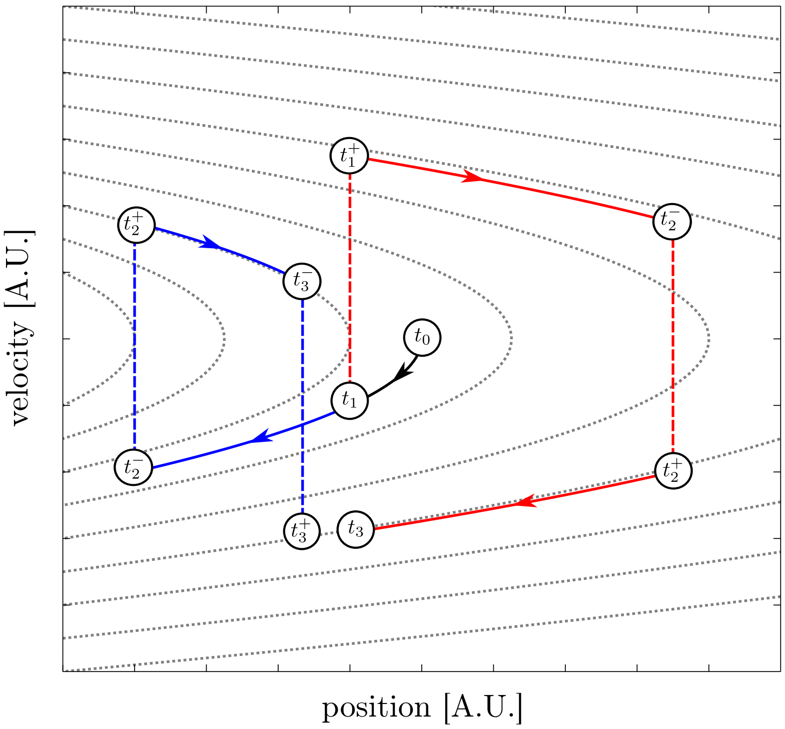

Figure 6.18.: Sketch of classical phase space trajectories of MZI in linear gravity potential. The colors blue and red indicate the lower ans upper path, respectively. The laser induced velocity kicks are represented by dashed lines.

final contributions are

$$\langle \mathbf{z} \rangle_{a1}(t_4) = \begin{pmatrix} -\frac{g}{2} t_{04}^2 + v_G t_{23} \\ -g t_{04} \end{pmatrix}, \tag{6.121a}$$

$$\langle \mathbf{z} \rangle_{b1}(t_4) = \begin{pmatrix} -\frac{g}{2} t_{04}^2 + v_G t_{12} \\ -g t_{04} \end{pmatrix}, \tag{6.121b}$$

$$\langle \mathbf{z} \rangle_{a1b1}(t_4) = \begin{pmatrix} -\frac{g}{2} t_{04}^2 + \frac{v_G}{2} t_{13} \\ -g t_{04} \end{pmatrix}, \tag{6.121c}$$

$$\langle \mathbf{z} \rangle_{a2}(t_4) = \begin{pmatrix} -\frac{g}{2} t_{04}^2 + v_G t_{24} \\ -g t_{04} + v_G \end{pmatrix}, \tag{6.121d}$$

$$\langle \mathbf{z} \rangle_{b2}(t_4) = \begin{pmatrix} -\frac{g}{2} t_{04}^2 + v_G (t_{12} + t_{34}) \\ -g t_{04} + v_G \end{pmatrix}, \tag{6.121e}$$

$$\langle \mathbf{z} \rangle_{a2b2}(t_4) = \begin{pmatrix} -\frac{g}{2} t_{04}^2 + \frac{v_G}{2} (t_{13} + 2 t_{34}) \\ -g t_{04} + v_G \end{pmatrix}. \tag{6.121f}$$

Having calculated the distribution centers, one can easily find the classical contributions to the final WIGNER function by applying the formulas from section 6.3.4. They are

$$f_{a1}(\mathbf{z},t_4) = f_0\left(X - v_G t_{23} - V t_{04},\, V\right), \tag{6.122a}$$

$$f_{b1}(\mathbf{z},t_4) = f_0\left(X - v_G t_{12} - V t_{04},\, V\right), \tag{6.122b}$$

$$f_{a2}(\mathbf{z},t_4) = f_0\left(X - v_G t_{24} - (V - v_G) t_{04},\, V - v_G\right), \tag{6.122c}$$

$$f_{b2}(\mathbf{z},t_4) = f_0\left(X - v_G t_{12} - (V - v_G) t_{04},\, V - v_G\right). \tag{6.122d}$$

We have transformed the phase space coordinates to the freely falling frame, using

$$X = x + \tfrac{1}{2} g t_{04}^2, \qquad V = v + g t_{04}. \tag{6.123}$$

This way, the WIGNER functions that have been subject to linear gravity are formally similar to their freely propagating counterparts expressed in (6.100a)-(6.100d). Furthermore, the interference terms are

$$f_{a1b1}(\mathbf{z},t_4) = \cos\left[G\left(V + \frac{v_G}{2}\right)(t_{23} - t_{12}) - G\frac{g}{2}\left(t_{01}^2 - 2t_{02}^2 + t_{03}^2\right) + \delta\zeta\right] \times f_0\left(X - V t_{04} - \frac{v_G}{2} t_{13},\, V\right) \tag{6.124a}$$

for the first output port and

$$f_{a2b2}(\mathbf{z},t_4) = -\cos\left[G\left(V - \frac{v_G}{2}\right)(t_{23} - t_{12}) - G\frac{g}{2}\left(t_{01}^2 - 2t_{02}^2 + t_{03}^2\right) + \delta\zeta\right] \times f_0\left(X - (V - v_G) t_{04} - \frac{v_G}{2}(t_{13} + 2t_{34}),\, V - v_G\right) \tag{6.124b}$$

for the second. Once again, some terms are familiar from the discussion of the free MZI in the last subsection: the oscillation is oriented along the velocity axes in phase space and its frequency is proportional to the asymmetry of the interferometer. Having been subject to gravitational acceleration since release, the velocity argument is shifted by $g t_{04}$. Moreover, the offset of the laser fields (ζ_1, ζ_2, ζ_3) influence the oscillation phase. In contrast to the results (6.102), however, the interference term depends on $G(g/2)(t_{01}^2 - 2t_{02}^2 + t_{03}^2)$. This phase contribution is related to the mean position of the distribution by the time of each laser pule application. It depends on the time spans in which the atoms have been subject to constant acceleration before entering a particular laser field. For asymmetric interferometers, this term merely introduces yet another offset to the interference fringes. Nevertheless, it has useful consequences for symmetric cases, as we will discuss below. Again, for providing a physical explanation for the offset to the oscillation phases $\overline{\varphi}_{\ell\ell'}$, we take a look at the actions that are accumulated along the paths. For classical transport in a linear gravity potential between the time instances t_i and t_j, one finds

$$S(t_j) = S(t_i) + M\left[\left(\frac{v_i^2}{2} - g x_i\right) t_{ij} - g v_i t_{ij}^2 + \tfrac{1}{3} g^2 t_{ij}^3\right], \tag{6.125}$$

where we have abbreviated $x_i = x(t_i)$ and $v_i = v(t_i)$. In addition to action accumulation due to classical transport, like before, the laser-induced phase leaps related to the kick operator $\exp[\pm i(\mathbf{G}\hat{\mathbf{x}} + \zeta_i)]$ lead to

$$S(t_i^+) = S(t_i^-) \pm \hbar(\mathbf{G}\mathbf{x} + \zeta_i). \tag{6.105}$$

Going through the complete sequence, the final actions are found to be

$$S_{a1}(t_4) = M\frac{g^2}{3}t_{04}^3 - \hbar G\left[\left(g t_{04} + \frac{v_G}{2}\right)t_{23} - \frac{g}{2}\left(t_{02}^2 - t_{03}^2\right)\right] + \hbar(\zeta_2 - \zeta_3), \tag{6.126a}$$

$$S_{b1}(t_4) = M\frac{g^2}{3}t_{04}^3 - \hbar G\left[\left(g t_{04} + \frac{v_G}{2}\right)t_{12} - \frac{g}{2}\left(t_{01}^2 - t_{02}^2\right)\right] + \hbar(\zeta_1 - \zeta_2), \tag{6.126b}$$

$$S_{a2}(t_4) = M\frac{g^2}{3}t_{04}^3 - \hbar G\left[\left(g t_{04} - \frac{v_G}{2}\right)t_{24} - \frac{g}{2}t_{02}^2\right] + \hbar\zeta_2, \tag{6.126c}$$

$$S_{b2}(t_4) = M\frac{g^2}{3}t_{04}^3 - \hbar G\left[\left(g t_{04} - \frac{v_G}{2}\right)(t_{12} + t_{34}) - \frac{g}{2}\left(t_{01}^2 - t_{02}^2 + t_{03}^2\right)\right] + \hbar(\zeta_1 - \zeta_2 + \zeta_3). \tag{6.126d}$$

Like in the case of free propagation between the laser pulses in (6.106), the action depends on the time intervals in which the trajectories have traveled with kicked velocity. The term $Mg^2t_{04}^3/3$ is common to all paths and thus irrelevant when considering differences between actions. Contributions of the form $gt_{0i}^2/2$ are connected to the position of the distribution part by the time they enter a laser field at time t_i.

Utilizing the actions given in equations (6.126), we can express the offsets to the oscillation phases again as

$$\overline{\varphi}_{a1b1}(t_4) = \frac{1}{\hbar}\left[S_{b1}(t_4) - S_{a1}(t_4)\right], \tag{6.127a}$$

$$\overline{\varphi}_{a2b2}(t_4) = \frac{1}{\hbar}\left[S_{b2}(t_4) - S_{a2}(t_4)\right]. \tag{6.127b}$$

These allow us to write all terms in the oscillatory factor of expressions (6.124) that do not depend on v as a simple difference of actions.

Position density

The correlation matrix which is essential for calculating the position density profile can be written as a product comprising the initial correlation matrix and the matrix part of the affine transformation $\hat{\mathscr{U}}$. Since both propagators, (6.98) and (6.120), have identical matrices, the resultant density of an MZI with linear gravity has the same shape as in case of free propagation. Additionally, frequency and orientation of the oscillations in phase space are identical in both cases. The only difference is that constant acceleration shifts both, the distribution centers as well as the oscillation offset. Expressions for the position density will, however, still have the form (6.110) and (6.111), plugging in appropriate position offsets δx_ℓ and phase offsets $\overline{\varphi}_{\ell\ell'}$. These can be easily read off the results above. Moreover, the wave vector of the interference fringes $\mathbf{k}_{\text{if}}$ is the same as given in (6.113).

Symmetric interferometers

In order to conveniently examine the influence of interference onto the relative distribution of density among the output ports, we consider again a symmetric interferometer setup, including

$$t_{12} = t_{23} = T,$$
$$|\gamma_{a1}| = |\gamma_{b1}| = |\gamma_{a2}| = |\gamma_{b2}| = \tfrac{1}{2}.$$

For this choice of parameters, the final Wigner function becomes

$$\begin{aligned} f(\mathbf{z}, t_4) = \cos^2\!\left(\tfrac{\delta\zeta}{2} - \tfrac{1}{2}GgT^2\right) f_0\big(V - Vt_{04} - v_G T,\ V\big) \\ + \sin^2\!\left(\tfrac{\delta\zeta}{2} - \tfrac{1}{2}GgT^2\right) f_0\big(V - (V - v_G)t_{04} - v_G T,\ V - v_G\big), \end{aligned} \tag{6.128}$$

abbreviating again $X = x + gt_{04}^2/2$ and $V = v + gt_{04}$. We again assume the output ports to be sufficiently separated in position space. In the same way we arrived at expression (6.119), we find the relative populations of the output ports to be

$$\frac{n(\mathbf{x}, t_4)}{n(\mathbf{x}, t_4) + n(\mathbf{x} + \mathbf{v}_G t_{34}, t_4)} = \cos^2\!\left(\tfrac{\delta\zeta}{2} - \tfrac{1}{2}GgT^2\right), \tag{6.129a}$$

$$\frac{n(\mathbf{x} + \mathbf{v}_G t_{34}, t_4)}{n(\mathbf{x}, t_4) + n(\mathbf{x} + \mathbf{v}_G t_{34}, t_4)} = \sin^2\!\left(\tfrac{\delta\zeta}{2} - \tfrac{1}{2}GgT^2\right), \tag{6.129b}$$

One can measure gravitational acceleration [116] by varying the interferometer time $2T$ and reading off the frequency of the population oscillation between both ports.

The dependence of the relative population on the interferometer time is connected to different phases that are accumulated along different paths through the interferometer. Note, however, that this phase difference does not come from the dynamical phase accumulation during classical transport. It is rather a result of the phase leaps that are induced by the laser pulses along different paths. The offset in each path's co-moving frame depends on how long it has been freely falling before entering the laser pulses. In detail, the lower path is unaffected by the first pulse, kicked by the second when it sees an offset $-gt_{02}^2/2$, and kicked back by the third when the offset is $-gt_{03}^2/2$. Analogously, the upper path is kicked and kicked back, seeing offsets $-gt_{01}^2/2$ and $-gt_{02}^2/2$, respectively. The phase difference, that is connected to these different offsets, is just GgT^2 in case of a symmetric interferometer. This gives rise to the population oscillation expressed in equations (6.129).

7 Ray tracing with coherent matter waves in three dimensions

The present chapter treats the numerical computation of time-evolved phase space distributions and associated observables. Suppose evolution is properly described by the semi-classical limit of the quantum LIOUVILLE equation (3.40), neglecting all terms carrying non-zero powers of $\hbar$ (i.e. truncated WIGNER approach). Having now formulated a partial differential equation, i.e. the classical LIOUVILLE equation, a manifest – or maybe naive – strategy for finding a solution would be to discretize phase space and numerically iterate the distribution on this grid. This may indeed be practical for one-dimensional systems that entail a two-dimensional phase space grid. Provided the grid spacing is sensibly chosen and the WIGNER function is in some sense well-behaved, this strategy demands manageable numerical effort. Going to realistic three-dimensional settings, however, things are heavily complicated by considering the corresponding six dimensional phase space. Even very coarse grids with, say, $2^4 = 16$ points along each dimension consists of $2^{12} = 4\,096$ grid points in total. Needless to say that any grid that is supposed to reproduce a proper distribution function with some details will be far beyond what current machines can handle. Thus, we dismiss the approach of solving the partial differential equation directly and utilize a ray tracing approach for matter waves described in the following subsections. As the name suggests, matter wave ray tracing is completely analog to optical ray tracing. In the latter method, optical fields, are propagated *not* by solving MAXWELL 's equations but rather by tracing rays through a given optical setup.

We introduce some basic concepts of our ray tracing approach before we elaborate on how observables are computed. To demonstrate its applicability, we conclude this chapter with showing some simulation results.

7.1 Ray tracing concepts

In previously used terms, switching from the PDE approach to the ray tracing approach, is nothing else than going from SCHRÖDINGER to the HEISENBERG picture. As we discussed in detail in section 2.2.1, directly solving the LIOUVILLE equation is one of two dual concepts for describing phase space dynamics. The other alternative is to reconstruct the final WIGNER function with values of the initial distribution flowing on classical trajectories through phase space. These trajectories are solutions of HAMILTON 's equations of motion (2.3). The analogy to optical ray tracing is most striking if interactions between particles are ignored. In this case, the trajectories are independent of each other and hence dynamics takes place in a six-dimensional phase space. Moreover, calculations can be very efficiently parallelized.

Including binary interactions between N particles, the proper frame for microscopic dynamics is a $6N$-dimensional phase space. As we discussed in section 2.4.3, the WIGNER function of the microscopic phase space may, under certain circumstances, be reduced to an effective single-particle distribution, living in a macroscopic six-dimensional phase space. In this case, interaction effects are covered by non-linear mean field interactions. One way to include these interactions into the ray tracing procedure is to reconstruct the density profile $n(\mathbf{x})$ in each iteration step. This is done by binning the phase space points to a 3D position space grid [117,118]. Alternatively, we can equip the trajectories with an effective interaction that is equivalent to the inter-particle interaction in terms of distribution function evolution. Note that in this context 'trajectories' does not necessarily refer to (physical) particles of a cloud of $N \approx 10^4$ atoms. They are rather abscissas, sampling the phase space distribution. Each of these sampling points may be thought of as representing the dynamics of a batch of physical particles. It is thus also called quasi- or super-particle.

Assuming relatively low densities, we neglect inter-particle interactions in this work, discussing a ray tracing formalism with independent phase space trajectories.

7.1.1 Classical transport

A simple ray tracing procedure for numerical computation of time-dependent WIGNER functions can be given as following. Suppose the initial distribution $f_0(\mathbf{z})$ is known. Make a sampling, i.e. a set of phase space points $\{\mathbf{z}_{\nu(t_0)}\}$ lying in the support of f_0 and compute their associated function values $F_\nu = f_0(\mathbf{z}_{\nu(t_0)})$. Now, solve HAMILTON 's equations – if necessary numerically – for each sample point $\mathbf{z}_\nu$ with $\mathbf{z}_{\nu(t_0)}$ being the initial condition. Note that the HEISENBERG picture implies that the values F_ν remain unchanged during classical transport. They are "attached" to their associated phase space points which travel along the classical trajectories. As a result, at a final time instance t_j, we obtain a collection of points which are scattered across a limited area in phase space, each one carrying a different value. A naive way to recover the distribution function $f(\mathbf{z}, t_j)$ would be to interpolate the scattered data on a rectangular grid. This is obviously not the best idea since we are forced to revert to six-dimensional grids we wanted to avoid in the first place. Anyway, our ultimate aim is not the computation of the WIGNER function itself, but rather expectation values of observables we can calculate with it. As we discuss further below, this notion can be exploited to bypass six-dimensional grids when calculating three-dimensional or scalar observables.

In order to put the above ideas in a more mathematical language, we make some definitions. First, as a finite representation of a phase space distribution function f, we define the collection of r phase space points together with associated distribution values. We call the ordered set of r phase space points at a certain time instance,

$$\underline{\mathbf{z}}(t) = \Big(\mathbf{z}_1(t), \ldots, \mathbf{z}_r(t)\Big), \tag{7.1}$$

a *phase space element* (PSE). It can be pictured either as a collection of points in six-dimensional phase space, or as a single point in (an element of) a $6r$-dimensional phase space. Each PSE is connected to an ordered set of initial distribution values,

$$\begin{aligned} \underline{F} &= \Big(f_0(\mathbf{z}_{1}(t_0)), \ldots, f_0(\mathbf{z}_{r}(t_0))\Big) \\ &= f_0(\underline{\mathbf{z}}(t_0)), \end{aligned} \tag{7.2}$$

In the last step, we have implied the function f_0 to act on each member of the PSE separately. Moreover, similar to the formalism in the previous chapter, classical transport can be expressed in terms of the classical propagator $\hat{\mathcal{U}}(t)$. For evolution between the time instances t_i and t_j, we write

$$\begin{aligned} \underline{\mathbf{z}}(t_j) &= \Big(\hat{\mathcal{U}}(t_{ij})\,\mathbf{z}_1(t_i), \ \ldots, \hat{\mathcal{U}}(t_{ij})\,\mathbf{z}_r(t_i)\Big) \\ &= \hat{\mathcal{U}}(t_{ij})\,\underline{\mathbf{z}}(t_i). \end{aligned} \tag{7.3}$$

Talking about numerics, the propagators of classical transport can in general be well approximated by symplectic integrators [52]. In our favorite special case of quadratic Hamiltonians, that are elaborately discussed in section 2.3, propagators are given by affine transformations

$$\underline{\mathbf{z}}(t_j) = \hat{\mathcal{U}}(t_{ij})\,\underline{\mathbf{z}}(t_i) + \overline{\mathbf{z}}(t_{ij}), \tag{7.4}$$

where vector addition and matrix multiplication of $\underline{\mathbf{z}}$ have also been defined element-wise.

In summary, the main characteristics of classical transport are utilization of HAMILTON's equations and invariance of distribution values at their solutions.

7.1.2 Non-classical interferometer elements

In the last section, we have introduced some definitions which are useful for describing propagation of rays through phase space, assuming classical transport is valid. As we have seen before, interferometer elements which are realized by rapidly oscillating laser fields are far outside the regime of classical transport. Like in the last chapter, the non-classical devices have to be treated separately and we have to extend our formalism in order to cover them adequately.

First beam splitter

Recalling the results from section 6.2, a two-path beam splitter splits an incoming distribution into three copies. All of which have envelopes that are equal in their shapes but displaced by $\mathbf{0}$, $\mathbf{v}_G/2$, and $\mathbf{v}_G$ along the velocity axes. To reflect these results in the ray tracing formalism, we split each point of an incoming PSE into three copies which are displaced accordingly.

In terms of our notation, a PSE right before the laser pulse is written as $\underline{\mathbf{z}}(t_1^-)$. Passing the beam splitter, it shall be mapped onto three PSEs

$$\underline{\mathbf{z}}_a(t_1^+) = \underline{\mathbf{z}}(t_1^-), \tag{7.5a}$$

$$\underline{\mathbf{z}}_{ab}(t_1^+) = \underline{\mathbf{z}}(t_1^-) + \tfrac{1}{2}\mathbf{z}_G, \tag{7.5b}$$

$$\underline{\mathbf{z}}_b(t_1^+) = \underline{\mathbf{z}}(t_1^-) + \mathbf{z}_G, \tag{7.5c}$$

In subsequent evolution through the interferometer, each of these three PSEs is affected differently by classical transport as well as non-classical interferometer elements. We are therefore not considering not just a single PSE but several channels of PSEs. These channels correspond to the unkicked, the kicked, and the interference contribution to the total distribution. We call the composite entity $\underline{\underline{\mathbf{z}}} \equiv (\underline{\mathbf{z}}_a, \underline{\mathbf{z}}_{ab}, \underline{\mathbf{z}}_b)$ the *set of phase space channels* (PSC). This way, an incoming state that has a collection of points in the first channel and none in the others can be written as $\underline{\underline{\mathbf{z}}}(t_1^-) = (\underline{\mathbf{z}}(t_1), \emptyset, \emptyset)$. Passing the beam splitter, it is mapped onto the output state represented by

$$\underline{\underline{\mathbf{z}}}(t_1^+) = \left(\underline{\mathbf{z}}(t_1^-), \quad \underline{\mathbf{z}}(t_1^-) + \tfrac{1}{2}\mathbf{z}_G, \quad \underline{\mathbf{z}}(t_1^-) + \mathbf{z}_G\right). \tag{7.6}$$

Thus, in our ray tracing formalism, the laser pulses act on the complete set of phase space channels $\underline{\underline{\mathbf{z}}}$ rather than on individual phase space elements $\underline{\mathbf{z}}_\ell$.

In addition to the fragmentation of the envelope, the interference term of the contribution f_{ab} is spatially oscillating, described by the position dependent phase $\mathbf{Q}_0\mathbf{z}$. Consequently, the proper distribution values belonging to the interference channel are products of the original values $f_0(\underline{\mathbf{z}}(t_0))$ with factors $\cos \mathbf{Q}_0 \overline{\mathbf{z}}(t_1)$. Yet again, we combine the interference pattern phases of all points into a single object $\underline{\varphi}_{ab}$. Right after the beam splitter, at $t = t_1^+$ it reads

$$\begin{aligned} \underline{\varphi}_{ab}(t_1^+) &= \left(\mathbf{Q}_0^\mathsf{T}\,\mathbf{z}_1(t_1^+), \ldots, \mathbf{Q}_0^\mathsf{T}\,\mathbf{z}_r(t_1^+)\right) \\ &= \mathbf{Q}_0^\mathsf{T}\,\underline{\mathbf{z}}_{ab}(t_1^+), \end{aligned} \tag{7.7}$$

depending on all phase space locations of the PSE. In contrast to classical transport, the distribution values associated to the interference channel *do* change each time they pass an interferometer element. Using the beam splitter model introduced in section 6.3.1, the distribution values after the laser pulse become

$$\underline{F}_{aa}(t_1^+) = |\alpha_1|^2 f_0(\underline{\mathbf{z}}_a(t_0)), \tag{7.8a}$$

$$\underline{F}_{ab}(t_1^+) = 2|\alpha_1||\beta_1| \cos(\mathbf{Q}_0\,\underline{\mathbf{z}}_{ab}(t_1^+))\, f_0(\underline{\mathbf{z}}_{ab}(t_0)), \tag{7.8b}$$

$$\underline{F}_{bb}(t_1^+) = |\beta_1|^2 f_0(\underline{\mathbf{z}}_b(t_0)). \tag{7.8c}$$

The values of all channels are then combined to

$$\underline{\underline{F}} = (\underline{F}_{aa}, \underline{F}_{ab}, \underline{F}_{bb}). \tag{7.9}$$

After leaving the beam splitter, the state is again subject to classical transport. The evolution of the set of all phase space points $\underline{\underline{\mathbf{z}}}$ is expressed by applying the operator $\hat{\mathscr{U}}(t_{12})$ to the constituents,

$$\begin{aligned}\underline{\underline{\mathbf{z}}}(t_2^-) &= \hat{\mathscr{U}}(t_{12})\,\underline{\underline{\mathbf{z}}}(t_1^+)\\ &= \left(\hat{\mathscr{U}}(t_{12})\,\underline{\mathbf{z}}_1(t_1^+),\, \dots,\, \hat{\mathscr{U}}(t_{12})\,\underline{\mathbf{z}}_r(t_1^+)\right),\end{aligned} \tag{7.10}$$

while the phases of the interference channel $\underline{\varphi}_{ab}$ remain constant until the next laser pulse.

π-pulse

In order to find a map for PSEs that adequately describes the behaviour of phase space distributions passing π-pulse, we consider the WIGNER function right before the application of the laser,

$$f(\mathbf{z}, t_2^-) = \left(\tfrac{M}{2\pi\hbar}\right)^3 \int \mathrm{d}^3\xi\; e^{-i\frac{M}{\hbar}\xi\mathbf{v}}\, \langle \mathbf{x} + \tfrac{\xi}{2} | \hat{\rho}(t_2^-) | \mathbf{x} - \tfrac{\xi}{2} \rangle, \tag{7.11}$$

including the density matrix

$$\hat{\rho}(t_2^-) = \hat{U}(t_{12})\,\hat{U}_{\mathrm{bs}}\,\hat{U}(t_{01})\,\hat{\rho}_0\,\hat{U}^\dagger(t_{01})\,\hat{U}^\dagger_{\mathrm{bs}}\,\hat{U}^\dagger(t_{12}), \tag{7.12}$$

to the one right after the π-pulse,

$$f(\mathbf{z}, t_2^+) = \left(\tfrac{M}{2\pi\hbar}\right)^3 \int \mathrm{d}^3\xi\; e^{-i\frac{M}{\hbar}\xi\mathbf{v}}\, \langle \mathbf{x} + \tfrac{\xi}{2} | \hat{U}_\pi\, \hat{\rho}(t_2^-)\, \hat{U}^\dagger_\pi | \mathbf{x} - \tfrac{\xi}{2} \rangle, \tag{7.13}$$

where $\hat{U}_{\mathrm{bs}}$ and $\hat{U}_\pi$ are given in expression (6.66) and (6.67), respectively. According to the transformation of the WIGNER function, the PSE channels after the laser pulse are

$$\underline{\underline{\mathbf{z}}}(t_2^+) = \left(\underline{\mathbf{z}}_a(t_2^-) + \mathbf{z}_G,\quad \underline{\mathbf{z}}_{ab}(t_2^-),\quad \underline{\mathbf{z}}_b(t_2^-) - \mathbf{z}_G\right). \tag{7.14}$$

One recognizes the momentum exchange between the classical channels which are the first and the last component of $\underline{\underline{\mathbf{z}}}(t_2^+)$ in this notation. At the same time, the phase of the oscillatory pattern leaps about $-2\mathbf{G}\mathbf{x}$ which leads to

$$\begin{aligned}\underline{\varphi}_{ab}(t_2^+) &= \underline{\varphi}_{ab}(t_1^-) - 2\mathbf{Q}_0\,\underline{\mathbf{z}}_{ab}(t_2^+)\\ &= \mathbf{Q}_0\left(\underline{\mathbf{z}}_{ab}(t_1^+) - 2\underline{\mathbf{z}}_{ab}(t_2^+)\right)\end{aligned} \tag{7.15}$$

at the output of the π-pulse. This phase leap is connected to the sudden change of the oscillation.

contrib. label	splitter	redirector	recombiner	sum of kicks
$a1$	0	$+\mathbf{z}_G$	$-\mathbf{z}_G$	0
$b1$	$+\mathbf{z}_G$	$-\mathbf{z}_G$	0	0
$a2$	0	$+\mathbf{z}_G$	0	$+\mathbf{z}_G$
$b2$	$+\mathbf{z}_G$	$-\mathbf{z}_G$	$+\mathbf{z}_G$	$+\mathbf{z}_G$
$a1b1$	$+\mathbf{z}_G/2$	0	$-\mathbf{z}_G/2$	0
$a2b2$	$+\mathbf{z}_G/2$	0	$+\mathbf{z}_G/2$	$\mathbf{z}_G$
$a1b2$	$+\mathbf{z}_G/2$	0	0	$\mathbf{z}_G/2$
$a2b1$	$+\mathbf{z}_G/2$	0	0	$\mathbf{z}_G/2$
$a1a2$	0	$+\mathbf{z}_G$	$-\mathbf{z}_G/2$	$\mathbf{z}_G/2$
$b1b2$	$+\mathbf{z}_G$	$-\mathbf{z}_G$	$+\mathbf{z}_G/2$	$\mathbf{z}_G/2$

Table 7.1.: Overview of kicks in non-classical interferometer elements

Second beam splitter and detection

As we saw in section 6.3.3, the phase space distribution after the second beam splitter comprises 10 parts in total. These are 4 classical distributions $f_{\ell\ell}$ and 6 terms $f_{\ell\ell'}$ describing the interference between them. The transformations of the Wigner envelopes leads to the following map of classical PSE channels.

$$\underline{\mathbf{z}}_{a1}(t_3^+) = \underline{\mathbf{z}}_a(t_3^-) - \mathbf{z}_G, \tag{7.16a}$$

$$\underline{\mathbf{z}}_{b1}(t_3^+) = \underline{\mathbf{z}}_b(t_3^-), \tag{7.16b}$$

$$\underline{\mathbf{z}}_{a2}(t_3^+) = \underline{\mathbf{z}}_a(t_3^-), \tag{7.16c}$$

$$\underline{\mathbf{z}}_{b2}(t_3^+) = \underline{\mathbf{z}}_b(t_3^-) + \mathbf{z}_G. \tag{7.16d}$$

Remember that the letters a and b refer to the path in the interferometer between t_1 and t_3 and the number in the indices to the output port. Next, for the interference channels one finds

$$\underline{\mathbf{z}}_{a1b1}(t_3^+) = \underline{\mathbf{z}}_{ab}(t_3^-) - \tfrac{1}{2}\mathbf{z}_G, \tag{7.16e}$$

$$\underline{\mathbf{z}}_{a2b2}(t_3^+) = \underline{\mathbf{z}}_{ab}(t_3^-) + \tfrac{1}{2}\mathbf{z}_G, \tag{7.16f}$$

$$\underline{\mathbf{z}}_{a1b2}(t_3^+) = \underline{\mathbf{z}}_{a2b1}(t_3^+) = \underline{\mathbf{z}}_{ab}(t_3^-), \tag{7.16g}$$

$$\underline{\mathbf{z}}_{a1a2}(t_3^+) = \underline{\mathbf{z}}_a(t_3^-) - \tfrac{1}{2}\mathbf{z}_G, \tag{7.16h}$$

$$\underline{\mathbf{z}}_{b1b1}(t_3^+) = \underline{\mathbf{z}}_b(t_3^-) + \tfrac{1}{2}\mathbf{z}_G. \tag{7.16i}$$

An overview of all velocity kicks given by the laser pulses is presented in table 7.1.

Finally, in order to completely determine the state at the output of the recombiner, one needs to know the phases of the interference terms' oscillations. The various laser-induced phase leaps are

$$\underline{\varphi}_{a1b1}(t_3^+) = \underline{\varphi}_{ab}(t_2^+) + \mathbf{Q}_0\, \underline{\mathbf{z}}_{ab}(t_3^+) + \zeta_3, \tag{7.17a}$$

$$\underline{\varphi}_{a2b2}(t_3^+) = \underline{\varphi}_{ab}(t_2^+) + \mathbf{Q}_0\, \underline{\mathbf{z}}_{ab}(t_3^+) + \zeta_3 + \pi, \tag{7.17b}$$

$$\underline{\varphi}_{a1b2}(t_3^+) = \underline{\varphi}_{ab}(t_2^+) + \mathbf{Q}_0\, \underline{\mathbf{z}}_{ab}(t_3^+) + \zeta_3 + \pi, \tag{7.17c}$$

$$\underline{\varphi}_{a2b1}(t_3^+) = \underline{\varphi}_{ab}(t_2^+), \tag{7.17d}$$

$$\underline{\varphi}_{a1a2}(t_3^+) = \mathbf{Q}_0\, \underline{\mathbf{z}}_{a}(t_3^+) + \zeta_3, \tag{7.17e}$$

$$\underline{\varphi}_{a1a2}(t_3^+) = \mathbf{Q}_0\, \underline{\mathbf{z}}_{a}(t_3^+) + \zeta_3 + \pi. \tag{7.17f}$$

Table 7.2 summarizes all phase leaps that alter the interference pattern during propagation. Just like the final WIGNER function given in section 6.3.3, which comprises 10 summands in total, the final function values $\underline{F}(t_3^+)$ can be divided into 10 channels,

$$\begin{aligned}\underline{F}(t_3^+) = \Big(&\underline{F}_{a1a1}(t_3^+),\ \underline{F}_{a1b1}(t_3^+),\ \underline{F}_{b1b1}(t_3^+),\\ &\underline{F}_{a1a2}(t_3^+),\ \underline{F}_{a1b2}(t_3^+),\ \underline{F}_{b1a2}(t_3^+),\ \underline{F}_{b1b2}(t_3^+),\\ &\underline{F}_{a2a2}(t_3^+),\ \underline{F}_{a2b2}(t_3^+),\ \underline{F}_{b2b2}(t_3^+)\Big).\end{aligned} \tag{7.18}$$

Note that we have arranged the contributions of the first and second output port in the first and third line of expression (7.18), respectively. The interference channels between the ports are written in the second line. Classical parts are represented by value sets of the form

$$\underline{F}_{\ell\ell}(t_3^+) = |\gamma_\ell|^2\, f_0(\underline{\mathbf{z}}_\ell(t_0)), \tag{7.19}$$

while the interference parts are described by

$$\underline{F}_{\ell\ell'}(t_3^+) = 2|\gamma_\ell||\gamma_{\ell'}|\, \cos\varphi_{\ell\ell'}\, f_0(\underline{\mathbf{z}}_{\ell\ell'}(t_0)). \tag{7.20}$$

The coefficients of the contributions are given in expression 6.70. The distribution values in the classical channels are, apart from coefficients γ_ℓ, identical to the initial function values. On the other hand, the values in the interference channels are modified with a factor $\cos\varphi_{\ell\ell'}$, that is related to the interference between the paths. Finally, until reaching the detector at $t = t_4$, the function values given above do not change any more.

7.1.3 Forward versus backward propagation

So far, we have discussed ray tracing as a method that propagates distribution samples *forward* in time. We start with sampling the initial function f_0 at a set of chosen points. After a complete

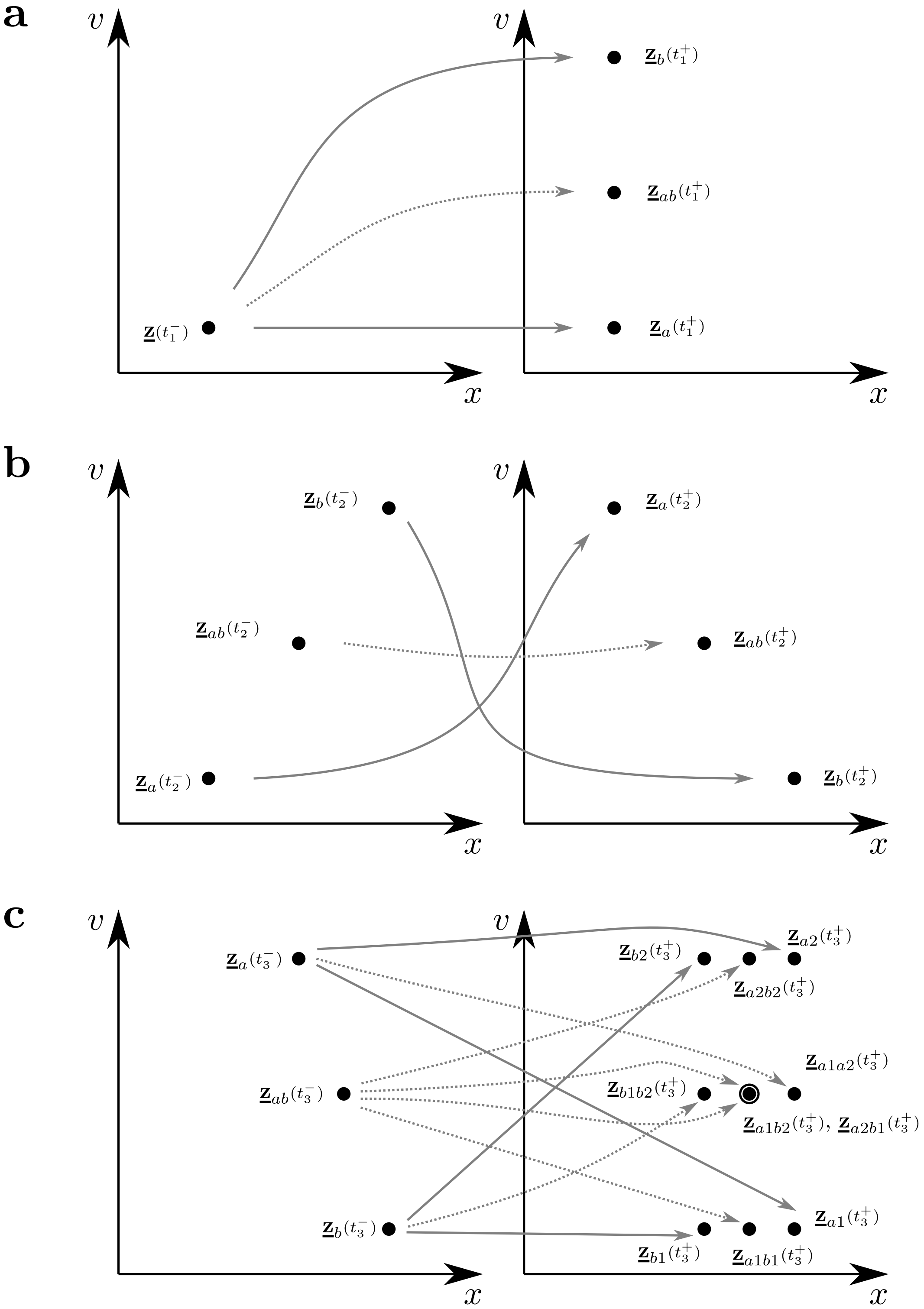
a
v
v
$\underline{\mathbf{z}}_b(t_1^+)$
$\underline{\mathbf{z}}_{ab}(t_1^+)$
$\underline{\mathbf{z}}(t_1^-)$
$\underline{\mathbf{z}}_a(t_1^+)$
x
x
b
v
v
$\underline{\mathbf{z}}_b(t_2^-)$
$\underline{\mathbf{z}}_a(t_2^+)$
$\underline{\mathbf{z}}_{ab}(t_2^-)$
$\underline{\mathbf{z}}_{ab}(t_2^+)$
$\underline{\mathbf{z}}_a(t_2^-)$
$\underline{\mathbf{z}}_b(t_2^+)$
x
x
c
v
v
$\underline{\mathbf{z}}_{a2}(t_3^+)$
$\underline{\mathbf{z}}_a(t_3^-)$
$\underline{\mathbf{z}}_{b2}(t_3^+)$
$\underline{\mathbf{z}}_{a2b2}(t_3^+)$
$\underline{\mathbf{z}}_{a1a2}(t_3^+)$
$\underline{\mathbf{z}}_{ab}(t_3^-)$
$\underline{\mathbf{z}}_{b1b2}(t_3^+)$
$\underline{\mathbf{z}}_{a1b2}(t_3^+)$, $\underline{\mathbf{z}}_{a2b1}(t_3^+)$
$\underline{\mathbf{z}}_{a1}(t_3^+)$
$\underline{\mathbf{z}}_b(t_3^-)$
$\underline{\mathbf{z}}_{b1}(t_3^+)$
$\underline{\mathbf{z}}_{a1b1}(t_3^+)$
x
x

Figure 7.1.: Illustration of mappings of phase space points passing a laser pulse. Part **a**: First beam splitter according to (7.5). Part **b**: π-pulse according to (7.14). Part **c**: Second beam splitter according to (7.16).

contrib. label	**splitter**	**redirector**	**recombiner**	**sum of leaps**
$a1b1$	$+\mathbf{Gx}$	$-2\mathbf{Gx}$	$+\mathbf{Gx}$	0
$a2b2$	$+\mathbf{Gx}$	$-2\mathbf{Gx}$	$+\mathbf{Gx}$	0
$a1b2$	$+\mathbf{Gx}$	$-2\mathbf{Gx}$	$+2\mathbf{Gx}$	$\mathbf{Gx}$
$a2b1$	$+\mathbf{Gx}$	$-2\mathbf{Gx}$	0	$-\mathbf{Gx}$
$a1a2$	0	0	$+\mathbf{Gx}$	$\mathbf{Gx}$
$b1b2$	0	0	$+\mathbf{Gx}$	$\mathbf{Gx}$

Table 7.2.: Overview of interference phase leaps in non-classical interferometer elements. Note that in addition to the position-dependent phases ($\propto$ **Gx**) the phase offsets of the laser pulses (denoted with ζ) contribute to the phase of the interference pattern.

propagation sequence, we obtain a set of final distribution values with associated phase space coordinates. These will depend on our choice of initial sampling points. However, as expressions of the form $f_0(\hat{\mathcal{U}}^{-1}\,\mathbf{z})$ suggest, the evaluation of the final Wigner function is actually done by propagating *backwards* in time to query the initial values. We illuminate this notion with a brief example.

Assume we follow the channel '$a1b1$' along its propagation through the MZI. In terms of initial sampling points $\underline{\mathbf{z}}_0$, their final pendants in the associated channel are $\underline{\mathbf{z}}_{a1b1}(t_4) = \hat{\mathcal{U}}_{a1b1}\underline{\mathbf{z}}_0$. A definition of $\hat{\mathcal{U}}_{a1b1}$ can be found in expression (6.80). According to the propagation rules of last subsection, the corresponding distribution values are

$$\underline{F}_{a1b1}(t_4) = 2|\gamma_{a1}||\gamma_{b1}|\,\cos\left[\mathbf{Q}_0\left(\underline{\mathbf{z}}_{ab}(t_1+\tfrac{\tau}{2}) - 2\underline{\mathbf{z}}_{ab}(t_2+\tfrac{\tau}{2}) + \underline{\mathbf{z}}_{ab}(t_3+\tfrac{\tau}{2})\right)\right] f_0(\underline{\mathbf{z}}_0). \tag{7.21}$$

In deed, this result depends on the initial sampling $\underline{\mathbf{z}}_0$ being subject to different propagators. However, typically we want to evaluate the final distribution *not* in terms on initial abscissas but rather at certain points in phase space. Now, in order to reformulate equation (7.21) in terms of specified final sampling points $\underline{\mathbf{z}}_{a1b1}(t_4)$, one has to express the initial points as back-propagated versions of the final abscissas, $\underline{\mathbf{z}}_0 = \hat{\mathcal{U}}^{-1}_{a1b1}\,\underline{\mathbf{z}}_{a1b1}(t_4)$. We obtain

$$\begin{aligned}\underline{F}_{a1b1}(t_4) = {}& \\ &\cos\left[\mathbf{Q}_0\left(\hat{\mathcal{U}}^{-1}(t_{13})\,\hat{\mathcal{K}}^{-1}_{-G/2}\,\hat{\mathcal{U}}^{-1}(t_{34}) - 2\,\hat{\mathcal{U}}^{-1}(t_{23})\,\hat{\mathcal{K}}^{-1}_{-G/2}\,\hat{\mathcal{U}}^{-1}(t_{34}) + \hat{\mathcal{U}}^{-1}(t_{34})\right)\underline{\mathbf{z}}_{a1b1}(t_4)\right] \\ &\qquad \times f_0\left(\hat{\mathcal{U}}^{-1}_{a1b1}\,\underline{\mathbf{z}}_{a1b1}(t_4)\right).\end{aligned} \tag{7.22}$$

This expression resembles the corresponding contribution to the final Wigner function discussed in section 6.3.3.

Thus, ray tracing with backwards propagation is not only convenient for evaluating final distributions at specified points, we can furthermore recognize previous results from chapter 6. Nevertheless, as we show in the following section, we need both, forward *and* backward propagation, for practical calculations.

7.2 Computing observables

As we noted above, we want to efficiently calculate observable values without constructing the final Wigner function completely. These values are generally obtained by integrating $f(\mathbf{z}, t)$ over some or all axes in phase space. As we discussed in the introduction chapters, expectation values of observables are obtained by

$$\langle a \rangle = \int \mathrm{d}^6 z \, f(\mathbf{z}) a(\mathbf{z}). \tag{7.23}$$

Examples are the mean momentum or the mean velocity of an atom cloud along the i-th coordinate axis, for which one has to insert $a(\mathbf{z}) = x_i$ and $a(\mathbf{z}) = v_i$, respectively. In the following, we will frequently consider the density at position $\mathbf{x}'$, denoted as $n(\mathbf{x}')$, which implies $a(\mathbf{z}) = \delta(\mathbf{x} - \mathbf{x}')$.

Of course it is numerically impossible to integrate an unknown function along entire axes in phase space. Therefore, we first have to gain some rough ideas about the final distribution, in order to adjust our integration method. These "rough ideas" will be represented by *pilot distributions*, introduced in the next subsection.

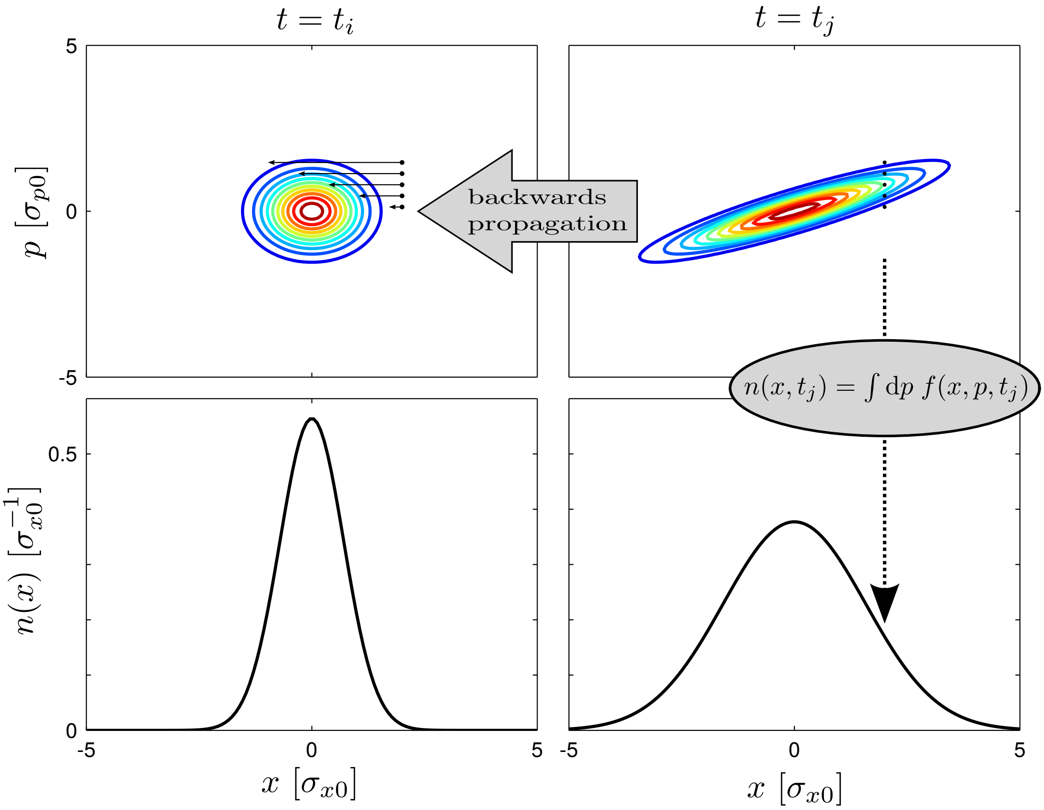

Figure 7.2.: Illustration of computation of density profile by summing over back-propagated phase space points for free propagation in 1D.

We consider propagation of Gaussian distributions with quadratic Hamiltonians as ideal case. Corresponding results are conveniently expressed by affine transformations (see e.g. section 2.3. Proper integration areas for the true (read: potentially non-Gaussian distribution) can then be deduced from the parameters of the Gaussian distribution. The problems we want to tackle with ray tracing methods shall be small deviations from the ideal case. This means that we require the distribution functions to differ only slightly from a perfect Gaussian and higher-than-quadratic contributions to Hamiltonian to be small corrections.

7.2.1 Pilot distributions

In order to narrow down the location and extent of the final distributions' support, we start our simulation procedure by propagating a pilot distribution through the system forward in time. Therefore, we take the center $\bar{\mathbf{z}}_{(t_0)}$ and correlation matrix $\mathsf{C}_{(t_0)}$ of the initial distribution and define a PSE that represents this data properly. With these parameters, we can write the initial pilot distribution as

$$f_0^{(\mathrm{p})}(\mathbf{z}) = N\,\frac{\exp\left[-(\mathbf{z}-\bar{\mathbf{z}}_{(t_0)})^{\mathsf{T}}\,\mathsf{C}_{(t_0)}\,(\mathbf{z}-\bar{\mathbf{z}}_{(t_0)})\right]}{\sqrt{\pi^6 \det \mathsf{C}_{(t_0)}}}, \tag{7.24}$$

being a Gaussian that approximates the true initial distribution $f_0(\mathbf{z})$. The pilot distribution is an auxiliary object that enables us to chose the optimal method for numerical integration.

Envelopes

Center and widths of a single distribution envelope are sufficiently represented by 7 rays. First, the center is given by

$$\bar{\mathbf{z}}(t_0) = \langle \mathbf{z} \rangle_{f_0}\,. \tag{7.25}$$

Next, the widths and orientations are given by the correlation matrix which can be encoded by six phase space vectors. These may be constructed as follows. Being symmetric, the correlation matrix can be diagonalized (see appendix A),

$$\mathsf{C}_{(t_0)} = \mathsf{P}\ \mathrm{diag}(\sigma_1^2, \ldots, \sigma_6^2)\ \mathsf{P}^{\mathsf{T}}, \tag{7.26}$$

where $\sigma_1^2, \ldots, \sigma_6^2$ are the eigenvalues of the correlation matrix $\mathsf{C}_{(t_0)}$. This means they satisfy

$$(\mathsf{C} - \sigma_i^2 \mathbb{1})\,\mathbf{e}_i = \mathbf{0}. \tag{7.27}$$

The transformation matrix in equation (7.26) comprises the eigenvectors as columns,

$$\mathsf{P} = (\mathbf{e}_1, \ldots, \mathbf{e}_6). \tag{7.28}$$

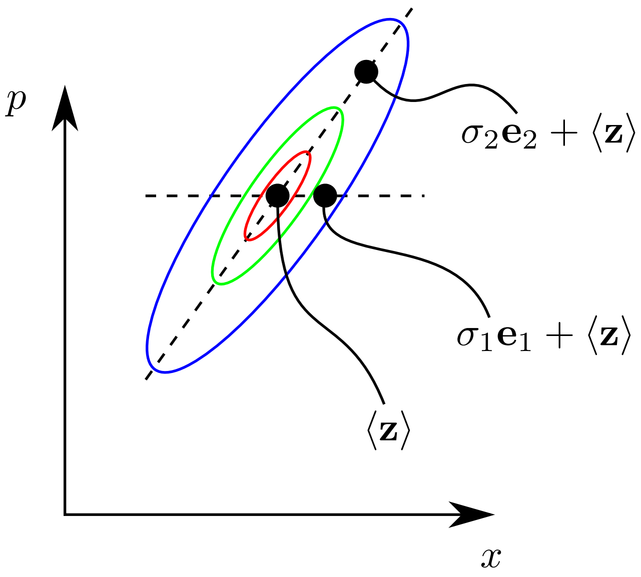
p
$\sigma_2 \mathbf{e}_2 + \langle \mathbf{z} \rangle$
$\sigma_1 \mathbf{e}_1 + \langle \mathbf{z} \rangle$
$\langle \mathbf{z} \rangle$
x

Figure 7.3.: Representing 1D phase space distribution with 3 phase space points.

Hence, the correlation matrix can be represented by a set of six vectors,

$$\boldsymbol{\sigma}_i(t_0) = \sigma_i \, \mathbf{e}_i, \quad i = 1, \ldots, 6. \tag{7.29}$$

They can be combined into a matrix

$$\begin{aligned} \Sigma(t_0) &= (\boldsymbol{\sigma}_1(t_0), \ldots, \boldsymbol{\sigma}_6(t_0)) \\ &= \mathsf{P}\,\mathrm{diag}(\sigma_1, \ldots, \sigma_6), \end{aligned} \tag{7.30}$$

which is the Cholesky decomposition of the correaltion matrix, $\mathsf{C} = \Sigma\Sigma^{\mathsf{T}}$. Altogether, the set of seven phase space points

$$\underline{\mathbf{z}}^{(\mathrm{p})}(t_0) = \Big(\bar{\mathbf{z}}(t_0), \quad \bar{\mathbf{z}}(t_0) + \boldsymbol{\sigma}_1(t_0), \quad \ldots \quad , \quad \bar{\mathbf{z}}(t_0) + \boldsymbol{\sigma}_6(t_0)\Big) \tag{7.31}$$

constitutes the *pilot phase space element* containing information about the center and the correlation matrix of the associated distribution f_0. It can be pictured as a six armed cross in phase space that is a skeleton of the real distribution it describes. An illustration of this ray representation for a 1D case is shown in figure 7.3. Clearly, for describing the final Wigner function of an MZI, we have to define a pilot distribution for each channel. Concerning non-classical interferometer elements such as beam splitters, the Wigner function is fragmented into several channels and, likewise, the pilot distribution values and sampling points are fragmented into corresponding channels. The final PSEs are given by

$$\underline{\mathbf{z}}^{(\mathrm{p})}_{\ell}(t_4) = \hat{\mathcal{U}}_{\ell}(t_{04})\, \underline{\mathbf{z}}^{(\mathrm{p})}_{\ell}(t_0), \tag{7.32a}$$

$$\underline{\mathbf{z}}^{(\mathrm{p})}_{\ell\ell'}(t_4) = \hat{\mathcal{U}}_{\ell\ell'}(t_{04})\, \underline{\mathbf{z}}^{(\mathrm{p})}_{\ell}(t_0). \tag{7.32b}$$

Using this expressions, the final pilot distributions in the classical channels can be written as

$$f^{(\mathrm{p})}_{\ell\ell}(\mathbf{z},t) = N\,|\gamma_\ell|^2\,\frac{\exp\left[-(\mathbf{z}-\bar{\mathbf{z}}_\ell(t))^{\mathsf{T}}\,\mathsf{C}^{-1}(t)\,(\mathbf{z}-\bar{\mathbf{z}}_\ell(t))\right]}{\sqrt{\pi^6\det\mathsf{C}(t)}}, \tag{7.33}$$

its correlation matrix is given by

$$\begin{aligned}\mathsf{C}(t) &= \Sigma(t)\,\Sigma^{\mathsf{T}}(t)\\ &= \mathsf{U}(t_{04})\,\Sigma(t_0)\left(\mathsf{U}(t_{04})\,\Sigma(t_0)\right)^{\mathsf{T}}\\ &= (\boldsymbol{\sigma}_1(t),\ldots,\boldsymbol{\sigma}_6(t))^{\mathsf{T}}(\boldsymbol{\sigma}_1(t),\ldots,\boldsymbol{\sigma}_6(t)).\end{aligned} \tag{7.34}$$

Similarly, the interference terms are

$$f^{(\mathrm{p})}_{\ell\ell'}(\mathbf{z},t) = 2N\,|\gamma_\ell||\gamma_{\ell'}|\,\cos\varphi_{\ell\ell'}\,\frac{\exp\left[-(\mathbf{z}-\bar{\mathbf{z}}_{\ell\ell'}(t))^{\mathsf{T}}\,\mathsf{C}^{-1}(t)\,(\mathbf{z}-\bar{\mathbf{z}}_{\ell\ell'}(t))\right]}{\sqrt{\pi^6\det\mathsf{C}(t)}}, \tag{7.35}$$

where the pilot phases are discussed below. The complete distribution

$$f^{(\mathrm{p})} = \sum_{\ell} f^{(\mathrm{p})}_{\ell} + \sum_{\ell<\ell'} f^{(\mathrm{p})}_{\ell\ell'} \tag{7.36}$$

approximates the true Wigner function in its most basic characteristics, these are its center and their widths.

Interference pattern

The contributions that describe the interference between classical paths exhibit rapid oscillations in phase space. These may render numerical integration cumbersome if not impossible. Thus, we will have to “separate” the strongly oscillating term from the rest of the slowly varying integrand. Therefore, we require the pilot distribution channels to be a guidance, not only for centers and widths of the true distribution, but also for its oscillations in phase space. To each interference channel we hence associate a pilot oscillation phase

$$\varphi^{(\mathrm{p})}_{\ell\ell'} = \mathbf{Q}^{(\mathrm{p})}_{\ell\ell'}\,\mathbf{z} + \overline{\varphi}^{(\mathrm{p})}_{\ell\ell'} \tag{7.37}$$

comprising an interference vector $\mathbf{Q}^{(\mathrm{p})}_{\ell\ell'}$ and an offset $\overline{\varphi}^{(\mathrm{p})}_{\ell\ell'}$. The latter is independent of $\mathbf{z}$. Being subject to quadratic Hamiltonians, for example, the interference vector is transformed by simple matrix multiplication,

$$\mathbf{Q}^{(\mathrm{p})}_{\ell\ell'}(t_j) = \mathsf{U}^{\mathsf{T}}(t_{ij})\,\mathbf{Q}^{(\mathrm{p})}_{\ell\ell'}(t_i). \tag{7.38}$$

Geometrically speaking, the interference pattern is rotated, stretched and compressed and can thus always be described in the form of (7.37). In contrast, higher-order Hamiltonians entail more complicated transformations that may distort the initially straight-lined interference pattern, which cannot be described by a constant interference vector anymore. Again, we assume these higher-than-quadratic contributions to be sufficiently small so that expression (7.37) gives a good approximation to the interference pattern of a certain channel.

7.2.2 Integrating phase space distributions

Consider for instance, we want to calculate the position density $n(\mathbf{x})$ at a certain point $\mathbf{x}$ after some propagation time t, being aware only of center $\overline{\mathbf{z}}$ and correlation matrix C of the pilot distribution. Aiming for an efficient numerical integration method that requires a minimal number of function evaluations, we have to exploit all "hints" that are given by the pilot distribution $f^{(\mathrm{p})}$. The details of these methods depend to large extend on how fast the integrand oscillates. In any case, we divide the final distribution parts $f_{\ell\ell'}(\mathbf{z}, t_4)$ into products of two or more functions, one of them being the propagated initial pilot distribution $f_0(\Sigma^{-1}(\mathbf{z}-\overline{\mathbf{z}}))$. The latter is given in terms of the pilot PSE.

Non- or slowly oscillating distribution parts

Writing the true Wigner function as

$$f_{\ell\ell'}(\mathbf{z}, t) = f_0^{(\mathrm{p})}\Big(\Sigma^{-1}(t)\,(\mathbf{z}-\overline{\mathbf{z}}(t))\Big)\, g(\mathbf{z}, t), \tag{7.39}$$

i.e. a product of the Gaussian pilot distribution $f^{(\mathrm{p})}$, expressed in (7.37), and an initially unknown function g, the integral of $f(\mathbf{z})$ over some or all axes can be approximated by Gauss-Hermite quadrature. As pointed out in appendix A.4, this integration method works well if g is a polynomial of limited order. A condition that is very likely to be satisfied by the classical parts of the final Wigner function, $f_{\ell\ell}$, but clearly violated by rapidly oscillating interference parts[1], $f_{\ell\ell'}$. We start with discussing the former case before treating the latter ones.

If we can assume the ratio of the true distribution and the pilot, g, to be a limited order polynomial, we can directly utilize expression A.27 to integrate $f_{\ell\ell'}(\mathbf{z})$ over all axes. The Gauss-Hermite quadrature rule [119, 120] reads

$$\int_{\mathbb{R}^6} \mathrm{d}^6\mathbf{z}\, f_{\ell\ell'}(\mathbf{z}, t) \approx |\det\Sigma| \sum_{|\underline{m}|\leq r} \tilde{w}_{\underline{m}}\, f_{\ell\ell'}(\mathbf{z}_{\underline{m}}(t),\ t), \tag{7.40}$$

with 6-tuples $\underline{m} = (m_1, \ldots, m_6)$ and their sum $|\underline{m}| = m_1 + \ldots + m_6$. The number of phase space points r, is the number of abscissas sampling $f_{\ell\ell'}$. The series coefficients are products of the corresponding quadrature weights $\tilde{w}_{\underline{m}} = \tilde{w}_{m_1} \cdot \ldots \cdot \tilde{w}_{m_6}$. The nodes where the final distribution is evaluated are given by

$$\mathbf{z}_{\underline{m}}(t) = \Sigma(t)\, \xi_{\underline{m}} + \overline{\mathbf{z}}(t), \tag{7.41}$$

---

[1] Although it is possible to approximate the oscillatory modulation in the support of the Gaussian envelope by a finite-order polynomial, one had to go to very high orders to achieve sufficient accuracy. Apart from requiring more function evaluations, the largest coefficient of a Hermite polynomial H_m grows very fast with increasing the order. This makes numerical root finding more and more unstable.

using the dimensionless vector $\xi = (\xi_{m_1}, \ldots, \xi_{m_6})^\mathsf{T}$ whose components are the n_i-th roots of the r-th order HERMITE polynomial. If $g(\mathbf{z})$ is of order $2r-1$ or lower, the equation (7.40) is exact. In this procedure, the correlation matrix $\mathsf{C} = \Sigma\Sigma^\mathsf{T}$ and the offset $\bar{\mathbf{z}}$ determine the phase space locations of the integration abscissas. They do not necessarily coincide with the correlation matrix and offset of the complete distribution to integrate, f. Nevertheless, the parameters Σ and $\bar{\mathbf{z}}$ are obtained from the pilot PSE, as prescribed in the last subsection, and should therefore provide a good approximation to the true distribution f.

For classical contributions $f_{\ell\ell}$, the values of the final distribution in the sum in (7.40) are calculated by propagating abscissas $\mathbf{z}_{\underline{m}}$ backwards in time and query the values of the initial distribution at the back-propagated abscissas,

$$f_{\ell\ell}(\mathbf{z}_{\underline{m}(t_4)},\ t_4) = |\gamma_\ell|^2\, f_0\left(\hat{\mathscr{U}}_\ell^{-1}(t_{04})\, \mathbf{z}_{\underline{m}(t_4)}\right). \tag{7.42}$$

Like before, the forward-propagated WIGNER function is expressed as the initial distribution with back-propagated phase space coordinates. Tracing back phase space trajectories, starting at the integration abscissas (7.41), to evaluate the corresponding distribution values can be considered the core routine of our ray tracing procedure. In case classical transport is ruled by quadratic Hamiltonians, one can revert to analytic results given in section 6.3.4. These are used as a benchmark to our numerical algorithm.

Integration with GAUSS-HERMITE quadrature may be not only suitable for classical contributions but also for interference terms that are slowly oscillating in phase space. These may for example occur in the output ports of a nearly symmetric MZI. Periodic modulations are included simply by attaching an interference phase to each abscissa,

$$f_{\ell\ell'}(\mathbf{z}_{\underline{m}(t_4)},\ t_4) = 2|\gamma_\ell||\gamma_{\ell'}|\ \cos\left(\varphi_{\ell\ell'}(\mathbf{z}_{\underline{m}(t_4)})\right) f_0\left(\hat{\mathscr{U}}_{\ell\ell'}^{-1}(t_{04})\, \mathbf{z}_{\underline{m}(t_4)}\right). \tag{7.43}$$

Assuming the oscillation to be sufficiently slow, i.e. $|\nabla_z \varphi| \ll |\det \Sigma|$, the ratio of $f_{\ell\ell'}$ to the Gaussian $f_0^{(\mathrm{p})}(\Sigma^{-1}(\mathbf{z}-\bar{\mathbf{z}}))$ is still well approximated by a limited order polynomial. The value of $\varphi_{\underline{m}}$ can be calculated successively while propagating the abscissas to the initial time instance. Starting with a phase of zero, we add a phase leap every time the rays pass a non-classical interferometer element as given in table 7.2. This procedure was exemplified in section 7.1.3.

In addition to integrals of distributions over complete phase space, we also consider observables which are obtained by integrating only over part of all phase space axes. The most important quantity of this kind is the position density $n(\mathbf{x})$. Following expression (A.28), we find

$$n(\mathbf{x},t) = \int_{\mathbb{R}^3} \mathrm{d}^3\mathbf{v}\, f(\mathbf{x},\mathbf{v}) = \sum_{|\underline{m}|\le r} \tilde{w}_{\underline{m}}\, f(\mathbf{x}, \mathbf{v}_{\underline{m}(\mathbf{x},t)}). \tag{7.44}$$

The sampling points in velocity subspace

$$\mathbf{v}_{\underline{m}(\mathbf{x},t)} = \mathsf{A}_{vv}^{-1/2}\xi_{\underline{m}} - \mathsf{A}_{vv}^{-1}\mathsf{A}_{vx}(\mathbf{x}-\bar{\mathbf{x}}) + \bar{\mathbf{v}} \tag{7.45}$$

are determined by the position $\mathbf{x}$, the position and velocity parts of the pilot's offset, $\bar{\mathbf{x}}$ and $\bar{\mathbf{v}}$, respectively. The pilot's correlation matrix C has been subdivided into block matrices A_{xx}, A_{vv}, and A_{xv} as instructed in (A.9). Of course, the above calculation goes analogously if one wants to integrate e.g. over all position axes to obtain a density in velocity space $\tilde{n}(\mathbf{v})$ or over all but one axis to obtain a 1D density $n(x)$.

Furthermore, the above quadrature formula can be trivially extended to calculate all kinds of moments of the final distribution. These are given by integrals over the distribution times a polynomial in phase space coordinates, $\mathscr{P}(\mathbf{z})\,f(\mathbf{z})$, which are calculated simply by substituting $\mathscr{P}f$ for f on both sides of expression (7.40) and (7.44).

Strongly oscillating distribution parts

In contrast to slowly varying Gaussian-like distribution parts, rapidly oscillating contributions to the total WIGNER function are not suitable for GAUSS-HERMITE quadrature. Assuming the pilot interference vector $\mathbf{Q}^{(\mathrm{p})}$ to describe the oscillatory behavior sufficiently well, we separate the considered distribution as

$$f_{\ell\ell'}(\mathbf{z}) = \cos\left(\mathbf{Q}^{(\mathrm{p})}\,\mathbf{z} + \overline{\varphi}\right)\,\frac{\exp\left[-(\mathbf{z}-\bar{\mathbf{z}})^{\mathsf{T}}\,\mathsf{C}^{-1}\,(\mathbf{z}-\bar{\mathbf{z}})\right]}{\sqrt{\pi^6\det\mathsf{C}}}\,g(\mathbf{z}) \tag{7.46}$$

such that g is again a limited-order polynomial. The parameters $\bar{\mathbf{z}}$, C, and Σ are known from the pilot PSE. This way, we can apply the recipe from appendix A.5 to obtain the integral

$$\int_{\mathbb{R}^6} \mathrm{d}^6z\; f_{\ell\ell'}(\mathbf{z}) = 2^6\,\cos\left(\mathbf{Q}^{(\mathrm{p})}\,\bar{\mathbf{z}} + \overline{\varphi}\right)\,e^{-\mathbf{q}^2/4}\sum_{l=0}^{\infty}\cos\left(\tfrac{l\pi}{2}+\overline{\varphi}\right)\sum_{|\underline{m}|=l} c_{\underline{m}}\mathbf{q}^{\underline{m}}. \tag{7.47}$$

The monomials in the sum are explicitly written as $\mathbf{q}^{\underline{m}} = q_1^{m_1}\cdot\ldots\cdot q_6^{m_6}$ with the dimensionless vector $\mathbf{q} \equiv \Sigma^{\mathsf{T}}\,\mathbf{Q}^{(\mathrm{p})}$ being the scaled interference vector. Its absolute value is a measure for the number of oscillations within the support of the envelope. The sum coefficients $c_{\underline{m}}$ are obtained by projection of g onto the multivariate HERMITE polynomials $H_{\underline{m}}(\mathbf{z}) = H_{m_1}(z_1)\cdot\ldots\cdot H_{m_6}(z_6)$ with respect to the Gaussian weight function $f^{\,(\mathrm{p})}$,

$$c_{\underline{m}} = \int_{\mathbb{R}^6}\mathrm{d}^6z\;\frac{\exp\left[-(\mathbf{z}-\bar{\mathbf{z}})^{\mathsf{T}}\,\mathsf{C}^{-1}\,(\mathbf{z}-\bar{\mathbf{z}})\right]}{\sqrt{\pi^6\det\mathsf{C}}}\,H_{\underline{m}}\left[\Sigma^{-1}(\mathbf{z}-\bar{\mathbf{z}})\right]\,g(\mathbf{z}). \tag{7.48}$$

A consequence of g being a limited-order polynomial is that the coefficients $c_{\underline{m}}$ are non-zero only for a limited number of combinations $\underline{m}$. Consequently, the sum in (7.48) terminates after a few terms with $l \leq r'$. Hence, the integral (7.47) is limited by the factor $\exp(-\mathbf{q}^2/4)$. This means, for growing magnitudes of $\mathbf{q}$, which either means shorter laser wave length or larger atom cloud (e.g. via temperature increase), contributions from interference terms to the density become negligible. The projection integral (7.48) can again be calculated with GAUSS-HERMITE quadrature,

$$c_{\underline{m}} = \tfrac{1}{\pi^3} \sum_{|\underline{m}'|\leq r'} w_{\underline{m}'} H_{\underline{m}}\big(\Sigma^{-1}(\mathbf{z}_{\underline{m}'} - \overline{\mathbf{z}})\big)\; g(\mathbf{z}_{\underline{m}'}). \tag{7.49}$$

Remember that the abscissas $\mathbf{z}_{ulm'}$ are part of the r-th order quadrature rule. Hence, the matrix elements the linear equation (7.49), $w_{\underline{m}'} H_{\underline{m}}(\Sigma^{-1}(\mathbf{z}_{\underline{m}'} - \overline{\mathbf{z}}))$, are fixed by the orders r and r'. The former is just our choice of quadrature order. The latter relates to the function g. Accurate results are obtained for $r > r'$.

Again, the function evaluations $f(\mathbf{z}_{\underline{m}})$ and $g(\mathbf{z}_{\underline{m}})$ involve backward propagation to the initial distribution, as instructed in (7.42).

7.2.3 Description of algorithm

We now have available the ingredients to formulate a ray tracing procedure for the calculation of observables that correspond to propagated states at the detector of a MZI. The complete algorithm is sketched in figure 7.4.

The first step is propagate the pilot distribution (or pilot PSE) forward in time. The final pilot distributions then contain basic informations of (or approximations to) the true final distribution.

Concerning numerical integration that is involved in the computation of observables, we exploit the pilot distribution to make an educated guess for optimal integration method and abscissas. Thereby, we have to consider all channels. This means, in each channel we generate a set of abscissas. Propagating them backwards in time, of course, each channel hosts different trajectories leading to different samplings of the initial distribution. This is exemplified in figure 7.5 for density calculation after a single beam splitter. Clearly, as long as basic system parameters (e.g. trap frequencies, particle mass, etc.) are not changed, we can use the same pilot distribution that has been generated once, over and over again for computing different observable.

7.3 Results of simulating a Mach-Zehnder interferometer

We now present results of applying the ray tracing algorithm described in section 7.2.3. Therefore, we consider an MZI with symmetric beam splitters, implying

$$|\gamma_{a1}| = |\gamma_{b1}| = |\gamma_{a2}| = |\gamma_{b2}| = \tfrac{1}{2}. \tag{7.50}$$

The initial state shall be a thermal cloud of $N_p = 10^5$ rubidium atoms, held in a harmonic trap with frequencies $(\omega_1, \omega_2, \omega_3) = 2\pi(127.3,\ 127.3,\ 31.8)$ Hz. The lattice vector of the optical potentials is assumed to be $\mathbf{G} = (0,\ 0,\ 31.42)\,\mu\text{m}^{-1}$. The latter corresponds to a laser wave length of $\lambda_l \approx 400$ nm.

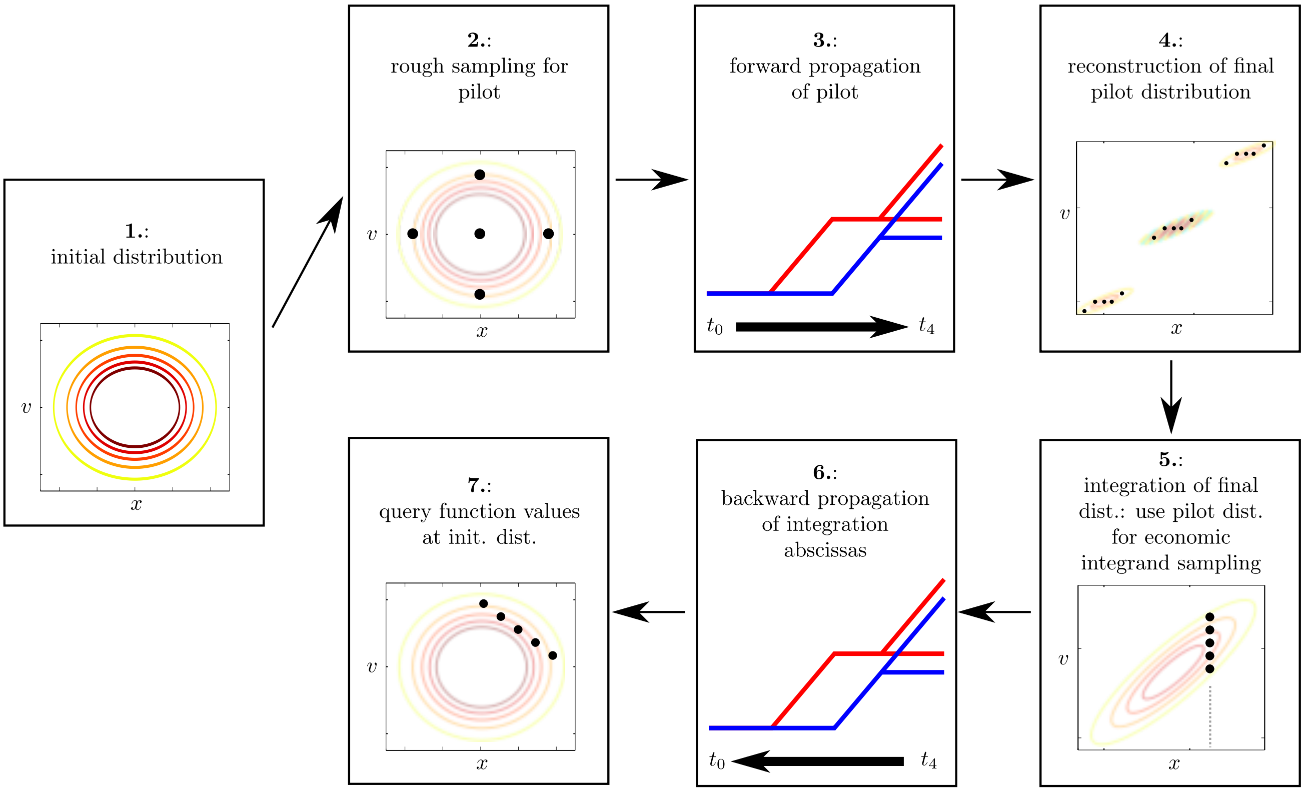
1.:
initial distribution
v
x
2.:
rough sampling for pilot
v
x
3.:
forward propagation of pilot
t_0
t_4
4.:
reconstruction of final pilot distribution
v
x
5.:
integration of final dist.: use pilot dist. for economic integrand sampling
v
x
6.:
backward propagation of integration abscissas
t_0
t_4
7.:
query function values at init. dist.
v
x

Figure 7.4.: Schematic overview of observable computation via ray tracing. For a given set of experimental parameters, the upper row (steps 1-4) has to be executed once to determine the final pilot distribution. For each observable value, e.g. for the position density at each position, the lower row (steps 5-7) has to be run through anew.

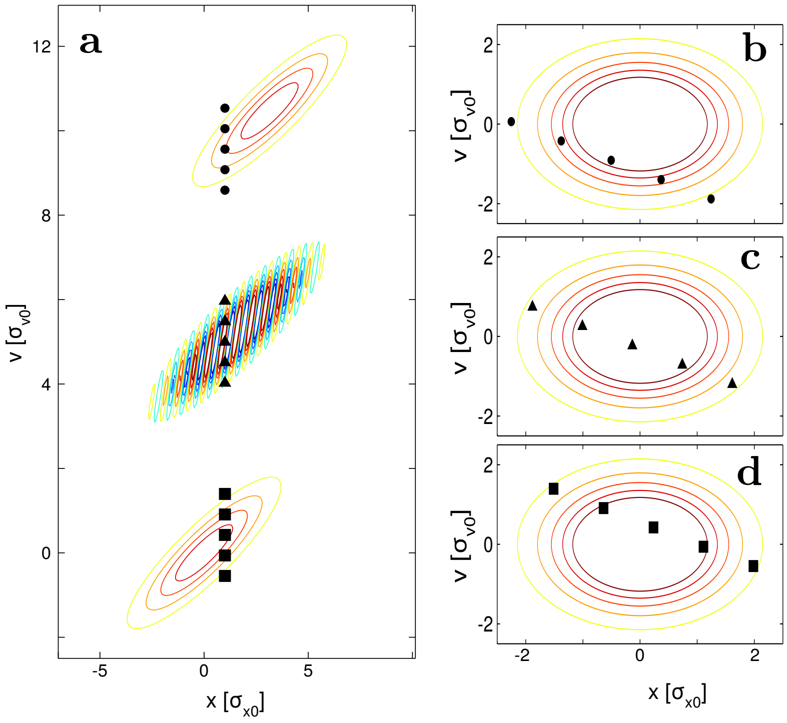

Figure 7.5.: Quadrature abscissas for calculating the position density after a single beam splitter in one dimension. Initial distribution is a Gaussian in a harmonic trap with frequency ω. Parameters are $\sigma_{x0}G = 0.6$, $\omega t_{01} = 1.5$, $\omega t_{12} = 0.3$. Part **a**: Abscissas for integrating the final WIGNER function along the velocity axis, overlaid with iso-lines of all pilot distribution parts. The interference term of the pilot distribution is additionally modulated according to the pilot interference vector. Parts **b**, **c**, **d**: Back-propagated abscissas overlaid with iso-lines of initial distribution for lower (**d**), upper (**b**), and interference (**c**) channel.

7.3.1 Interference fringes of an asymmetric interferometer

To begin with, we examine the oscillatory pattern of the density profile that results from an asymmetric MZI ($t_{12} \neq t_{23}$) with free propagation between the laser pulses. We consider the three-dimensional density of the first output port along the direction of the laser pulse, $n_{11}(0,0,x)$. A detailed discussion of the second output port is omitted since the main characteristics of its interference fringes (i.e. k_{if}, $\mathscr{C}_{\text{if}}$) are identical to those of output port 1. According to the results (6.110) and (6.111) from section 6.3.5 it is written as

$$n_{11}(0,0,x) = \tfrac{1}{4} \frac{N}{\sqrt{\pi^3 \det \mathrm{C}_{x(t_4)}}} \times \left\{ e^{-\frac{(x-v_G t_{23})^2}{\sigma^2(t_4)}} + e^{-\frac{(x-v_G t_{12})^2}{\sigma^2(t_4)}} + 2\mathscr{C}_{\text{if}} \cos(k_{\text{if}} x)\, e^{-\frac{(x-v_G t_{13}/2)^2}{\sigma^2(t_4)}} \right\}. \tag{7.51}$$

We have denoted the width along the third laser pulse direction, which is common to all contributions, as σ. It is given in terms of the initial width as

$$\sigma(t) = \sqrt{1+\omega^2 t^2}\, \sigma_0, \tag{7.52}$$

where ω is the trap frequency along the laser pulse direction. The initial width is given in terms of the this frequency, the temperature and the particles' mass,

$$\sigma_0^2 = \tfrac{\hbar}{M\omega} \frac{1}{\tanh\left(\frac{\hbar\omega}{2k_B T}\right)}, \tag{7.53}$$

according to section 3.2.3. For quantitatively discussing frequency and contrast of the interference fringes, we compute the absolute value of the Fourier transform of expression (7.51),

$$\begin{aligned} |\tilde{n}(k)| &= |\int \mathrm{d}x\, e^{-ikx}\, n_{11}(0,0,x)| \\ &= N\sqrt{\tfrac{\sigma^2}{\pi^2 \det \mathrm{C}_x}} \left[\cos^2 \tfrac{k v_G (t_{23}-t_{12})}{2}\, e^{-\sigma^2 k^2/4} + \frac{\mathscr{C}_{\text{if}}}{2} \sum_{\mp} e^{-\sigma^2 (k \mp k_{\text{if}})/4} \right] \end{aligned} \tag{7.54}$$

It has a central maximum at $k = 0$ and two outer maxima at $k = \pm k_{\text{if}}$. Obviously, the contrast of the fringes is given as the ratio of the outer maxima to the central maximum.,

$$\mathscr{C}_{\text{if}} = \frac{|\tilde{n}(+k_{\text{if}})| + |\tilde{n}(-k_{\text{if}})|}{|\tilde{n}(0)|}. \tag{7.55}$$

Analytic expressions for fringe frequency and contrast are given in equations (6.113) and (6.112), respectively. In the current setting, they can be written as

$$k_{\text{if}} = \frac{\omega^2\, t_{04}(t_{23}-t_{12})}{1+\omega^2 t_{04}^2}\, G, \tag{7.56}$$

$$\mathscr{C}_{\text{if}} = \exp\left[-\tfrac{1}{4} \frac{\omega^2 (t_{23}-t_{12})^2}{1+\omega^2 t_{04}^2}\, \sigma_0^2 G^2 \right]. \tag{7.57}$$

Temperature dependence of fringe contrast

First, we want to demonstrate occurrence of interference fringes in the density profile of a single output port. The contrast of these fringes should decrease for higher temperatures. This is expressed in relation (7.53), showing that the initial width σ_0 becomes larger if T is increased. An extended phase space distribution means an interference term that consists of more oscillations. These, in turn, cancel each other quickly in the course of free expansion. The dependence of the fringe contrast on the initial width is expresses in relation (7.57).

In our example, the time spans between the laser pulses are $t_{01} = 20\mathrm{ms}$ (release - 1st beam splitter), $t_{12} = 10\mathrm{ms}$ (1st beam splitter - π-pulse), $t_{23} = 9.9\mathrm{ms}$ (π-pulse - 2nd beam splitter), $t_{34} = 10\mathrm{ms}$ (2nd beam splitter - detector). Figure 7.6 shows the resultant density for a choice of different temperatures 100nK, 500nK, and 1000nK.

One can already recognize a loss of contrast for higher temperatures by only regarding the 2D and 1D slices of the density in the left and middle column, respectively (parts **a**, **b**, **d**, **e**, **g**, **h**). The loss of contrast is however most obvious when considering the absolute value of FOURIER transform of the 1D density slices in the right column (**c**, **f**, **i**). Here, the reduction on $\mathscr{C}_{\mathrm{if}}$ is revealed by the decreasing ratio of side maxima to the central maximum according to equation (7.55).

For creating the 1D plots (figure 7.6, parts **b**, **e**, **h**), we calculated density values on a position grid with 512 points. For the 2D plots (figure 7.6, parts **a**, **d**, **g**) we used a mesh grid with 64×64 points. Absolute values of the FOURIER transforms of the 1D-density sclices (figure 7.6, **c**, **f**, **i**) were computed with fast-FOURIER-transform routines (FFT). The density contributions from the classical terms were computed with GAUSS-HERMITE quadrature using $r = 5 \times 5 \times 5 = 125$ abscissas. Although this is an extremely low number for numerically integrating the three-dimensional velocity distribution at a particular position, the quadrature rule would be exact even for Gaussians times an eleventh-order polynomial and not just a simple Gaussian. In addition, the interference terms exhibit oscillations along some velocity axis. For medium oscillation frequencies the GAUSS-HERMITE quadrature is replaced by the trapezoidal rule, using 32 abscissas along that direction. Thus, for computing the density contribution from an interference term at a single position, we use $r = 5 \times 5 \times 32 = 800$ abscissas. Finally, since the complete WIGNER function in the first output port comprises two classical and one interference term, for creating each 2D plot in figure 7.6 we have propagated $r_{\mathrm{tot}} = 4,300,800$ rays in total.

7.3.2 Free expansion of interference fringes

Next, we examine how the final density profile changes with variable time span between recombination and detection, t_{34}, keeping all other time spans (t_{03}, t_{12}, t_{23}) fixed. The wave number of the interference fringes, depending on the laser pulse timings is given in equation (7.56). For

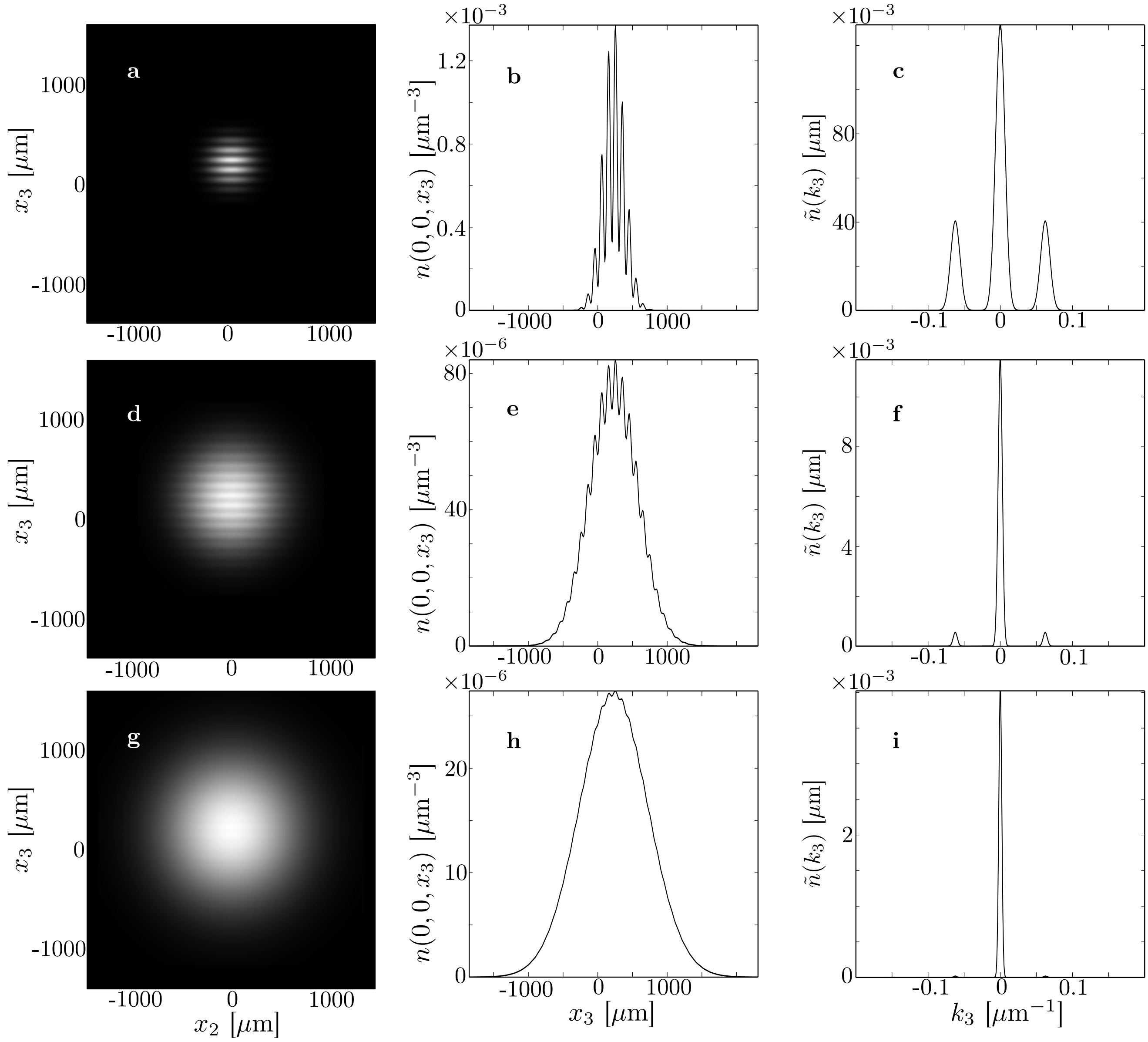

Figure 7.6.: Ray tracing results of position density after passing an asymmetric MZI. Various temperatures of the initial state are considered. These are $T = 100$nK (1st row, **a**, **b**, **c**), $T = 500$nK (2nd row, **d**, **e**, **f**), and $T = 1000$nK (3rd row, **g**, **h**, **i**). The left column (parts **a**, **d**, **g**) shows 2D slices in the x_2-x_3-plane with x_1=0 of the 3D density. The middle column (parts **b**, **e**, **h**) displays the densities along the x_3 axis with $x_1 = x_2 = 0$. The right column (parts **c**, **f** ,**i**) shows the absolute values of Fourier transforms of densities along the x_3 axis, depicted in the middle columns. Initial state parameters are $(\omega_1, \omega_2, \omega_3) = 2\pi(127.3,\ 127.3,\ 31.8)$Hz, $M = 87$amu, $N = 10^5$. MZI parameters are $t_{01} = 20$ms, $t_{12} = 10$ms, $t_{23} = 9.9$ms, $t_{34} = 10$ms, $\mathbf{G} = (0,\ 0,\ 31.42)\mu\text{m}^{-1}$.

the current disscussion we also consider the corresponding wave length $\lambda_{\text{if}} = 2\pi/k_{\text{if}}$. It was given in equation (6.114) and explicitely reads

$$\lambda_{\text{if}}(t_{34}) = \frac{2\pi}{G}\,\frac{1+\omega^2(t_{03}+t_{34})^2}{\omega^2(t_{03}+t_{34})(t_{23}-t_{12})}. \tag{7.58}$$

We saw that it grows linearly in the asymptotic limit

$$\lambda_{\text{if}} \overset{t_{34}\to\infty}{\approx} \frac{2\pi}{G}\,\frac{t_{34}}{|t_{23}-t_{12}|}. \tag{6.115'}$$

Consequently, since the width of the cloud also grows linearly long time after its release, the number of fringes across the cloud remains constant in the long term.

For examining the expansion of the interference fringes, we keep the temperature fixed at $T = 100nK$ and vary the time spans between the second beam splitter and the detector, $t_{34} = (10,\ 50,\ 100)$ ms. All other parameters are the same as before. Looking at the results shown in figure 7.7, one can observe the typical spreading of the atom cloud being subject to free expansion. At the same time, the number of visible fringes in the middle column always adds up to ∼10. The growth of the fringe spacing and the equivalent decrease of the fringe wave number can also be observed in the right column of figure 7.7, where the outer maxima of the density's Fourier transform move to lower k-values as time progresses.

The number of rays that were used to create the plots in figure 7.7 is identical to the corresponding number of figure 7.6.

Comparison to analytic results

We can analyze the time dependence of fringe spacing and contrast more quantitatively by fitting the analytic result (7.54) to the absolute values of the FOURIER transforms of the density slices, $|\tilde{n}(k)|$. Using more values for the time span t_{34} and applying non-linear least-square fitting procedures [121], we obtain values for fringe spacing and contrast that are plotted in figure 7.8. The data points that are connected to our ray tracing formalism are identical to the analytical curves. The fringe spacing grows linearly with time and is smaller for "more asymmetric" interferometer schemes, i.e. for larger values of $|t_{12} - t_{23}|$. The contrast increases for longer time spans t_{34} and approaches the optimum $C_{\text{if}} = 1$. This suggests that the fringe pattern can be observed most clearly for long time spans between recombination and detection. Mind however that C_{if} is a relative quantity and the maximum density is constantly decreasing as time evolves. Hence, in a real experiment, going to longer time spans t_{34}, it becomes increasingly difficult to distinguish an interference pattern from noise recorded by a ccd-camera.

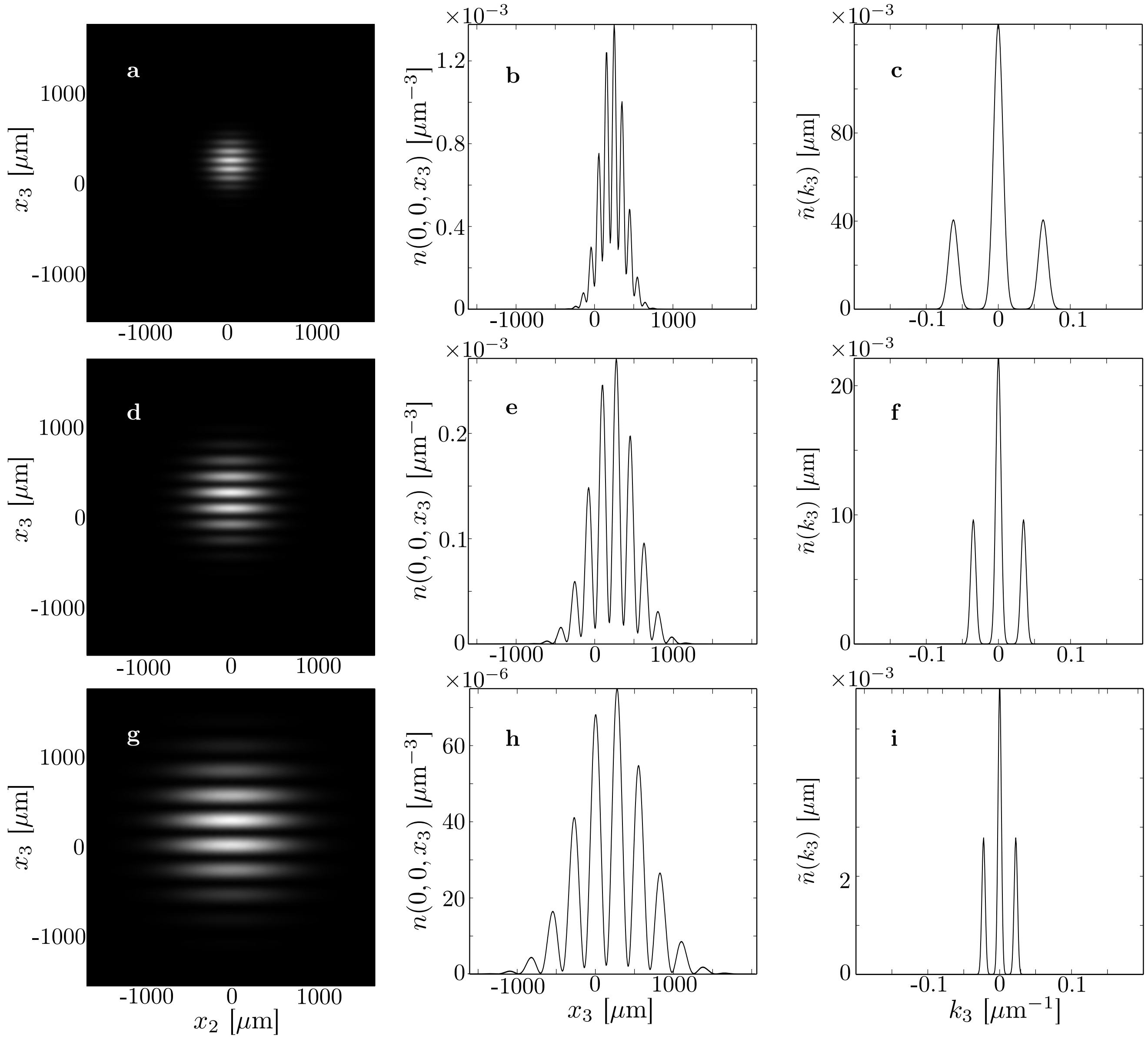

Figure 7.7.: Position densities after passing a MZI for various timespans between recombination and detection, t_{34}. These are $t_{34} = 10$ms (1st line, **a**, **b** ,**c**), $t_{34} = 50$ms (2nd line, **d**, **e** ,**f**), and $t_{34} = 100$ms (3rd line, **g**, **h** ,**i**). The left column (parts **a**, **d**, **g**) shows 2D slices in the x_2-x_3-plane with x_1=0 of the 3D density. The middle column (parts **b**, **e**, **h**) displays the density along the x_3 axis with $x_1 = x_2 = 0$. The right column (parts **c**, **f** ,**i**) shows the absolute value of the Fourier transform of the density along the x_3 axis, depicted in the middle columns. Initial state parameters are $(\omega_1, \omega_2, \omega_3) = 2\pi$(127.3, 127.3, 31.8)Hz, $M = 87$amu, $T = 100$nK, $N = 10^5$. MZI parameters are $t_{01} = 20$ms, $t_{12} = 10$ms, $t_{23} = 9.9$ms, $\mathbf{G} = (0,\ 0,\ 31.42)\mu\text{m}^{-1}$.

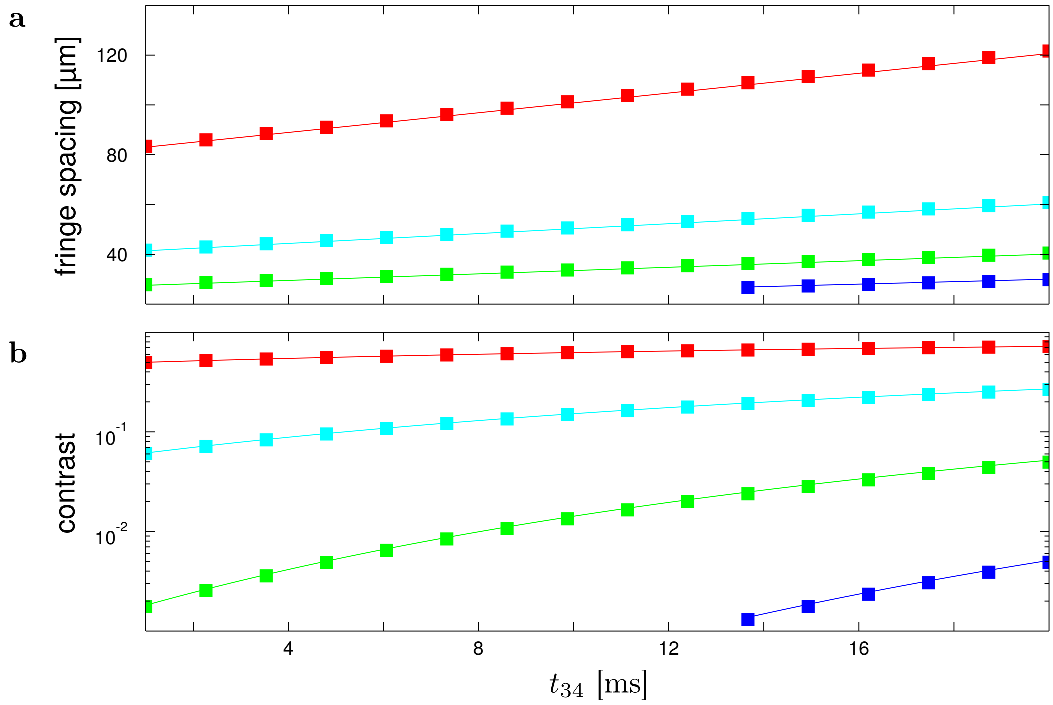

Figure 7.8.: Fringe spacing (part **a**) and contrast (part **b**) over free expansion time after second beam splitter, t_{34}, in case of an asymmetric MZI. Several asymmetries $t_{12} - t_{23}$ are compared: $t_{12} - t_{23} = 0.1$ ms (red), $t_{12} - t_{23} = 0.2$ ms (green), $t_{12} - t_{23} = 0.3$ ms (cyan), and $t_{12} - t_{23} = 0.4$ ms (blue). Squares denote ray tracing results. Solid lines are analytic curves for λ_{if} and $\mathscr{C}_{\mathrm{if}}$ according to expressions (7.58) and (7.57), respectively. Other parameters are $t_{01} = 20$ ms, $t_{12} = 10$ ms, $N_p = 10^5$, $M = 87$ amu, $T = 100$ nK, $G = 31.42\,\mu\mathrm{m}^{-1}$. Initial trap is harmonic with $(\omega_1, \omega_2, \omega_3) = 2\pi(127.3,\ 127.3,\ 31.8)$Hz.

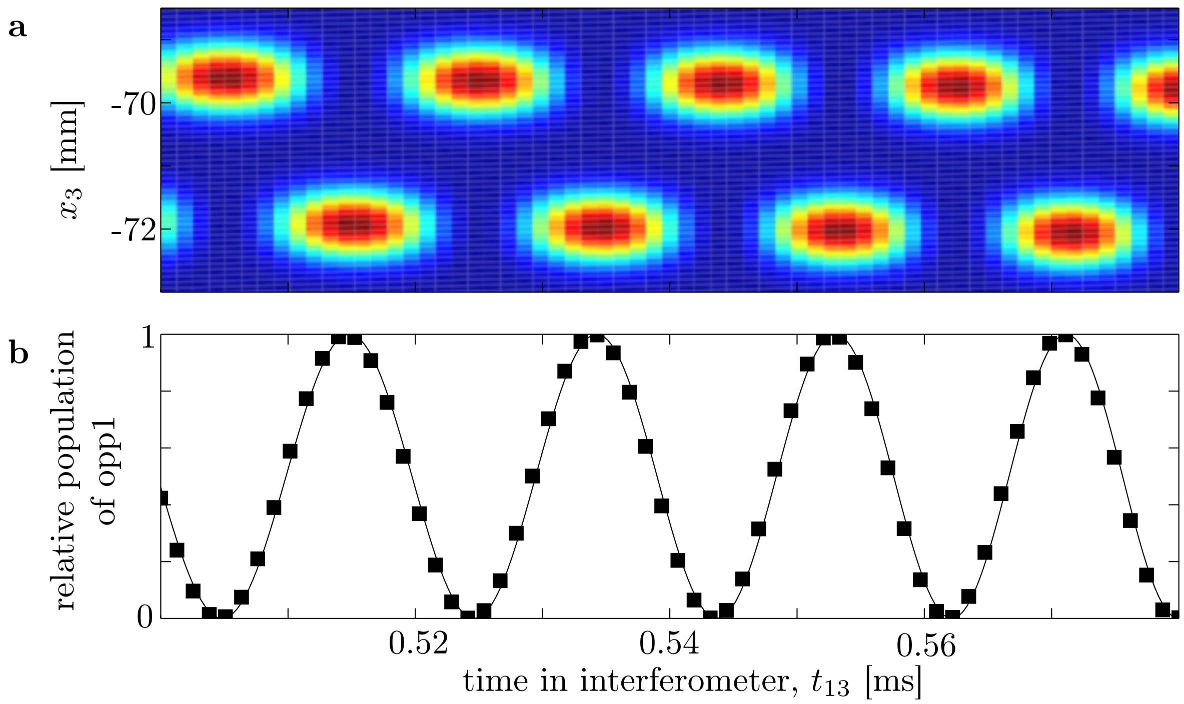

Figure 7.9.: Population of output ports after a symmetric MZI ($t_{12} = t_{23}$) under influence of constant gravity acceleration $\dot{x}_3 = -g = 9.81\mu\mathrm{m}/\mathrm{ms}^2$. Part **a**: Ray tracing results for complete position density $n = n_{11} + n_{22}$ over vertical direction x_3 and interferometer time t_{13}. Part **b**: Relative population of output port 1 ober interferometer time t_{13}. Squares denote ray tracing results. Solid line is analytic result according to equation (6.129). Other parameters are $t_{01} = 20$ms, $t_{34} = 100$ms, $N = 10^5$, $M = 87$ amu, $T = 100$nK, $G = 31.42\mu\mathrm{m}^{-1}$. Initial trap is harmonic with $(\omega_1, \omega_2, \omega_3) = 2\pi(127.3,\ 127.3,\ 31.8)$Hz.

7.3.3 Symmetric interferometer with linear gravity

Apart from interference fringes in the position density, we can study the relative population of the output ports of the interferometer. As we have seen in the end of section 6.3.6, the population of the output ports of a symmetric MZI ($t_{12} = t_{23}$) is oscillating as the interferometer time t_{13} is varied. The associated density profiles are separated in position space by $v_G t_{34}$. If this separation is sufficiently large, we can use expression (6.129) to analytically calculate the relative population of the output ports,

$$\frac{n(\mathbf{x}, t_4)}{n(\mathbf{x}, t_4) + n(\mathbf{x} + \mathbf{v}_G t_{34}, t_4)} = \cos^2\left(\frac{\delta\zeta}{2} - \frac{1}{2} G g T^2\right), \tag{6.129a}$$

$$\frac{n(\mathbf{x} + \mathbf{v}_G t_{34}, t_4)}{n(\mathbf{x}, t_4) + n(\mathbf{x} + \mathbf{v}_G t_{34}, t_4)} = \sin^2\left(\frac{\delta\zeta}{2} - \frac{1}{2} G g T^2\right). \tag{6.129b}$$

In order to determine the relative populations from the ray tracing results, we fit a sum of two Gaussians to the density slices along the x_3 axis. To this end, we utilize again non-linear least-square fitting. Using the same initial conditions and optical potential as before and time spans $t_{01} = 20\text{ms}$, $t_{34} = 100\text{ms}$, the results we obtain for varying interferometer times $t_{13} = t_{12}/2 = t_{23}/2$ are shown in figure 7.9. We have chosen a long time span between recombination and detection, t_{34}, so that the clouds of the output ports have enough time to separate spatially and are clearly distinguishable in figure part **a**. In part **b**, the ray tracing results are overlaid with the analytical values which show perfect agreement. The oscillation of output port population can be exploited to measure the gravitational acceleration [116].

Summary

This work considers the semi-classical description of two applications involving cold atoms. This is, on one hand, the behavior of a BOSE-EINSTEIN condensate in hybrid systems, i.e. in contact with a microscopic object (carbon nanotubes, fullerenes, etc.). On the other, the evolution of phase space distributions in matter wave interferometers utilizing ray tracing methods was discussed.

For describing condensates in hybrid systems, one can map the GROSS-PITAEVSKII equation, a differential equation in the complex-valued macroscopic wave function, onto a system of two differential equations in density and phase. Neglecting quantum dispersion, one obtains a semi-classical description which is easily modified to incorporate interactions between condensate and microscopical object. In our model, these interactions comprise attractive forces (CASIMIR-POLDER forces) and loss of condensed atoms due to inelastic collisions at the surface of the object. Our model exhibited the excitation of sound waves that are triggered by the object's rapid immersion, and spread across the condensate thereafter. Moreover, local particle loss leads to a shrinking of the bulk condensate. We showed that the total number of condensed particles is decreasing potentially in the beginning (large condensate, strong mean field interaction), while it decays exponentially in the long-time limit (small condensate, mean field inetraction negligible).

For representing the physics of matter wave interferometers in phase space, we utilized the WIGNER function. In semi-classical approximation, which again consists in ignoring the quantum dispersion, this representation is subject to the same equation of motion as classical phase space distributions, i.e. the LIOUVILLE equation. This implies that time evolution of the WIGNER function follows a phase space flow that consists of classical trajectories (classical transport). This means, for calculating a time-evolved distribution, one has know the initial distribution and one has to solve the classical equations of motion.

Concerning the initial distribution, we have studied a stationary solution of the nonlinear LIOUVILLE equation, the LAMBERT density. We saw that it agrees very well with results from single-particle quantum mechanics as well as the MAXWELL-BOLTZMANN distribution in the weakly interacting limit. Likewise, in the strongly interacting limit, familiar results of the THOMAS-FERMI approximation are recovered.

A distribution that is first prepared in a trap and then released can be described quite conveniently in terms of WIGNER functions. However, propagation in optical potentials associated to the interferometer elements (beam splitter, π-pulse) do not satisfy the condition of the semi-classical approximation. Nevertheless, one finds discrete before-after mappings that describe

the effect of these elements on incident distributions. This leads to several channels of phase space propagation which relate to the interferometer paths and interferences between them.

The formalism for Wigner functions in an interferometer can be translated straightforwardly into a ray tracing algorithm. As mentioned above, this algorithm solves the classical equations of motion and computes time-evolved distributions, using values of the initial distribution. This procedure, in contrast to most analytical solutions, does not require the Hamilton function to be quadratic (e.g. free propagation, const. acceleration, harmonic oscillator). We compared simulation results to analytic expressions in case of freely propagating Gauss distribution. They showed perfect agreement, especially for the functional dependence of wave length and contrast of interference fringes on the laser pulse timings.

Part III.

Appendix

A Gaussian distributions

A.1 Basic properties

A general anisotropic Gauss-distribution in $\mathbb{R}^D$ can be parametrized by its center $\bar{\mathbf{x}}$ and its correlation matrix $\mathsf{C} = 2\langle\!\langle \mathbf{x}\,\mathbf{x}^\mathsf{T} \rangle\!\rangle$ (see section 2.2.3),

$$\mathscr{G}_\mathsf{C}^{(D)}(\mathbf{x}-\bar{\mathbf{x}}) = \frac{\exp\left[-(\mathbf{x}-\bar{\mathbf{x}})^\mathsf{T}\mathsf{C}^{-1}(\mathbf{x}-\bar{\mathbf{x}})\right]}{\sqrt{\pi^D \det \mathsf{C}}}, \tag{A.1}$$

with D-dimensional vector $\mathbf{x} = (x_1, ..., x_D)^\mathsf{T}$. Assuming the correlation matrix C to be symmetric, we can diagonalize it as

$$\mathsf{C} = \mathsf{P}\,\mathsf{D}\,\mathsf{P}^\mathsf{T}, \tag{A.2}$$

where the transformation P is orthogonal, i.e. $\mathsf{P}^{-1} = \mathsf{P}^\mathsf{T}$, and D is the diagonal matrix of eigenvalues of C,

$$\mathsf{D} = \begin{pmatrix} \lambda_1 & & 0 \\ & \ddots & \\ 0 & & \lambda_D \end{pmatrix}. \tag{A.3}$$

The distribution $\mathscr{G}_\mathsf{C}^{(D)}(\mathbf{x}-\bar{\mathbf{x}})$ is normalizable if all of these eigenvalues have a strictly positive real part. We define the sigma matrix as

$$\Sigma = \mathsf{P}\,\mathsf{D}^{1/2}, \tag{A.4}$$

which allows us to write $\mathsf{C} = \Sigma\,\Sigma^\mathsf{T}$ and thus to simplify the bilinear form in the exponent of equation (A.1), $\mathbf{x}^\mathsf{T}\,\mathsf{C}^{-1}\,\mathbf{x} = \xi^\mathsf{T}\xi$, with the transformed vector $\xi = \Sigma^{-1}\mathbf{x}$. The Jacobian of this transformation is $\sqrt{\det \mathsf{C}}$. Interpreting the above distribution as a density, we write

$$\mathrm{d}^D x\ \mathscr{G}_\mathsf{C}^{(D)}(\mathbf{x}-\bar{\mathbf{x}}) = \mathrm{d}^D \xi\ \mathscr{G}_\mathbb{1}^{(D)}(\xi), \tag{A.5}$$

where the special Gaussian distribution

$$\mathscr{G}_\mathbb{1}^{(D)}(\xi) = \frac{e^{-\xi^\mathsf{T}\xi}}{\pi^{D/2}} \tag{A.6}$$

is the normal form of Gaussian distributions, also called normal distribution. It is radially symmetric and has width 1/2.

Instead of using definition (A.4), we also can decompose the correlation matrix into a product of matrices that are also symmetric. Therefor, we insert unity $\mathbb{1} = \mathsf{P}^\mathsf{T}\mathsf{P}$ into the diagonalization relation (A.2), obtaining

$$\begin{aligned} \mathsf{C} &= \mathsf{P}\,\mathsf{D}^{1/2}\,\mathsf{P}^\mathsf{T}\,\mathsf{P}\,\mathsf{D}^{1/2}\,\mathsf{P}^\mathsf{T} \\ &= \mathsf{C}^{1/2}\,\mathsf{C}^{1/2}, \end{aligned} \tag{A.7}$$

where we have identified $\mathsf{C}^{1/2} = \mathsf{P}\,\mathsf{D}^{1/2}\,\mathsf{P}^\mathsf{T}$.

A.2 Integrals over arbitrary axes

This section considers integrals of Gaussians in $\mathbb{R}^{D+M}$ that run over a subspace $\mathbb{R}^M \subset \mathbb{R}^{D+M}$ which shall be called *integration subspace*. Clearly, this procedure yields a distribution in $\mathbb{R}^D$. The M coordinates of $\mathbb{R}^M$ are labeled $\mathbf{y} = (y_1, ..., y_M)^\mathsf{T}$ and are referred to as unobserved axes. On the other hand, the D coordinates of its complement that remains un-integrated are labeled $\mathbf{x} = (x_1, ..., x_D)^\mathsf{T}$ and termed observed axes. The elements $\mathbf{z}$ of the complete space $\mathbb{R}^{D+M}$ are given by a concatenation of vectors from both subspaces, $\mathbf{z} = (x_1, ..., x_D, y_1, ..., y_M)^\mathsf{T}$. With this naming convention, the subspace integral we want to calculate reads

$$I = \int_{\mathbb{R}^M} \mathrm{d}^M y\ \mathscr{G}^{(D+M)}_{\mathsf{C}_z}(\mathbf{z} - \overline{\mathbf{z}}), \tag{A.8}$$

For further analysis, we divide the correlation matrix into four blocks that represent mappings within or between the two subspaces, respectively,

$$\mathsf{C}_z^{-1} \equiv \begin{pmatrix} \mathsf{A}_{xx} & \mathsf{A}_{xy} \\ \mathsf{A}_{yx} & \mathsf{A}_{yy} \end{pmatrix}. \tag{A.9}$$

Consequently, the bilinear form in the explonential function of the Gaussian expands as

$$\mathbf{Z}^\mathsf{T}\mathsf{C}_z^{-1}\mathbf{Z} = \mathbf{X}^\mathsf{T}\mathsf{A}_{xx}\mathbf{X} + \mathbf{X}^\mathsf{T}\mathsf{A}_{xy}\mathbf{Y} + \mathbf{Y}^\mathsf{T}\mathsf{A}_{yx}\mathbf{X} + \mathbf{Y}^\mathsf{T}\mathsf{A}_{yy}\mathbf{Y}, \tag{A.10}$$

with abbreviations $\mathbf{Z} = \mathbf{z} - \overline{\mathbf{z}}$, $\mathbf{X} = \mathbf{x} - \overline{\mathbf{x}}$, and $\mathbf{Y} = \mathbf{y} - \overline{\mathbf{y}}$. From C_z^{-1} being a symmetric matrix it directly follows that A_{xx} and A_{yy} are symmetric and that $\mathsf{A}_{yx} = {\mathsf{A}_{xy}}^\mathsf{T}$. In order to separate $\mathbf{x}$-dependent terms, one can compactly write

$$\mathbf{Z}^\mathsf{T}\mathsf{C}_z^{-1}\mathbf{Z} = \mathbf{X}^\mathsf{T}\mathsf{C}_x^{-1}\mathbf{X} + \boldsymbol{\eta}^\mathsf{T}\boldsymbol{\eta}, \tag{A.11}$$

identifying an effective correlation matrix of the distribution in the observed subspace,

$$\mathsf{C}_x^{-1} = \mathsf{A}_{xx} - \mathsf{A}_{xy}\mathsf{A}_{yy}^{-1}\mathsf{A}_{yx}, \tag{A.12}$$

and transformed coordinates in the integration subspace,

$$\boldsymbol{\eta} = \mathsf{A}_{yy}^{1/2}(\mathbf{y}-\overline{\mathbf{y}}) + \mathsf{A}_{yy}^{-1/2}\mathsf{A}_{yx}(\mathbf{x}-\overline{\mathbf{x}}). \tag{A.13}$$

Substituting the integration variable $\mathbf{y}$ in (A.8) with $\boldsymbol{\eta}(\mathbf{x},\mathbf{y})$ gives rise to a factor $1/\det A_{yy}$. Furthermore, one can write the normalization factor of $\mathscr{G}_{\mathsf{C}_z}^{(D+M)}$ in terms of the block matrices as

$$\begin{aligned} \det \mathsf{C}_z^{-1} &= \det\begin{pmatrix} \mathsf{A}_{xx} & \mathsf{A}_{xy} \\ \mathsf{A}_{yx} & \mathsf{A}_{yy} \end{pmatrix} = \det \mathsf{A}_{yy}\ \det(\mathsf{A}_{xx} - \mathsf{A}_{xy}\mathsf{A}_{yy}^{-1}\mathsf{A}_{yy}) \\ &= \det \mathsf{A}_{yy}\ \det \mathsf{C}_x^{-1}. \end{aligned} \tag{A.14}$$

Finally, expression (A.8) can be calculated,

$$\begin{aligned} \int_{\mathbb{R}^M} \mathrm{d}^M y\ \mathscr{G}_{\mathsf{C}_z}^{(D+M)}(\mathbf{z}-\overline{\mathbf{z}}) &= \frac{e^{-(\mathbf{x}-\overline{\mathbf{x}})^\mathsf{T}\mathsf{C}_x^{-1}(\mathbf{x}-\overline{\mathbf{x}})}}{\sqrt{\pi^D \det \mathsf{C}_x}}\ \frac{1}{\pi^{M/2}} \int_{\mathbb{R}^M} \mathrm{d}^M \eta\ e^{-\boldsymbol{\eta}^\mathsf{T}\boldsymbol{\eta}} \\ &= \frac{e^{-(\mathbf{x}-\overline{\mathbf{x}})^\mathsf{T}\mathsf{C}_x^{-1}(\mathbf{x}-\overline{\mathbf{x}})}}{\sqrt{\pi^D \det \mathsf{C}_x}}. \end{aligned} \tag{A.15}$$

Gauss-Cosine integrals

Another important integral occurring in this work runs over the product of a cosine and a Gaussian. Since the cosine is just the sum of two complex exponentials, the above results can be easily modified to solve this Gauss-cosine integral,

$$\begin{aligned} \int_{\mathbb{R}^M} \mathrm{d}^M y\ \cos(\mathbf{Q}^\mathsf{T}\mathbf{z})\ \mathscr{G}_{\mathsf{C}_z}^{(D+M)}(\mathbf{z}) &= \mathfrak{Re}\ e^{i\mathbf{q}_x^\mathsf{T}\mathbf{x}} \int_{\mathbb{R}^M} \mathrm{d}^M y\ \frac{e^{-\mathbf{z}^\mathsf{T}\mathsf{C}_z^{-1}\mathbf{z}+i\mathbf{q}_y^\mathsf{T}\mathbf{y}}}{\sqrt{\pi^{D+M}\det \mathsf{C}_z}} \\ &= e^{-\frac{1}{4}\mathbf{q}_y^\mathsf{T}\mathsf{A}_{yy}^{-1}\mathbf{q}_y}\ \cos\left[\left(\mathbf{q}_x - \mathsf{A}_{xy}\mathsf{A}_{yy}^{-1}\mathbf{q}_y\right)^\mathsf{T}\mathbf{x}\right] \frac{e^{-\mathbf{x}^\mathsf{T}\mathsf{C}_x^{-1}\mathbf{x}}}{\sqrt{\pi^D \det \mathsf{C}_x}}, \end{aligned} \tag{A.16}$$

where the oscillation vector has been divided as $\mathbf{Q} = (\mathbf{q}_x, \mathbf{q}_y)^\mathsf{T}$.

A.3 Hermite polynomials

One particularly useful class of functions in the context of Gaussian distributions is given by HERMITE polynomials. A comprehensive discussion of their features can for example be found in [75]. We present here only a collection of properties which are relevant for this work. To begin with, HERMITE polynomials are orthogonal in the domain $(-\infty, \infty)$ with respect to a Gaussian weight function,

$$\int_{-\infty}^{\infty} \mathrm{d}x\, H_n(x) H_m(x)\, e^{-x^2} = \delta_{nm} \sqrt{2\pi}\, n!. \tag{A.17}$$

They are thus well suited for expanding functions with Gaussian envelopes. In turn, HERMITE polynomials can be expressed as a series expansion,

$$H_n(x) = \sum_{\ell=0}^{\lfloor \frac{n}{2} \rfloor} \frac{(-1)^\ell n!}{\ell!(n-2\ell)!} (2x)^{n-2\ell}, \tag{A.18}$$

where the floor function $\lfloor \frac{n}{2} \rfloor$ returns the closes lower integer. Furthermore, representations which explicitly comprise Gaussian functions are the RODRIGUES formula,

$$H_n(x) = (-1)^n e^{x^2} \left(\frac{\mathrm{d}}{\mathrm{d}x} \right)^n e^{-x^2}, \tag{A.19}$$

the generating function,

$$\sum_{n=0}^{\infty} \frac{H_n(x)}{n!} z^n = e^{2xz - z^2}, \tag{A.20}$$

and the integral representation

$$H_n(x) = \frac{2^n e^{x^2}}{i^n \sqrt{\pi}} \int_{-\infty}^{\infty} \mathrm{d}t\ t^n e^{-t^2 + 2ixt}. \tag{A.21}$$

A.4 Gauss-Hermite quadrature

GAUSS quadratures [119, 120] are numerical integration formulas involving a specified choice of abscissas and corresponding weights. For N-th order quadrature, these abscissas are the roots of an N-th order polynomial and the accuracy of the formula is of order $2N - 1$. As the name suggests, GAUSS-HERMITE quadrature utilizes the roots of HERMITE polynomials.

One-dimensional case

In the 1D case, the quadrature formula comprises the integral over the product of an arbitrary function with a Gaussian,

$$\begin{aligned}\int_{-\infty}^{\infty} \mathrm{d}x\, e^{-x^2} g(x) &\approx \mathcal{Q}_N^{(1)}[f] \\ &= \sum_{n=1}^{N} w_n\, g(\xi_n),\end{aligned} \tag{A.22}$$

where ξ_n are roots of N-th order Hermite polynomial and the weights are given as

$$w_n = \frac{2^{N-1} N! \sqrt{\pi}}{N^2 H_{N-1}^2(\xi_n)}. \tag{A.23}$$

Like all Gaussian quadrature formulas, expression (A.22) is exact if $g(x)$ is polynomial of degree $2N-1$ or lower. Sets of abscissas and associated weights are either tabled [75] or easily accessible by program packages (e.g. [122]). Suppose now, we have a function

$$f(x) = e^{-\frac{(x-\overline{x})^2}{\sigma^2}}\, g(x) \tag{A.24}$$

that can be written as a product of a general Gaussian and a function g. Then expression (A.22) can be reformulated to a more practical version,

$$\begin{aligned}\int_{-\infty}^{\infty} \mathrm{d}x\, f(x) &\approx \mathcal{Q}_N^{(1)}[f] \\ &= \sigma \sum_{n=1}^{N} \tilde{w}_n\, f(\sigma \xi_n + \overline{x})\end{aligned} \tag{A.25}$$

with modified weights $\tilde{w}_n = \exp(-\xi_n^2)\, w_n$.

Multi-dimensional case

Generalization from one- to multi-dimensional case is straightforward. For integration over all axes of a multivariate function that can be written as

$$f(\mathbf{z}) = \exp\left[-(\mathbf{z}-\overline{\mathbf{z}})^{\mathsf{T}}\, \mathrm{C}_z^{-1}\, (\mathbf{z}-\overline{\mathbf{z}})\right] g(\mathbf{z}) \tag{A.26}$$

one finds

$$\begin{aligned}\int_{\mathbb{R}^D} \mathrm{d}^D\mathbf{z}\, f(\mathbf{z}) &\approx \mathcal{Q}_N^{(D)}[f] \\ &= \det \Sigma_z \sum_{|\underline{n}|\leq N} \tilde{w}_{\underline{n}}\, f\left(\Sigma_z \xi_{\underline{n}} + \overline{\mathbf{z}}\right)\end{aligned} \tag{A.27}$$

with tuple $\underline{n} = (n_1, \ldots, n_D)$, its sum $|\underline{n}| = n_1 + \ldots + n_D$, product of weights $\tilde{w}_{\underline{n}} = \tilde{w}_{n_1} \cdot \ldots \cdot \tilde{w}_{n_D}$, and abscissa vectors $\boldsymbol{\xi}_{\underline{n}} = (\xi_{n_1}, \ldots, \xi_{n_D})^{\mathsf{T}}$. We made use of definitions from the beginning of this chapter.

For integration over arbitrary axes, we can revive notation from A.2 and use transformation (A.13) to obtain

$$\int_{\mathbb{R}^M} \mathrm{d}^M \mathbf{y}\, f(\mathbf{x}, \mathbf{y}) \approx \sum_{|\underline{n}| \leq N} \tilde{w}_{\underline{n}}\, f(\mathbf{x}, \mathbf{y}_{\underline{n}(\mathbf{x})}) \tag{A.28}$$

with $\mathbf{y}_{\underline{n}(\mathbf{x})} = \mathsf{A}_{yy}^{-1/2} \boldsymbol{\xi}_{\underline{n}} - \mathsf{A}_{yy}^{-1} \mathsf{A}_{yx} (\mathbf{x} - \Delta\mathbf{x}) + \Delta\mathbf{y}$. The tuple $\underline{n}$ has $M < D$ elements.

A.5 Oscillating integrands with Gaussian-like envelope

One-dimensional case

Consider intergeneration with an integrand of the form

$$f(x) = e^{-x^2} \cos(qx + \zeta)\, g(x). \tag{A.29}$$

We define an 1D oscillating integrand with Gaussian-like envelope as

$$\mathscr{I}_q^{(1)}[g] = \frac{1}{\sqrt{\pi}} \int_{-\infty}^{\infty} \mathrm{d}x\, e^{-x^2} \cos(qx + \zeta)\, g(x) \tag{A.30}$$

Assume we can expand the function g in terms of Hermite polynomials,

$$g(x) = \sum_n c_n H_n(x) \tag{A.31}$$

with expansion coefficients

$$c_n = \frac{1}{\sqrt{\pi}} \int_{-\infty}^{\infty} \mathrm{d}x\, e^{-x^2} H_x(x)\, g(x). \tag{A.32}$$

By virtue of its linearity, we can perform the integral (A.30) term by term, involving expressions

$$\begin{aligned} \mathscr{I}_q^{(1)}[H_n] &= \mathfrak{Re} \frac{1}{\sqrt{\pi}} e^{i\zeta} \int_{-\infty}^{\infty} \mathrm{d}x\, e^{-x^2 + iqx} H_n(x) \\ &= 2 \cos\left(\tfrac{n\pi}{2} + \zeta\right) q^n\, e^{-q^2/4}, \end{aligned} \tag{A.33}$$

where we have applied relation (A.21). Consequently, the result of (A.30) can be assembled to

$$\mathscr{I}_q^{(1)}[g] = 2e^{-q^2/4} \sum_n c_n \cos\left(\tfrac{n\pi}{2} + \zeta\right) q^n \tag{A.34}$$

Multi-dimensional case

The above result can be straightforwardly generalized to the D-dimensional case. Let the integrand be

$$f(\mathbf{x}) = e^{-\mathbf{x}^2} \cos(\mathbf{qx} + \zeta)\, g(\mathbf{x}). \tag{A.35}$$

With the compact notations $\underline{n} \equiv (n_1, \ldots, n_D)$, $|\underline{n}| = n_1 + \ldots + n_D$, $H_{\underline{n}}(\mathbf{x}) = \prod_{i=1}^{D} H_{n_i}(x_i)$, and $\mathbf{q}^{\underline{n}} \equiv q_1^{n_1} \cdot \ldots \cdot q_D^{n_D}$, one obtains

$$\mathscr{I}_{\mathbf{q}}^{(D)}[g] = \frac{1}{\pi^{D/2}} \int_{\mathbb{R}^D} \mathrm{d}^D x \; e^{-\mathbf{x}^2} \cos(\mathbf{qx} + \zeta)\, g(\mathbf{x}). \tag{A.36}$$

We expand the g-function again in Hermite polynomials,

$$g(\mathbf{x}) = \sum_N \sum_{|\underline{n}|=N} c_{\underline{n}} H_{\underline{n}}(\mathbf{x}), \tag{A.37}$$

having coefficients

$$c_{\underline{n}} = \frac{1}{\pi^{D/2}} \int_{\mathbb{R}^D} \mathrm{d}^D x \; e^{-\mathbf{x}^2} H_{\underline{n}}(\mathbf{x})\, g(\mathbf{x}). \tag{A.38}$$

Hence, the result of the integral (A.36) is

$$\mathscr{I}_{\mathbf{q}}^{(D)}[g] = 2^D e^{-q^2/4} \sum_N \cos\left(\tfrac{N\pi}{2} + \zeta\right) \sum_{|\underline{n}|=N} c_{\underline{n}}\, \mathbf{q}^{\underline{n}}. \tag{A.39}$$

B The Lambert function

B.1 Definition and approximations

The Lambert function $W(z)$ or *product logarithm* [123] is implicitly defined as solution of

$$We^W = z. \tag{B.1}$$

for $-1/e < z < \infty$. It attains the value W(-1/e)=-1 and vanishes linearly at the origin $W(0) = 0$. Its derivative

$$W'(z) = \frac{W}{z(1+W)}. \tag{B.2}$$

is always positive. Thus, the Lambert function is strictly monotonic increasing.

Small argument approximation

From definition (B.1) one can calculate a Taylor series expansion,

$$W(z) = \sum_{n=1}^{\infty} \frac{(-n)^{n-1}}{n!} z^n. \tag{B.3}$$

The series coefficients are rapidly increasing with order n, limiting its radius of convergence to $z < 1/e$. A linear approximation $W(z) = z + O(z^2)$ is useful for very small arguments, $z \ll 1/e$.

Large argument approximation

In case of large arguments $z \gg 1$, the Lambert function approximately satisfies

$$W(z) = \ln(z) - \ln\big(\ln(z)\big) + \frac{\ln\big(\ln(z)\big)}{\ln(z)}, \tag{B.4}$$

which is dominated by the logarithmic term. The graph of $W(z)$ is plotted in Fig. B.1 along the above approximations. Expression (B.4) apparently fits the original form of $W(z)$ very well for arguments $z > 3$. The simple approximation $\ln(z)$ does not come as close, but still, it roughly resembles the large-argument behavior of the Lambert function. In summary, we have two approximations to $W(z)$ which are applicable on well separated domains of the argument. In between these domains, for $z \approx 1$, both expressions (B.3), (B.4), fail to provide useful approximations.

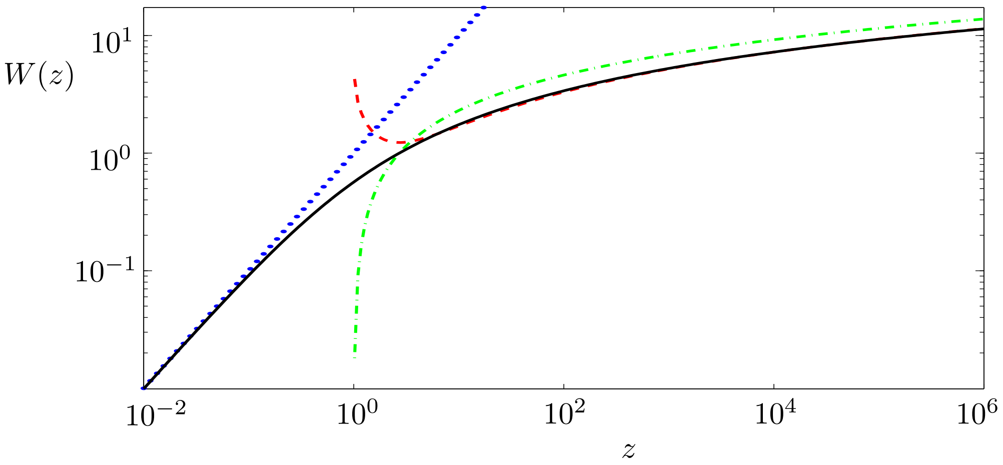

Figure B.1.: Lambert function $W(z)$ (black solid line), the linear argument approximation $W(z) = z$ (blue dots), the large argument approximation of Eq. (B.4) (red dashed line), and simplified approximation $W(z) = \ln(z)$ (green dash-dotted line).

B.2 Useful integrals

Calculating observables with the Lambert density (4.13) in case of a D-dimensional radially symmetric harmonic oscillator, one encounters overlap integrals of the form

$$\mathscr{I}_D^{(m)}(\nu) = \frac{1}{(2\pi)^{D/2}} \int \mathrm{d}^D x\, W\left(e^{\nu - \mathbf{x}^2/2}\right)^m . \tag{B.5}$$

By virtue of radial symmetry, the D-dimensional integral can be reduced to an one-dimensional radial integral with $\mathrm{d}^D x = 2\pi^{D/2} r^{D-1} \mathrm{d}r / \Gamma(D/2)$. Substituting $y = \mathbf{x}^2/2$, we write

$$\mathscr{I}_D^{(m)}(\nu) = \frac{1}{\Gamma\left(\frac{D}{2}\right)} \int_0^\infty \mathrm{d}y\; y^{D/2-1}\, W\left(e^{\nu - y}\right)^m . \tag{B.6}$$

An integer exponent $m \geq 1$ is required for higher powers in the density, e.g., mean-field energies with $n^2(\mathbf{x})$. Like the Lambert function, $\mathscr{I}_D^{(m)}(\nu)$ is strictly monotonic increasing. While seeking approximate expressions, it may be more convenient to regard the overlap integrals as functions of $z = \exp(\nu)$ rather than ν.

For $\nu \to -\infty$, or likewise $z \to 0$, the Lambert function in (B.6) may be replaced by identity, yielding

$$\mathscr{I}_D^{(m)}(\ln(z)) \approx \frac{z^m}{\Gamma\left(\frac{D}{2}\right)} \int_0^\infty \mathrm{d}y\; y^{D/2-1} e^{-my} = \frac{z^m}{m^{D/2}} . \tag{B.7}$$

As long as the value of the argument z stays below $1/e$, we can use the Lambert function's power series expansion in order to successively improve the lowest order approximation. Integrals with $m = 1$, which appear in the normalization condition as well as in non-interacting energy contributions, are then given by

$$\mathscr{I}_D^{(1)}(\ln(z)) = \sum_{l=1}^{\infty} \frac{(-l)^{l-1}}{l!\, l^{D/2}} z^l. \tag{B.8}$$

Those with $m = 2$ emerge inside contributions representing two-body interactions. Their series expansion reads

$$\mathscr{I}_D^{(2)}(\ln(z)) = \sum_{l,l'=1}^{\infty} \frac{(-l)^{l-1}(-l')^{l'-1}}{l!l'!\,(l+l')^{D/2}} z^{l+l'}. \tag{B.9}$$

In the opposite limit, for $\nu \to \infty$, integral (B.6) is dominated by contributions from $y \ll \nu$ for which we can approximate the Lambert function $W(z)$ with $\ln(z)$. Neglecting contributions from higher y, we cut off the integral at $y = \nu$, and obtain

$$\begin{aligned}\mathscr{I}_D^{(m)}(\nu) &\approx \frac{1}{\Gamma\left(\frac{D}{2}\right)} \int_0^{\nu} \mathrm{d}y\; y^{D/2-1}(\nu - y)^m \\ &= \frac{m!}{\Gamma\left(\frac{D}{2}+m+1\right)} \nu^{D/2+m}.\end{aligned} \tag{B.10}$$

In figure B.2, numerically computed values of $\mathscr{I}_D^{(m)}(\nu)$ are plotted for several parameter values and for negative and positive arguments separately. In part **a**, one recognizes the exponential decay as $\nu \to -\infty$. Part **b** shows the algebraic growth described in (B.10) for $\nu \to \infty$.

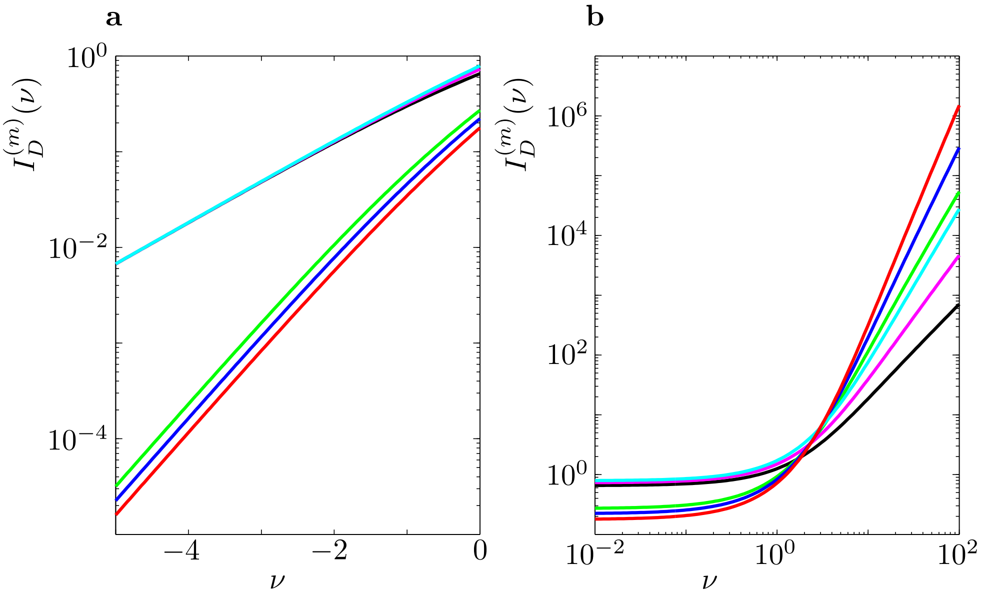

Figure B.2.: Behaviour of $\mathscr{I}_D^{(m)}(\nu)$ versus ν for dimension $D = 1, 2, 3$ and powers of the Lambert function $m = 1, 2$. Left figure (a) for $\nu < 0$ and right figure (b) for $\nu > 0$. Parameter values D and m are as follows. $D = 1$ and $m = 1$ (black). $D = 1$ and $m = 2$ (green). $D = 2$ and $m = 1$ (magenta). $D = 2$ and $m = 2$ (blue). $D = 3$ and $m = 1$ (cyan). $D = 3$ and $m = 2$ (red).

Bibliography

[1] S. Chu, J. Bjorkholm, A. Ashkin, and A. Cable, "Experimental observation of optically trapped atoms," *Phys. Rev. Lett.*, vol. 57, pp. 314–317, Jul 1986.

[2] A. Aspect, E. Arimondo, R. Kaiser, N. Vansteenkiste, and C. Cohen-Tannoudji, "Laser cooling below the one-photon recoil energy by velocity-selective coherent population trapping," *Phys. Rev. Lett.*, vol. 61, pp. 826–829, Aug 1988.

[3] P. Lett, R. Watts, C. Westbrook, W. Phillips, P. Gould, and H. Metcalf, "Observation of atoms laser cooled below the doppler limit," *Phys. Rev. Lett.*, vol. 61, pp. 169–172, Jul 1988.

[4] M. H. Anderson, J. R. Ensher, M. R. Matthews, C. E. Wieman, and E. A. Cornell, "Observation of Bose-einstein condensation in a dilute atomic vapor," *Science*, vol. 269, pp. 198–201, July 1995.

[5] K. B. Davis, M. O. Mewes, M. R. Andrews, N. J. Vandruten, D. S. Durfee, D. M. Kurn, and W. Ketterle, "Bose-einstein condensation in a gas of sodium atoms," *Phys. Rev. Lett.*, vol. 75, pp. 3969–3973, Nov. 1995.

[6] W. Ketterle, D. S. Durfee, and D. M. Stamper-Kurn, "Making, probing and understanding bose-einstein condensates," *P. Int. Scs. Phys.*, vol. 140, pp. 67–176, 1999.

[7] S. N. Bose, "Plancks gesetz und lichtquantenhypothese," *Z. Phys.*, vol. 26, p. 178, 1924.

[8] A. Einstein *Sitzber. Kgl. Preuss. Akad. Wiss.*, p. 261, 1924.

[9] A. Einstein *Sitzber. Kgl. Preuss. Akad. Wiss.*, p. 3, 1925.

[10] G. Baym and C. J. Pethick, "Ground-state properties of magnetically trapped bose-condensed rubidium gas," *Phys. Rev. Lett.*, vol. 76, pp. 6–9, Jan. 1996.

[11] F. Dalfovo and S. Stringari, "Bosons in anisotropic traps: Ground state and vortices," *Phys. Rev. A*, vol. 53, pp. 2477–2485, Apr 1996.

[12] C. W. Gardiner and P. Zoller, "Quantum kinetic theory: A quantum kinetic master equation for condensation of a weakly interacting bose gas without a trapping potential," *Physical Review A*, vol. 55, pp. 2902–2921, Apr. 1997.

[13] D. Jaksch, C. W. Gardiner, and P. Zoller, “Quantum kinetic theory .2. simulation of the quantum boltzmann master equation,” *Physical Review A*, vol. 56, pp. 575–586, July 1997.

[14] C. W. Gardiner and P. Zoller, “Quantum kinetic theory. iii. quantum kinetic master equation for strongly condensed trapped systems,” *Physical Review A*, vol. 58, pp. 536–556, July 1998.

[15] D. Jaksch, C. W. Gardiner, K. M. Gheri, and P. Zoller, “Quantum kinetic theory. iv. intensity and amplitude fluctuations of a bose-einstein condensate at finite temperature including trap loss,” *Physical Review A*, vol. 58, pp. 1450–1464, Aug. 1998.

[16] E. Zaremba, T. Nikuni, and A. Griffin, “Dynamics of trapped bose gases at finite temperatures,” *J. Low Temp. Phys.*, vol. 116, pp. 277–345, Aug. 1999.

[17] C. J. Pethick and H. Smith, *Bose-Einstein Condensation in Dilute Gases; 2nd ed.* Cambridge Univ. Press, 2008.

[18] L. Pitaevskii and S. Stringari, *Bose-Einstein Condensation*. International Series of Monographs on Physics, Clarendon Press, 2003.

[19] F. Dalfovo, S. Giorgini, L. P. Pitaevskii, and S. Stringari, “Theory of bose-einstein condensation in trapped gases,” *Rev. Mod. Phys.*, vol. 71, pp. 463–512, Apr. 1999.

[20] O. Morsch and M. Oberthaler, “Dynamics of bose-einstein condensates in optical lattices,” *Rev. Mod. Phys.*, vol. 78, pp. 179–215, Jan. 2006.

[21] I. Bloch, J. Dalibard, and W. Zwerger, “Many-body physics with ultracold gases,” *Rev. Mod. Phys.*, vol. 80, pp. 885–964, Jul-Sep 2008.

[22] D. Hunger, S. Camerer, T. W. Hansch, D. Konig, J. P. Kotthaus, J. Reichel, and P. Treutlein, “Resonant coupling of a bose-einstein condensate to a micromechanical oscillator,” *Phys. Rev. Lett.*, vol. 104, p. 143002, Apr. 2010.

[23] D. Hunger, S. Camerer, M. Korppi, A. Jockel, T. W. Hansch, and P. Treutlein, “Coupling ultracold atoms to mechanical oscillators,” *C. R. Phys.*, vol. 12, pp. 871–887, Nov. 2011.

[24] B. Jetter, J. Markle, P. Schneeweiss, M. Gierling, S. Scheel, A. Gunther, J. Fortagh, and T. E. Judd, “Scattering and absorption of ultracold atoms by nanotubes,” *New Journal of Physics*, vol. 15, p. 073009, July 2013.

[25] C. T. Weiß, P. V. Mironova, J. Fortágh, W. P. Schleich, and R. Walser, “Immersing carbon nanotubes in cold atomic gases,” *Phys. Rev. A*, vol. 88, p. 043623, Oct 2013.

[26] P. Schneeweiss, M. Gierling, G. P. Visanescu, D. E. Kern, T. Judd, A. Gunther, and J. Fortagh, “Dispersion forces between ultracold atoms and a carbon nanotube,” *Nat Nano*, vol. 7, pp. 515–519, Aug. 2012.

[27] M. Gierling, P. Schneeweiss, G. Visanescu, P. Federsel, M. Häffner, D. P. Kern, T. E. Judd, A. Günther, and J. Fortagh, “Cold-atom scanning probe microscopy,” *Nat. Nanotechnol.*, vol. advance online publication, pp. –, May 2011.

[28] M. Fink, T. O. Muller, J. Eiglsperger, and J. Madronero, “Interaction of atomic quantum gases with a single carbon nanotube,” *Europhys. Lett.*, vol. 102, p. 33001, May 2013.

[29] A. D. Cronin, J. Schmiedmayer, and D. E. Pritchard, “Optics and interferometry with atoms and molecules,” *Rev. Mod. Phys.*, vol. 81, pp. 1051–1129, Jul 2009.

[30] C. Cohen-Tannoudji and D. Guéry-Odelin, *Advances in Atomic Physics: An Overview*. World Scientific, 2011.

[31] G. M. Tino, L. Cacciapuoti, K. Bongs, C. Borde, P. Bouyer, H. Dittus, W. Ertmer, A. Gorlitz, M. Inguscio, A. Landragin, P. Lemonde, C. Lammerzahl, A. Peters, E. Rasel, J. Reichel, C. Salomon, S. Schiller, W. Schleich, K. Sengstock, U. Sterr, and M. Wilkens, “Atom interferometers and optical atomic clocks: new quantum sensors for fundamental physics experiments in space,” *Nucl. Phys. B, Proc. Suppl.*, vol. 166, pp. 159–65, 2007.

[32] F. Sorrentino, K. Bongs, P. Bouyer, L. Cacciapuoti, M. de Angelis, H. Dittus, W. Ertmer, A. Giorgini, J. Hartwig, M. Hauth, S. Herrmann, M. Inguscio, E. Kajari, T. Könemann, C. Lämmerzahl, A. Landragin, G. Modugno, F. Pereira dos Santos, A. Peters, M. Prevedelli, E. M. Rasel, W. P. Schleich, M. Schmidt, A. Senger, K. Sengstok, G. Stern, G. M. Tino, and R. Walser, “Sai: a compact atom interferometer for future space missions,” *Microgravity Sci. Technol.*, vol. 22, Mar 2010.

[33] F. Sorrentino, Y.-H. Lien, G. Rosi, L. Cacciapuoti, M. Prevedelli, and G. M. Tino, “Sensitive gravity-gradiometry with atom interferometry: progress towards an improved determination of the gravitational constant,” *New J. Phys.*, vol. 12, no. 9, p. 095009, 2010.

[34] S. Herrmann, E. Göklü, H. Müntinga, A. Resch, T. van Zoest, H. Dittus, and C. Lämmerzahl, “Testing fundamental physics with degenerate quantum gases in microgravity,” *Microgravity Science and Technology*, vol. 22, no. 4, pp. 529–538, 2010.

[35] N. Gaaloul, H. Ahlers, T. Schulze, Y. Singh, S. Seidel, W. Herr, W. Ertmer, and E. Rasel, “Quantum tests of the equivalence principle with atom interferometry,” *Acta Astronautica*, vol. 67, pp. 1059 – 1062, 2010.

[36] T. Könemann, W. Brinkmann, E. Göklü, C. Lämmerzahl, H. Dittus, T. van Zoest, E. Rasel, W. Ertmer, W. Lewoczko-Adamczyk, M. Schiemangk, A. Peters, A. Vogel, G. Johannsen,

S. Wildfang, K. Bongs, K. Sengstock, E. Kajari, G. Nandi, R. Walser, and W. Schleich, "A freely falling magneto-optical trap drop tower experiment," *Appl. Phys. B: Lasers Opt.*, vol. 89, no. 4, pp. 431–438, 2007.

[37] T. van Zoest, N. Gaaloul, Y. Singh, H. Ahlers, W. Herr, S. T. Seidel, W. Ertmer, E. Rasel, M. Eckart, E. Kajari, S. Arnold, G. Nandi, W. P. Schleich, R. Walser, A. Vogel, K. Sengstock, K. Bongs, W. Lewoczko-Adamczyk, M. Schiemangk, T. Schuldt, A. Peters, T. Konemann, H. Muntinga, C. Lammerzahl, H. Dittus, T. Steinmetz, T. W. Hansch, and J. Reichel, "Bose-einstein condensation in microgravity," *Science*, vol. 328, pp. 1540–1543, June 2010.

[38] J. Rudolph, N. Gaaloul, Y. Singh, H. Ahlers, W. Herr, T. A. Schulze, S. T. Seidel, C. Rode, V. Schkolnik, W. Ertmer, E. M. Rasel, H. Muntinga, T. Konemann, A. Resch, S. Herrmann, C. Lammerzahl, T. van Zoest, H. Dittus, A. Vogel, A. Wenzlawski, K. Sengstock, N. Meyer, K. Bongs, M. Krutzik, W. Lewoczko-Adamczyk, M. Schiemangk, A. Peters, M. Eckart, E. Kajari, S. Arnold, G. Nandi, W. P. Schleich, R. Walser, T. Steinmetz, T. W. Hansch, and J. Reichel, "Degenerate quantum gases in microgravity," *Microgravity Science and Technology*, vol. 23, pp. 287–292, June 2011.

[39] H. Müntinga, H. Ahlers, M. Krutzik, A. Wenzlawski, S. Arnold, D. Becker, K. Bongs, H. Dittus, H. Duncker, N. Gaaloul, C. Gherasim, E. Giese, C. Grzeschik, T. W. Hänsch, O. Hellmig, W. Herr, S. Herrmann, E. Kajari, S. Kleinert, C. Lämmerzahl, W. Lewoczko-Adamczyk, J. Malcolm, N. Meyer, R. Nolte, A. Peters, M. Popp, J. Reichel, A. Roura, J. Rudolph, M. Schiemangk, M. Schneider, S. T. Seidel, K. Sengstock, V. Tamma, T. Valenzuela, A. Vogel, R. Walser, T. Wendrich, P. Windpassinger, W. Zeller, T. van Zoest, W. Ertmer, W. P. Schleich, and E. M. Rasel, "Interferometry with bose-einstein condensates in microgravity," *Phys. Rev. Lett.*, vol. 110, p. 093602, Feb 2013.

[40] Y. Castin and R. Dum, "Bose-einstein condensates in time dependent traps," *Phys. Rev. Lett.*, vol. 77, pp. 5315–5319, Dec. 1996.

[41] Y. Kagan, E. L. Surkov, and G. V. Shlyapnikov, "Evolution of a bose-condensed gas under variations of the confining potential," *Phys. Rev. A*, vol. 54, pp. R1753–R1756, Sept. 1996.

[42] Y. Kagan, E. L. Surkov, and G. V. Shlyapnikov, "Evolution of a bose gas in anisotropic time-dependent traps," *Phys. Rev. A*, vol. 55, pp. R18–R21, Jan 1997.

[43] G. Nandi, R. Walser, E. Kajari, and W. P. Schleich, "Dropping cold quantum gases on earth over long times and large distances," *Phys. Rev. A*, vol. 76, p. 063617, Dec 2007.

[44] H. Goldstein, *Classical mechanics*. Addison-Wesley world student series, Addison-Wesley Press, 1950.

[45] F. Scheck, *Theoretische Physik 1: Mechanik*. Springer-Lehrbuch, Springer, 2009.

[46] R. Abraham and J. E. Marsden, *Foundations of Mechanics*. AMS Chelsea publishing, AMS Chelsea Pub./American Mathematical Society, 1978.

[47] R. Balescu, *Equilibrium and Nonequilibrium Statistical Mechanics*. John Wiley and Sons, 1975.

[48] J.-P. Serre, *Lie Algebras and Lie Groups*. Springer, 1964.

[49] R. P. Feynman, "An operator calculus having applications in quantum electrodynamics," *Phys. Rev.*, vol. 84, pp. 108–128, Oct 1951.

[50] R. M. Wilcox, "Exponential operators and parameter differentiation in quantum physics," *Journal of Mathematical Physics*, vol. 8, no. 4, pp. 962–982, 1967.

[51] W. Witschel, "Ordered products of exponential operators by similarity transformations," *Int. J. Quantum Chem.*, vol. 20, no. 6, pp. 1233–1241, 1981.

[52] H. Yoshida, "Construction of higher-order symplectic integrators," *Phys. Lett. A*, vol. 150, pp. 262–268, Nov. 1990.

[53] F. Schwabl, *Statistical Mechanics*. Advanced Texts in Physics, Springer, 2006.

[54] C. Gardiner, *Stochastic Methods: A Handbook for the Natural and Social Sciences*. Springer Series in Synergetics, Springer Berlin Heidelberg, 2009.

[55] A. Messiah, *Quantum mechanics*. No. Bd. 1 in Quantum Mechanics, North-Holland Pub. Co., 1961.

[56] L. E. Ballentine, *Quantum Mechanics - A Modern Development*. World Scientific Publ Co Pte Ltd, 1998.

[57] F. Impens and D. Guery-Odelin, "Classical phase-space approach for coherent matter waves," *Physical Review A*, vol. 81, p. 065602, June 2010.

[58] C. J. Borde, "Theoretical tools for atom optics and interferometry," *Comptes Rendus De L Academie Des Sciences Serie Iv Physique Astrophysique*, vol. 2, pp. 509–530, APR-MAY 2001.

[59] V. Arnol'd, *Ordinary Differential Equations*. Springer-Textbook, New York, 1992.

[60] A. Gerrard and J. Burch, *Introduction to Matrix Methods in Optics*. Dover Books on Physics, Dover, 1994.

[61] M. Bonitz, *Quantum Kinetic Theory*. Teubner-Texte zur Physik, Teubner, 1998.

[62] A. A. Vlasov, "The vibrational properties of an electron gas," *Zh. Eksp. Teor. Fiz.*, vol. 8, p. 291, 1938.

[63] L. D. Landau and E. M. Lifshitz, *Statistical Physics*. Elsevier Science, 2013.

[64] O. Penrose, “On the quantum mechanics of helium .2.,” *Philos. Mag.*, vol. 42, no. 335, pp. 1373–1377, 1951.

[65] O. Penrose and L. Onsager, “bose-einstein condensation and liquid helium,” *Phys. Rev.*, vol. 104, no. 3, pp. 576–584, 1956.

[66] M. Hillery, R. F. Oconnell, M. O. Scully, and E. P. Wigner, “Distribution-functions in physics - fundamentals,” *Phys. Rep.*, vol. 106, no. 3, pp. 121–167, 1984.

[67] W. Schleich, *Quantum Optics in Phase Space*. Wiley-VHC, 2001.

[68] A. Messiah, *Quantum mechanics*. No. Bd. 2 in Quantum Mechanics, North-Holland Pub. Co., 1962.

[69] H. Weyl, “Quantenmechanik und gruppentheorie,” *Z. Phys.*, vol. 46, no. 1-2, pp. 1–46, 1927.

[70] H. J. Groenewold, “On the principles of elementary quantum mechanics,” *Physica*, vol. 12, no. 7, pp. 405 – 460, 1946.

[71] J. W. Negele and H. Orland, *Quantum Many-Particle Systems*. Westview Press, 1998.

[72] A. L. Fetter and D. W. Walecka, *Qunatum Theory of Many-Particle Systems*. McGraw-Hill, 1971.

[73] Y. Castin, “Bose-einstein condensates in atomic gases: simple theoretical results,” in *Coherent atomic matter waves*, pp. 1–136, Springer, 2001.

[74] S. Stringari, “Collective excitations of a trapped bose-condensed gas,” *Phys. Rev. Lett.*, vol. 77, pp. 2360–2363, Sept. 1996.

[75] M. Abramowitz and I. A. Stegun, *Handbook of Mathematical Functions*. New York: Dover, 1964.

[76] S. Schmid, A. Härter, and J. Hecker Denschlag, “Dynamics of a cold trapped ion in a bose-einstein condensate,” *Phys. Rev. Lett.*, vol. 105, p. 133202, Sep 2010.

[77] C. Zipkes, S. Palzer, C. Sias, and M. Kohl, “A trapped single ion inside a bose-einstein condensate,” *Nature*, vol. 464, pp. 388–U79, Mar. 2010.

[78] H. B. G. Casimir and D. Polder, “The influence of retardation on the london-van der waals forces,” *Phys. Rev.*, vol. 73, no. 4, pp. 360–372, 1948.

[79] D. Tabor and R. H. S. Winterton, “Direct measurement of normal and retarded van der waals forces,” *Proceedings Of The Royal Society Of London Series A-mathematical And Physical Sciences*, vol. 312, no. 1511, p. 435, 1969.

[80] J. D. Jackson, *Classical Electrodynamics Third Edition*. Wiley, third ed., August 1998.

[81] I. N. Bronshtein, K. A. Semendyayev, G. Musiol, and H. Mühlig, *Handbook of Mathematics*. Springer, 2007.

[82] S. Salsa, *Partial Differential Equations in Action: From Modelling to Theory*. Universitext, Springer, 2008.

[83] H. Fizeau, "Sur les hypotheses relatives a l'ether luminex, et sur une experience qui parait demontrer que le movement des corps change la vitene avec aquelle la lumiere se propage dans leur interjeur," *Ann. Phys. Chem.*, vol. 165, p. 457, 1853.

[84] A. Michelson, "The relative motion of earth and ether," *Am. J. Sci.*, vol. 22, p. 20, 1881.

[85] L. Rayleigh, "On copying diffraction-gratings, and on some phenomena connected there-with," *Philos. Mag.*, vol. 11, p. 196, 1881.

[86] C. Fabry and A. Perot, "Théorie et applications d'une nouvelle méthode de spectroscopie interférentielle," *Ann. Chem. Phys.*, vol. 16, p. 115, 1899.

[87] M. Born, E. Wolf, and A. Bhatia, *Principles of Optics: Electromagnetic Theory of Propagation, Interference and Diffraction of Light*. Cambridge University Press, 1999.

[88] L. de Broglie, "Waves and quanta," *Nature*, vol. 112, p. 540, October 1923.

[89] C. Davisson and L. H. Germer, "Diffraction of electrons by a crystal of nickel," *Phys. Rev.*, vol. 30, pp. 705–740, Dec 1927.

[90] I. Estermann and O. Stern, "Beugung von molekularstrahlen," *Z. Phys.*, vol. 61, no. 1-2, pp. 95–125, 1930.

[91] U. Bonse and H. Rauch, *Neutron interferometry. Proceedings of an international workshop. Institut Max von Laue - Paul Langevin, Grenoble. 5-7 June, 1978*. Oxford, 1979.

[92] P. E. Moskowitz, P. L. Gould, S. R. Atlas, and D. E. Pritchard, "Diffraction of an atomic-beam by standing-wave radiation," *Phys. Rev. Lett.*, vol. 51, no. 5, pp. 370–373, 1983.

[93] D. W. Keith, M. L. Schattenburg, H. I. Smith, and D. E. Pritchard, "Diffraction of atoms by a transmission grating," *Phys. Rev. Lett.*, vol. 61, pp. 1580–1583, Oct 1988.

[94] P. Meystre, *Atom Optics*. Springer, 2001.

[95] P. Meystre and M. Sargent, *Elements of Quantum Optics*. SpringerLink: Springer e-Books, Springer, 2007.

[96] S. Gupta, A. E. Leanhardt, A. D. Cronin, and D. E. Pritchard, "Coherent manipulation of atoms with standing light waves," *Comptes Rendus De L Academie Des Sciences Serie Iv Physique Astrophysique*, vol. 2, pp. 479–495, Apr-may 2001.

[97] C. Keller, J. Schmiedmayer, A. Zeilinger, T. Nonn, S. Durr, and G. Rempe, "Adiabatic following in standing-wave diffraction of atoms," *Appl. Phys. B: Lasers Opt.*, vol. 69, pp. 303–309, Oct. 1999.

[98] P. J. Martin, P. L. Gould, B. G. Oldaker, A. H. Miklich, and D. E. Pritchard, "Diffraction of atoms from a standing light-wave," *Physica B & C*, vol. 151, pp. 255–261, July 1988.

[99] P. L. Gould, G. A. Ruff, and D. E. Pritchard, "Diffraction of atoms by light – the near-resonant kapitza-dirac effect," *Phys. Rev. Lett.*, vol. 56, pp. 827–830, Feb. 1986.

[100] P. L. Kapitza and P. A. M. Dirac, "The reflection of electrons from standing light waves," *Proceedings of the Cambridge Philosophical Society*, vol. 29, p. 297, 1933.

[101] D. L. Freimund, K. Aflatooni, and H. Batelaan, "Observation of the kapitza-dirac effect," *Nature*, vol. 413, pp. 142–143, Sept. 2001.

[102] C. V. Raman and N. S. N. Nath, "the diffraction of light by high frequency sound waves," *Proc. Indian Acad. Sci.*, vol. 2A, p. 406, 1935.

[103] M. K. Oberthaler, R. Abfalterer, S. Bernet, C. Keller, J. Schmiedmayer, and A. Zeilinger, "Dynamical diffraction of atomic matter waves by crystals of light," *Phys. Rev. A*, vol. 60, pp. 456–472, Jul 1999.

[104] S. Bernet, R. Abfalterer, C. Keller, M. K. Oberthaler, J. Schmiedmayer, and A. Zeilinger, "Matter waves in time-modulated complex light potentials," *Phys. Rev. A*, vol. 62, p. 023606, Jul 2000.

[105] M. Kozuma, L. Deng, E. W. Hagley, J. Wen, R. Lutwak, K. Helmerson, S. L. Rolston, and W. D. Phillips, "Coherent splitting of bose-einstein condensed atoms with optically induced bragg diffraction," *Phys. Rev. Lett.*, vol. 82, pp. 871–875, Feb. 1999.

[106] C. Borde, *Atom Interferometry*, ch. Matter-wave interferometers: a synthetic approach. Academic Press Inc, 1997.

[107] P. J. Martin, B. G. Oldaker, A. H. Miklich, and D. E. Pritchard, "Bragg scattering of atoms from a standing light-wave," *Phys. Rev. Lett.*, vol. 60, pp. 515–518, Feb. 1988.

[108] C. G. Shull, "Observation of pendellosung fringe structure in neutron diffraction," *Phys. Rev. Lett.*, vol. 21, no. 23, pp. 1585–&, 1968.

[109] P. P. Ewald, "Zur begründung der kristalloptik," *Ann. Phys.*, vol. 359, no. 23, pp. 519–556, 1917.

[110] S. S. Szigeti, J. E. Debs, J. J. Hope, N. P. Robins, and J. D. Close, "Why momentum width matters for atom interferometry with bragg pulses," *New Journal of Physics*, vol. 14, p. 023009, Feb. 2012.

[111] H. Ammann and N. Christensen, “Delta kick cooling: A new method for cooling atoms,” *Phys. Rev. Lett.*, vol. 78, pp. 2088–2091, Mar 1997.

[112] M. Morinaga, I. Bouchoule, J.-C. Karam, and C. Salomon, “Manipulation of motional quantum states of neutral atoms,” *Phys. Rev. Lett.*, vol. 83, pp. 4037–4040, Nov 1999.

[113] J. M. McGuirk, M. J. Snadden, and M. A. Kasevich, “Large area light-pulse atom interferometry,” *Phys. Rev. Lett.*, vol. 85, pp. 4498–4501, Nov. 2000.

[114] H. Muller, S. W. Chiow, Q. Long, S. Herrmann, and S. Chu, “Atom interferometry with up to 24-photon-momentum-transfer beam splitters,” *Phys. Rev. Lett.*, vol. 100, p. 180405, May 2008.

[115] A. Peters, K. Y. Chung, and S. Chu, “High-precision gravity measurements using atom interferometry,” *Metrologia*, vol. 38, no. 1, pp. 25–61, 2001.

[116] M. Kasevich and S. Chu, “Measurement of the gravitational acceleration of an atom with a light-pulse atom interferometer,” *Appl. Phys. B: Lasers Opt.*, vol. 54, pp. 321–332, May 1992.

[117] A. Griffin, T. Nikuni, and E. Zaremba, *Bose-Condensed Gases at Finite Temperatures*. Cambridge Univ. Press, 2009.

[118] R. W. Hockney and J. W. Eastwood, *Computer Simulation Using Particles*. Taylor & Francis, 1988.

[119] A. R. Krommer and C. W. Ueberhuber, *Numerical Integration: On Advanced Computer Systems*. Lecture Notes in Artificial Intelligence, Springer, 1994.

[120] P. J. Davis and P. Rabinowitz, *Methods of Numerical Integration*. Dover Books on Mathematics Series, Dover Publications, 2007.

[121] `http://docs.scipy.org/doc/scipy-0.14.0/reference/generated/scipy.optimize.curve_fit.html`, May 2014.

[122] `http://docs.scipy.org/doc/scipy-0.14.0/reference/generated/scipy.special.hermite.html`, May 2014.

[123] R. M. Corless, G. H. Gonnet, D. E. G. Hare, D. J. Jeffrey, and D. E. Knuth, “On the lambert w function,” *Adv. Comput. Math.*, vol. 5, no. 4, pp. 329–359, 1996.

Zusammenfassung

Die vorliegende Arbeit beschäftigt sich mit semiklassischen Beschreibungen zweier Anwendungen von kalten Atomen. Dabei handelt es sich zum einen um das Verhalten von BOSE-EINSTEIN Kondensaten in hybriden Systemen, d.h. im Kontakt mit anderen mikroskopischen Objekten (Karbon-Nanoröhrchen, Fullerene etc.). Zum anderen wurde die Evolution von Phasenraum-Verteilungen in Materiewellen-Interferometern mit Hilfe von Raytracing-Methoden untersucht.

Zur Beschreibung von Kondensaten in hybriden Systemen, kann die GROSS-PITAEVSKII-Gleichung, eine Differentialgleichung in der koplexwertigen makroskopischen Wellenfunktion, abgebildet werden auf ein System von zwei Differentialgleichungen in Dichte und Phase. Unter Vernachlässigung der Quantendispersion, erhält man eine semiklassische Beschreibung, die sich sehr einfach modifizieren lässt, um die Wechselwirkung von Kondensat und mikroskopischem Objekt zu berücksichtigen. Diese Wechselwirkung umfasst in unserem Modell attraktive Kräfte (CASIMIR-POLDER-Kräfte) und Verlust kondensierter Atome durch inelastische Stöße an der Oberfläche des mikroskopischen Objekts. Unser Modell zeigte die Anregung von Schallwellen, welche nach dem plötzlichen Eintauchen des Objekts entstehen und sich anschließend über das gesamte Kondensat ausbreiten. Weiterhin führt lokaler Teilchenverlust dazu, dass das Kondensat insgesamt schrupft. Es zeigte sich, dass die Gesamtzahl kondensierter Atome zu Beginn (großes Kondensat, starke Selbst-Wechelwirung) potentiell abnimmt, während sie im Langzeit-Limes (kleines Kondensat, Selbst-Wechelwirkung vernachlässigbar) exponentiell sinkt.

Um die Physik von Materiewellen-Interferometern im Phasenraum darzustellen, benutzten wir die WIGNER-Funktion. In der semiklassischen Näherung, die auch hier wieder in der Vernachlässigung der Quantendispersion besteht, folgt diese der gleichen Bewegungsgleichung wie klassische Phasenraumverteilungen, nämlich der LIOUVILLE-Gleichung. Dies impliziert, dass die Zeitentwicklung von WIGNER-Funktionen dem Phasenraum-Fluss folgt, der durch die klassischen Trajektorien gegeben ist (klassischer Transport). Das heißt um eine Zeit-entwickelte Verteilung zu bestimmen muss man erstens die Anfangsverteilung kennen und zweitens klassische Bewegungsgleichungen lösen.

Bezüglich der Anfangsverteilung haben wir eine stationäre Lösung der nichtlinearen LIOUVILLE-Gleichung, die sog. LAMBERT-Dichte, untersucht. Es zeigte sich, dass diese sehr gut mit Ergebnissen der Einteilchen-Quantenmechanik, sowie der MAXWELL-BOLTZMANN-Verteilung im schwach wechselwirkenden Grenzfall übereinstimmt. Auch im stark wechselwirkenden Grenzfall konnten die bekannten Ergebnisse der THOMAS-FERMI-Näherung reproduziert werden.

Eine Verteilung, die erst in einer Atomfalle präpariert und anschließend freigelassen wird, lässt sich zwar sehr gut mit WIGNER-Funktionen im Rahmen von klassischem Transport beschreiben.

Die Propagation in den optischen Potentialen der Interferometer-Elemente (Strahlteiler-Puls, π-Puls) erfüllen jedoch nicht die Voraussetzung der semiklassischen Näherung. Nichtsdestotrotz findet man diskrete vorher-nachher-Abbildungen, welche die Wirkung dieser Elemente auf WIGNER-Funktionen beschreiben. Dies führt dazu, dass man mehrere Kanäle der Phasenraum-Propagation betrachten muss. Jene beziehen sich auf die verschiedenen Interferometer-Pfade und Interferenzen zwischen ihnen.

Der Formalismus für WIGNER-Funktionen im Interferometer lässt sich nun in einen Raytracing-Algorithmus übersetzen. Dieser löst, wie oben angedeutet, die klassischen Bewegungsgleichungen und konstruiert mit Hilfe der bekannten Anfangsverteilung eine Zeit-entwickelte Verteilung. Er ist dabei nicht auf eine quadratische HAMILTON-Funktion (z.b. freie Propagation, konst. Beschleunigung, harmonischer Oszillator) angewiesen, welche in den meisten Fällen Voraussetzung für analytische Lösungen ist. Wir haben Simulationsergebnisse mit analytischen Resultaten im Fall von frei propagierenden GAUSS-Verteilungen verglichen. Dabei zeigte sich speziell für die funktionale Abhängigkeit von Wellenlänge und Kontrast der Interferenzmuster zu zeitlichen Abständen der Laser-Pulse perfekte Übereinstimmung von Simulation und Theorie.

Publications, Posters, and Talks

- M. Schneider, R. Walser
  "*Probing Carbon Nanotubes with cold gases*"
  Talk at DPG spring meeting 2011, Dresden

- M. Schneider, R. Walser
  "*Using hybrid systems to probe BEC features*"
  Poster at DPG spring meeting 2012, Stuttgart

- M. Schneider, R. Walser
  "*Ray tracing for matter waves*"
  Poster at DPG spring meeting 2013, Hannover

- H. Müntinga, H. Ahlers, M. Krutzik, A. Wenzlawski, S. Arnold, D. Becker, K. Bongs, H. Dittus, H. Duncker, N. Gaaloul, C. Gherasim, E. Giese, C. Grzeschik, T. W. Hänsch, O Hellmig, W. Herr, S. Herrmann, E. Kajari, S. Kleinert, C. Lämmerzahl, W. Lewoczko-Adamczyk, J. Malcolm, N. Meyer, R. Nolte, A. Peters, M. Popp, J. Reichel, A. Roura, J. Rudolph, M. Schiemangk, M. Schneider, S. T. Seidel, K. Sengstock, V. Tamma, T. Valenzuela, A. Vogel, R. Walser, T. Wendrich, P. Windpassinger, W. Zeller, T. van Zoest, W. Ertmer, W. P. Schleich, and E. M. Rasel
  "*Interferometry with Bose-Einstein Condensates in Microgravity*"
  Phys. Rev. Lett. 110, 093602 (2013)

- M. Schneider, R. Walser
  "*Simulating matter wave interferometers with classical rays*"
  Poster at DPG spring meeting 2014, Berlin

- M. Schneider
  "*Semi-classical description of matter wave interferometers*"
  Talk at IAP colloquium 10.02.2015, Darmstadt

- M. Schneider, R. Walser
  "*A uniform continuation of the Thomas-Fermi limit: The Lambert approximation*"
  Paper in preparation

- M. Schneider, R. Walser
  "*Simulating matter wave interferometers with classical rays*"
  Paper in preparation

Curriculum vitae

Mathias Schneider

* 2. Juli 1984 in Bad Schwalbach

Kasier-Wilhelm-Ring 72
55118 Mainz

mathias2784@web.de

Hochschullaufbahn

05.2010 bis heute	Doktorand und Wissenschaftlicher Mitarbeiter in der AG Theoretische Quantendynamik (Prof. Dr. R. Walser), Institut für Angewandte Physik, Darmstadt
02.2009 bis 02.2010	Diplomand in der AG Theoretische Quantenoptik (Prof. Dr. M. Fleischhauer), TU Kaiserslautern
06.2007 bis 04.2010	Hauptstudium in Physik an der TU Kaiserslautern Vertiefungsrichtung: Theoretische Physik Nebenfach: Mathematik **Abschluss: Diplom-Physiker**
10.2004 bis 06.2007	Grundstudium in Physik an der TU Kaiserslautern Nebenfach: Biologie

Schulbildung

08.1995 bis 03.2004	Bischöfliches Willigis-Gymnasium Mainz **Abschluss: Abitur**

Erklärung zur Dissertation

Hiermit versichere ich, die vorliegende Dissertation ohne Hilfe Dritter nur mit den angegebenen Quellen und Hilfsmitteln angefertigt zu haben. Alle Stellen, die aus Quellen entnommen wurden, sind als solche kenntlich gemacht. Diese Arbeit hat in gleicher oder ähnlicher Form noch keiner Prüfungsbehörde vorgelegen.

Darmstadt, den 16. Dezember 2014

(M. Schneider)